HAL
open science

Lasers à pérovskites hybrides halogénées en microcavité

Paul Bouteyre

To cite this version:

Paul Bouteyre. Lasers à pérovskites hybrides halogénées en microcavité. Optique [physics.optics]. Université Paris Saclay (COmUE), 2019. Français. NNT : 2019SACLN069 . tel-02460292

HAL Id: tel-02460292

https://theses.hal.science/tel-02460292

Submitted on 30 Jan 2020

HAL is a multi-disciplinary open access archive for the deposit and dissemination of scientific research documents, whether they are published or not. The documents may come from teaching and research institutions in France or abroad, or from public or private research centers.

L'archive ouverte pluridisciplinaire **HAL**, est destinée au dépôt et à la diffusion de documents scientifiques de niveau recherche, publiés ou non, émanant des établissements d'enseignement et de recherche français ou étrangers, des laboratoires publics ou privés.

université PARIS-SACLAY

école normale supérieure paris–saclay

NNT : 2019SACLN069

Hybrid halide perovskite-based microcavity lasers

Thèse de doctorat de l'Université Paris-Saclay
préparée à Ecole Normale Supérieure Paris-Saclay

Ecole doctorale n°572 Ondes et Matière (EDOM)
Spécialité de doctorat : Optique et photonique

Thèse présentée et soutenue à Orsay, le 18 décembre 2019, par

PAUL BOUTEYRE

Composition du Jury :

Jacqueline Bloch Directrice de recherche, CNRS, C2N (UMR 9001)	Présidente
Sébastien Chenais Professeur des Universités, Université Paris 13, LPL (UMR 7538)	Rapporteur
Joël Leymarie Professeur des Universités, Université Clermont Auvergne (UCA), Institut Pascal (UMR 6602)	Rapporteur
Samuel Stranks Lecturer, Clare College, Cavendish Laboratory	Examinateur
Hai Son Nguyen Maître de Conférences, Ecole Centrale de Lyon, INL (UMR 5270)	Examinateur
Emmanuelle Deleporte Professeure des Universités, ENS Paris-Saclay, LAC (UMR 9188)	Directrice de thèse
Fabien Bretenaker Directeur de Recherche, CNRS, LAC (UMR 9188)	Invité
Qihua Xiong Professeur des Universités, Nanyang Technological University, Singapore	Invité

Thèse de doctorat

Remerciements

Je tiens à exprimer ma profonde gratitude à ma directrice de thèse, Emmanuelle Deleporte, pour sa bienveillance, son soutien et ses conseils lors de ces trois années de thèse. Je la remercie de m'avoir proposé ce sujet de thèse, et de tout le temps passé pour m'aider sur divers aspects, tel que la rédaction de ce manuscrit.

Je remercie Fabien Bretenaker du groupe GLOP du laboratoire Aimé Cotton et Hai Son Nguyen de l'INL Lyon, qui ont co-encadré ma thèse et qui m'ont conseillé dans leurs domaines d'expertise. Je remercie également les autres membres de l'équipe Nanophotonique, Jean-Sébastien Lauret, Damien Garrot et Gaëlle Trippé-Allard, qui m'ont été d'une très grande aide.

Je souhaite remercier tous les membres du jury de ma thèse: Sébatien Chenais et Joël Leymarie, les rapporteurs de mon manuscrit, Jacqueline Bloch, la présidente du jury, Samuel Stranks et Hai Son Nguyen, les examinateurs de ma soutenance, Qihua Xiong et Fabien Bretnaker, membres invités du jury, et bien entendu Emmanuelle Deleporte, ma directrice de thèse.

Je remercie la Direction Générale de l'Armement (DGA) et l'ENS Paris-Saclay, qui ont co-financé ma thèse. Je remercie Philippe Adam, mon tuteur DGA, pour son interêt porté à ma thèse, et qui n'a malheureusement pas pu être présent le jour de ma soutenance.

Je remercie Rasta Ghasemi de l'Institut d'Alembert de l'ENS Paris-Saclay pour le dépôt des couches d'argent. Je remercie également Fabienne Goldfarb et Loïc Rondin, qui m'ont rendu service lors de ma thèse.

Je remercie tous les doctorants, post-doctorants et stagiaires, que j'ai pu recontrer dans l'équipe pérovskite (Hiba, Ferdinand, Géraud, Cosme, Gabriel, Thomas C. et Joanna), l'équipe GLOP (Pascal, Gregory, Yifan, Debanuj, Aliou, Hui et Chitram) et plus généralement au laboratoire Aimé Cotton (Aurélien, Adrien, Caroline, Timothée, François, Thomas L., Feriel, Florian, Julie, Loïc, Clément, Baptiste, Shen, Thibault, Mélissa, Lucile O.C., Lucile V., Kelly, Henri, Benjamin, Raphaël, Lucas et Ky-Luc). J'ai passé un agréable moment en votre compagnie lors de ces trois années au sein du laboratoire, lors des afterworks de folie, des flacs endiablées, des goûters de 17h, des marathons, trails et tri-relais, des recherches insensées d'anagrammes et d'acronymes, des parties de babyfoot et de basket-boulettes enfiévrées (merci l'arbitre!).

Je tiens à remercier ma famille: mes parents, Jean-Yves et Anne, ma soeur Mylène, mon oncle Daniel et ma tante Agnès pour leur soutien lors de mes études et de ma thèse.

Enfin, un grand merci à My de m'avoir beaucoup soutenu pendant la rédaction de ma thèse et la préparation de ma soutenance. Je te souhaite bon courage pour la fin de ta thèse, et je serai là bien entendu pour te soutenir également!

Contents

Introduction **1**

1 The halide perovskites for green laser emission **5**

1 "Conventional lasing" vs. "Polaritonic lasing" 6

1.1 The optically active material 7

1.1.1 Exciton in a semiconductor 7

1.1.2 The oscillator strength 11

1.1.3 The refractive index 12

1.2 The microcavity photonic mode 15

1.3 The weak and strong coupling regimes 17

1.3.1 Preamble 17

1.3.2 Quantum description: the simple model of the two-level oscillator 18

1.3.3 Weak coupling regime 19

1.3.4 Strong coupling regime 20

1.3.5 Classical description of the strong coupling regime 23

1.4 Polaritonic lasing : the case of a laser based on a microcavity in strong coupling regime 25

1.4.1 Photoluminescence of a microcavity in the strong coupling regime 25

1.4.2 Polaritonic lasing 28

1.4.3 Differences between polaritonic and photonic lasing 32

2 Halide perovskites: a new material for lasers in the weak and strong coupling regimes 37

2.1 Characteristics of halide perovskites 38

2.1.1 The 3D halide perovskites 38

2.1.2 The low-dimensional perovskites 40

2.2 Laser in the weak coupling regime with halide perovskites 42

2.2.1 The green gap for solid-state emitting devices 42

2.2.2 Lasing in the weak coupling regime with halide perovskites . 42

2.3 Strong coupling with perovskites: towards perovskite-based polaritonic lasers 49

2.3.1 Context: the strong coupling and polariton lasing in the literature . . . 49
2.3.2 Strong coupling regime and polariton lasing with 2D perovskites . . . 51
2.3.3 The strong coupling regime and polariton lasing with 3D perovskites . . . 58
2.3.4 Summary of halide perovskite-based polaritons . . . 65
3 Conclusion of the chapter . . . 66

2 Experimental methods **69**
1 Deposition methods of the microcavity layers . . . 70
1.1 Spin-coating method . . . 70
1.2 Deposition of the MAPB perovskite . . . 71
1.2.1 One-step deposition . . . 71
1.2.2 Two-step deposition . . . 72
1.3 Deposition of the PMMA layer . . . 73
1.4 Deposition of the silver layer . . . 74
2 Methods for the layers characterizations . . . 74
2.1 Optical microscope . . . 74
2.2 Contact profilometry . . . 74
2.3 Atomic Force Microscopy (AFM) . . . 74
2.4 Spectrophotomer Perkim Elmer . . . 75
2.4.1 Absorption measurements . . . 75
2.4.2 Diffuse reflectance . . . 75
2.4.3 Specular reflectivity measurements . . . 76
3 Optical experimental set-ups . . . 76
3.1 Optical instruments . . . 76
3.1.1 Laser and white light sources . . . 76
3.1.2 Spectrometers and CCD . . . 77
3.1.3 Objectives and Lenses . . . 77
3.2 PL spectroscopy . . . 78
3.2.1 Principle . . . 78
3.2.2 Set-up number 1 in "LAC" laboratory . . . 78
3.2.3 Set-up number 2 in "LAC" laboratory . . . 79
3.3 µPL . . . 79
3.4 Fourier spectroscopy . . . 79
3.4.1 Principle . . . 79
3.4.2 Focal length of the Fourier Lens . . . 80
3.4.3 Maximum distance between the fourier lens and the spectrometer lens . . . 81
3.4.4 Correction of the measured PL and reflectivity maps . . . 82

3.4.5 Raw data processing of the CCD camera results 83
3.4.6 Set-up in "INL" laboratory 85
3.4.7 Set-up in "LAC" laboratory 85
4 Conclusion of the chapter 86

3 Design, fabrication and characteristics of the MAPB based microcavity 87
1 Simulation of the passive cavity 88
1.1 The commercial Bragg mirror 88
1.2 The refractive indices used for the simulation 90
1.3 Simulation of the passive microcavity 91
1.4 Calculation of the effective refractive index 92
2 Deposition and characterization of the optically active layer : the MAPB layer 93
2.1 Microscope images of the MAPB layers 93
2.2 Photoluminescence and absorption of the MAPB Layer 94
2.3 Profilometry of the MAPB layers 96
2.4 AFM image of the MAPB layer 97
3 Deposition and characterization of the spacing layer : the PMMA layer . . . 98
3.1 Empirical law for the PMMA thickness 98
3.2 Microscopy images of the PMMA layers 99
3.3 Profilometry of the deposited PMMA layer 99
3.4 AFM image of the MAPB+PMMA layer 100
4 Deposition of the closing silver mirror 101
5 Summary of the different roughnesses 101
6 Characterization of the complete microcavity 102
6.1 Variation of the detuning 102
6.2 Reflectivity spectrum 104
7 Conclusion of the chapter 106

4 Strong coupling regime in the 3λ/2 MAPB-based microcavity 107
1 Motivations 108
2 Reflectivity spectra obtained with the spectrophotometer 108
3 Angle-resolved photoluminescence and angle-resolved reflectivity by Fourier spectroscopy 110
4 Fitting of the polaritonic dispersions 111
4.1 Collection of the experimental dispersions 111
4.2 Fitting of the experimental dispersions 111
4.3 Discussion on the obtained parameters 113
4.4 Final results on the ARR and ARPL maps 115
5 Bottleneck effect of the lower polariton photoluminescence 117
6 Discussion on the MAPB exciton stability at room temperature 118
7 Simulations of the results 120

7.1 Influence of the roughness on the simulated reflectivity and photoluminescence . . . 120
7.1.1 Simulation of reflectivity spectra obtained with the spectrophotometer . . . 120
7.1.2 Simulation of the angle-resolved reflectivity and photoluminescence maps . . . 122
7.2 Influence of the MAPB refractive index . . . 126
7.2.1 Simulation with an experimental extinction coefficient . . . 127
7.2.2 Simulation with a customized MAPB refractive index . . . 129
7.3 Predictions of the strong coupling for other microcavity designs . . . 133
8 Conclusion of the chapter . . . 135

5 Lasing action of the 3λ/2 MAPB-based microcavity 137
1 Concept of the random lasing . . . 138
1.1 Introduction to random lasing . . . 138
1.2 Characteristics of the random lasing with coherent feedback . . . 139
2 Random lasing of the MAPB/PMMA layer . . . 141
2.1 PL spectroscopy of the MAPB/PMMA sample . . . 141
2.2 Angle-resolved photoluminescence of the MAPB/PMMA sample . . . 144
2.3 Discussion on the nature of the random lasing . . . 144
3 Lasing action of the 3λ/2 MAPB-based microcavity . . . 145
3.1 PL spectroscopy of the 3λ/2 MAPB-based microcavity . . . 145
3.2 Angle-resolved photoluminescence of the 3λ/2 MAPB-based microcavity . . . 148
3.3 Expected emission angles and emission divergences . . . 151
3.4 Discussion on the nature of the microcavity lasing . . . 154
4 Conclusion of the chapter . . . 155

Conclusion 157

Appendices III
A Control measurements for the pump power-dependent measurements in Chapter 5 . . . III
B Conversion of the lasing thresholds . . . IV
C Additionnal data for the ARPL maps in Chapter 5 . . . V
C.1 Position RL2 in figure 5.6 . . . V
C.2 Position 1 in figure 5.12 a) . . . VI
C.3 Position 2 in figure 5.12 b) . . . VII
C.4 Position 3 in figure 5.12 c) . . . VIII
C.5 Position 4 in figure 5.12 d) . . . IX
D Fit with the two-level system of the ARPL maps in Chapter 5 . . . X
E Slices at given angles and energies of the ARPL maps in Chapter 5 . . . XI

F Estimation of the polariton propagation length XII

Bibliography **XXXVII**

Résumé de la thèse **XXXIX**

Introduction

Today, any new technology permitting a reduction of energy consumption is welcome to cope with global warming. In the context of lighting, which accounts for 15% of worldwide electricity consumption and 5% of global greenhouse gas emissions, light-emitting diodes (LEDs) has emerged as a breakthrough due their high power conversion efficiencies and low cost compared to the incandescent bulbs. In this respect, the Nobel Prize of Physics in 2014 was awarded jointly to Isamu Akasaki, Hiroshi Amano and Shuji Nakamura for their pioneering work in the early 1990s on high-performance blue-emitting LEDs [1]. On the other hand, laser diodes, which are similar to the LEDs, are the most common type of lasers. Their directional and coherent light is useful for a wide range of applications such as for optical fibre telecommunication, lasing printing, DVD and Blu-rays. However, the solid-state emitting devices, LEDs and laser diodes, suffer from a drop of efficiency when emitting in the green wavelength region. This problem is commonly referred to as the "green gap problem" [2–4]. Much research is therefore conducted to improve the already used materials to bridge the green gap. Another approach is, however, to look at different materials which would permit to obtain light-emitting devices with high efficiencies in the green region.

Another breakthrough in the early 1990s in the research community was the first experimental observation of cavity exciton-polaritons in 1992 by Weisbuch et al. [5]. The cavity exciton-polaritons results from the strong coupling regime between a photonic mode in a microcavity and the excitons of a semiconductor, electron-hole pairs bound by Coulomb interaction. As a result, the exciton-polaritons are coherent superpositions of the photonic and excitonic states. More simply, one can see the excitons–polaritons as half-light half-matter quasiparticles. Intriguing physical properties are inherited due to the hybrid nature of the exciton-polaritons and one of which is the Bose-Einstein condensation of exciton-polaritons which was first theoretically proposed in 1996 by Imamoglu et al.[6] and experimentally demonstrated in 2006 by Kasprzak et al. [7]. The polariton condensation in a microcavity results in an emission of an amplified coherent light and is consequently also referred to as polaritonic lasing. This peculiar lasing mechanism allows reaching lasing thresholds two orders of magnitude lower than the usual lasers. This threshold reduction would lead to a reduction of electrical consumption of solid-state lasers, which explain the keen interest from the research community on exciton-polaritons.

Recently, the 3D hybrid halide perovskites ($CH_3NH_3PbX_3$, with X a halogen (I, Br, Cl)) and derivatives have gained much attention in the semiconductor community. 3D halide perovskites have first emerged in 2012 within the framework of photovoltaics with perovskite-based solar cells reaching today efficiencies of 25.2% [8], which is higher than the polycrystalline Silica-based solar cells. One of the crucial advantages of such halide perovskites is their low-temperature and solution-processed deposition methods which represent a low cost of production. Additionally, since 2014, the halide perovskites have been found to possess excellent emission properties [9–11]. For example, the halide perovskites emission wavelengths can be tuned in the entire visible spectrum via chemistry substitutions [12]. Moreover, exciton-polaritons have previously been observed on the 2D perovskites counterparts before the thesis started. Even though the lasing actions are obtained via optical pumping, the good charge transport properties of the perovskites [13, 14] give hope towards the realization of halide perovskite-based diode lasers or even polaritonic lasers emitting in a broad range of wavelengths, including the green region.

In the context of the green gap problem for the solid-state lasers and the new coming halide perovskite-based lasers, I studied, in this PhD, microcavities containing the green-emitting bromide perovskite $CH_3NH_3PbBr_3$ in the prospect of obtaining a perovskite-based polaritonic laser.

Chapter 1 first introduces the physical concepts of the weak and strong coupling regimes needed to understand the excitons-polaritons and the differences between the conventional lasers and the polaritonic lasers. The second part of the chapter concerns the state of the art of conventional lasers based on halide perovskites. Finally, the state of the art of the strong coupling regimes obtained with halide perovskites is detailed as well as the reported halide perovskite polaritonic lasing actions. The halide perovskites are confronted to other materials regarding the strong coupling regime.

The perovskite green laser developed in this thesis is at the crossroads of several very active topics. Therefore, Chapter 1 is the longest chapter of this PhD manuscript as different states of the art are detailed as exhaustively as possible. Most of the work on 3D halide perovskite lasing and strong coupling reviewed in this chapter concerns studies published during the preparation of the PhD thesis; only a few were published beforehand.

Chapter 2 presents the experimental methods used during the thesis. The perovskite spin-coating deposition methods and the characterization instruments are first introduced. Finally, the experimental optical set-ups are detailed: the photoluminescence (PL) spectroscopy set-up and the Fourier spectroscopy set-up allowing to perform angle-resolved reflectivity and photoluminescence measurements.

Chapter 3 details the design, the conception and the characterization measurements of the $CH_3NH_3PbBr_3$-based microcavity. A large surface $3\lambda/2$ $CH_3NH_3PbBr_3$-based microcavity is then fabricated and its roughness is studied.

In chapter 4, the strong coupling regime of the $CH_3NH_3PbBr_3$-based microcavity is demonstrated in both angle-resolved reflectivity and photoluminescence measurements. In this chapter, the microcavity is pumped at low densities. This result is particularly important for the perovskite community as it is the first observation of the strong coupling regime containing a spin-coated layer of 3D perovskite. Moreover, the strong coupling regime is obtained with a large surface gain medium with a low production cost and with good charge transport properties. This is interesting regarding polaritonic devices. This work led to a publication in ACS Photonics [15].

In Chapter 5, the lasing action of the $CH_3NH_3PbBr_3$-based microcavity is studied. A random lasing emitting in the green and directionally filtered by the lower polariton dispersion curve was demonstrated in the bromide perovskite-based microcavity. The angle of emission can be controlled by changing the microcavity detuning. The results is interesting for the fundamental physics as it combines two intriguing physical phenomena: the cavity exciton-polariton and the random lasing. The control of the random lasing emission direction is also interesting for optoelectronic applications. The results presented in this chapter are in preparation for a second publication.

Chapter 1

The halide perovskites for green laser emission

Contents

1 "Conventional lasing" vs. "Polaritonic lasing" 6

1.1 The optically active material 7

1.2 The microcavity photonic mode 15

1.3 The weak and strong coupling regimes 17

1.4 Polaritonic lasing : the case of a laser based on a microcavity in strong coupling regime 25

2 Halide perovskites: a new material for lasers in the weak and strong coupling regimes 37

2.1 Characteristics of halide perovskites 38

2.2 Laser in the weak coupling regime with halide perovskites 42

2.3 Strong coupling with perovskites: towards perovskite-based polaritonic lasers 49

3 Conclusion of the chapter 66

Introduction

This chapter aims at describing the state of the art of halide perovskites in the context of solid-state lasers. The halide perovskites are compared in terms of laser performance with different materials such as inorganic semiconductors, organic materials, emerging new materials such as the transition metal dichalcogenides (TMDs). In this chapter, two modes of lasers are considered: the lasers in weak coupling regime, referred as conventional lasers, and the lasers in strong coupling regime, the polaritonic lasers. The first part of this chapter describes the theoretical background used in the thesis, namely the weak and strong coupling regimes between a semiconductor exciton, electron-hole pair bound by Coulomb interaction, and the photonic mode of a planar microcavity. This section then describes the differences between conventional lasers and polaritonic lasers. Finally, the second part of the chapter introduces the halide perovskites and presents the state of the art of the halide perovskite-based lasers in weak coupling, the strong coupling with halide perovskites and the halide perovskite-based polaritonic lasers.

1 "Conventional lasing" vs. "Polaritonic lasing"

Two different regimes can occur when an optically active material is coupled to a photonic mode of a photonic structure: strong and weak coupling regimes. The nature of the coupling depends on whether the light-matter interaction overcomes the photonic mode and material losses. The case of the weak coupling corresponds to the conventional lasers: the optical resonator defines the lasing emission wavelength. In the strong coupling regime, photonic and emitter states are mixed and give rise to polaritons, bosonic quasi-particles, which are coherent superpositions of the two states. In our case, we focus on exciton-polaritons arising from the strong coupling between the exciton of organic or inorganic materials and the photonic mode of a planar microcavity. As bosonic quasiparticles, the Bose-Einstein condensation of exciton-polaritons can take place when polariton population at the fundamental state exceed unity. And the so called polariton laser is the coherent emission of photons escaping from the Bose-Einstein condensate. In this section, we first introduce the concepts needed for the optically active material: the excitonic state, the oscillator strength of an optical transition, and the Lorentz oscillator model for the complex refractive index. In a second time, the photonic mode of a microcavity is described. In a third time, the theoretical aspects of the weak and strong coupling regimes are presented, and finally, the mechanisms of lasers in weak and strong coupling are detailed.

1.1 The optically active material

1.1.1 Exciton in a semiconductor

Electronic band in a semiconductor

In a semiconductor, the available energy levels of the electrons are in the form of a valence band and a conduction band separated by the gap energy, E_G. At zero temperature, the valence band is the highest fully occupied band, and the conduction band the lowest unoccupied one. The electrons of the valence band correspond to the electronic outer shell of atoms and participate in the chemical bondings in the crystal. Under an excitation (thermal energy, optical excitation, etc..) the electrons at the top of the valence band can be promoted to the conduction band. The promoted electrons can then freely move and participate in the material conduction. Simultaneously, the vacancy of the promoted electron in the valence band behaves as a quasi-particle, the hole, with a positive charge, $+e$, with e the elementary charge.

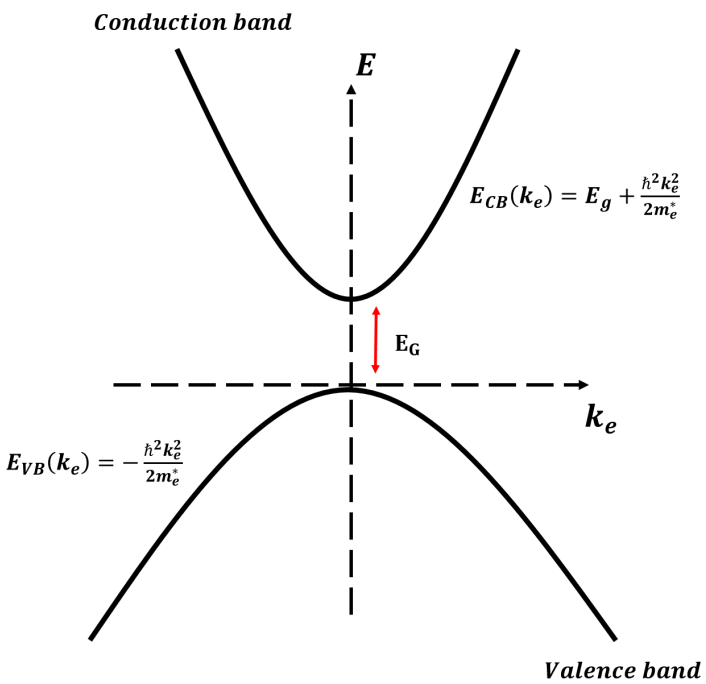

Figure 1.1: Energy dispersion of a semiconductor

The valence and conduction bands are dependent on the electron wavenumber, k_e. In the case of direct band-gap semiconductors, the bottom of the conduction band and the top of the valence band are situated at the same wavevector, considered null here for simplicity. At low momenta around this point, the valence and conduction band dispersion curves can be approximated as parabolas, shown in figure 1.1, and whose respective dispersion curves are given by equation 1.1:

$$\mathrm{E_{CB}}(k_e) = \mathrm{E_G} + \frac{\hbar^2 k_e^2}{2m_e^*} \quad \text{and} \quad \mathrm{E_{VB}}(k_e) = 0 - \frac{\hbar^2 k_e^2}{2m_h^*}, \tag{1.1}$$

where the top of the valence band is taken as the energy origin, m_e^* is the electron effective mass and m_h^* the hole effective mass. Note that the hole behaves like an electron with a positive charge and an inverted energy dispersion with respect to the momentum axis.

Absorption and Photoluminescence of semiconductors

Figure 1.2 a) shows the direct band-gap semiconductor absorption process. When an electron of the valence band absorbs a photon of energy $\hbar\omega$ larger that the gap energy $\mathrm{E_G}$, the electron is promoted to the conduction band and a hole is promoted to the valence band, creating an electron-hole pair. The absorption coefficient of a 3D semiconductor is then null for photon energies below the gap energy and is proportional to the density of state of a 3D semiconductor, i.e $(\hbar\omega - \mathrm{E_G})^{\frac{1}{2}}$ [16] (See figure 1.2 b)).

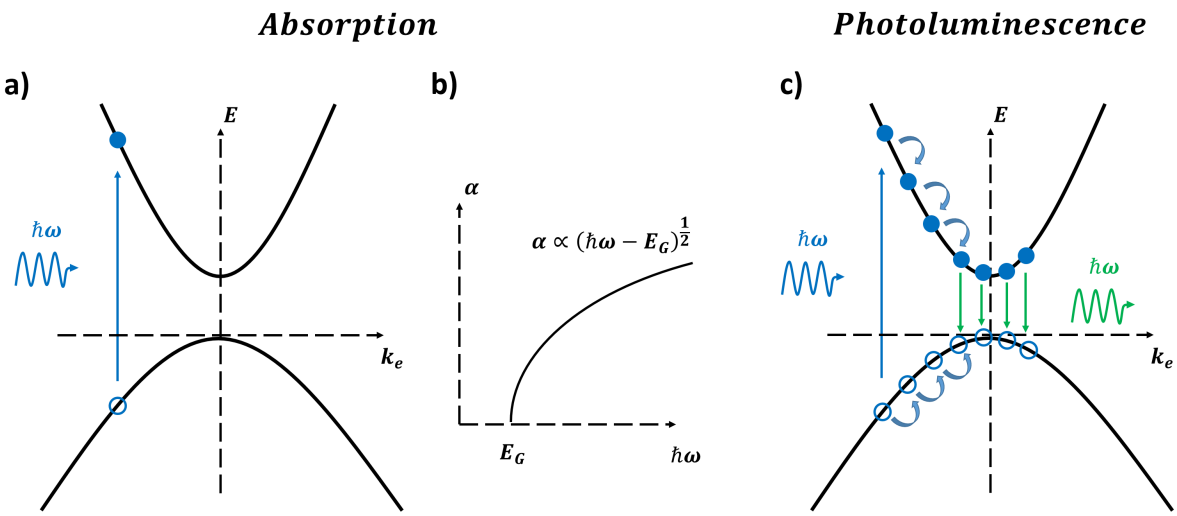

Figure 1.2: Absorption and photoluminescence processes in a semiconductor

Semiconductors can emit light through the processes of electroluminescence and photoluminescence. In the first process, the electron is excited via current injection into the semiconductor and in the second process by shining the semiconductor with photons of energies higher than the bang gap energy as shown in figure 1.2 c). Only the second process will be considered in the following as only optical excitation has been performed in this thesis. As described above, electron-hole pairs are created when the semiconductor absorbs photons of energy $\hbar\omega$. The electrons and the holes then relax along their respective bands by emitting phonons, vibration modes within the crystals. Electrons (holes) then accumulate at the bottom (top) of the conduction (valence) band with an energy spectrum width of about the thermal energy, $k_\mathrm{B}\mathrm{T}$. Finally, electrons and holes of the same momentum recombine by emitting a photon at an energy close to the bandgap energy.

However, in some semiconductors, resonances occur in the absorption spectrum at energies lower than the energy gap, and the photoluminescence (PL) is redshifted with respect to the energy gap. These resonances cannot be described without taking into consideration the Coulomb interaction between the negatively charged electron and the positively charged hole, which gives rise to a new quasi-particle: the exciton.

Excitons

An exciton in a semiconductor is a quasi-particle formed by an electron-hole pair bonded by the Coulomb interaction [16]. Two types of excitons can be observed (see figure 1.3): the Wannier-Mott exciton (free exciton) and the Frenkel exciton (tightly bound exciton). The Wannier-Mott excitons occur mainly in inorganic semiconductors, their radii cover several atoms of the lattice, and the exciton can be considered as moving freely within the crystal and is then referred to as free exciton. The Frenkel excitons are more generally observed in organic semiconductors, and their radii are comparable to the inter-atomic distance of the lattice. In this case, the excitons are tightly bound to one atom of the lattice, which hinders its mobility. In the following, only the Wannier-Mott excitons (free excitons) are considered.

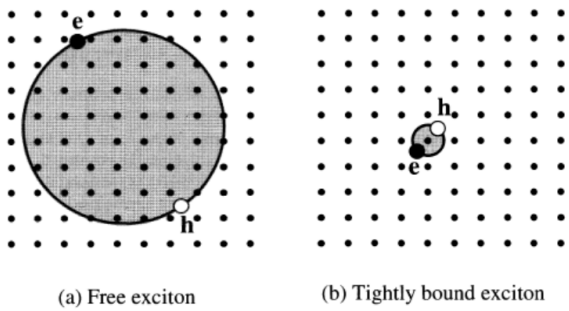

Figure 1.3: Two types of excitons in a crystal : the Wannier-Mott exciton and the Frenkel exciton. Extracted from [16]

As the radius of the free exciton is much larger than the lattice inter-atomic distance, the dielectric constant, ϵ_r, of the environment surrounding the exciton can be considered as uniform. Such as the hydrogen atom, the free exciton is composed of a positive and a negative charge bonded by the Coulomb interaction. Hence, the solutions from the Schrödinger equation of the hydrogenoid model can be extrapolated. This results, for the free exciton, into discrete available binding energies, E_b^n, with their corresponding discrete available radii, r_X^n, both related to the principal quantum number n given by:

$$\mathrm{E}_b^n = \frac{m_\mathrm{X}^*}{m_0}\frac{1}{\epsilon_r^2}\frac{\mathrm{R_H}}{n^2} = \frac{\mathrm{R_X}}{n^2} \quad \text{and} \quad r_\mathrm{X}^n = \frac{m_0}{m_\mathrm{X}^*}\epsilon_r n^2 a_\mathrm{H} = n^2 a_\mathrm{X}, \tag{1.2}$$

where m_0 is the free electron mass, ϵ_r the relative permittivity, $m_\mathrm{X}^* = (m_e^* m_h^*)/(m_e^* + m_h^*)$ the reduced exciton mass (m_e^* and m_h^* are the electron and hole effective masses, respec-

tively), R_H the Rydberg constant and a_H the Bohr radius. One can introduce the exciton Rydberg constant $R_X = (\frac{m_X^*}{m_0}\frac{1}{\epsilon_r^2})R_H$ and the exciton Bohr radius $a_X = \frac{m_0\epsilon_r}{m_X^*}a_H$. The excitons are then characterized by their binding energy, E_b, and radius, r_X, inversely proportional to the binding energy. An exciton is stable when its binding energy is larger than the phonon mode energies. The most energetic phonon for a given temperature has an energy of the order of the thermal energy k_bT. An exciton is then considered stable when its binding energy is higher than the thermal energy, i.e. $E_b > k_bT$. For the free excitons, the binding energies are of the order of a few to tens of meV.

Like the hydrogen atom, the energies available for the free excitons, E_X^n, lie relatively to their ionization limit, which is here at the gap energy E_G, leading to:

$$E_X^n = E_G - E_b^n, \tag{1.3}$$

where E_b^n is the binding energy of the exciton in the nth level. In general, the binding energy, E_b, refers to the binding energy of the exciton in the ground state, i.e. when n=1.

As the excitons are composed of electrons and holes, their energies are also dispersive and depend on the exciton momentum $k_X = k_e + k_h$. The exciton energy dispersion can be approximated for low momenta by a parabolic dispersion as shown in figure 1.4 a) :

$$E_X^n(k_X) = E_{X0}^n + \frac{\hbar^2 k_X^2}{2M_X^*}, \tag{1.4}$$

where $E_{X0}^n = E_G - E_b^n$ is the exciton energy at $k_X = 0$ and $M_X^* = m_e^* + m_h^*$ the exciton total effective mass.

Figure 1.4 b) shows the absorption of a semiconductor exhibiting free excitons. It is composed of the continuum absorption of the electron-hole pairs at energies higher than the gap energy (see figure 1.2) and by the resonances at each exciton energy with a linewidth γ_X. The exciton linewidth quantifies the losses of the exciton, which depend on many factors such as its coupling with the radiative continuum, optical and acoustical phonon vibrations, non-radiative trapping. The losses lead to a finite coherence lifetime of the exciton $t_X = \frac{\hbar}{\gamma_X}$.

From equation 1.2, the ground state free exciton, $n = 1$, has the largest binding energy and the smallest radius. The excited excitons, $n \geq 1$, have lower binding energies and larger radii, which make them less stable than the ground state excitons. In general, only the free excitons at the ground state are observed due to their increased stability and larger distance from the absorption continuum. For these reasons, only the ground state free exciton will be considered in the following with an energy noted E_X :

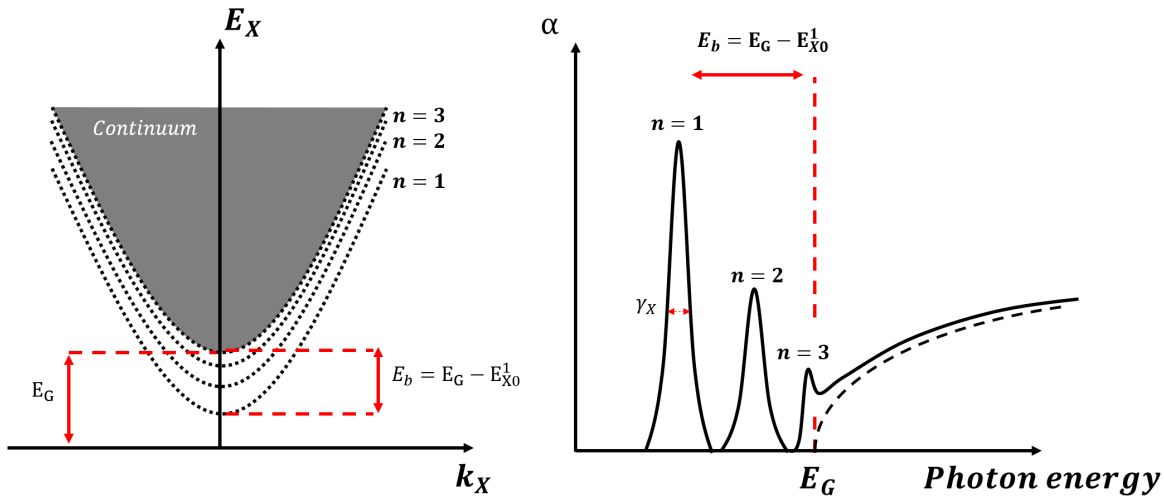

Figure 1.4: a) Energy dispersion of an exciton b) Absorption of a semiconductor exhibiting an exciton

$$E_X(k_X) = E_{X0} + \frac{\hbar^2 k_X^2}{2M_X^*}. \tag{1.5}$$

1.1.2 The oscillator strength

The oscillator strength, f_{osc}, is a dimensionless quantity between 0 and 1 describing the strength of a given electronic transition, i.e. the probability for the transition to occur. This quantity characterizes the radiative coupling between the transition and the electromagnetic environment. Thus for light-matter interaction applications, a large oscillator strength is desired. For instance, in the case of an exciton, the lower the exciton radius (i.e. the higher the exciton binding energy), the larger the exciton oscillator strength. Indeed, the probability of radiative recombination of an electron-hole pair increases when the electron and the hole are closer within the crystal.

In the quantum description, the oscillator strength of a transition between two energy levels is proportional to the square transition dipole moment multiplied by the energy difference between the two levels[17]:

$$f_{osc} = \frac{2m_0}{3\hbar^2}(E_f - E_i)|\langle i|\mathbf{d}|f\rangle|^2, \tag{1.6}$$

where m_0 is the electron mass, $\hbar$ the reduced Planck constant, $E_{i,f}$ the initial and final energy levels and $|\langle i|\mathbf{d}|f\rangle|^2$ the square of the transition dipole matrix.

In general, this relation is not practical to measure the oscillator strength of a given transition in a material. The oscillator strength can, however, be obtained from the absorption spectra as it is the parameter which determines the intensity of the transition absorption line. When the transition absorption can be approximated by a Gaussian func-

tion, the oscillator strength can be obtained by integrating the absorption coefficient over the transition resonance [18]:

$$f_{osc} = \frac{m_0 c}{N\pi e^2} \int \alpha(\nu) d\nu, \tag{1.7}$$

where N (cm^{-3}) is the absorber concentration, c the light velocity, e the fundamental charge and ν the photon frequency.

Another method to obtain the oscillator strength from a material is by fitting the dielectric function with the Lorentz oscillator model or similar models. The Lorentz oscillator model will be further discussed in the following section describing the material refractive index.

1.1.3 The refractive index

The complex refractive index of a material is defined by $\tilde{n} = n + ik$ with n the refractive index and k the extinction coefficient. It classically describes the propagation of light in a material and thus is an important feature to consider when studying light-matter interaction. The refractive index is related to the complex dielectric constant of the material, $\tilde{\epsilon} = \epsilon_1 + i\epsilon_2$ and the relative permeability constant of the material, μ_r. For the non-magnetic materials, in which $\mu_r = 1$, the expression of the refractive index is:

$$n = \sqrt{\frac{1}{2}[\sqrt{\epsilon_1^2 + \epsilon_2^2} + \epsilon_1]} \quad \text{and} \quad k = \sqrt{\frac{1}{2}[\sqrt{\epsilon_1^2 + \epsilon_2^2} - \epsilon_1]}. \tag{1.8}$$

The material energy-dependent absorption coefficient can also be derived from the dielectric function and depends on the extinction coefficient k, not to be confused with the wavenumber k:

$$\alpha(E) = \frac{4\pi E k(E)}{hc}. \tag{1.9}$$

In order to obtain the refractive index and the absorption coefficient of a material, one should get its dielectric constant. The Lorentz oscillator model is a theoretical approach to describe the energy-dependent dielectric constant of a material.

The Lorentz model

In the Lorentz oscillator model, the electrons are considered to be bound to the atom nucleus by a spring-like force. When an applied electric field interacts with the electron's charge, the electron is moved from its position, and the spring-like force pushes the electron back to its original position. As a consequence, the electron oscillates around its equilibrium position. The electrons displacements then create a dipole moment which produces a dielectric susceptibility $\tilde{\chi} = 1 - \tilde{\epsilon}$. When the applied electric field is oscillating

with a pulsation ω, one can retrieve the relation between the complex dielectric constant, $\tilde{\epsilon}$, as a function of the electric field frequency [16]:

$$\tilde{\epsilon}(\omega) = 1 + \frac{Ne^2}{m_0\epsilon_0}\frac{1}{(\omega_0^2 - \omega^2 + i\eta\omega)}, \tag{1.10}$$

where ϵ_0 is the vacuum electric permittivity, N the electron density, m_0 the mass of the electron, e the elementary charge, ω_0 and η are the resonant frequency and the damping constant of the oscillator.

Usually, the optically active materials have several absorption resonances, and so the dielectric function can be considered as the sum of several Lorentz oscillators as such:

$$\tilde{\epsilon}(\omega) = \epsilon_\infty + \frac{Ne^2}{m_0\epsilon_0}\sum\frac{f_j}{(\omega_{0j}^2 - \omega^2 + i\eta_j\omega)}. \tag{1.11}$$

We insert here ϵ_∞ the permittivity at high frequency and f_j the dimensionless oscillator strength for each oscillator. From the Lorentz oscillator model, the oscillator strengths are all equal to 1, meaning that all the resonances participate with the same intensity to the light absorption process. However, experiments show that the oscillator strengths vary for different resonances with values less than 1, i.e. $f_j < 1$. The equation 1.11 generalizes the Lorentz model to several transitions with different oscillator strengths.

After multiplying by the constant $\hbar^2$ the nominator and the denominator of the fraction in equation 1.11, one can get the energy-dependent dielectric function:

$$\tilde{\epsilon}(E) = \epsilon_\infty + \sum\frac{A_j}{(E_{0j}^2 - E^2) + i\gamma_j E}, \tag{1.12}$$

where $A_j(eV^2) = (Ne^2\hbar^2)/(m_0\epsilon_0)$ is the constant related to the oscillator strength of an oscillator, E_{0j} (eV) is the resonance energy of the oscillator, γ_j (eV) is the homogeneous linewidth and E (eV) the photon energy.

Figure 1.5 shows the dielectric function, the refractive index, and the absorption coefficient for an example of two oscillators using equations 1.12, 1.8 and 1.9. In this example, one sharp oscillator is located at 2.3 eV ($E_{01} = 2.3$ eV, $A_{01} = 50$ eV^2, $\gamma_{01} = 200$ meV) and another oscillator at 4.2 eV ($E_{02} = 4.2$ eV, $A_{02} = 200$ eV^2, $\gamma_{02} = 800$ meV). The permittivity at high frequency, ϵ_∞, was set at 10. The figures show that an oscillator gives a Lorentzian shape to the extinction and absorption coefficients, k and α. The intensity of the Lorentzian is proportional to the oscillator strength, f_j, the width to the homogeneous linewidth γ_j and the position to E_{0j}. The oscillator also affects the real part of refractive index n in the same energy region with the shape of a Lorentzian derivative.

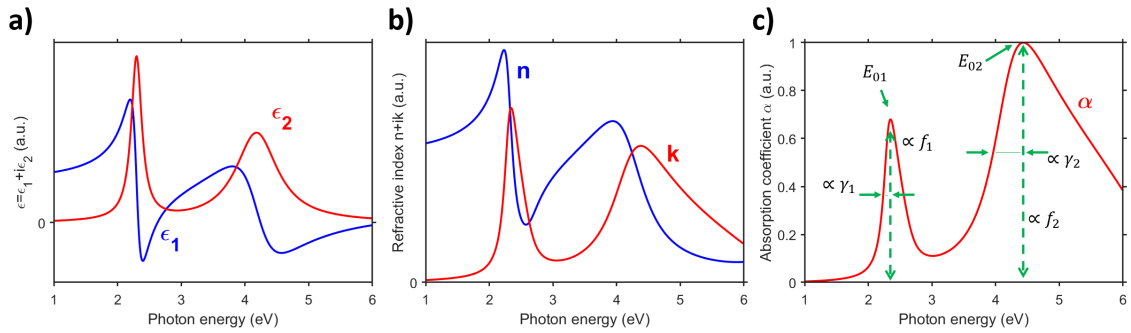

Figure 1.5: Example of a system exhibiting two Lorentz oscillators ($E_{01} = 2.3eV$, $A_{01} = 50eV^2$, $\gamma_{01} = 200meV$, $E_{02} = 4.2eV$, $A_{02} = 200eV^2$, $\gamma_{02} = 800meV$, ϵ_∞=10). a) Dielectric constant $\epsilon_1 + i\epsilon_2$, b) refractive index $n + ik$ and c) absorption coefficient α calculated using the equations 1.12. The effect of the parameters are shown on c).

Although this model is based on simple hypothesis, it is still used nowadays to describe the dielectric constant and refractive index of atoms, molecules and solids. For example, in a semiconductor, the exciton resonances can be characterized as Lorentz oscillators and the band to band absorption as another large Lorentz oscillator. One can then obtain an idea of the exciton linewidth, γ_X, and the exciton oscillator strength, f_X.

The Tauc-Lorentz model

However, the Lorentz oscillator model does not describe very well the effect of the bandgap E_G in the semiconductor absorption. To better describe the dielectric constant of the semiconductors, one can take into account the Tauc joint density of states in the Lorentz model, leading to the Tauc-Lorentz model [19]. For a semiconductor, the Lorentz oscillators describe the excitonic transitions and the Tauc joint density of states the semiconductor absorption continuum. In this model, the imaginary part of the dielectric function is the product of the imaginary part of the dielectric function of a Lorentz oscillator and the dielectric imaginary part from the Tauc joint-density of states [20]. This results in the following expression:

$$\begin{cases} \epsilon_2 = \frac{A_{TL}\gamma(E-E_G)^2}{(E^2-E_0^2)^2+\gamma^2E^2}\frac{1}{E} & (E > E_G), \\ \epsilon_2 = 0 \quad (E \leq E_G), \end{cases} \tag{1.13}$$

where E_0 is the oscillator resonance energy and γ is the linewidth parameter, both describing the same physical quantities as the Lorentz parameters described above. The parameter $A_{TL}(eV^2) = A_L * A_T$ is here the product of the parameter related to the Lorentz oscillator strength, A_L, and the Tauc coefficient A_T. The real part of the dielectric function, ϵ_1, can be retrieved by performing the Kramers-Kronig transformation of ϵ_2.

1.2 The microcavity photonic mode

Now that all the elements to describe the light-matter interactions have been introduced, the photonic modes in a microcavity are discussed in this subsection.

A photonic structure confines the light in one, two, or three dimensions, forming photonic modes with a dispersion defined by the structure. In the case of a planar microcavity (see figure 1.6 a)), the light is confined in one dimension between two mirrors separated by a distance of a few times the half emission wavelength ($L_{cav} = p\lambda/2$, p is an integer). In the normal direction of the planar microcavity, the photonic mode momenta have discrete values due to the confinement: $k_{\perp} = \frac{p\pi}{L_{cav}}$. However, the photons momenta k are composed of a normal and a parallel component, i.e. $k = k_{\perp} + k_{//}$, which leads to a photonic mode energy dispersion given by eq. 1.14 :

$$E_{ph}(k_{//}) = \frac{\hbar c}{n_{eff}} k = \frac{\hbar c}{n_{eff}} \sqrt{(\frac{p\pi}{L_{cav}})^2 + k_{//}^2}, \tag{1.14}$$

with n_{eff} the effective refractive index of the microcavity and $k_{//}$ the in-plane momentum of the photonic mode. As for the excitons, the dispersion can be approximated as a parabolic dispersion at low $k_{//}$ (see figure 1.6 b)), given by:

$$E_{ph}(k_{//}) \approx E_0 + \frac{\hbar^2 k_{//}^2}{2M_{ph}^*}. \tag{1.15}$$

where $M_{ph}^* = \frac{\hbar n_{eff}}{cL_{cav}}$ is the effective mass of the photon of the photonic mode and E_0 is the photonic mode energy at zero momentum.

The effective mass of the photonic mode is analogous to the effective mass of the electron and the hole in a semiconductor. This quantity describes the curvature of the parabola at low $k_{//}$: the lighter the photonic mode mass, the sharper the parabola. In general, the photonic mode mass is four orders of magnitude lighter than the exciton mass [21] meaning that the photonic mode dispersion is much sharper than the exciton dispersion.

To observe the photonic modes, one needs to measure the microcavity absorption, A, as a function of the in-plane wavenumber $k_{//}$. Indeed, absorption measurements permit to obtain dispersion curves in a system. In general, the microcavity mirrors have reflectivity coefficients, which makes the cavity transmission very low. As a consequence, the absorption can be obtained directly from reflectivity measurements as $A = 1-R-T \approx 1-R$, with R the reflectivity and T the transmittance. In addition, one can find a relation between the in-plane wavenumber, $k_{//}$, and the angle of observation θ (see figure 1.6 a)):

$$k_{//} = \frac{E}{c\hbar} sin(\theta). \tag{1.16}$$

Angle-resolved reflectivity is hence a key experimental method to probe the microcavity photonic modes. From equations 1.14 and 1.16 one can retrieve the angle-dependent photonic mode dispersion :

$$E(\theta) = \frac{E_0}{\sqrt{1 - \frac{sin^2(\theta)}{n_{eff}^2}}}. \tag{1.17}$$

Figure 1.6 c) sketches the expected absorption spectrum of the microcavity at normal incidence. The absorption is characterized by an absorption line at E_0, the energy of absorption at normal incidence. The width of a photonic mode absorption line is noted γ_{ph} and is further discussed in the following.

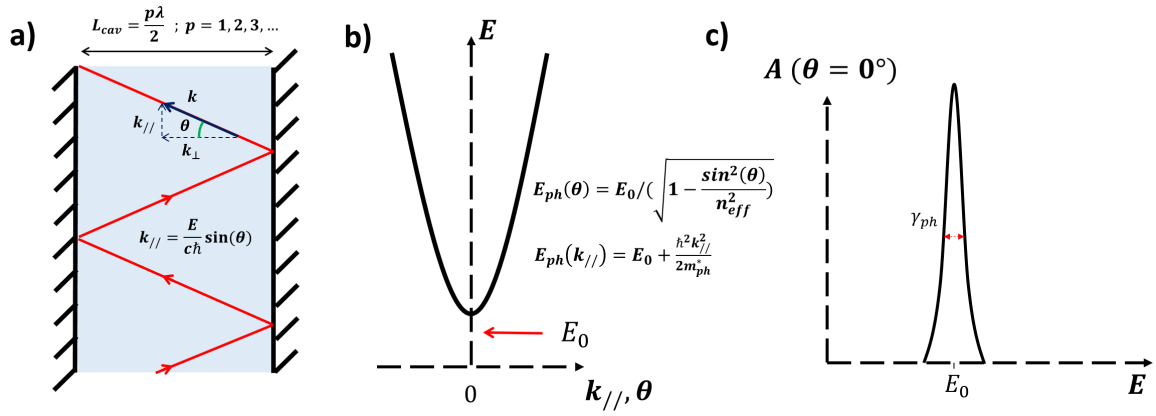

Figure 1.6: a) Sketch of a microcavity b) Energy dispersion of a microcavity photonic mode as function of the in-plane wavenumber $k_{//}$ or of the incident angle θ. c) Absorption spectrum of a microcavity at normal incidence (0°)

In photonic structures, losses occur by photon leakage across boundaries (a mirror in a planar microcavity for example), by photon absorption or scattering. The losses can be expressed by the photonic mode linewidth $\gamma_{ph} = \frac{\hbar}{t_{ph}}$ which is inversely proportional to the photon coherence time t_{ph} within the photonic structure. The non-dimensional quality factor $Q = \frac{E_{ph}(0)}{\gamma_{ph}} = \frac{E_{ph}(0)t_{ph}}{\hbar}$ indicates the quality of a given photonic structure and is a parameter which in general is desired to be maximized to obtain the strong coupling regime.

1.3 The weak and strong coupling regimes

In the two previous parts, we have defined all the physical aspects useful to describe light-matter interaction in a medium and the photonic modes in microcavities. This part then describes the interaction between the photonic mode and an optically active material.

1.3.1 Preamble

Before presenting the concept of the weak/strong coupling, the main physical quantities needed for the description are summarized, and the detuning δ is introduced:

- $\mathbf{E_X}(k_X) = E_{X0} + \frac{\hbar^2 k_X^2}{2M_X^*}$ is the exciton dispersion;
- $\mathbf{M_X^*}$ is the exciton total effective mass;
- $\mathbf{f_X}$ is the oscillator strength of the exciton describing the interaction strength of the exciton with the light;
- $\mathbf{t_X}$ is the exciton lifetime;
- γ_X is the exciton linewidth, in eV, which is related to the exciton lifetime $t_X = \hbar/\gamma_X$;
- $\mathbf{E_{ph}}(\mathbf{k}_{//}) = E_0 + \frac{\hbar^2 k_{//}^2}{2M_{ph}^*}$ is the photonic mode dispersion for low $k_{//}$;
- $\mathbf{M_{ph}^*}$ is the photonic mode effective mass;
- $\mathbf{E_{ph}}(\theta) = E_0/\sqrt{1-\sin^2(\theta)/(n_{eff}^2)}$ is the angle-dependent photonic dispersion;
- $\mathbf{t_{ph}}$ is the photon lifetime in the microcavity;
- γ_{ph} is the cavity linewidth, in eV, which describes the optical losses in the microcavity related to the photon lifetime in the cavity $t_{ph} = \hbar/\gamma_{ph}$;
- **Q** is the microcavity quality factor which describes the quality of the microcavity and is directly dependent on the photonic mode lifetime $Q = \frac{E_{ph}(0)}{\gamma_{ph}} = \frac{E_{ph}(0)\,t_{ph}}{\hbar}$.

Figure 1.7 a) shows the in-plane wavenumber-dependent dispersion curves of the exciton and the photonic mode. Because the exciton effective mass is about four order of magnitudes heavier than the photonic mode effective mass, the exciton dispersion can be considered as flat in the characteristic region of $k_{//}$ of the photonic mode dispersion. When the photonic dispersion is zoomed in, see figure 1.7 b), the exciton energy can be considered constant and will be noted as E_X. At $k_{//} = 0$, the difference of energy between the excitonic energy E_X, and the photonic energy at normal incidence E_0 is defined by the detuning $\delta = E_0 - E_X$. Another essential feature to consider is the in-plane wavenumber for which the exciton energy crosses the photonic mode energy (see the green dots in figure 1.7 b)). The crossings of the two energies only occurs when the detuning δ is negative. The same remarks apply to the angle-dependent dispersion curves.

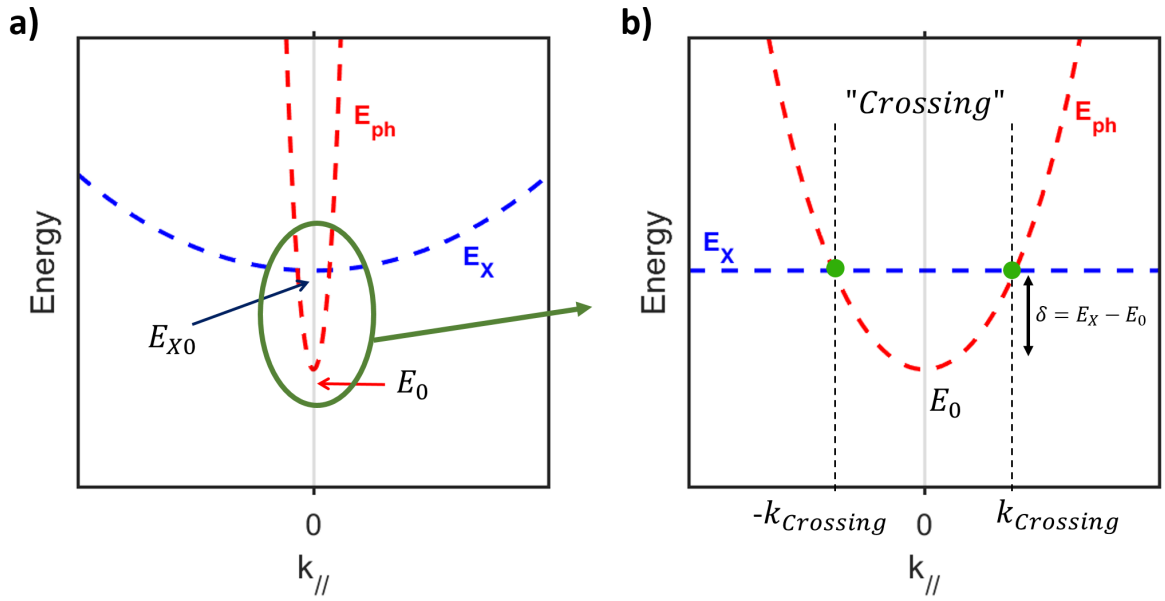

Figure 1.7: Energy dispersion of a microcavity photonic mode along the excitonic dispersion : a) for large $k_{//}$ and b) for low $k_{//}$

1.3.2 Quantum description: the simple model of the two-level oscillator

The coupling regime between an exciton and a photonic structure can be explained by considering a simple two-level model in the basis composed by the photonic state of energy $E_{ph}(\theta)$ and the excitonic state of energy E_X:

$$|ph\rangle = \begin{pmatrix} 1 \\ 0 \end{pmatrix} \quad , \quad |X\rangle = \begin{pmatrix} 0 \\ 1 \end{pmatrix}. \tag{1.18}$$

The losses of the two states are taken into account by adding to the energy their respective complex linewidths γ_{ph} and γ_X. The resulting Hamiltonian is then [1] :

$$H = \begin{pmatrix} E_{ph}(\theta) - i\gamma_{ph} & g \\ g & E_X - i\gamma_X \end{pmatrix}, \tag{1.19}$$

where g is the coupling strength between the exciton and the photonic mode and depends on f_X, the exciton oscillator strength, and V, the modal volume of the photonic mode [22]:

$$g = \sqrt{\frac{e^2}{4\pi\epsilon_0\epsilon_r}\frac{f_X}{V}} \propto \sqrt{\frac{f_X}{V}}. \tag{1.20}$$

In the following, we will keep in mind that the coupling strength g is proportional to the square root of the ratio of the exciton oscillator strength to the microcavity modal volume, i.e. $g \propto \sqrt{f_X/V}$.

[1] This Hamiltonian is non-hermitian but permits to take into account the losses in a simpler way than by considering the coupling of the system with the external continuum of states.

The diagonalization of the Hamiltonian gives rise to two new eigenvectors, $|\mu^+>$ and $|\mu^->$ of eigenvalues:

$$\mu^{+,-}(\theta) = \frac{1}{2}[E_{ph}(\theta) + E_X - i(\gamma_{ph} + \gamma_X)] \pm \sqrt{g^2 + \frac{1}{4}[E_X - E_{ph}(\theta) + i(\gamma_{ph} - \gamma_X)]^2}, \tag{1.21}$$

where the imaginary parts of $\mu^{+,-}$ correspond to the eigenstates linewidths $\gamma_\mu^{+,-}$ and the real part to the eigenstates energies $E_\mu^{+,-}$.

A characteristic of the strong coupling is a splitting of energies separated by a Rabi splitting energy, $\hbar\Omega$, that we introduce here:

$$\hbar\Omega = \sqrt{4g^2 - (\gamma_{ph} - \gamma_X)^2}. \tag{1.22}$$

The strong coupling regime occurs if the Rabi splitting $\hbar\Omega$ is a real number. This implies that the coupling strength g is higher than half of the absolute value of the difference between the photonic and excitonic linewidths γ_{ph} and γ_X :

$$g \geq \frac{|\gamma_{ph} - \gamma_X|}{2}. \tag{1.23}$$

If this condition is not met, the system is in the weak coupling regime.

1.3.3 Weak coupling regime

Let us now consider only the case of the angle for which the excitonic energy crosses the photonic mode dispersion, i.e. when $E_X = E_{ph}(\theta_{crossing})$ (see the green dots in figure 1.7 b)). The two eigenvalues of the system at this angle are:

$$\mu^{+,-}(\theta_{crossing}) = E_X - \frac{1}{2}[i(\gamma_{ph} + \gamma_X)] \pm \frac{1}{2}\hbar\Omega. \tag{1.24}$$

In the case of the weak coupling, i.e. when $g \leq \frac{|\gamma_{ph}-\gamma_X|}{2}$, $\hbar\Omega$ is a purely imaginary number. As a consequence, the energies $E_\mu^{+,-}$, related to the real parts of $\mu^{+,-}(\theta_{crossing})$, are degenerate:

$$E_\mu^{+,-}(\theta_{crossing}) = E_{ph}(\theta_{crossing}) = E_X. \tag{1.25}$$

Hence, the coupled system exhibits only one energy at this angle/momentum. When one obverses the coupled system absorption at this angle, only one absorption line appears at the excitonic/photonic mode energy (see figure 1.8 a)). For other angles, where the photonic mode is out of resonance, the coupled system energies are exactly the energies of the exciton and the photonic mode, E_X and E_{ph} (see figure 1.8 b).

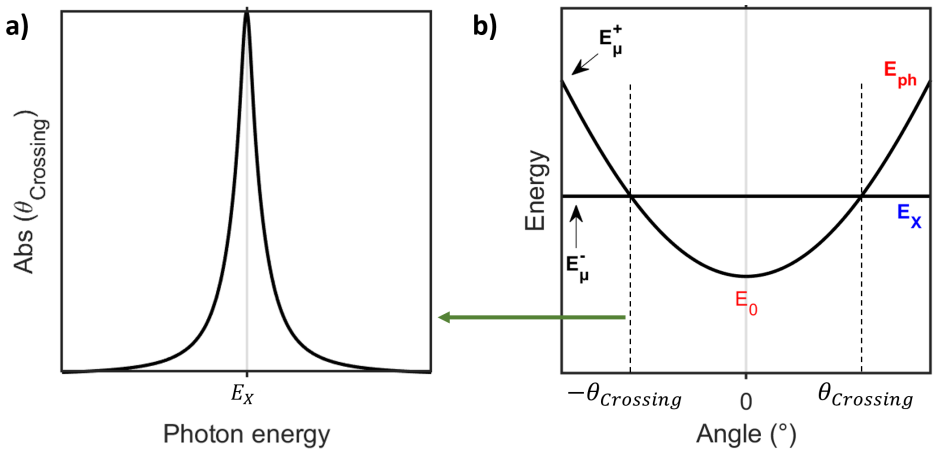

Figure 1.8: a) Absorption spectrum at the crossing point of an excitonic medium-based microcavity in weak coupling regime. b) E nergy dispersion curves of an excitonic medium-based microcavity in weak coupling regime.

However, at the crossing angle of the two dispersion curves, the imaginary parts of the eigenvalues $\mu^{+,-}$ given by the equation 1.30 are different, which lifts the linewidth degeneracy:

$$\gamma^{+,-}(\theta_{crossing}) = -\frac{1}{2}[(\gamma_{ph} + \gamma_X)] \pm \frac{i}{2}\hbar\Omega. \tag{1.26}$$

In a few words, this results in a higher rate of emission of the optically active material due to its weak coupling to the resonant photonic mode. This phenomenon is known as the Purcell effect [23].

1.3.4 Strong coupling regime

In the weak coupling regime, the Rabi oscillations occurring in the system are slower than the decoherence times of the exciton and photonic states, t_X and t_{ph}. However, when the coupling strength overcomes the photonic and excitonic losses, the Rabi oscillations become faster than the decoherence times leading to a splitting of the energies. Following the two-level model, when $g \geq \frac{|\gamma_{ph}-\gamma_X|}{2}$, the Rabi splitting $\hbar\Omega$ is a real number and the system energies at the crossing points are split while the linewidths have an equal value of $(\gamma_X + \gamma_{ph})/2$:

$$\mu^{+,-}(\theta_{crossing}) = E_{ph}(\theta_{crossing}) \pm \frac{1}{2}\hbar\Omega. \tag{1.27}$$

At the crossing angle/momentum, the absorption spectrum of the system then exhibits two lines separated by the Rabi splitting $\hbar\Omega$ (see figure 1.9 a). The crossing point in the case of strong coupling is replaced by an anticrossing point. In general, as the observation of the strong coupling requires to observe the split energies, another condition for the strong coupling is needed: the Rabi splitting energy should be larger than the mean linewidth of the exciton and the photonic mode to observe the two separate split energies:

$$\hbar\Omega \geq \frac{\gamma_{ph} + \gamma_X}{2}. \tag{1.28}$$

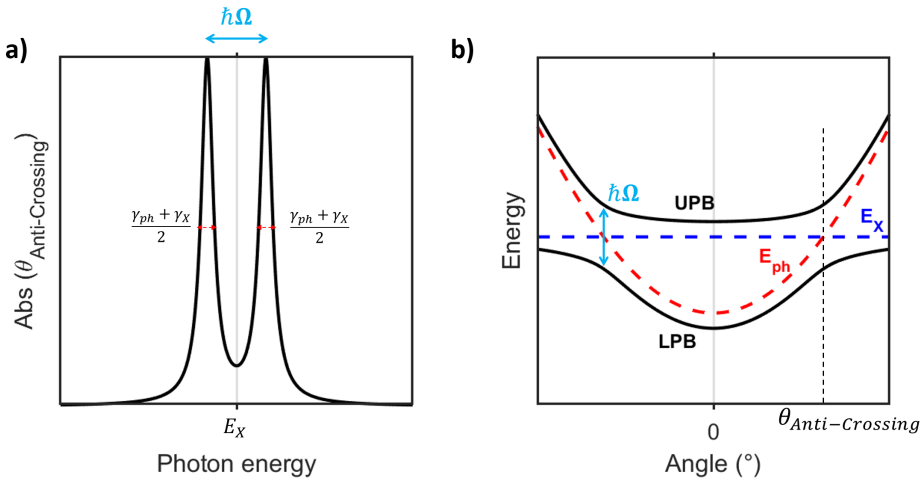

Figure 1.9: a) Absorption spectra at the anti-crossing point of an excitonic medium-based microcavity in strong coupling regime. b) Energy dispersion curves of an excitonic medium-based microcavity in strong coupling regime: the lower polariton branch (LPB) and the upper polariton branch (UPB). The dashed lines represent the bare exciton energy (in blue) and the bare photonic mode (in red).

For other angles/momenta, the system exhibits energies different from the excitonic and the photonic mode energies. Their dispersion curves are represented in figure 1.9 b. On the contrary to the weak coupling, the excitonic and photonic mode state are not the eigenstates of the system. The eigenstates are coherent superpositions of the excitonic and photonic states: the lower and upper polaritons (LP and UP) which are two new quasi-particles, part photon and part exciton, whose eigenvectors are:

$$\begin{cases} |\mathrm{UPB},\theta\rangle = \alpha_{\mathrm{UPB}}\left|ph,\theta\right\rangle + \beta_{\mathrm{UPB}}\,|\mathrm{X}\rangle\,, \\ |\mathrm{LPB},\theta\rangle = \alpha_{\mathrm{LPB}}\left|ph,\theta\right\rangle + \beta_{\mathrm{LPB}}\,|\mathrm{X}\rangle\,, \end{cases} \tag{1.29}$$

associated with the eigenvalues :

$$\mu_{\mathrm{LP,UP}}(\theta) = \frac{1}{2}[\mathrm{E}_{ph}(\theta) + \mathrm{E_X} - i(\gamma_{ph} + \gamma_{\mathrm{X}})] \pm \sqrt{g^2 + \frac{1}{4}[\mathrm{E_X} - \mathrm{E}_{ph}(\theta) + i(\gamma_{ph} - \gamma_{\mathrm{X}})]^2}, \tag{1.30}$$

where the imaginary and real parts of $\mu_{\mathrm{LP,UP}}(\theta)$ correspond respectively to the polaritons linewidths and the polaritons energies. $\alpha_{\mathrm{LPB,UPB}}$ and $\beta_{\mathrm{LPB,UPB}}$ are the projections of the polaritons on the photonic and excitonic states. Their square moduli, $|\alpha_{\mathrm{LPB,UPB}}|^2$ and $|\beta_{\mathrm{LPB,UPB}}|^2$ are the photonic and excitonic weights of the polaritons, also known as the exciton and photonic fractions of the polariton, which are shown on figure 1.10. At the anti-crossing points, both the lower and upper polaritons have an equal portion of photon and exciton, i.e $|\alpha_{\mathrm{LPB,UPB}}|^2 = 0.5$ and $|\beta_{\mathrm{LPB,UPB}}|^2 = 0.5$. However, the portion of photon and exciton are unbalanced at other angles/momenta. At low angles/momenta, the lower (upper) polariton is mostly photonic (excitonic), and at large angles/momenta mostly excitonic (photonic).

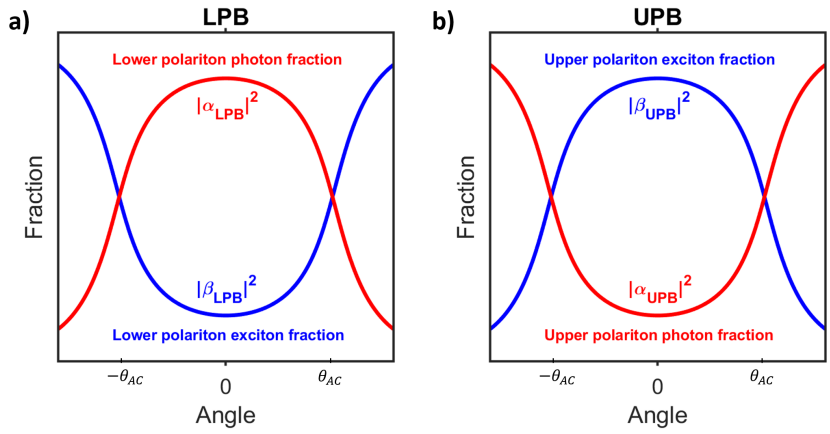

Figure 1.10: Photonic and exciton fractions $|\alpha_{LPB,UPB}|^2$ and $|\beta_{LPB,UPB}|^2$ of: a) the LPB and b) the UPB

Close to $k_{//} = 0$, the dispersion curves become parabolic-like and we can define an effective mass for the upper and lower polaritons: $M_{LPB,UPB}$. As the polaritons are hybrid states, their mass and linewidth (related to their lifetime) depends on the photonic and excitonic effective masses and linewidths weighted by the photon and exciton fractions $|\alpha_{LPB,UPB}|^2$ and $|\beta_{LPB,UPB}|^2$:

$$\frac{1}{M_{LPB,UPB}} = \frac{|\alpha_{LPB,UPB}|^2}{M_{ph}} + \frac{|\beta_{UPB,LPB}|^2}{M_X}, \tag{1.31}$$

$$\gamma_{LPB,UPB} = |\alpha_{LPB,UPB}|^2 \gamma_{ph} + |\beta_{UPB,LPB}|^2 \gamma_X. \tag{1.32}$$

Due to their hybrid nature, the polaritons possess the features of both the exciton and the photon. First, because the photon and the exciton are bosons with integer spins (the exciton is formed by two fermions with half-integer spins), the polaritons are bosonic quasi-particles. Due to their photonic part, polaritons are much lighter than the free electrons, can propagate ballistically over macroscopic distances [24], can be excited via optical pumping, and the potential landscape can be engineered through the photonic structure [25–27]. Due to their excitonic part, polaritons possess strong non-linearities properties as the exciton-exciton interaction is three order stronger than the Kerr photon-photon interaction [28].

These features make the polaritons interesting, both for fundamental physics and for applications. From the fundamental physics point of view, exciton-polaritons are considered as quantum fluid of light [29], which opens the way to study fascinating phenomena such as out-of-equilibrium Bose Einstein condensation [7], superfluidity [30], quantum vortex [31], analog black hole [32] and topological insulator [33, 34]. From the application point of view, the polaritons can be used to make novel all optical devices such as polariton laser [7], transistor [35], gates [35], interferometer [36], resonant tunnelling diodes [27], or optical routers [37], which all requires much lower threshold than conventional pure photonic devices.

1.3.5 Classical description of the strong coupling regime

In the previous section, the strong coupling regime has been described with a quantum mechanical approach. However, the observation of two anti-crossed energy dispersion curves in angle/momentum resolved absorption spectra of microcavities in the strong coupling regime can also be explained with a classical description: the transfer matrix method using the Lorentz Oscillator model (described previously).

The transfer matrix method

The transfer matrix method is used in optics to predict the propagation of electromagnetic waves in a succession of layers of different refractive indices [38]. This method is based on the Maxwell's equations and uses matrices to describe the propagation of monochromatic progressive electromagnetic plane wave through layers and interfaces. The matrices for the interfaces are retrieved with the electromagnetic boundaries conditions. As a result, one can retrieve the total reflectivity and transmission coefficients of a system containing a succession of dielectric layers.

Example of classical description of a system in strong coupling regime

Figure 1.11 shows an example of angle-resolved absorption spectra of a simulated microcavity using the matrix transfer method and the Lorentz oscillator model. The hypothetical microcavity is composed of a dielectric mirror of seven bi-layer of SiO_2/TiO_2, of an optically active material whose refractive index is given by a single Lorentz oscillator, of a layer of PMMA as a spacer layer to control the cavity detuning and of a silver mirror. The Lorentz oscillator represents here, at first approximation, the effect of an exciton to the material refractive index spectrum. Figure 1.11 shows four different results of the numerically angle-resolved absorption spectra depending on the optically active material refractive index.

Figure 1.11 a) corresponds to the case where the refractive index of the optically active material is a real constant set here to 2.25 and the extinction coefficient k is set at zero. In this case, the material is an optically passive material which leads to a passive microcavity. In the absorption map, a parabolic absorption dispersion can be observed, which is coherent with the parabolic dispersion of a passive microcavity described previously. Note that here the effective refractive index of the microcavity is constant as well as the photonic mode linewidth.

Figure 1.11 b) displays the case where the real part of the optically active material refractive index is obtained with one Lorentz oscillator ($E_0 = 2.3eV$, $A_0 = 0.3eV^2$, $\gamma_0 = 50meV$) while the extinction coefficient k is set at zero. The cavity effective refractive index is then dependent on the photon energy. This case is non-physical but is useful to under-

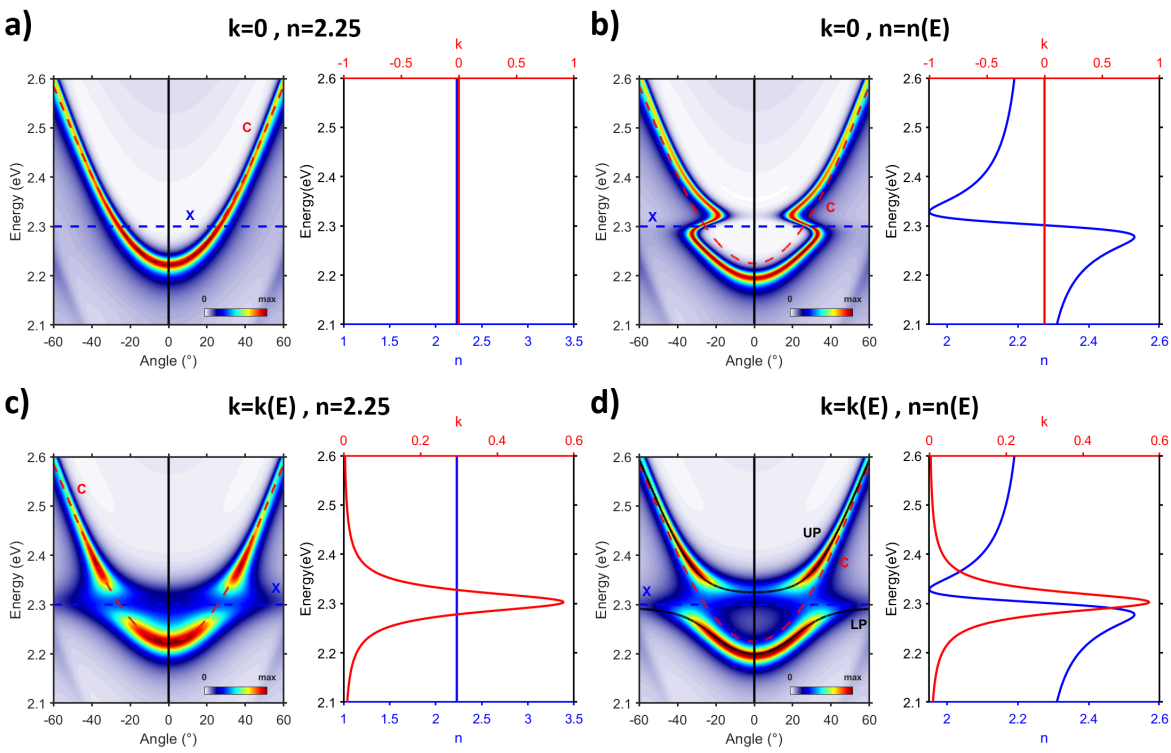

Figure 1.11: Simulated angle-resolved absorption spectra using the transfer matrix method. The pseudo-colour maps are in linear scale. The hypothetical microcavity is composed of a dielectric mirror of seven bi-layer of SiO_2/TiO_2, of an optically active material whose refractive index is given by a single Lorentz oscillator, of a layer of PMMA as a spacer layer to control the cavity detuning and of a silver mirror. a) case where the refractive index of the optically active material is a real constant set at 2.25 and the extinction coefficient k is set at zero. b) case where the real part of the optically active material refractive index is obtained with one Lorentz oscillator ($E_0 = 2.3eV$, $A_0 = 0.3eV^2$, $\gamma_0 = 50meV$) while the extinction coefficient k is set at zero. c) case where the extinction coefficient k is obtained with one Lorentz oscillator ($E_0 = 2.3eV$, $A_0 = 0.3eV^2$, $\gamma_0 = 50meV$) while the real part of the optically active material refractive index is set at 2.25. d) case of the optically active material whose refractive index is entirely described by a Lorentz oscillator ($E_0 = 2.3eV$, $A_0 = 0.3eV^2$, $\gamma_0 = 50meV$).

stand the role of the real part of the refractive index in the emergence of two anti-crossed energy dispersion curves in the strong coupling regime. We observe in the angle-resolved absorption that the energy dispersion is no longer parabolic. Instead, two "parabolas" appear and are linked with an S-shaped dispersion which is similar to the S-shape of the refractive index real part. Indeed, the deviation in angle of this dispersion curve from the cavity mode depends on the deviation of the microcavity effective refractive index to the constant effective refractive index found previously. The lower "parabola" is then redshifted with respect to the first case's parabola due to the increased effective refractive index, n_{eff} (and hence increased optical length, $n_{eff}L$), which leads to a lower cavity mode energy E_0. Similarly, the upper "parabola" is blueshifted with respect to the first case's parabola due to the reduced effective refractive index at higher energies.

Figure 1.11 c) illustrates the case where the extinction coefficient k is obtained with one Lorentz oscillator ($E_0 = 2.3eV$, $A_0 = 0.3eV^2$, $\gamma_0 = 50meV$) while the real part of the optically active material refractive index is set at 2.25. This case is also obviously non-physical but shows the role of the extinction coefficient k for the anti-crossing of the two energy dispersion curves. We observe here the same parabolic dispersion as in figure 1.11 a). However, because of the high absorption around the excitonic energy, the parabola is split into two. Note that a slight change of curvature occurs at the extremities of the two pieces of the split parabola.

Figure 1.11 d) presents the case of the optically active material whose complex refractive index is entirely described by a Lorentz oscillator. We obtain here two anti-crossed absorption energy dispersions which can be referred to as the lower and upper polaritons. The curvature of the two dispersions are similar to the curve of the two "parabolas" found in figure 1.11 b), however, the S-shape is not observable anymore because of the high absorption of the Lorentz oscillator around the excitonic energy. Moreover, the linewidths of the two dispersion curves are wider and angle-dependent, which is characteristic of the hybrid nature of the polaritons.

We showed here that both the real and imaginary parts of the refractive index of a Lorentz oscillator in the transfer matrix method can classically explain the polariton dispersion in a microcavity in the strong coupling regime. The classical description is a useful tool to predict and fit the polaritonic dispersion curves from a given microcavity. However, unlike the quantum model, it cannot predict the bosonic nature of the polaritons and the related physical phenomena such as polaritonic lasing.

1.4 Polaritonic lasing : the case of a laser based on a microcavity in strong coupling regime

1.4.1 Photoluminescence of a microcavity in the strong coupling regime

Before describing the polaritonic laser, which is one of the main applications of the cavity exciton-polaritons, one needs to describe the photoluminescence process of a microcavity in the strong coupling regime sketched in figure 1.12. We will only consider here weak optical excitations out of resonance, meaning optical excitations with photon energy $\hbar\omega_{exc}$ much higher than the polariton energies. In the following, this photoluminescence process is referred to as "polariton photoluminescence".

First, as the excitation photon energy is higher than the lower polariton band, the species that absorb the light are the electrons at large momenta (large compared to the polariton momenta) which creates hot electron-holes pair. This step corresponds to step

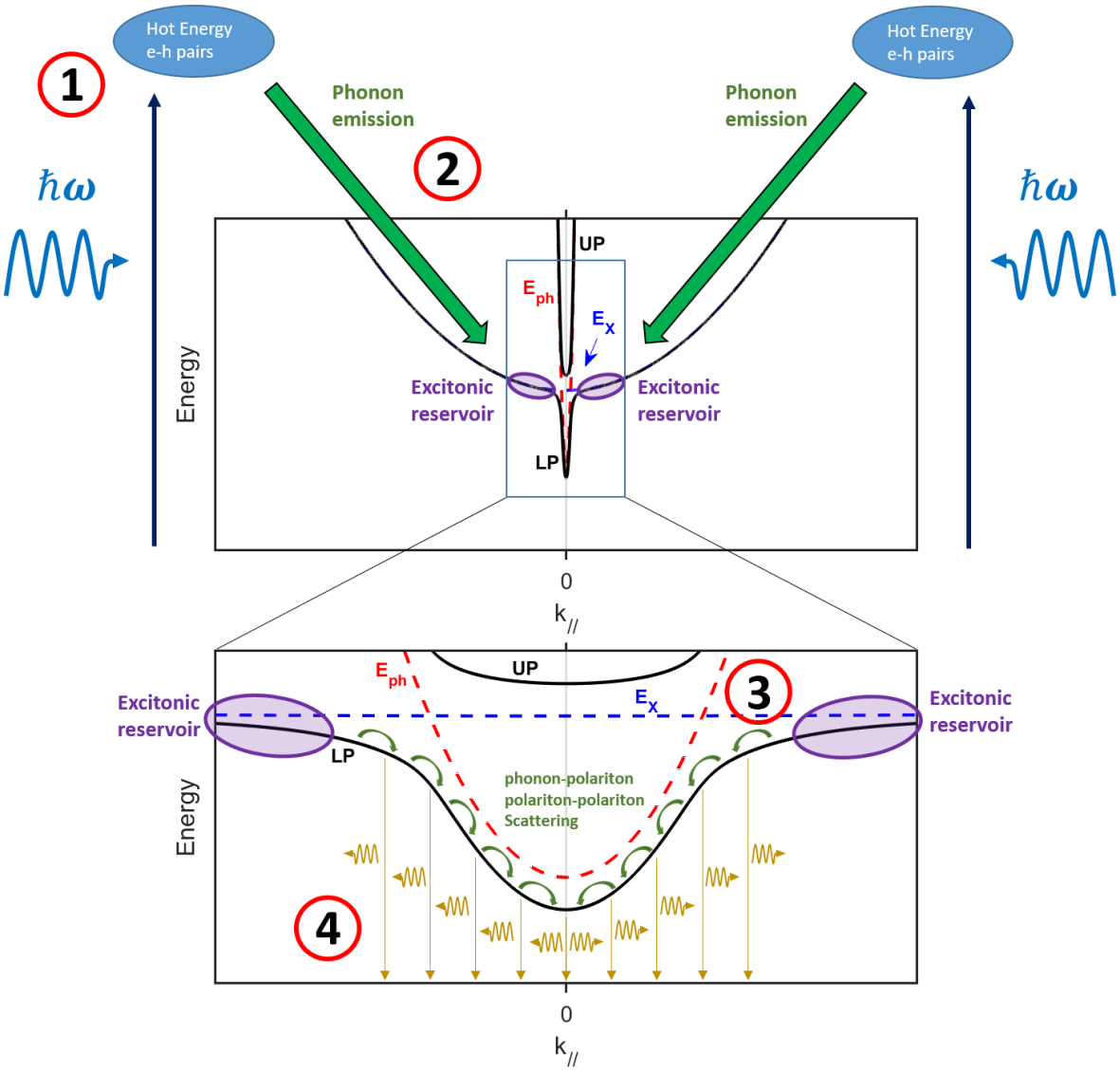

Figure 1.12: Sketch of the photoluminescence process of a microcavity in the strong coupling regime. The part above represents the full picture with step 1 corresponding to the photon absorption creating electron-hole pairs and step 2 corresponding to the exciton relaxation. The part below represents the close picture around the LPB with step 3 corresponding to the lower polariton relaxation and step 4 to the polariton dissociation resulting in the emission of photons.

1 in figure 1.12 and is the same absorption process like the one in a bare semiconductor. The Coulomb interaction between the electrons and holes creates excitons which relax along the excitonic band by emitting phonons (step 2). The excitonic relaxation is extremely effective in the states with large momenta as these states have a very large curvature, therefore a high state density. When the excitons reach the low momenta close to the lower polariton inflexion point, the polaritons are created. Because this relaxation process is almost instantaneous, all polaritons will first be populated in these states, called the excitonic reservoir, before relaxing in the lower momentum states. The polaritons then relax along the lower polariton branch after the inflexion point via the interactions of the polariton excitonic parts with phonons or other polaritons (step 3). As the lower po-

laritons are mostly excitonic at these momenta, the relaxation process is efficient. However, when the lower polaritons relax, the excitonic(photonic) fraction of the lower polaritons decreases(increases), which slows down the polariton relaxation scattering processes. Moreover, the polaritons lifetime is principally limited in the low momenta region by their photonic parts lifetime related to the microcavity quality factor. Consequently, the polaritons dissociate during the relaxation in the lower polariton branch, which leads to the exciton recombination and the emission of a photon conserving the polariton momentum and energy. This dissociation of polaritons along the lower polariton band leads to the "polariton photoluminescence" taking the form of the lower polariton branch (step 4).

We note that because of the high density of states of the excitonic reservoir, the relaxation pathways bypass the upper polariton branch, which means that no photoluminescence should be expected from the upper polariton branch. However, this is only true in the case of polaritons a large Rabi splitting energy $\hbar\Omega$ much larger than the thermal energy k_bT. In the case of systems exhibiting weak excitons (low exciton binding energies and oscillator strengths), for example in GaAs-based microcavities, cryogenic temperatures are needed to observe the excitons and hence the cavity exciton-polaritons. In these conditions, the thermal energy is of the order of magnitude of the Rabi splitting, and as a consequence, the "photoluminescence is thermalized" [39]. Hence, both the lower and upper polariton branches can be observed with photoluminescence measurements as it can be seen in figure 1.13 a) (the colour map is in log-scale) in an InGaAs quantum well-based microcavity extracted from [40]. In this case, the inflexion point of the lower polariton branch can be well distinguished.

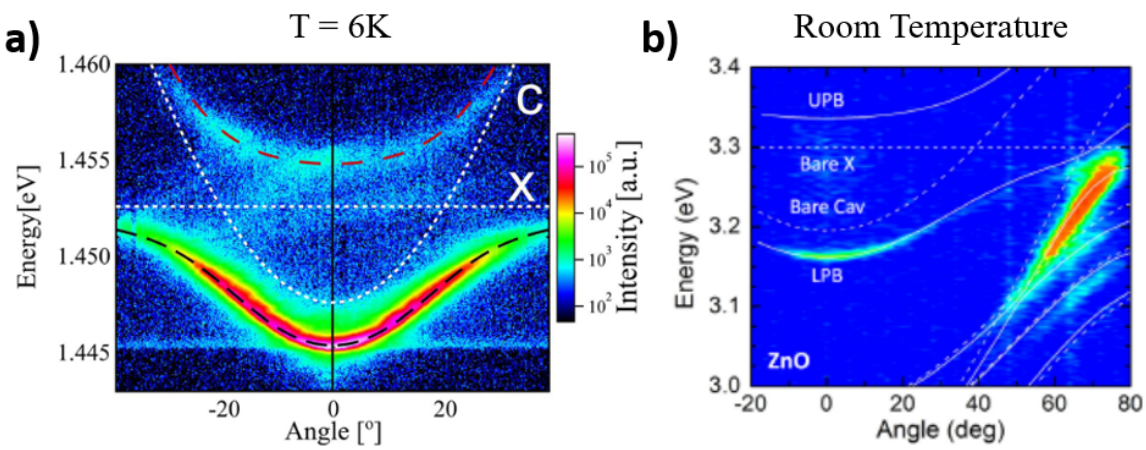

Figure 1.13: a) Photoluminescence of polaritons in an InGaAs quantum well-based microcavity where both the LPB and UPB can be observed. Extracted from from [40]. b) Photoluminescence of polaritons in a ZnO-based microcavity where only the LPB can be observed (the signal at high angles corresponds to the coupling of one of the Bragg mirror mode to the exciton). Extracted from [41].

In large bandgap semiconductors such as ZnO and GaN, as the Rabi splitting energy $\hbar\Omega$ is much higher than the thermal energy k_bT, only the photoluminescence from the lower polariton branch can be observed. Figure 1.13 b) shows the example, extracted from [41], of the photoluminescence of a ZnO-based microcavity in the strong coupling regime where only the lower polariton branch can be observed. Moreover, because the Rabi splittings are too large, the inflexion point of the lower polariton branch is hard to spot. For these two reasons, only reflectivity/transmissivity experiments can demonstrate the strong coupling regime by revealing the upper polariton branch and the anti-crossing of the dispersion curves. However, it is possible to suggest the strong coupling regime from angle-resolved photoluminescence spectra if the measured dispersion effective mass is much larger than the expected photonic effective mass.

1.4.2 Polaritonic lasing

Bose-Einstein condensation

The elementary particles can be classified into two categories: the fermions with half-integer spins and the bosons with integer spins. The fermions are governed by the Fermi-Dirac statistics and by the Pauli exclusion principle stating that no more than one fermion (of the same spin) can occupy the same quantum state. On the contrary, the bosons follow the Bose-Einstein statistics for which several bosons can occupy the same quantum state. The Bose-Einstein condensation, which is the massive occupation of the fundamental state, was predicted by Einstein in 1925 following the work of Bose [42]. The condensation occurs when the average distance between the bosons $d = \mathrm{N}^{-1/3}$, with N the boson density, is lower than the boson thermal De Broglie wavelength $\lambda_{\mathrm{DB}} = \sqrt{(2\pi\hbar^2)/(mk_b\mathrm{T})}$ which describes the spatial spread of the particle, i.e. its wave-function. To obtain Bose-Einstein condensation, one needs to control the temperature T and the bosons density N to satisfy this condition. For example, the first experimental demonstration of Bose-Einstein condensation was obtained with a diluted gas of rubidium, Rb, and the temperature needed was as low as $170n$K with a density of $2.5 \times 10^{12} cm^{-3}$ as the rubidium atoms are very heavy, around six order of magnitude heavier than the electrons [43].

Bose-Einstein condensation of the exciton-polaritons

Polaritons are composite bosons and can, in principle, condensate to the fundamental state at $k_{//} = 0$ when the right conditions of temperature and density are met. However, as the polariton system exhibit losses due to photon escape from the microcavity, and requires permanent re-injection, the polariton condensation process cannot be described by the text-book BEC theory with equilibrium thermodynamics. Indeed, polariton condensation takes place in an out-of-equilibrium system with the interplay of gain and losses [29]. It is a rich and complicated mechanism which is still subject of contempo-

rary research. Nevertheless, due to the bosonic nature, the criterion for polariton BEC to take place at a given polaritonic state is that the polariton population at this state exceed one. Indeed, this density condition will trigger the stimulated relaxation from all other states to this considered one. This results in the formation of a macroscopic and coherent state of polaritons, called polariton condensate.

Because of the polariton finite lifetime, photons of the polaritons in the condensate escape out of the cavity while conserving the coherence properties of the condensate. The process then leads to a coherent emission of light which is referred to as polaritonic lasing. Analogously to conventional laser, there exists for polaritonic lasers a pumping threshold for which the condensate is triggered and the gain overcomes the losses. As the system is permanently pumped, the excitonic reservoir is always present and coexists with the condensate. Similarly, under threshold, the excitonic reservoir coexists with the polaritons along the lower polariton branch. The coexistence of the condensate and the excitonic reservoir is the signature of a permanent injection, the polariton laser is the signature of a permanent loss.

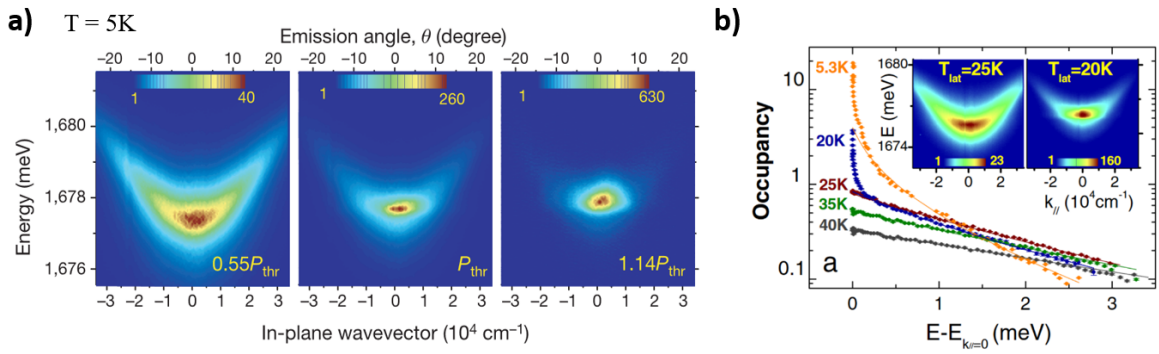

Figure 1.14: a) Angle-resolved photoluminescence below and above the threshold of the first experimentally demonstrated polaritonic laser in a CdTe-based microcavity at 5K. Extracted from [7]. b) Lower polariton occupancy factors as a function of the polariton momenta at different temperatures obtained in [44]. The inset shows the angle-resolved photoluminescence spectra above and below the temperature threshold. Extracted from [44]

Figure 1.14 a) shows the angle-resolved photoluminescence spectra under and above the threshold of the first experimentally demonstrated polaritonic laser in a CdTe-based microcavity at 5K with an estimated threshold density of $5.10^8 cm^{-2}$ [7]. Under the limit, the lower polariton branch photoluminescence is broadly distributed whereas above the threshold the photoluminescence is concentrated at $k_{//} = 0$, sign of the polariton condensation. Figure 1.14 b) shows another example of a polariton condensate in which the condensation is obtained by reducing the system temperature at a constant high excitation [44]. The graph shows plots of the polariton occupancy factors as a function of the polariton momenta at different temperatures. It can be seen than below the temperature of 25K the occupancy factor at $k = 0$ is higher than one, which demonstrates the polariton

condensation. The inset of figure 1.14 b) shows the angle-resolved photoluminescence spectra above and below the temperature threshold. These two examples illustrate that the polariton condensation is possible under the right condition of polariton density and temperature.

The two examples shown above were among the first demonstrations of polaritonic lasers. These polariton condensations were obtained at low temperatures because of the low binding energy of the CdTe excitons limiting the exciton stability at higher temperatures. Naturally, because of the light mass of the polaritons, the polaritonic lasing could be later demonstrated at room temperature with materials exhibiting stronger excitons such as GaN [45], ZnO [46], organic materials [47], and also perovskites [48, 49].

Bottleneck effect

Although Imamoglu et al. proposed the principle of the polaritonic laser in 1996 [6], the first experimental demonstration by Kasprzak et al. was obtained only ten years later [7]. The main difficulty faced by the polariton community was the so-called "bottleneck effect" which is the accumulation of the polaritons close to the inflexion point of the lower polariton branch. This accumulation is due to the long relaxation time, t_R, as well as the increased photonic portion of the polaritons in the most curved part of the lower polariton branch. The bottleneck effect, further detailed in the following, then prevents from obtaining a sufficient polariton density at $k = 0$ to trigger the condensate.

The first step in the polariton relaxation process is the extremely effective relaxation of the excitons to the excitonic reservoir. The relaxation occurs principally with the emission of optical phonons of large energy (compared to acoustic phonons) as the conditions of conversation of energy and momentum can be respected. The second step concerns the relaxation of polaritons from the excitonic reservoir to the state $k_{//} = 0$ in the most curved part of the lower polariton branch. Because of the steep curve, the scale of energy between the polaritons current states and the fundamental state becomes smaller than the optical phonons energy: the polaritons cannot relax to the fundamental state by emitting optical phonons. For this reason, the polaritons relax by emitting successively several acoustic phonons whose energies are much smaller than the energy scale. In addition, the scattering rate, proportional to the polariton excitonic part, is reduced the further the polariton relax along the lower polariton dispersion. As a consequence, the relaxation of polaritons is strongly slowed down. On the other hand, as the lower polariton branch bends, the photonic part of the polaritons increases which increases the probability of the polaritons to undergo radiative recombination. Therefore the relaxation time, t_R, is longer than the lower polariton lifetime, t_{LPB}, i.e. $t_R > t_{LPB}$, and the bottleneck occurs: the polaritons accumulate close to the inflexion point of the dispersion curve.

Figure 1.15 shows an example of the bottleneck effect observed in a ZnO-based microcavity extracted from [50]. In this case, when the detuning decreases, the bending of the dispersion curve is reduced. The angle for which the bottleneck occurs is lowered until the curve of the lower polariton branch is flat enough for the bottleneck effect to disappear.

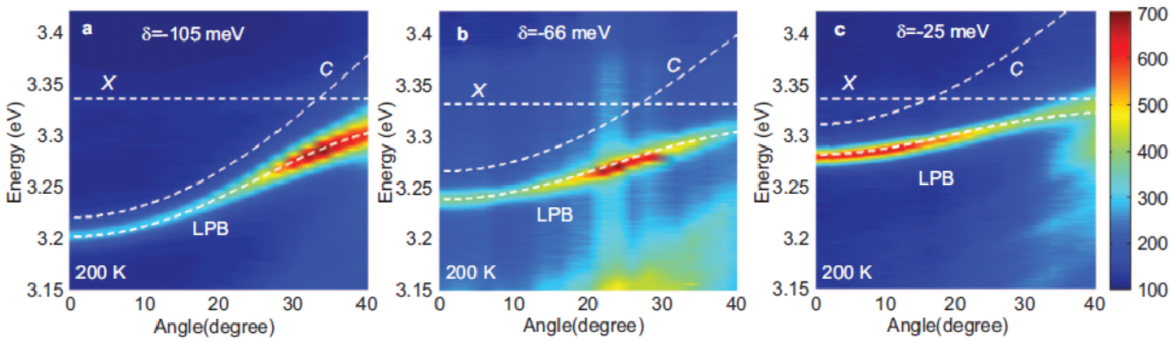

Figure 1.15: Polariton photoluminescence in a ZnO-based microcavity obtained at 200K for three different detunings. The Bottleneck effect is observed for the first two large detunings on the left and disappear for the lowest detuning on the right. Extracted from [50]

One of the conditions to observe polaritonic lasing is the polariton lifetime to be longer than the relaxation time, $t_{\mathrm{LPB}} > t_{\mathrm{R}}$. For this purpose, one can either decrease the relaxation time of the polariton, t_{R}, or increase the lifetime of the polariton, t_{LP}. The former solution is related to the detuning and the Rabi splitting and the latter to the cavity quality factor, $\mathrm{Q} = \frac{\mathrm{E}_{ph}(0)\, t_{ph}}{h}$, and the material quality. Indeed the defects in the material reduce both the cavity quality factor and the exciton lifetime as the defects can dissociate the excitons.

Another way to circumvent the bottleneck effect is to raise the exciton density in the reservoir by increasing the excitation. When the exciton density in the excitonic reservoir is high enough, the polariton-polariton interactions through their excitonic parts bring polaritons to higher energetic states and other polaritons to lower excited states by conservation of the energy and momentum [51]. The polaritons brought to higher states then relax back by interactions with acoustic phonons to the excitonic reservoir. This technique then reduces the relaxation time t_{R} of the polaritons. However, this approach increases the excitonic screening effects, which lower the exciton oscillator strength. This effect reduces the Rabi splitting until at a certain exciton density where the strong coupling regime is lost [52]. This transition from strong to weak coupling is called the Mott transition. Therefore, the most crucial parameter to improve is the cavity quality factor to increase the polariton lifetime and obtaining the polaritonic lasing before the Mott transition.

The bottleneck effect was first observed in small bandgap semiconductors such as GaAs and was solved by improving the quality factors to values higher than 30000, and with the polariton-polariton interactions. For large band gap semiconductors, however, the bottleneck effect is not as crucial. Indeed, the energy scale between the excitonic reservoir and the fundamental state are at the same order of magnitude of the optical phonon energies. The quality factor required for polaritonic lasing can then be as low as a thousand and the polariton-polariton interactions are not needed. For large detunings, however, the bottleneck effect still remains (see example in figure 1.15). Nevertheless, for logical device applications such as the polaritonic transistors, the polariton lifetime should be long and the non-linearities, from the polariton-polariton and polariton-exciton interactions, are required. Consequently, a large quality factor is still desired.

1.4.3 Differences between polaritonic and photonic lasing

The main difference between the polaritonic lasers, occurring in cavities in strong coupling regime, and photonic lasers, occurring in cavities in weak coupling regime, comes from the underlying mechanism giving rise to the light amplification and coherence:

- In the case of conventional lasers, lasing is the result of the stimulated emission process taking place in a gain medium in which there is an electronic population inversion. In semiconductors, electron-hole pairs act as the gain medium and the photons are the species being amplified and gaining the coherence. The electronic population inversion is required for the stimulated emission to balance the re-absorption of the emitted photons. The lasing threshold is then determined by the density needed for the inversion and also by the density required to compensate for the losses from the cavity defects.

- In the case of polaritonic lasers, the amplification and coherence come from the process of stimulated scattering initiated when the polariton density at the ground state ($k_{//} = 0$) reaches a threshold. In this case, the polaritons are the species being amplified and gaining the coherence. The emission of coherent light is the result of the photonic part of condensated polaritons leaking through one of the cavity mirrors. Therefore, the emission of light and the process of amplification and coherence building are independent. For this reason, the absorption of the emitted photon does not need to be balanced by the stimulated process, and therefore, the electronic population inversion is not required for the polariton lasers, often called a laser without inversion. The density required for the polariton lasers is the critical density described earlier to trigger the condensate. This density is in general 2-3 orders of magnitude lower than the densities for the electronic population inversion in conventional lasers [53]. As a consequence, the polaritonic lasers exhibit very low thresholds, which explain the very keen interest of the scientific community for such lasers.

The distinction between the two types of lasers is very clear regarding their mechanism. However, the difference is not that obvious in practice. Indeed, both the polaritonic

lasers and photonic lasers emit a coherent light with a high spatial and temporal coherence when a pumping threshold is reached. In both cases, one observes, at the threshold, a collapse of the linewidth, related to the increased temporal coherence, and an amplification of light. The coherent output light of a polaritonic laser is then not so different from the coherent light of a photonic laser.

In essence, a microcavity lasing emission is polaritonic if the microcavity is in strong coupling. However, even if the strong coupling is demonstrated at low densities of pumping, one needs to make sure that the system is still in strong coupling at the high densities required for lasing. Indeed, as mentioned above, the oscillator strength of the exciton is weakened at high density, which decreases the Rabi splitting until the strong coupling is lost at the Mott transition. Figure 1.16 shows an example of a ZnO-based microcavity losing the strong coupling at density around the lasing threshold [50]. In this case, the lasing takes place at normal incidence in the cavity mode.

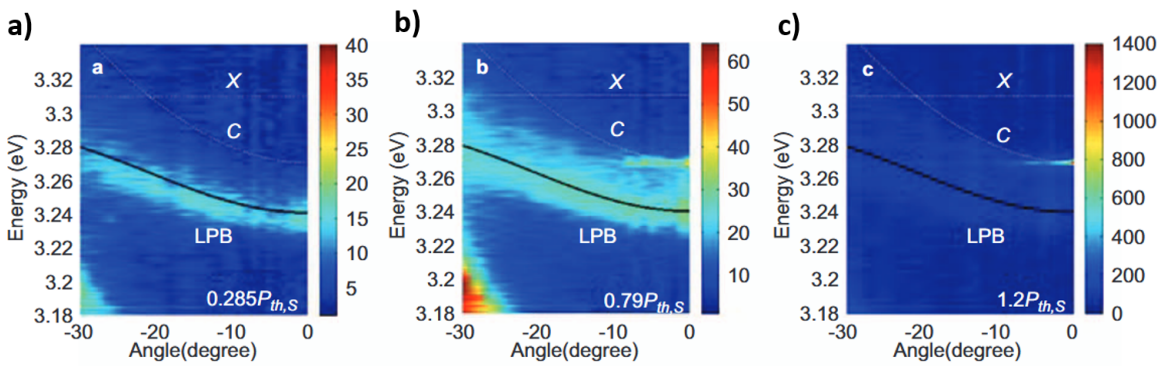

Figure 1.16: Example of a ZnO-based microcavity losing the strong coupling at density around the lasing threshold [50]. Angle-resolved photoluminescences pseudo-colour maps of the cavity at a) 0.285 P_{th}, b) 0.79 P_{th} c) 1.2 P_{th}, with P_{th} the lasing threshold power. The photoluminescence can only be observed in the lower polariton branch in a) and from both the lower polariton branch and the cavity dispersion in b). The lasing photoluminescence occurs only on the cavity mode in c). Extracted from [50]

The following then presents some properties of the polariton lasers differing from the photonic lasers, which can be used to distinguish between the two different lasers.

Double Thresholds

As mentioned above, due to its more efficient laser mechanism, the polaritonic laser thresholds can be 2 to 3 orders lower than the conventional laser thresholds [53]. In some systems exhibiting polaritonic lasing, a second threshold occurring at higher densities can be observed. This second threshold occurs at higher densities than the Mott density, which means that the laser at the second threshold is actually a photonic laser.

Figure 1.17 shows an example of a second threshold observed in a GaAs system in [54]: the first threshold corresponds to a polariton laser in the strongly coupled system and the second threshold to a photon laser when the strong coupling is lost.

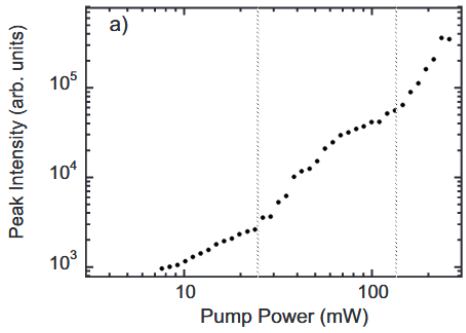

Figure 1.17: Example of a second threshold observed in a GaAs system in strong coupling in [54]: the first threshold corresponds to a polariton lasing in the system in strong coupling and the second threshold to a photon lasing when the strong coupling is lost. Extracted from [54]

Blueshift

In the majority of conventional lasers, the lasing modes redshift with pump intensity increasing because of the device heating. However, in the case of polaritonic lasing, the modes blueshift. This property has two origins. The first one is the already mentioned reduction of the Rabi splitting with higher exciton densities, which blueshifts the lower polariton band. This blueshift occurs in general at higher density than the polaritonic lasing threshold when the density is close to the Mott transition density. The second origin is due to the excitonic part of the polaritons. Indeed, the polaritons are bosons which can interact with one another or with the excitonic reservoir via Coulomb interactions thanks to their exciton parts. These interactions are repulsive, which leads to a blueshift of the polaritons energies. This blueshift can occur at densities around or lower than the lasing threshold.

Figure 1.18 shows an example of the polariton blueshift around the polariton lasing threshold observed in a microcavity containing $CsPbCl_3$ nanoplatelets in [48]. It is worth noting that the blueshift of the polaritonic lasing can also be observed in the case of the first polaritonic laser discussed above and shown in figure 1.14 a).

Linewidth

Both photonic and polaritonic lasers are characterized by a sharp decrease of the linewidth at the lasing threshold. However, in polaritonic lasers, the sharp decrease is followed by a continuous increase of linewidth. This is principally related to the emission blueshift mentioned just above and instabilities of the pumping intensities. The resulting measured emission is an average of emission with different blueshifts resulting in a

larger linewidth. Figure 1.19 shows the example of the microcavity containing $CsPbCl_3$ nanoplatelets in [48] showing the increase of the linewidth (in blue) above the polaritonic lasing threshold.

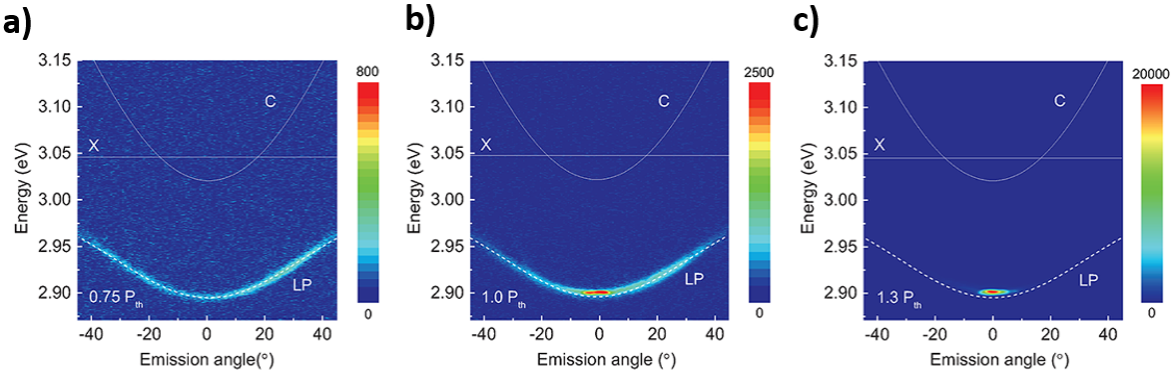

Figure 1.18: Polariton blueshift around the polariton lasing threshold observed in a microcavity containing $CsPbCl_3$ nanoplatelets in [48]. Angle-resolved photoluminescence pseudo-colour maps of the cavity at a) 0.75 P_{th}, b) 1.0 P_{th} c) 1.3 P_{th}, with P_{th} the lasing threshold power. A slight blueshift of the lower polariton dispersion and the polariton lasing peak, compared to the initial lower polariton dispersion (dashed white curves), can be observed at threshold b) and above threshold c). Extracted from [48]

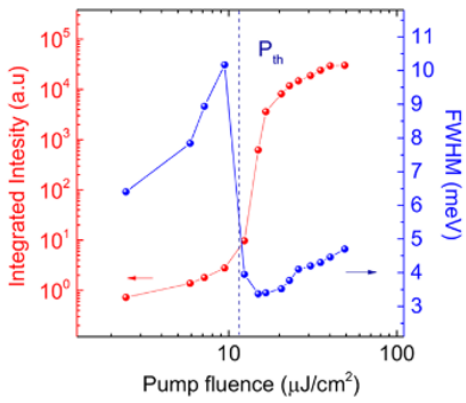

Figure 1.19: Evolution of the linewidth above the polariton threshold observed in a microcavity containing $CsPbCl_3$ nanoplatelets in [48]. In red is the integrated intensity as a function of the pumping intensity showing an amplification above the threshold. In blue is the polaritonic linewidth showing a sharp decrease at threshold followed by an increase. Extracted from [48]

Propagation of the condensate out of the excitation spot

As discussed previously, a polariton condensate always coexists with an excitonic reservoir. The excitonic reservoir only exists under the pumping spot and induce a local blueshift to the condensate due to the interaction between polaritons in the condensate and the excitons in the excitonic reservoir. Out of the excitation pump spot, the potential energy of the condensate is smaller. And if the excitation pump spot is small, the local blueshift forms a stiff potential hill in k-space which pushes the condensate out of $k_{//} = 0$.

The polariton acquires then kinetic energy, which leads to the polariton going up along the lower polariton dispersion at larger $k_{//}$ [55]. If the local blueshift amounts to V, then the wavevector of propagation is $k_{\mathrm{BEC}} = \sqrt{2\mathrm{V}m_{\mathrm{LPB}}/\hbar^2}$. The propagation length is given by $\mathrm{L} = v_{\mathrm{BEC}}\, t_{\mathrm{LPB}}$ where t_{LPB} is the polariton lifetime and $v_{\mathrm{BEC}} = \sqrt{2\mathrm{V}/m_{\mathrm{LPB}}}$ is the polariton velocity. The propagation is then only visible for pumping spot smaller than the propagation length.

Figure 1.20 shows an example of a propagating condensate emitting at large angles in a microcavity containing a $CsPbBr_3$ microwire in [49]. More details on the results of the studies shown in figures 1.18,1.19 and1.20 from [48] and [49] will be given in the part reviewing the strong coupling regimes obtained with perovskites.

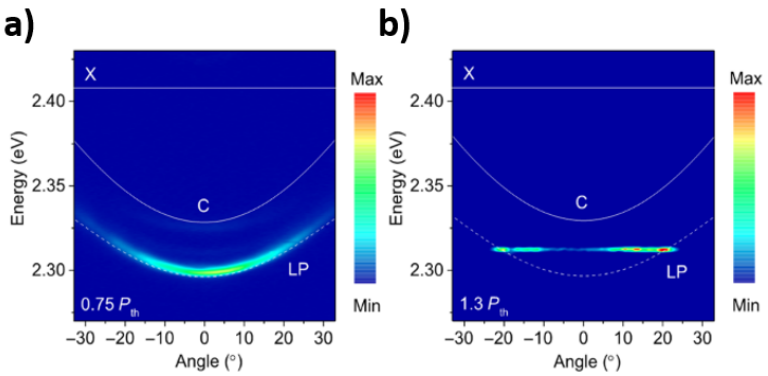

Figure 1.20: Example of an nonequilibrium coherent polariton condensates emitting at large angles in a microcavity containing a $CsPbBr_3$ microwire in [49]. Angle-resolved photoluminescence images of the cavity at a) 0.75 P_{th}, b) 1.3 P_{th}. Above the threshold, polariton lasing occur at the angles ±20°. Extracted from [49]

Nonlinearities

Finally, the polariton condensates are characterized by their non-linearites owing to the polariton excitonic part. The non-linearities are essential regarding the logical device applications and results from two distinct processes: the exciton-exciton interactions or the band-filling saturation at densities close to the Mott density. For the condensates at cryogenic temperatures with small bandgap semiconductors, the non-linearities come from the exciton-exciton interactions. Indeed, in these cases, the exciton are of the Wannier type. For large band gap semiconductors, generally exhibiting Frenkel excitons, the non-linearities are due to the band-filling saturation. This type of non-linearities are not really suitable for applications as the exciton can be easily screened. However, hybrid perovskites have been recently shown to be a large band gap material for which the exciton-exciton interactions govern the non-linearities [56]. This results goes in the way towards polaritonic logical devices based on perovskites operating at room temperature.

2 Halide perovskites: a new material for lasers in the weak and strong coupling regimes

Over the last decade, the 3D halide perovskites [2] have emerged in the framework of photovoltaics. More precisely, the pioneer works on halide perovskite-based solar cells were published in 2009 [57] and 2012 [58] with solar-cell efficiencies reaching 3.8% and 9.7%, i.e. the same order of magnitude as the organic-based solar cells studied for about two decades [8]. The crucial advantage of the halide perovskites is their low-temperature and solution-processed deposition in contrast with the expensive high-temperature techniques used for silicon. Naturally, the halide perovskites have brought attention to the scientific community, and the perovskite-based solar cells have reached today an efficiency of 25.2% [8], higher than the polycrystalline silicon-based solar cells. The stability of the material [59] and the toxicity of solar cells due to the presence of lead [60] are two obstacles to the commercial development of perovskite devices. However, much effort has been made by the perovskite community and significant progress has been obtained in terms of material stability (by encapsulation, material synthesis, improvement of contact materials, etc.) [59]. Regarding the toxicity, two approaches are under investigations: the encapsulation of the perovskites for preventing the leakage of Lead from the perovskite devices [61] and replacing lead by another divalent metal, for example Tin (Sn) [62].

In the meantime, as the perovskites hold promises in the photovoltaic field, their good optical properties are also interesting for light-emitting devices such as electroluminescent diodes and lasers. The easy tunability of the perovskite emission wavelength across the entire visible range via chemistry substitution is one of the main advantages in this matter [12]. The first observation of Amplified Spontaneous Emission (ASE) in perovskite occurred in 2014 [9], and it was rapidly followed by the first perovskite-based LEDs [12, 63] and Lasers [10, 11, 64–67]. The lasers mentioned here are lasers in weak coupling regime. Although the strong coupling has been studied with the counterparts 2D perovskites from 1998 [68], the first perovskite-based polaritonic laser has been obtained in 2017 with the 3D perovskite $CsPbCl_3$ [48].

In this second part, the properties of the 3D and low-dimensional halide perovskites are introduced. The state of the art of the perovskite lasers in the weak and strong coupling regimes is finally provided.

[2] The perovskite, named after the Russian mineralogist Lev Perovski, originally referred to the Calcium Titanate $CaTiO_3$ first discovered in 1839 in the Ural mountains of Russia by Gustav Rose. The name is now also applied to the materials with the same crystal structure AMX_3.

2.1 Characteristics of halide perovskites

2.1.1 The 3D halide perovskites

Figure 1.21 shows the crystal structure, AMX_3, of the 3D halide perovskite. A is a cation which can be organic, in general methylammonium $CH_3NH_3^+$ (MA) or formamidinium $HC(NH_2)_2^+$ (FA), or inorganic, generally caesium (Cs), or a mixture of these, for example, $Cs_{0.2}MA_{0.8}$. M is a divalent metal cation with a coordination number of 6 and is, in general, the lead Pb. Tin (Sn) -based halide perovskites also exist but are much less studied and performing than the lead counterparts. X is a halide and can be either bromide (Br), chloride (Cl), iodine (I), or a mixture of these halides. The inorganic part is organized in octahedra while the cations A fills the cuboctahedral holes.

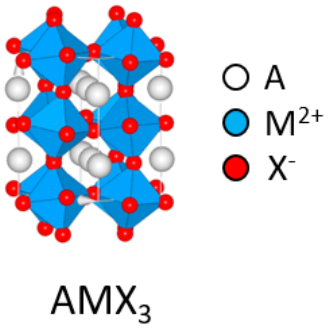

Figure 1.21: 3D halide perovskite crystal structure

The perovskites can be synthesized in different morphologies: in single crystals, in thin films, in quantum dots, nanoplatelets, nano/microwires. The properties of the perovskites of the same composition depend significantly on their morphology. For example, confinement effects occur in low dimension morphologies such as in quantum dots or nanowires, which blueshift the bandgap and strengthen the exciton stability. Also, the optical properties depend on the quality of the materials: for example, the perovskite single crystal and thin films, both three dimensional, differ because of the high crystal quality of the single crystal and the many defects in the polycrystalline thin films. Moreover, the optical properties also depend on the deposition methods. For example, the thin film can be composed of grains of different types and shapes depending on the experimental conditions.

One of the main properties of the 3D perovskites is the tunability of their gap energy, and hence of their emission wavelength, via chemical substitution. For example the Iodine-based perovskites $CH_3NH_3PbI_3$ and $CsPbI_3$ have a band gap around 1.6 eV and emit in the infrared, at around 780 nm. The bromide-based perosvkites $CH_3NH_3PbBr_3$ and $CsPbBr_3$ have a band gap around 2.3 eV and emit in the green at 540 nm and the chloride-based perosvkites $CH_3NH_3PbCl_3$ and $CsPbCl_3$ a band gap around 3 eV and emit in the blue at 400 nm. The perovskites $CH_3NH_3PbI_3$, $CH_3NH_3PbBr_3$ and $CH_3NH_3PbCl_3$ will be called respectively MAPI, MAPB and MAPCl in the following of the manuscript.

Figure 1.22 shows an example of halide substitution in Cs-based perovskites, extracted from [69]. The emission wavelength can be tuned continuously over the visible range by changing the stoechimoetry between the chloride, bromide and iodine.

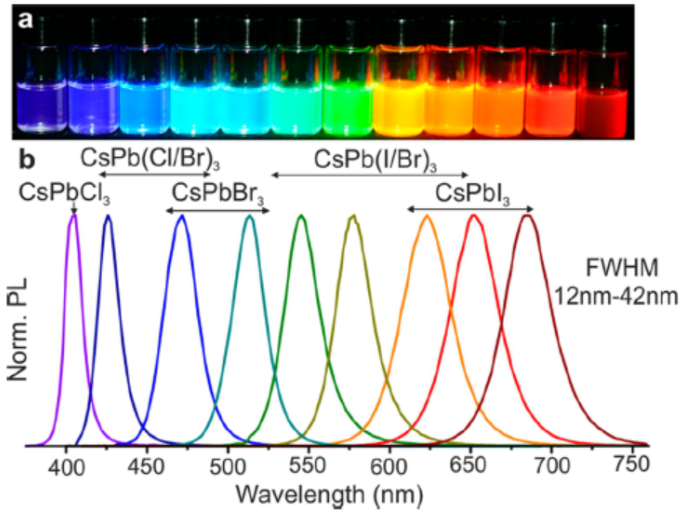

Figure 1.22: Example of wavelength tunability in Ceasium-based halide perovskites via halide subtution. Extracted from [69]

Besides the emission tunability, the perovskites possess a high absorption coefficient over the visible range thanks to their direct bandgap ($\sim 10^5 cm^{-1}$) [70], long-range carrier diffusion lengths larger than 1 µm [71], relatively high charge carrier mobility as high as 10 $cm^2.V^{-1}.S^{-1}$ [13, 14]. All these properties explain the good performances of the perovskite-based solar cells [72] and LEDs [12, 63]. The good transport properties give hope to achieve electrically injected perovskite based-lasers or polariton devices.

The stability of the exciton depends mostly on the halide composition of the perovskite. For the Iodine-based perovskites, the binding energy is around 16 meV at low temperature (10K) and close to zero at room temperature [73]. The consensus is that the free carriers are the species which dominate the optical properties, which is an additional advantage for obtaining high-efficiency solar cells. When the halide is changed from iodine to bromide or chloride the bandgap increases and also the binding energies. For the chloride-based perovskites, the exciton binding energies lie between 41 and 75 meV [69, 74–77], which is higher than the 25 meV thermal energy at room temperature. This implies that the excitons are stable at room temperature. In the case of the Bromide-based perovskites, various values between 15 to 110 meV can be found in the literature [75, 76, 78–88], which means that the nature of the species dominating the photophysics of the bromide-based materials is still not well known.

The stability in time, the photostability and the thermal stability of perovskites remain severe issues regarding the applications (solar cells, LEDs and lasers). For example, thin films of the perovskites MAPI are stable only for a few days as the perovskite trans-

forms gradually into crystals of PbI_2 through the action of light, oxygen and humidity. This degradation can be seen by the eye as the black MAPI turns into yellow after a few days [89]. However, the encapsulation of the perovskites can improve the stabilities as it protects the perovskite from the humidity. Furthermore, stability depends on the chemical composition of the perovskites. For example, the perovskites MAPB and MAPCl are much more stable than MAPI. Additionally, changing the cation MA (methylethylammonium) by FA (Formamidinium) or Cs (Caesium) increases the stability. The crystal quality is another essential aspect for the perovskite stability, as the grain boundaries favour the degradation. As a consequence, progress on stability has been achieved by optimizing the synthesis, composition and encapsulation of perovskites. As an illustration, carefully designed perovskite-based solar cell modules can pass the dark damp heat test for 1000 hours at 80% of humidity [90]. However, more work needs to be done on the perovskite stability for the perovskites-based solar cells to meet the market requirements, one of which is stable operation for at least 25 years.

In this PhD, the perovskite MAPB with a bandgap in the green has been chosen as it could address the green gap problem of LEDs and lasers. Because of the high absorption close to the bandgap of the perovskite, small thicknesses are required for lasing applications. Therefore, MAPB thin films with thicknesses of the order of a hundred nanometers deposited by spin-coating will be introduced in a microcavity.

2.1.2 The low-dimensional perovskites

When the organic cation A is larger than the anion (MA, FA, Cs), the structure of the perovskite becomes bi-dimensional. Figure 1.23 a) shows the structure of a 2D perovskite of chemical formula $(RNH_3)_2MX_4$ where R is a carbon group. These 2D perovskites have the particularity of self-organizing in alternative organic and inorganic multilayers when deposited. The 2D perovskites are composed of inorganic octahedra MX_6 layers separated by layers of the big organic molecules RNH_3. Confinement of the electrons and the holes within the inorganic parts occurs thanks to the higher potential in the organic layers than in the inorganic layers (see figure 1.23 b)) (ref). This makes the 2D perovskites natural multi-quantum well structures. The physics of the confinement in quantum wells is not going to be detailed here as no confinement occurs in the perovskite studied in this PhD. Briefly, the confinement blueshifts the material bandgap and brings closer the electron and the hole, which increases the exciton binding energy and the oscillator strengths. For example, the perovskite $(C_6H_5C_2H_4NH_3)_2PbI_4$, called hereafter PEPI, composed of phenylethylamine (PE), lead (Pb) and Iodine (I), has an emission wavelength blueshifted to the green compared to its 3D counterpart MAPI, which emits in the infrared. Moreover, the PEPI exciton is much more stable than the MAPI exciton with binding energies of a few hundred of meV (ref), and possesses a huge oscillator strength, which makes it suitable for light-emitting devices.

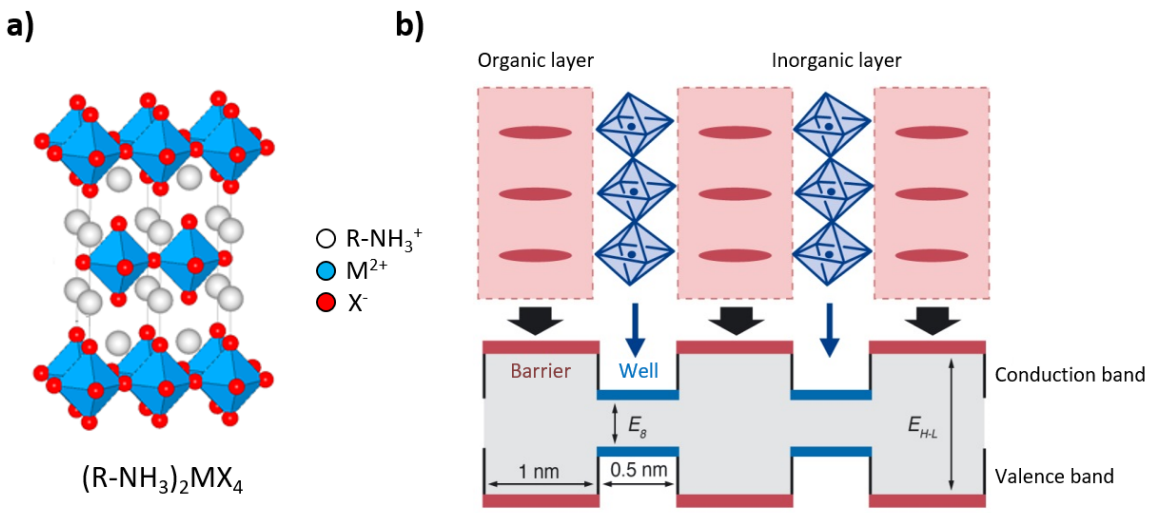

Figure 1.23: a) Crystal structure of a 2D perovskite b) Sketch of the 2D perovskite energy levels to illustrate the 2D perovskite organization in quantum wells

It is possible to control the confinement and hence the emission wavelength, binding energies, and oscillator strengths by realizing Ruddlesden-Popper perovskites, presented in figure 1.24, of chemical formula $(RNH_3)_2A_{n-1}M_nX_{3n+1}$, where M and X are the same elements as before and R and A are "big" and "small" organic cations. In the Ruddlesden-Popper perovskites, the number of inorganic layers between the organic parts varies the confinement. When $n = 1$, we retrieve the formula of the 2D perovskite described above, and when $n = \infty$, the 3D perovskite formula. For example, for the Ruddlesden-Popper perovskite $(C_6H_5C_2H_4NH_3)_2(CH_3NH_3)_{n-1}Pb_nI_{3n+1}$, one can continuously vary the exciton binding energies from a few meV (MAPI) to hundreds of meV (PEPI). For these reasons the Ruddlesden-Popper perovskites are also referred as 2D-3D perovskites.

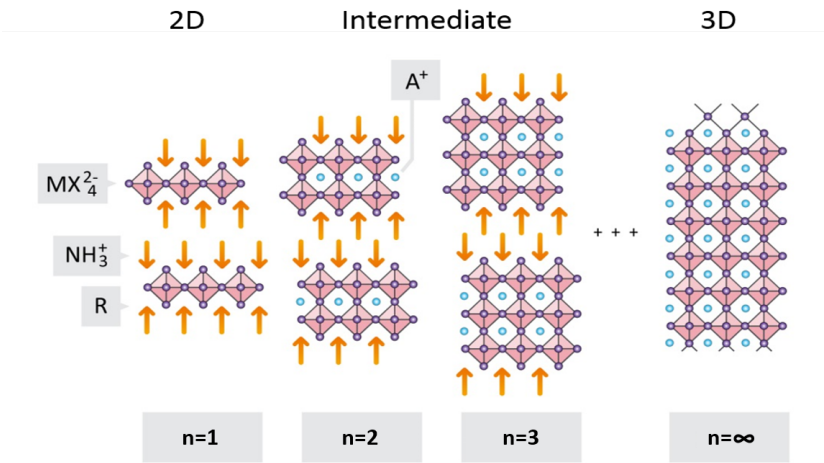

Figure 1.24: Sketch of the Ruddlesden-Popper perovskite with n varying from 1 to ∞

The advantages of the Ruddlesden-Popper compared to the 3D perovskites are their better optical properties (huge exciton binding energies, large oscillator strengths) and stability. For example, a one-year stable solar cell based on 2D-3D perovskites, yet with an efficiency of 11.9%, has been recently reported [91]. However, the charge transport of the 2D-3D perovskites suffer from the increased number of organic layers forming insulator barriers, which is a drawback for the current injection required for LEDs and Lasers [92].

2.2 Laser in the weak coupling regime with halide perovskites

2.2.1 The green gap for solid-state emitting devices

In 2014, the Nobel prize of physics was awarded jointly to Isamu Akasaki, Hiroshi Amano and Shuji Nakamura for the invention of blue efficient light-emitting diodes (LEDs) [1, 93, 94]. These LEDs based on nitrides of aluminium, gallium and indium are now the materials used commercially for blue-emitting LEDs and also for blue laser diodes (LD). The III-nitride semiconductors and alloys (for example, InGaN) possess energy gaps covering the entire visible spectrum. However, only the III-nitride semiconductor-based LEDs and Laser diodes emitting in the violet and the blue region are efficient. Replacing the Nitride by Phosphide and one obtains the III-phosphides semiconductors (for example, AlInGaP) which are the other leading materials for the commercial LEDs and Lasers. The III-phosphides and alloys can also cover multiple wavelengths and are efficient in the red region. Both the III-Nitride and III-Phosphide semiconductors are not performing in the green region. Figure 1.25 extracted from [2] whose data are collected from [3, 4] illustrates the drop of efficiency of the III-Nitrides and III-Phosphides LEDs in the green region. This region where the LEDs and laser diodes are rare and not performing is known as the "green gap" region. Finding a material which would resolve the "green gap" problem remains a challenge for the solid-state based lasers. Such a material should possess excellent optical properties in the green region and good charge transport properties while remaining at the lowest possible cost.

2.2.2 Lasing in the weak coupling regime with halide perovskites

Since the first observation of Amplified Spontaneous Emission (ASE) from a MAPI thin film in 2014 [9], followed the same year by the demonstrations of halide perovskite lasing in a vertical surface cavity [10], in perovskite nanoplatelets exhibiting whispering gallery modes [65], in polycrystalline perovskite thin films [66, 67] and in a spherical resonator [11], the halide perovskite has gained a lot of attention from the laser community. Essentially, the halide perovskites present high quantum yield (near unity) [64, 95], high absorption coefficient ($\sim 10^5 cm^{-1}$) [70], high optical gains (up to 3200 cm^{-1}) [96], low thresholds (as low as 0.220 $\mu J/cm^2$) [64] and more importantly, continuous wavelength tunability via chemistry substitutions [9, 69, 97, 98]: lasing action with halide perovskites has been achieved in the entire visible range and the near-infrared. These properties

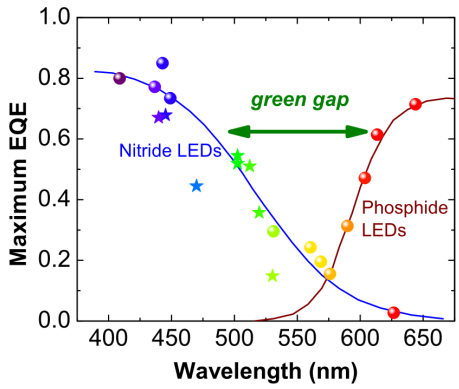

Figure 1.25: Maximum external quantum efficiencies of commercial III-Nitride and III-Phosphides LEDs illustrating the "green gap". The data points are taken from [3] and the data stars from [4]. Extracted from [2]

make the halide perovskites interesting for many applications and especially in the "green gap" region where the laser diodes are rare and not performing [2]. The main challenges for the perovskite-based lasers involve the perovskite structural stability and thermal stability [99]. As for the solar cells, progress was obtained on the structural stabilities via encapsulation, optimization of the interfaces and perovskite synthesis and composition. The thermal instabilities are due to the poor perovskite thermal conductivity, and for this reason, most of the lasing actions with halide perovskites were obtained with femtosecond or picosecond pulsed pump laser to limit heating from the pumping. Indeed, with a pulsed laser, the damage threshold is reduced, which allows reaching the lasing threshold. However, halide perovskite lasing could recently be achieved with continuous pumping [100–107], which constitutes as a progress on the thermal stability and as a crucial step for electrical injection. Electrically injected perovskite-based lasers have not yet been achieved.

In the following, we will review the main trends of research concerning lasing with halide perovskites. For more detailed information on this topic, the reader is invited to read the reviews on which this part is based [99, 108, 109].

The resonators for perovskite lasing

We will first describe the lasing action in perovskites occurring naturally within thin films or single crystals. Because of the high refractive index in the visible range, higher than 2, the reflectance at the perovskite-air interface is high, and the critical angles are small, which permits the light to be well confined within the crystal where the gain occurs. For these reasons, lasing action could occur directly in nanowires which are natural Fabry Perot cavities with the two end facets serving as cavity mirrors [64, 97, 110, 111]. The feedback needed for the lasing action can also be brought by whispering gallery modes, and lasing could hence be performed in perovskite nanoplates, microplates and micro-

spheres [65, 112–114]. Due to the high gain in perovskites, lasing could be obtained in highly scattering thin film without any well-defined modes; this lasing is referred as random lasing [66, 67, 115–118, 118–129]. More details on random lasing will be given in Chapter 4 of this manuscript. Figure 1.26 shows sketches of these three types of lasing that can occur directly from synthesised perovskites without any external feedback nor post-synthesis treatments.

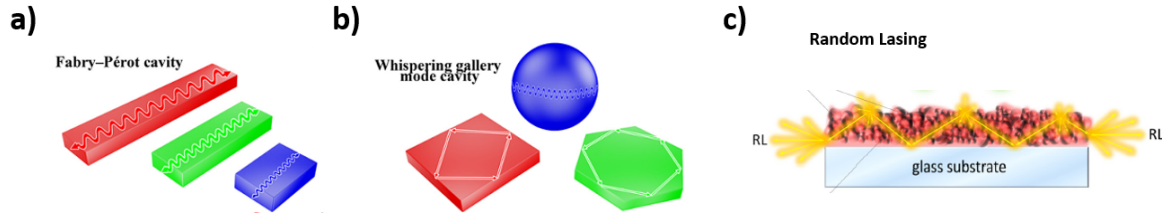

Figure 1.26: Sketches of the different types of resonators which can occur directly from perovskite without any external feedback a) Fabry Perot microcavity in perovskites nanowires b) Whispering gallery modes in perovskites nanoplates, microplates and microspheres c) Random lasing action in highly scattering perovskite thin films. a) b) extracted from [99] c) Extracted from [130]

Of course external feedback has been considered in different types of resonators: in VCSEL (Vertical Surface Emitting Laser) [10, 131], in Distributed Feedback (DFB) cavities [100, 102, 132], in photonic crystals [133, 134] and other external structures permitting whispering gallery modes, for example lasing could be obtained from silica microsphere surrounded by a layer of MAPI [11].

All the architectures of the perovskites lasers are in the nano or micro-scale. Indeed, because the perovskites have large absorption coefficients and high absorption close to the bandgap, the thickness of the perovskites should not be higher than a few hundred nanometers. Otherwise, the losses induced by the self-absorption would be higher than the gain and hence prevent from obtaining the lasing. The perovskite lasers reported in the literature are thus micro and nano-lasers.

Optical gain and quantum yield

Studies on the perovskite optical gain have been carried out, and values of a from several tens to few thousands of cm^{-1} have been measured for different kinds of perovskites (MAPI, Caesium based perovskites, Ruddlesden—Popper perovskites) [109]. When Xing et al. first demonstrated the ASE, the optical gain measured was of 250 cm^{-1} from a MAPI thin-film [9]. Later, a high gain of 3200 cm^{-1} could be obtained from a high-quality MAPI thin film deposited with an atomic layer deposition method [96]. Xing et al. also measured the quantum yield, PLQY, (ratio of the photon emitted to the photon absorbed) of the MAPI thin film above the ASE threshold close to 20% [9]. Thereafter, Zhu et al. could estimate the quantum yield of a high-quality MAPI nanowire to be near unity above the lasing threshold [64]. Moreover, Braly et al. could recently demonstrate an internal quan-

tum yield of passivated MAPI thin film of 92% [95]. The passivation of the thin film significantly decreased the non-radiative recombination at the film surface, which explains the high quantum efficiency. These results show that the perovskites possess intrinsic high optical gain and high quantum yields; the quality of the perovskite crystal is hence crucial for the lasing performance.

Quality factors

The quality factors, Q, obtained from perovskite-based lasers depend highly on the type of resonator and the perovskite crystal quality. For example, quality factors from optical microsphere can reach values of the order of 10^8 or even higher; however, due to the scattering induced by the perovskite thin films, the quality factors of perovskite-based microspheres are limited so far to values of the order of a thousand [108]. The quality factors obtained with perovskite-based lasers range from a hundred to several thousand [108, 109]. Amongst the highest quality factors reported, we can note as examples the quality factor of 7000 in a $CsPbBr_3$ microcrod [135], of 6100 in a Caesium perovskites-based microsphere [136], of 3600 in a MAPI-based nanowires [64], or 1420 in a perovskite VCSEL [137]. Such as for the optical gain or quantum yield, improving the crystal quality of the perovskites remains essential to improve the quality factors of perovskite-based lasers further and reach quality factors close to the ones of the conventional semiconductor micro-lasers. Increasing the quality factors is also important to decrease the lasing thresholds.

Pulsed lasers pumped perovskite lasers and thresholds

The perovskites-based lasers are in most cases pumped with femtosecond, picosecond or nanosecond pulsed lasers. In these cases, the achieved thresholds range from a fraction of $\mu J/cm^2$ to a few hundred of $\mu J/cm^2$ and are again dependent on the perovskite quality. As an illustration, the lowest threshold value of 0.220 $\mu J/cm^2$ was obtained in high-quality MAPI-based nanowires exhibiting the high-quality factor of 3600 [64], while the random lasing threshold of a highly scattering MAPI thin film is of 195 $\mu J/cm^2$ [67].

Multi-photon pulsed lasers pumped perovskite lasers and thresholds

Lasing with perovskite could also be obtained with two-photon pumping [138–141] three-photon pumping [142–144] or even 7-photon pumping [145]. The perovskite lasing thresholds with multi-photon pumping are increased compared to the one-photon pumping with values from several hundred of $\mu J/cm^2$ to few hundreds of mJ/cm^2 : for example 786 $\mu J/cm^2$ in a two-photon pumped MAPB microwire [138] and 130 mJ/cm^2 in a three-photon pumped MAPB microrod [143].

Continuous-wave optically pumped perovskite lasers and thresholds

Continuous-wave lasing is considered as a critical intermediate step in the hope of realizing electrically injected diode lasers. This is the reason why intense research has been carried out on continuous-wave pumped perovskites-based lasers. At the early ages, because of the poor thermal stability of the perovskites, the perovskite lasing action could only be obtained with pulsed lasers pumping. In 2016, Jia et al. could demonstrate, at 160K, a quasi continuous-wave lasing from a metal-clad MAPI DFB laser under 25 ns pulse pumping and a repetition rate of 25 MHz with a threshold around 5 kW/cm^2 [100]. Later, the authors could demonstrate, in a similar architecture, continuous-wave lasing with the perovskite MAPI with a threshold of 17 kW/cm^2 at 106K up to 160K [102]. The lasing could sustain for about an hour at 106K. These results can be explained by the high thermal conductivity of the Al_2O_3/Au/Si and Al_2O_3/sapphire substrates and of course, the low temperature of operation (100-160K). Alias et al. could demonstrate continuous-wave pumped ASE for the first time with a threshold of 89 kW/cm^2 at room temperature in a VCSEL architecture containing the perovskite MAPB with a sapphire substrate [101]. The authors attribute this result from optimization of the cavity modes with the perovskite gain, a sufficient cavity quality factor of 203, a good material quality (the authors worked with a passivated and annealed perovskite layer) and the good thermal stability of the device.

With thermal nanoimprint lithography (NIL), Li et al. could obtain high-quality factor (Q= 17872) MAPI-based DFB via a direct patterning onto the perovskite layers [104]. This method, at the same time, improved the perovskite emission characteristics. As a result, the lasing threshold could dramatically be reduced down to 13 W/cm^2, allowing to obtain continuous-wave lasing at room temperature for the first time. However, the lasing could only be sustained during 250s at 15 W/cm^2. Very recently, the same authors could demonstrate room-temperature continuous-wave lasing from a photonic crystal containing the perovskite MAPB with a threshold of 9.4W/cm^2 via the same thermal nanoimprint lithography technique [105]. The perovskite MAPB was chosen to improve the device stability as the MAPB perovskite is much more stable than the MAPI perovskite. Room-temperature continuous-wave lasing with perovskite could also be achieved in a DFB containing quantum dots of MAPB, MAPI, MAPCl in polyacrylonitrile films with thresholds of respectively 15, 24 and 58 W/cm^2 [106]. The authors explain the threshold reduction by the interaction between polyacrylonitrile and the perovskite quantum dots.

Continuous wave lasing could also be observed in $CsPbBr_3$ nanowires at cryogenic temperatures respectively at 4K with a threshold of 1.45 nW [107] and at 77K with a threshold of 6 kW/cm^2 [103].

To summarize, by the improvement of the quality factors, the reduction of the threshold and the optimization of the thermal stability of the devices (for example by including highly thermal conductive substrates), continuous-wave lasing with perovskites could be recently obtained at room temperature. However, there remains work on the perovskite stability over time, but overall these results give great hope towards electrically injected perovskite-based lasers. For more information on continuous-wave pumping perovskite-based lasers, the reader is invited to read the recent progress report on this topic [146].

Wavelength tunability

Another property of perovskite-based lasers is the possible continuous wavelength tunability covering the visible range and the near-infrared range. In 2014, Xing et al. could demonstrate ASE from different perovskites with different chemical compositions emitting at different wavelengths [9]. This result was particularly important as it showed that the perovskite could provide gain in the visible range, including the green gap region of the III–V semiconductor lasers. Figure 1.27 shows two examples of wavelength tunability from perovskites lasers, with CsPbX3 nanowires (with X a mixture of the halides I, Br and Cl) [98] (figure 1.27 a) and with perovskite nanowires containing a mixture of Formanidinium (FA) and Methyethyamonium (MA), and a mixture of halides (I, Br, Cl) [97] (figure 1.27 b). With the inclusion of the Formanidinium, near-infrared wavelengths can be reached (see figure 1.27 b). Another way to tune the emission wavelength is to play with the perovskite dimensionality, for example by varying the perovskite quantum dots size to vary the quantum confinement [69].

Engineering of perovskite lasers

As stated above, the emission wavelength of the perovskite lasers can be tuned via chemistry composition and/or the control of the dimensionality. However, after synthesis, the wavelength remains fixed. For practical reasons, it is interesting to be able to tune the emission wavelength post-synthetically. This post-synthetical tailoring of the emission wavelength is possible with halide perovskites via halide substitution with cation and anion exchange techniques [147–150]. For example, Li et al. could demonstrate a reversible transformation of the perovskite MAPB to MAPI via a vapour transport process [150]. Another approach is the halide substitution with inductively coupled plasma (ICP) etching [151], Zhang et al. could show that the lasing intensity and threshold remains unaffected through the reversible changes.

The lasing performances can be improved with passivation techniques, such as combining perovskites with graphene [152], plasmonic materials [153], ZnO nanoparticles [120], and surfactant ligands [154]. The improvements can be a lasing threshold reduction [120, 152, 153], emission enhancement [120, 152, 153] or an improved stability [154].

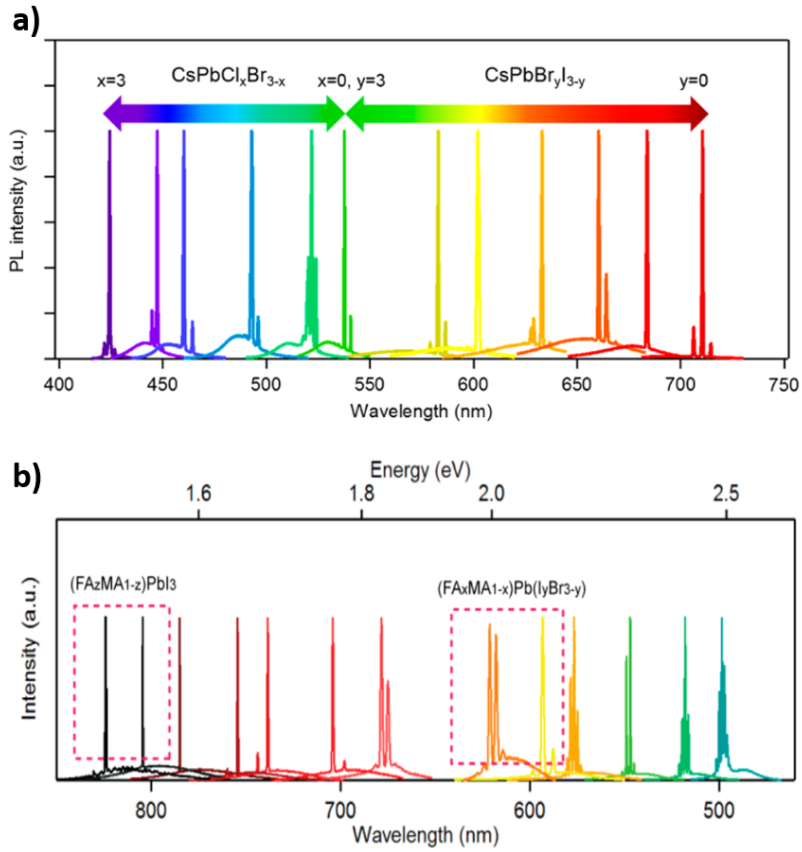

Figure 1.27: a) Lasing emission spectra of CsPbX3 nanowires (with X a mixture of the halide I, Br and Cl) covering the visible spectrum from [98]. Extracted from [98]. b) Lasing emission spectra of nanowires of perovskites containing a mixture of Formanidinium (FA) and Methyethyamonium (MA), and a mixture of halides (I, Br, Cl) from [97]. The emission wavelength covers the green region to the near-infrared region. Extracted from [97]

Patterning or shaping the perovskites into well-defined architectures is required for perovskite-based lasers or devices. One approach is to incorporate the perovskites by vapor-phase or spin-coated deposition methods in passive architectures such as microspheres [11], photonic crystals [133, 134], DBF [100, 102, 132], etc... Inverse opal structures where the perovskite is infiltrated were also considered to obtain 2D and 3D photonic crystals [155–157]. Directly patterning the already synthesised perovskites is another path for obtaining well-defined architectures. Semiconductor technology has been performed to directly pattern the perovskites, such as nanoimprint lithography [158–161], electron-beam lithography [162], solvent-assisted gel printing (SAGP) [163], X-ray lithography [164], laser direct writing (LDW) [165, 166], wettability-assisted photolithography (WAP) [167], inductively coupled plasma (ICP) etching [162], focused-ion beam etching [168, 169].

One of the many applications explored with perovskites are the nanolaser arrays, which are intensively investigated with conventional semiconductors towards their possible use in highly integrated photonic devices. Top-down lithography and nanoimprinting can

precisely build uniform pattern but would increase the price of the devices. For these reasons, many techniques at lower cost have been proposed to fabricate perovskite-based nanowire arrays [170–173].

2.3 Strong coupling with perovskites: towards perovskite-based polaritonic lasers

In the following, the strong coupling and polaritonic lasing obtained with halide perovskites will be put in the context of the field of the strong coupling. A first part will give the general context, and a second part will focus on strong coupling with perovskites.

2.3.1 Context: the strong coupling and polariton lasing in the literature

Strong coupling regime

The strong coupling was first theoretically proposed by J.J. Hopfield in 1958 [174] to describe the light propagation in semiconductors, and observed in ZnO bulk crystals by Hopfield and Thomas in 1965 [175]. The cavity polaritons , analogue to the bulk polaritons, were first experimentally demonstrated in 1992 by Weisbuch et al. [5] with an AlGaAs quantum wells-based microcavity thanks to the progress on semiconductor epitaxy. This work became the pioneering work not only for the cavity polaritons but for photonic crystal polaritons or nanowire polaritons. Since then, the strong coupling regime has been demonstrated with many types of materials : with inorganic semiconductors such as GaAs [5, 39], ZnO [176, 177] or GaN [176, 177], with organic materials [47, 178–180], more recently with monolayers of transitional metal dichalcogenides (TMDs) [181, 182] and of course with halide perovskites [68].

There are many exciting potential polaritonic applications and many of them could be demonstrated in lab prototypes such as the polaritonic lasers [7, 47], polariton transistors [35] and interferometer [36], resonant tunneling diodes [27], optical gates [35] and router [37]. However, only a few of these were electrically injected, a key step for real exploitation [183–186]. The majority of the prototypes were obtained under optical pumping, and some were only demonstrated at low temperature. Therefore, one needs to find a material with good transport mobilities, exhibiting strong excitons with large binding energies and large oscillator strength for obtaining the polaritons at room temperature. Moreover, such polaritonic devices would require the polariton to propagate through macroscopic distance. Thus, the material should be homogeneous on a large thin-film surface. Concerning the thickness, the strong coupling in microcavities requires the gain material thickness to be a few times the emission half wavelength ($n\lambda/2$). Finally, the material deposition, synthesis and patterning into microstructures should be available at the lowest possible cost.

Due to the maturity of the technologies used for their fabrication, the GaAs based microcavities exhibiting strong coupling are the most developed and accomplished systems for both fundamental research on polariton, for example, the study of out of equilibrium Bose-Einstein condensates, and for the research related to the polaritons applications. In this regard, most of the proof-of-concepts of polaritonic devices listed above have been achieved with GaAs systems. Nevertheless, the strong coupling can only be achieved at cryogenic temperature due to the small GaAs excitonic binding energies. Large bandgap semiconductors such as GaN and ZnO are more suited for obtaining room temperature polaritons due to their higher exciton binding energies. However, the technologies required for the deposition of inorganic semiconductors, GaAs, ZnO and GaN, and the engineering to incorporate them into microstructures remain at a high price (high temperature and high vacuum are required).

The soft chemistry and low-temperature synthesis and deposition of the organic materials make them more relevant for low-cost polaritonic devices. Moreover, the organic materials in which the strong coupling has been demonstrated exhibit very strong excitons, with binding energies of a few hundred meV. Nevertheless, their poor transport properties reveal as a major drawback for electrical injection. In the meantime, the TMDs combine the low-cost deposition aspect, strong excitons and good transport properties, but their fragility prevents so far their deposition in large areas.

Polariton lasers

The polariton lasers have been obtained through optical excitation with many kinds of materials, at low temperature in CdTe [7] and GaAs [187] and at room temperature with materials exhibiting stronger excitons such as GaN [45], ZnO [46] and organic materials [47].

The strong coupling could also been obtained with electrical injection. The first polaritonic LEDs were obtained in 2005 with polyelectrolyte/J aggregate dye bilayers [188] and later with other organic materials [189, 190], carbon nanotubes [191], inorganic semiconductor such as ZnO [192], GaN [193] and GaAs[194–197] and this even at 315K [197]. Very recently polaritonic LEDs were reported with Van der Waals materials [198].

The work on polariton LEDs was a first step towards electrically injected polariton lasers which could be obtained in GaAs systems at low temperature with or without the help of a magnetic field [183–185] or with GaN at room temperature [186].

2.3.2 Strong coupling regime and polariton lasing with 2D perovskites

Before 3D perovskites $CH_3NH_3PbX_3$ emerged as potential materials for the photovoltaic field in 2012, their 2D counterparts were the most studied due to their excellent excitonic properties. Between the first demonstration of strong coupling regime with perovskites by Fujita et al. in 1998 [68] and the beginning of the perovskite "fever" with 3D perovskites, most of the strong coupling demonstrations were done with phenylethylamine (PE)-based 2D perovskites and more especially with the Iodine-based perovskite PEPI emitting in the green. More precisely, 11 out of the 17 reports published at that time concern the perovskite PEPI. Before the perovskite "fever", the studied 2D perovskites were spin-coated thin films of rather low quality and the quality factors were subsequently low. Due to the large oscillator strengths, strong coupling regime could still be observed despite the low quality factors. However, polaritonic lasing could not be observed. After the emergence of 3D perovskites in the photovoltaic field, a lot of work was done on the crystal quality and strong coupling regime could be obtained with systems containing synthesised or exfoliated single-crystal thin films in the prospect of polaritonic lasing.

Strong coupling regime with 2D perovskite thin films

The first demonstration of the strong coupling with perovskites has been achieved in a distributed feedback (DFB) resonator containing the perovskite PEPI [68] whose sample's sketch is given in figure 1.28 a). Like the planar microcavities, the DFB structures possess photonic modes with a given dispersion. When the incident light angle is tilted along the direction of the periodic grating (x-direction in figure 1.28 a)), the observed photonic mode dispersion curves are in the form of cones represented by black lines in figure 1.28 b). The dashed lines in figure 1.28 b) correspond to replicas of the dispersion represented by a black solid line. Figure 1.28 c) shows the theoretical polariton dispersion curves (black solid lines) in a DFB in strong coupling regime in the case of a negative detuning ($\Delta E < 0$) and along the grating direction, k_x. The DFB photonic mode curve is plotted as a dashed black line and the exciton energy annotated by E_0. The anti-crossing region is zoomed-in in figure 1.28 d). When the incident light angle is tilted along the perpendicular direction of the grating (y-direction in figure 1.28 a)), there is no waveguide effect from the grating and the observed photonic modes are then similar to cavity photonic modes.

The strong coupling in the DFB structure has been demonstrated in angle-resolved transmission measurements in the grating direction and the perpendicular direction in [68], and a Rabi splitting of 100 meV has been measured in both cases. The quality factors of the photonic modes are not given in this article. The obtained Rabi splitting is really large compared to the Rabi splitting in GaAs based-microcavities but remains lower than the expected Rabi splitting considering the high oscillator strength of PEPI. The authors explain this feature by the rather poor spatial overlap between the exciton and the pho-

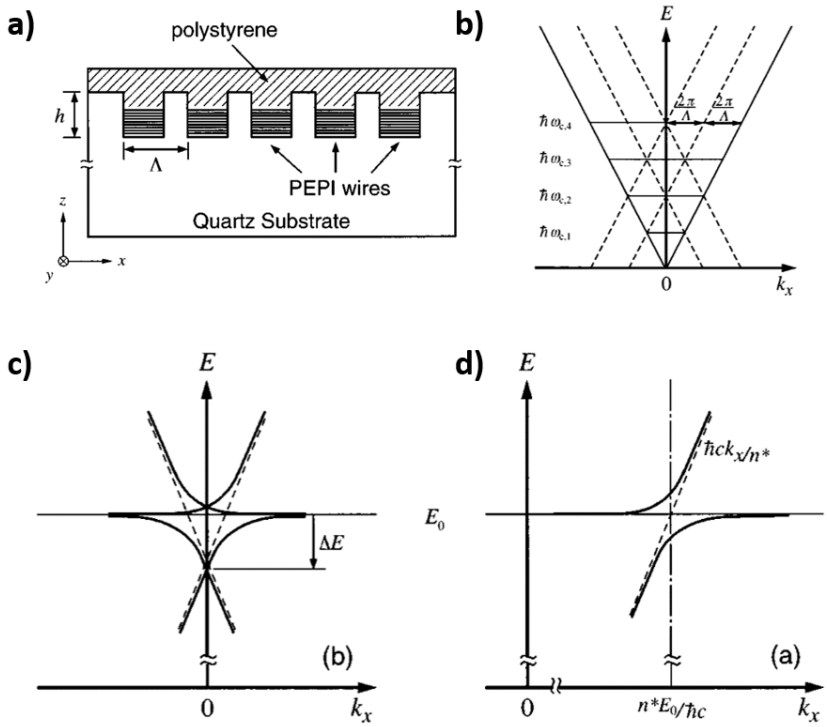

Figure 1.28: a) Sketch of the distributed feedback (DBF) structure studied by Fujita et al. [68] b) Photonic modes represented as black lines in the the direction of the periodic grating (x-axis in a)) of the DFB. The dashed lines correspond to replicas of the dispersion represented by a black solid line. c) Theoretical polariton dispersion in the DFB along the grating direction, k_x, in the case of a negative detuning ($\Delta E < 0$). The lower and upper polariton dispersion curves are plotted as black solid lines, the DFB photonic mode curve as a dashed black line, and the exciton line is annotated as E_0. d) Zoom of the anti-crossed region of the LPB and UPB dispersion curves. Extracted from [68]

tonic mode field in their structure. In [199], the authors studied the photoluminescence under nonresonant excitation of the same structure with a Rabi splitting of 75 meV and observed an enhancement of the photoluminescence for modes resonant with the exciton. In [200], the authors proposed a theoretical interpretation of the results found in [68] and [199].

Shimizu and Ishihara also studied the strong coupling regime in DFB structures in 2002 [201] and observed non-linearities of the polariton dispersion curves due to the exciton part of the polaritons. With pump-probe measurements, they showed that the transmission dips blueshift during the pump pulse due to the change of the polariton dispersion caused by excitonic Stark effect.

The aforementioned DFB structures can be regarded as 1D photonic crystals [3] and hence, other types of photonic crystal can be considered. Indeed, strong coupling with the perovskite PEPI has also been demonstrated with photonic crystals in 2 dimensions

[3] In these cases, not in the subwavelength regimes

[202] with a Rabi splitting of 100 meV and three dimensions [203] with a Rabi splitting of 240 meV. Figure 1.29 shows the sketches of these two photonic crystal structures. In the first case, the patterning is similar to the DFB expanded to the second direction in the plan. The Rabi splitting of 100 meV is identical to the ones found in the DFB structure. The structure of the second case is different: it is composed of an arrangement of silica microspheres infiltrated by the perovskite PEPI (named PAPI in this article). The Rabi splitting is here more than twice larger than in the case of the 1D and 2D photonic crystals meaning that the spatial overlap between the excitons and the photonic mode field has been strongly improved in this 3-dimensional photonic crystal.

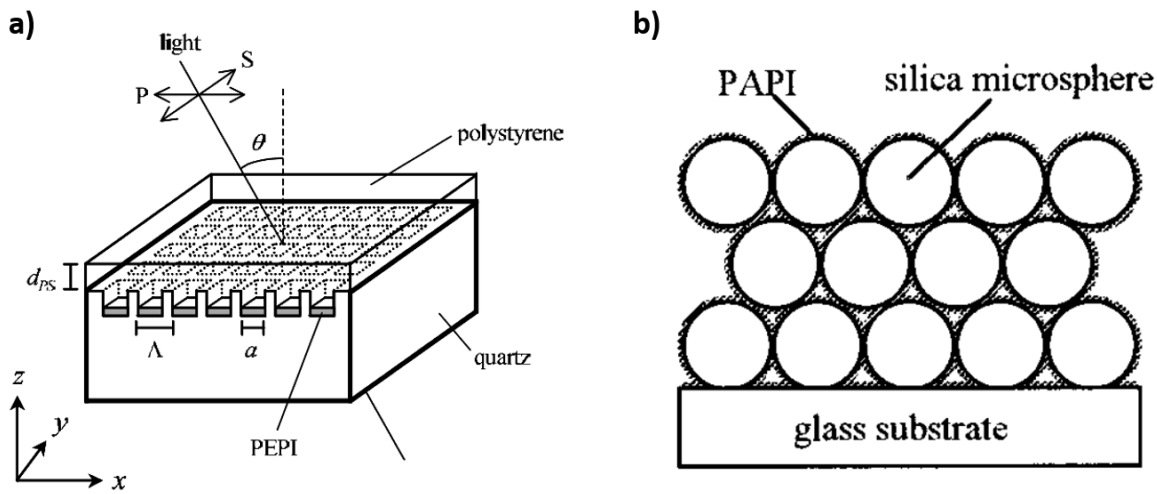

Figure 1.29: a) Sketch of the 2D photonic crystal in [203]. Extracted from [203]. b) Sketch of the 3D photonic crystal in [202]. Extracted from [202].

Planar microcavities were later considered by our group to study the strong coupling with 2D perovskites. The microcavities were at first in general composed of a bottom dielectric mirror, a spin-coated perovskite layer, either one spacer layer above or two spacer layers beneath and above the perovskite layer and a silver layer as the top mirror. These microcavities will be hereafter called DBR/Ag microcavities, where DBR holds for dielectric Bragg reflectors. The spacer layers were in general polymer layers such as PMMA (Poly(methyl)metacrylate). The 2D perovskites-based microcavities were closed by a silver mirror deposited by evaporation, which did not damage the perovskite protected by the spacer layer. Figure 1.30 shows an example of one of the microcavities studied along with its angle-resolved reflectivity spectra and polariton dispersion curves.

The quality factors of these microcavities were limited both by the quality of the polycrystalline perovskite thin films and the silver mirrors. However, despite the low-quality factors, the strong coupling could still be observed due to the very strong 2D perovskite oscillator strength. The strong coupling could be observed at room temperature in microcavities containing the PEPI perovskite or pFPEPI doped PMMA perovskite (pf for p-fluorophenethylamine) with Rabi splittings of 89.6 meV [205], 140 meV [206] 136, 150 and

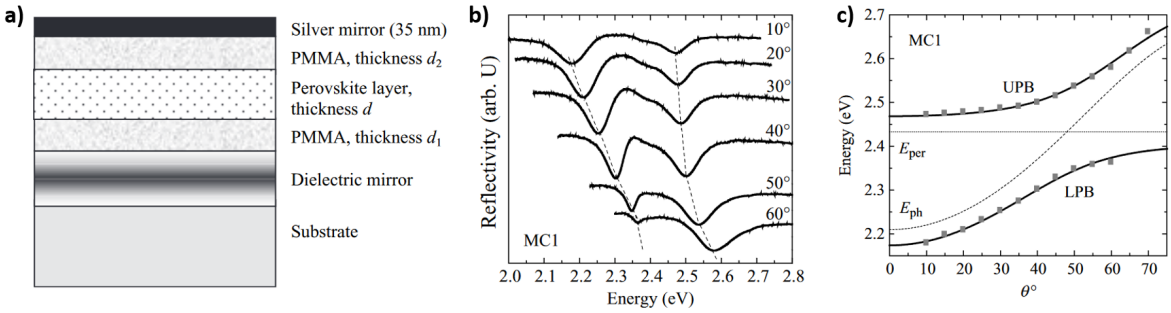

Figure 1.30: a) Microcavities studied in [204] along with its angle-resolved reflectivity spectra b) and polariton branches dispersion curves c). Extracted from [204]

190 meV [204] and with quality factors as low as 25. In the latter case, our group showed that the Rabi splitting could be controlled by changing the design of the microcavities. Indeed, the spatial overlap between the exciton and the photonic field can be enhanced by placing the excitons at the field antinodes (see figure 1.31). With the perovskite CHPI, similar to PEPI with the phenylethylamine (PE) replaced by cyclohexenyl-ethyl-ammonium (CH), the strong coupling, with Rabi splittings of respectively 160 and 130 meV, could even be observed in a microcavity with two silver mirrors or even in a microcavity with one silver mirror while the interface with air was used as the second mirror [207] . In these two cases, the quality factor was even lower than in DBR/Ag microcavities.

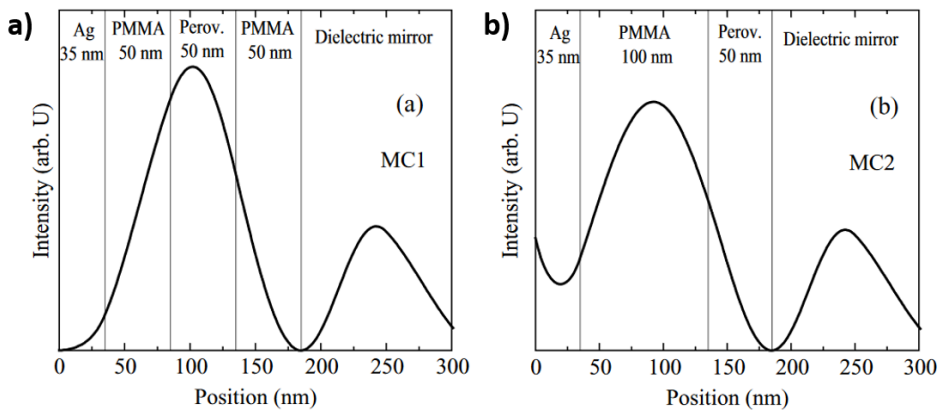

Figure 1.31: a) and b) Example of two microcavities studied in [204] with different designs. The spatial overlap between the exciton and the cavity photonic field is better in the first case. Extracted from [204]

In DBR/Al microcavities, the strong coupling regime could be observed with 2D perovskites emitting in the UV, for example, with the perovskite PEPCl, the iodine of PEPI being replaced by chloride (Quality factor Q of 15 and Rabi splitting $\hbar\Omega$ of 230 meV) [208, 209]. In this case, an aluminium mirror was chosen as it is more suitable in the UV region.

Despite the many reports demonstrating the strong coupling, polaritonic lasing has not been obtained in the 2D perovskite-based microcavities and photonic crystals. This

is probably due to the bottleneck effect as the large Rabi splitting, caused by the large oscillator strength, makes the slope of the LPB at low angle/momenta rather steep and hence the polariton relaxation time long. Moreover, because the perovskites were deposited in thin films, many defects could hinder the exciton lifetime, and the poor quality factor reduced the cavity photon lifetime significantly. All these reasons made the polariton lifetime shorter than the relaxation time. Indeed Lanty et al. in [204] suggested that the increase of the photoluminescence at large angles from their cavities was related to the bottleneck effect. Later, Gaëtan Lanty demonstrated the bottleneck effect from these microcavities in his PhD manuscript (in French) [210], by dividing the polariton emission at each angle/momentum by the photonic fraction β^2 to obtain the polariton population along the LPB (see figure 1.32). In order to address these problems, different axes of improvement were considered: decrease the relaxation time of the perovskite, increase the polariton lifetime by improving the cavity quality factor, by either increasing the closing mirror reflectivity or the material quality.

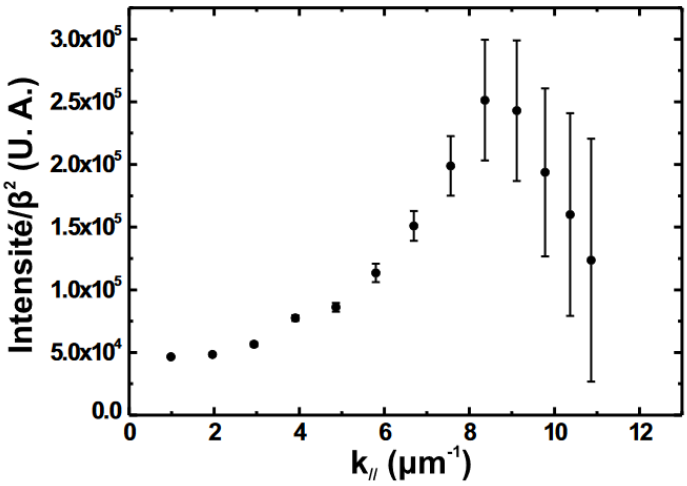

Figure 1.32: Polariton population showing the bottleneck effect measured in a cavity from [204] obtained by dividing the polariton emission at each angle/momentum by the photonic fraction β. Extracted from [210]

A way to decrease the relaxation time of the polaritons is to reduce the LPB slope by coupling the microcavity photonic mode with the 2D perovskite and another material also exhibiting excitons. In the case of the strong coupling in these systems, the two exciton transitions involved lead to three polariton modes, the upper, middle, and lower polaritons. In general, the lower polariton branch possesses a reduced slope compared to the systems with only one exciton transition. This method has been used by our group in [211] where strong coupling has been obtained in the UV range in a microcavity containing the perovskite PEPB and the organic material ZnTPP (Zn-tetraphenyl-porphyrin) or in a microcavity containing the perovskite MFMPB (5-methyl-2-furanmethanamonium bromide-based 2D perovskite) and ZnO [212]. The sketch of the latter case's microcavity and the polariton branches is given in figure 1.33.

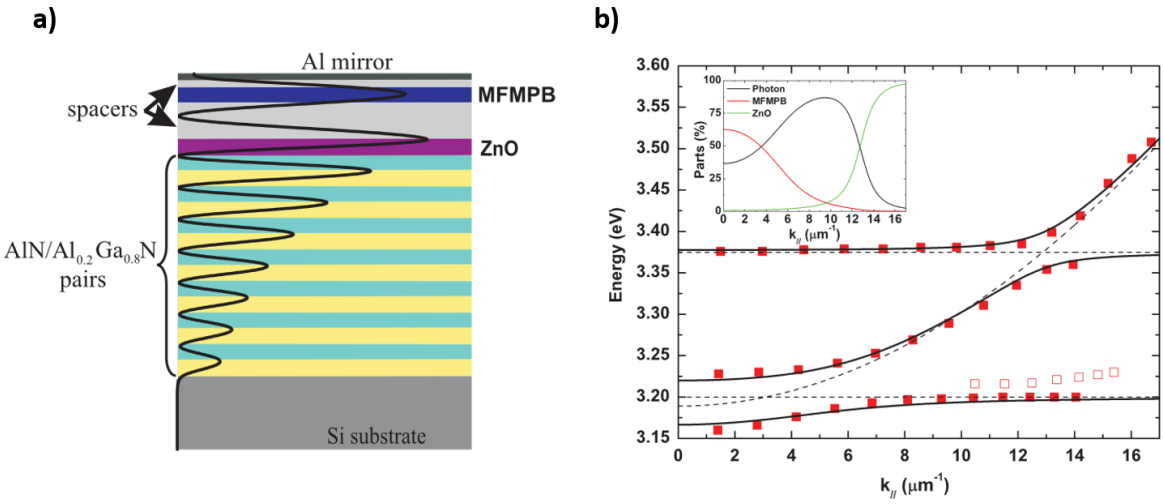

Figure 1.33: a) Sketch of the microcavity studied in [210] b) dispersion of the lower, middle and upper polaritons of the hybrid microcavity. Extracted from [210]

Regarding the improvement of the microcavity quality factors, one has to improve the reflectivity of the closing mirror. Due to the fragility of the perovskite thin films, the high-temperature deposition methods used for dielectric materials, such as epitaxy, CVD (Chemical vapour deposition) or sputtering, for example, could not be applied to deposit the top dielectric mirror directly on the half microcavity containing the perovskite. Han et al. [213, 214] proposed a technique depicted in figure 1.34 to deposit a dielectric mirror on top of a fragile active material without degrading the material. Briefly, an external top dielectric mirror (DBR) is placed on top of the half cavity inside a recipient filled with a liquid which is non-destructive for the gain material. The liquid is later removed, and the evaporation of the remaining solvent inside the microcavity keeps both parts fixed. With this technique, Han et al. could obtain a quality factor of 2500 from a passive cavity and a quality factor of 86 from a perovskite containing cavity in the strong coupling regime [214]. The decrease between the two quality factors is due to the roughness of the perovskite spin-coated thin film. However, this quality factor of 86 remains 3.5 times higher than the ones of the microcavities in [204–206]. Using this technique, and taking advantage of a top Bragg mirror containing sub-micrometric sphere-like defects, Nguyen et al. could observe zero-dimensional polaritons at room temperature with quality factors reaching 750 [215].

Strong coupling with 2D perovskites high quality single crystals

At this point, it could have been shown that the good excitonic properties of the 2D perovskites make them suitable as low-cost materials for the strong coupling. However, the huge oscillator strength combined with the poor quality of the perovskite thin films has revealed as an obstacle for the realisation of the polaritonic lasing. Indeed, the polariton relaxation time is too long compared to the polariton lifetime limited by the small

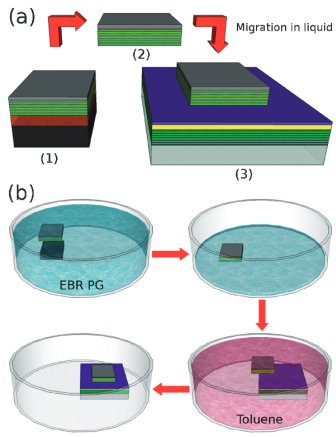

Figure 1.34: Sketch of the top Bragg mirror deposition method in [214]. Extracted from [214]

quality factors and the exciton lifetime. The two latter features are both related to the low quality of the perovskites spin-coated layers. Moreover, the fragility of these layers prevents from depositing monolithically a top dielectric mirror leading to a reduced quality factor. The poor vertical transport properties of these 2D perovskites is another issue concerning the electrical injection needed in the polaritonic-based devices. However, since 2012, much work has been done on the optimisation of the perovskite crystals quality. In particular, crystals with much better quality such as thin single crystals (synthesised or exfoliated) appeared recently.

Fieramosca et al. could demonstrate the strong coupling regime with 2D perovskites thin single crystals without an external optical cavity as the crystal end-facets serve as mirrors [216]. The perovskites studied were the butylammonium (BAI), octylammonium (OCT) and phenethylammonium (PE) based 2D perovskites, called here BAPI, OCTPI and PEPI. The thin single crystals were obtained by exfoliating bulk crystals obtained with the AVCC technique developed in our team [217] (Anti-solvent Vapor-assisted Crystallization). The quality of these crystals is much better than in the spin coated thin films; however, their thicknesses are of the order of a few micrometers. As a consequence, several optical modes occur inside the crystal, which hinders the light-matter coupling. Nevertheless, several LPB branches could be observed in angle-resolved reflectivity experiments (see figure 1.35). The authors showed that by varying the carbon group of the 2D perovskites, they could change the confinement of the exciton and as a result, the Rabi splitting with values of 103, 146 and 210 meV respectively for PEPI, OCTPI and BAPI.

Wang et al. also obtained strong coupling with a thick PEPI exfoliated single crystal and could embed thick and much thinner exfoliated PEPI and PEPB single crystals in a double Bragg mirror microcavity [218]. The deposition of the second mirror was done with e-beam evaporation onto the 2D perovskite. The quality factor of 2200 found here is much higher compared to the first quality factor of 2D perovskite-based microcavities. From the microcavities, the strong coupling between the cavity mode, the Bragg modes

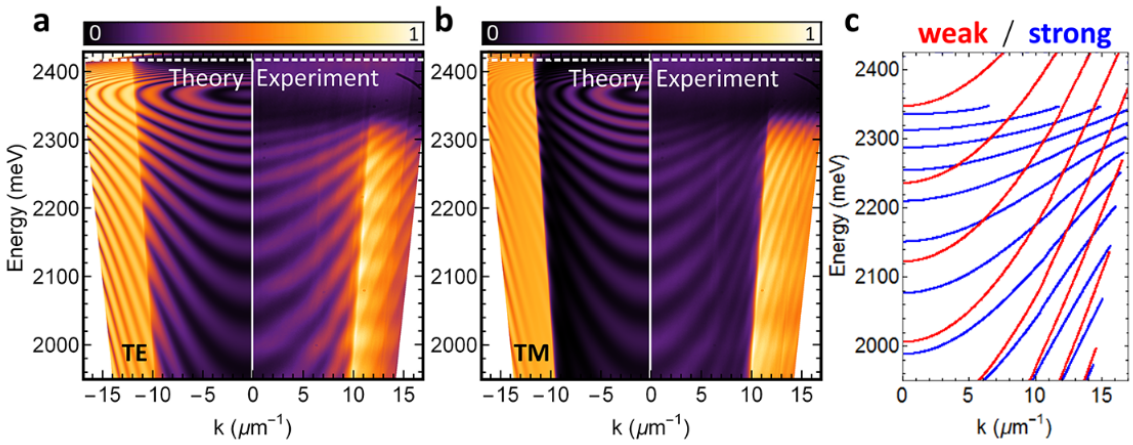

Figure 1.35: Angle-resolved reflectivity maps both in TE (a) and TM (b) polarization along with the simulated spectra of the thick PEPI crystal in [216]. (c) shows the theoretical cavity modes along with the theoretical LPB branches. Extracted from [216]

and the exciton could be demonstrated. Later Fieramosca and al. also could embed thin exfoliated PEPI single crystals in a double Bragg mirror microcavity using a sputtering technique [56] to deposit the top mirror. From this microcavity, the authors could observe strong non-linearities due to polariton-polariton interaction. The authors also obtained these non-linearities from a thick single PEPI crystal without external mirrors.

2.3.3 The strong coupling regime and polariton lasing with 3D perovskites

After the first demonstrations of lasing with halide perovskites, the 3D perovskites gained attention in the perovskite polariton community. Although their excitonic properties are weaker than in the 2D perovskites from the lack of natural confinement provided by the organic layers, the 3D perovskites possess better charge transport properties than 2D perovskites, which makes them more suitable for electrical injection. The 3D perovskites studied have morphologies with much better crystal quality than spin-coated thin films such as nano/microwires, microplates and nanoplatelets.

Strong coupling in nanowire-based microcavity

In the case of nanowires and nanoplatelets, the Rabi splitting is increased due to the size reduction of the photonic resonator (with lateral characteristic sizes of a few hundreds of nanometres), which notably reduces the modal volume. Indeed, the coupling strength g is proportional to the square root of the ratio of the oscillator strength to the modal volume, $g \propto \sqrt{f_{osc}/V_m}$.

Park et al. [219] observed in 2016 lasing action from $CsPbI_3$, $CsPbBr_3$, $CsPbCl_3$ nanowires. Lasing can occur in nanowires without an external cavity as the nanowires serve both as the gain medium and the cavity with the two end-facets as mirrors and the trans-

verse surfaces forming a light waveguide. However, the authors observed an unusual spectral spacing of the nanowire laser modes. Figure 1.36 shows an example of the unusual mode spacing from three different $CsPbBr_3$ nanowires in another study [103]. It was suggested that the unusual spacing could come from the strong light-matter coupling. However, the strong coupling has not been demonstrated in this study but only suggested. It was only one year later that the strong coupling could be demonstrated in a 3D perovskite-based micro/nanowires [220].

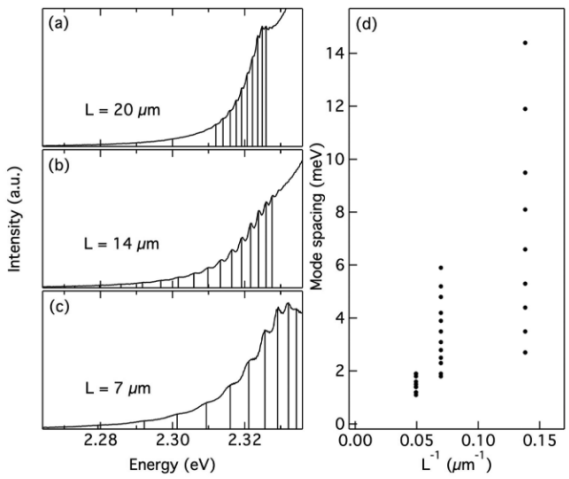

Figure 1.36: Photoluminescence spectra of three $CsPbBr_3$ nanowires of different size (a) 20 μm (b) 14 μm (c) 7 μm from [103]. Only the low energy part of the photoluminescence is shown. (d) Mode spacing increasing whith decreasing energies. Extracted from [103].

Before describing the strong coupling with halide perovskites-based nanowires, one needs to consider the experimental differences related to the observation of the polaritons between the usual microcavities and the nanowires. Both the microcavity and nanowire are optical resonators; however, while the former presents macroscopic lateral distances (µm up to cm^2), the latter exhibits lateral dimensions equivalent to the emission wavelength (hundreds of nm) [103]. This results in the diffraction of the light escaping the nanowire end-facets. Also, because of the size of the nanowires, the detunings are negative and very large, and the confinement in the lateral directions makes the effective photon mass one order of magnitude heavier than in microcavities. The effective photonic mass can be obtained from $M_{ph} = (\pi\hbar/c)(a^{-2} + b^{-2})^{\frac{1}{2}}$, where a and b are the lateral dimensions [221]. As a result, the anti-crossing occurs at momenta higher than the free photon momenta and can not be observed with the usual angle-resolved measurements.

To obtain the LPB dispersion, one needs to collect the modes energies from the photoluminescence lasing spectra (see figure 1.37). The momenta of these modes are unknown as the momentum-resolved PL cannot be performed. However, the momentum spacing, $\pi j/L$ with j an integer and L the nanowire length, is known and the wavenumber is determined by $k_{//} = \pi j/L + k_0$ with k_0 the unknown momentum of the zeroth mode.

The following consists in considering the microcavity E(k) relation: $E(k) = \hbar c k_{//}/\sqrt{\epsilon(\omega)}$ with epsilon the dielectric constant of the nanowire's medium approximated by a Lorentz model. By fitting the E(k) relations to the experimental energies, with k_0 and the Lorentz parameters as free parameters, one can get the nanowire dispersion. This dispersion is later fitted with the strong coupling model (see figure 1.37). This method was used in [220, 222–224]. The approach in [103] was slightly different as it considered another E(k) relation depending of the effective photonic mass, $M_{ph} = (\pi\hbar/c)(a^{-2}+b^{-2})^{\frac{1}{2}}$, known from the measurement of the nanowire lateral sizes a and b. At the end, and for all the cases, only the LPB in a small region around the anti-crossing and above the light cone could be obtained (see figure 1.37).

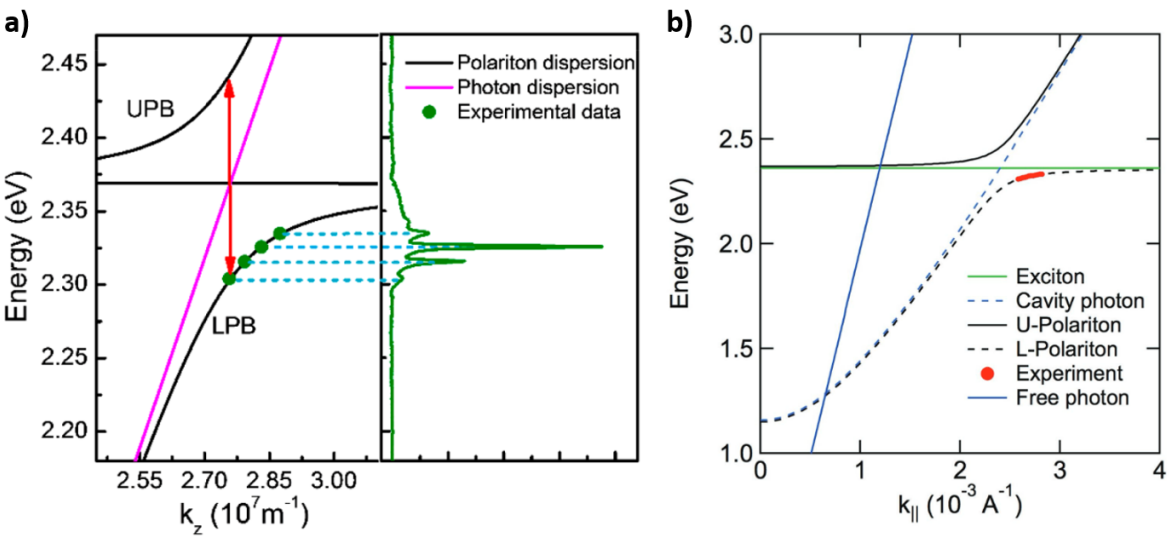

Figure 1.37: a) On the right: lasing emission of a $CsPbBr_3$ nanowire in [222]. On the left: fitting of the polaritonic dispersion curves obtained from the energies of the lasing peaks. Extracted from [222] b) Experimental lower polariton dispersion of a $CsPbBr_3$ nanowire in [103] (in red) along with the fitted dispersion curves of the upper polariton (solid black line) and lower polariton (dashed black line). The green line corresponds to the bare exciton energy, the dashed blue line to the nanowire photonic mode dispersion and the solid blue line to the free photon cone. Extracted from [103].

As the small lateral sizes of the nanowires reduce the mode volume, very large Rabi splittings could be obtained. In MAPB micro/nanowires, the Rabi splittings obtained were of 268, 390 meV [220] or even of 564 meV [223]. The very large Rabi splitting of the latter case is due to the coupling of the nanowires with surface plasmons from a layer of silver (Ag). Wang et al. showed that the Rabi splitting of $CsPbX_3$ nanowires vary depending on the halide (210, 146 and 103 for respectively the Chloride, Bromide and Iodine-based nanowires) [222], coherent with the variation of the exciton strength with respect to the change of halide. Values of 200 meV [103] and even from 401 to 656 meV [224] were reported in $CsPbBr_3$ nanowires. The giant Rabi splitting of the latter one denotes excellent confinement of the electric field inside the nanowire.

The variation of the Rabi splitting as a function of the nanowires lengths and so the modal volume has been studied [220, 223, 224] confirming the dependence on f/V of the Rabi splitting $\hbar\Omega$. The group velocity $dE/dk_{//}$ and so the group refractive index, $n_g = c/v_g$ were also studied as a function of the Rabi splittings [220, 223, 224]. An enhancement of the group refractive index has been shown for large Rabi splitting, which leads to a reduction of the group velocity, which is characteristic of polaritons and could be interesting for slow-light applications.

Polaritonic lasing could not be obtained in three of these studies [220, 222, 223] where only photonic lasing could be observed. For example, Zhang et al. ruled out the possibility of polaritonic lasing due to the lack of blueshift of the lasing peaks. However, the lasing peak blueshift, characteristic of polaritonic lasing, could be obtained in other studies [103, 224] and this even with continuous-wave pumping (77K) [103]. At first Evans et al. concluded that the lasing taking place in their nanowires was polaritonic lasing, but the authors recently reported new results and recognized that the lasing was instead originating from the coupling between nondegenerate electron-hole plasma and plasmons [111]. Du et al. [224] showed that the lasing threshold occurring in the bottleneck region drastically decreased when the Rabi splitting was higher than 400 meV and concluded that this was due to the transition from a photonic lasing to a polaritonic lasing. This polaritonic lasing has been possible thanks to the much better quality factors compared to the vertical microcavities.

Polaritonic lasing with 3D perovskites-based microcavities

In 2017, Su et al. obtained for the first time polaritonic lasing with perovskites [48]. The authors incorporated high-quality $CsPbCl_3$ nanoplatelets in a double DBR microcavity with a quality factor of 300. Figures 1.38 a) and b) show the sketch of the studied microcavity and the microscopy/fluorescence images of the $CsPbCl_3$ nanoplatelets. From angle-resolved reflectivity and photoluminescence measurements, the strong coupling could be demonstrated with a large Rabi Splitting of 265 meV. The microcavity was then pumped with a femtosecond pulse laser (100fs, 1kHz repetition rate) and when the threshold of $12\mu J/cm^2$ was reached the Bose-Einstein condensation of the lower polaritons could be observed as shown in figure 1.38 c,d and f. Figure 1.38 f) shows the log-log PL intensity (in red) and the semi-log Full Width at Half Maximum (FWHM) (in blue) as a function of the pump power at null in-plane wavenumber, $k_{//} = 0$. The sharp increase of the PL intensity followed by saturation and the sharp decrease of the linewidth at the threshold is a signature of the polaritonic lasing, yet this characteristic can also be observed in the case of photonic lasers. However, the increase of the PL linewidth before the threshold and after the threshold can be attributed to the polaritons non-linearities, i.e. the exciton-polariton and polariton-polariton interactions. It can be seen at the threshold and above threshold that the LPB photoluminescence is blueshifted in respect with the

LPB dispersion below threshold marked as the dashed white dispersion (see figure 1.38 c,d and e. Figure 1.38 g) depicts this behaviour by plotting the blueshift of the emission at $k_{//} = 0$ below and above the threshold and shows a sharp blueshift below the threshold and a slight blueshift above the threshold. The authors showed that the blueshift and increase in linewidth were dominated by polariton interactions with the excitonic reservoir below the threshold and polariton-polariton interactions above the threshold. To further demonstrate the polaritonic nature of the lasing, interferometry measurements have been performed. The spatial image of the condensate emission has been taken in a Michelson in which the image has been reversed in one arm (see figure 1.38 h and i). Interferences occur in the superposed image (see figure 1.38 j) confirming the long-range spatial coherence of the polariton.

In 2018, Su et al. showed another polariton condensate in another perovskite-based microcavity [49] with $CsPbBr_3$ microwires (see figure 1.39 a and b). In this case, the photon is not only confined in the direction of the microcavity (z-axis in figure 1.39 a) but also in the lateral direction of the microwire (y-axis in figure 1.39 a). For this reason, the microcavity exhibits several cavity modes that can be strongly coupled to the excitonic transition. When the long axis x is parallel to the spectrometer slit several lower polariton branches can be observed in the angle-resolved photoluminescence spectrum (see figure 1.39 c) with the lowest energetic LPB being predominant. When the y-axis is set parallel (see figure 1.39 d), the angle-resolved photoluminescence map shows discrete polaritons states induced by the optical confinement from the small $CsPbBr_3$ width. Figures 1.39 e and f shows the angle-resolved photoluminescence spectra below and above the polaritonic lasing threshold of the microcavity in the case when the x-axis is set parallel to the spectrometer enter slit. However, unlike in the previous case, the Bose-Einstein condensation does not occur at the null momentum/angle, but at the angles $\pm 20°$. This condensation at non-null momentum is the signature of the polariton condensate propagation in the microwire. The authors showed the emission blueshift and linewidth increase below and above the threshold and also interference fringes from Michelson interferometry to demonstrate the polaritonic nature of the lasing results. The propagation properties of this quasi-condensate were then investigated: for that, the end of the microwire was pumped in a small area (red dashed circle in figure 1.39 g (i)) which leads to interference fringes in the microwire microcavity (see experimental result in figure 1.39 g (ii) and theoretical result in figure 1.39 g (iii)). This result means that the polariton propagated to the other end of the microwire, was reflected and propagated back to the pumping region and interfered with new coming polariton. This proved that some polaritons could propagate over 60 µm. The authors also calculated a polariton group velocity of 10 µm/ps, several times larger than in GaAs-based microcavities and a polariton lifetime of 3 ps.

At the time this manuscript is being written, really recent reports on perovskite-based polaritons condensate are published on Arxiv: Su et al. demonstrates this time the polariton on microcavities based on $CsPbBr_3$ micropillar array creating an array of polariton condensates [225]; Bao et al. obtained polaritonic lasing in a microcavity containing

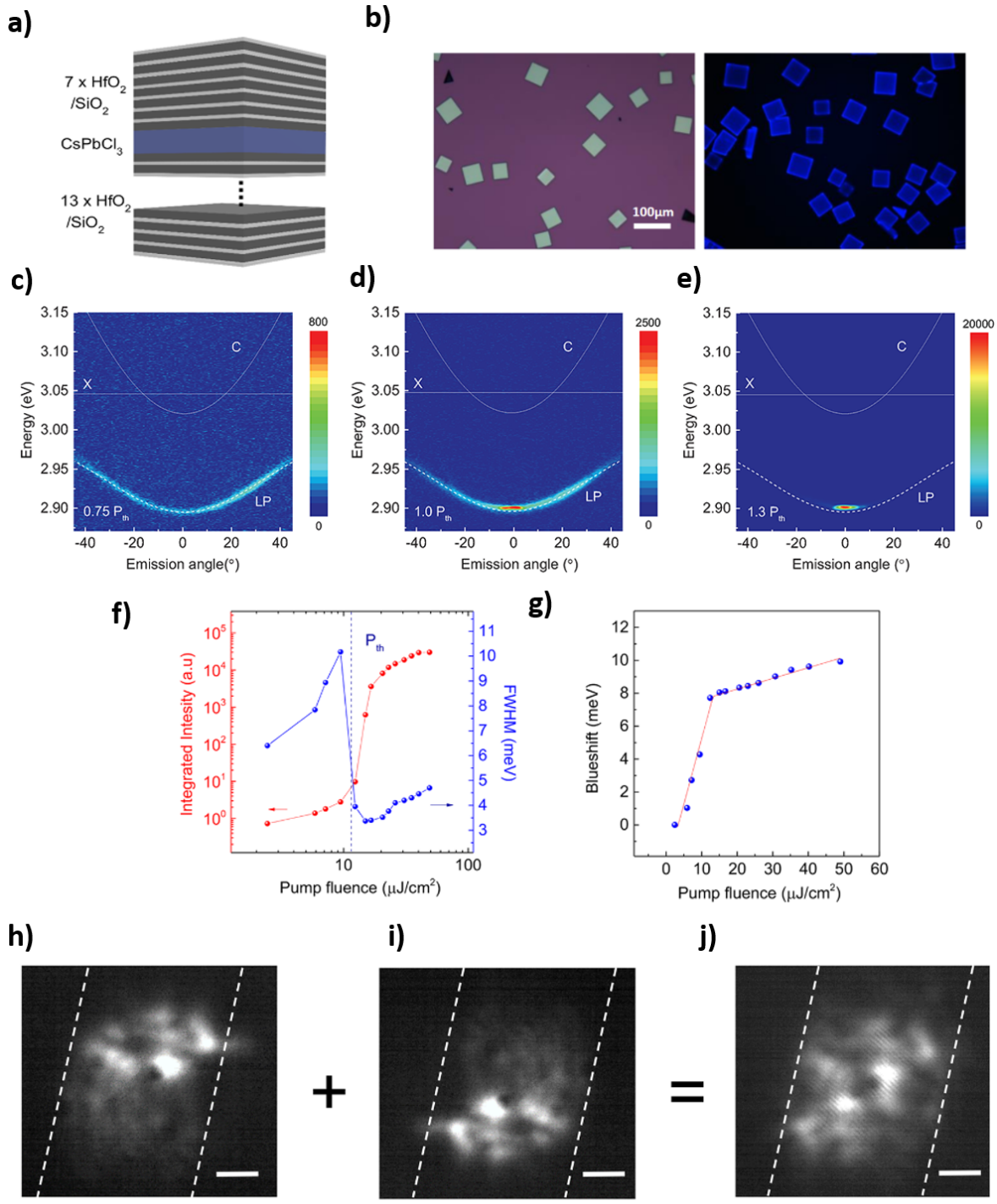

Figure 1.38: a) Sketch of the microcavity containing $CsPbCl_3$ nanoplatelets in [48]. b) Microscope and fluorescence images of the $CsPbCl_3$ nanoplatelets. c) d) and e) Angle-resolved photoluminescence spectra of the microcavity under the lasing threshold ($0.75P_{th}$) at threshold (P_{th}) and above threshold ($1.3P_{th}$). f) Log-log PL intensity (in red) and the semi-log Full Width at Half Maximum (FWHM) (in blue) as a function of the pump power at null in-plane wavenumber, $k_{//} = 0$. g) Blueshift of the emission at $k_{//} = 0$ below and above the threshold h) Spatial image of the polariton lasing emission in one arm of the Michelson i) Reverse image in the other arm of the Michelson and j) superposition of the two images showing interferences. Extracted from [48].

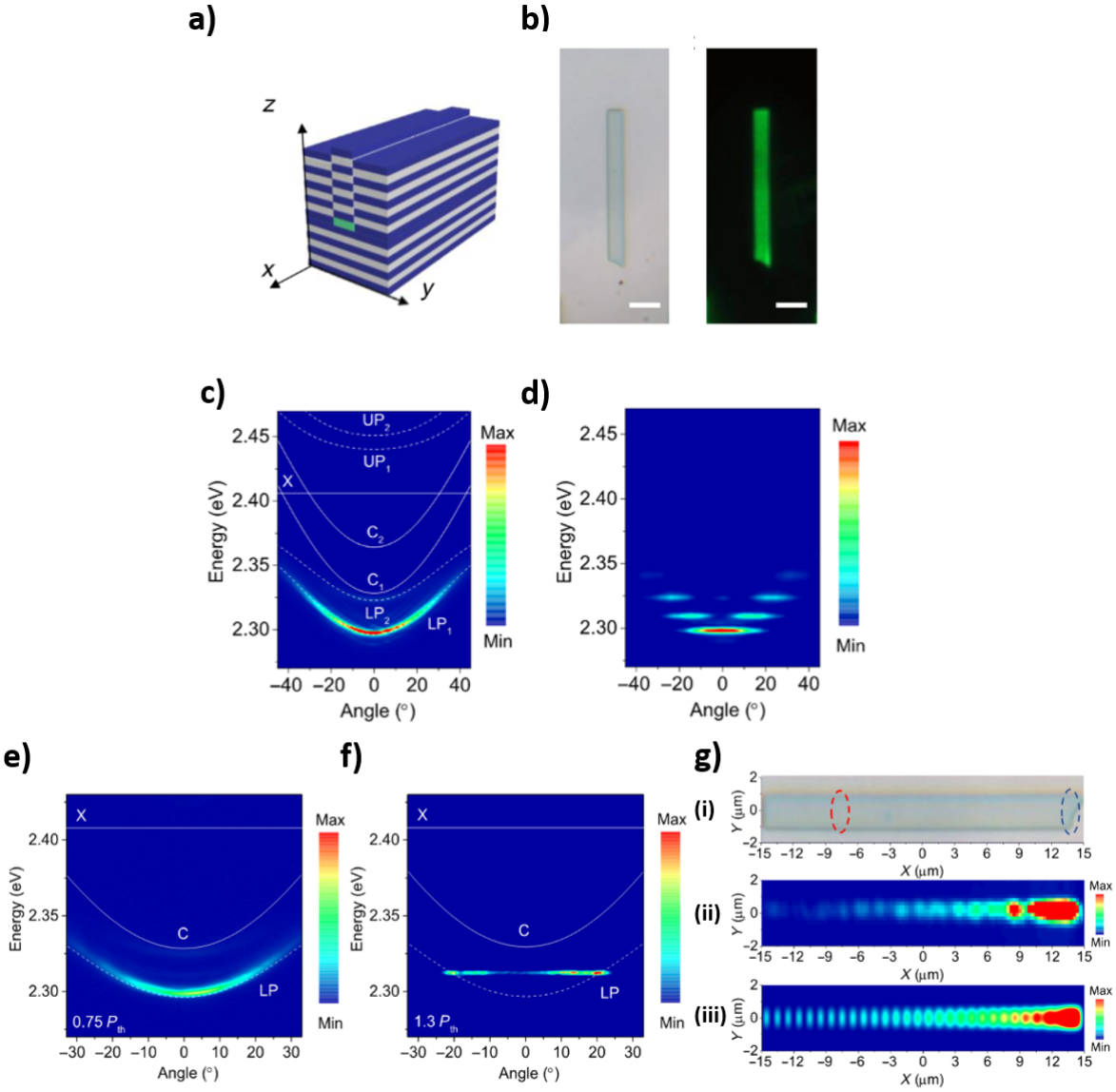

Figure 1.39: a) Sketch of the microcavity containing a $CsPbBr_3$ microwire in [49]. b) Microscope and fluorescence images of the microcavity. c) Angle-resolved photoluminescence of the microcavity when the x-axis (see the sketch of a)) of the microcavity is set parallel to the spectrometer slit. Two LPB branches can be observed. d) Angle-resolved photoluminescence of the microcavity when the y-direction is set parallel to the entrance slit of the spectrometer. Discrete polariton states can be observed. e) Angle-resolved photoluminescence of the microcavity (x-axis parallel to the spectrometer slit) under the lasing threshold (0.75 P_{th}) and f) above the threshold (1.3 P_{th}). g) Schematic of the interferences experiment in the microwire microcavity (i) image of the microwire microcavity with the red circle indicating the pumping spot (the blue circle is not detailed in this manuscript) (ii) experimental result (iii) theoretical result. Extracted from [49].

$CsPbBr_3$ microplates, involving the excited Ryberg state n=2 of the exciton [226]. These intriguing results raise the perovskites as serious candidates for polariton lasing both for the polariton applications but also for fundamental research on polariton Bose-Einstein condensation.

2.3.4 Summary of halide perovskite-based polaritons

The following table 1.1 summarizes the strong-coupling results obtained with halide perovskites and compares the different perovskites, photonic structures, quality factors, Rabi splittings and the specificities. One of the results of this PhD with MAPB thin-film [15] detailed in chapter 4 of this manuscript is included.

Perovskite	Dimensionality	Morphology	Structure	Quality factor (Below threshold)	Rabi Splitting ($\hbar\Omega \setminus meV$)	Comments	Year	Reference
PEPI	2D	Thin film	DFB		100		1998	Fujita et al. [68]
PEPI	2D	Thin film	DFB		75	Same structure as [68]	1999	Fujita et al. [199]
PEPI	2D	Thin film	DFB			Theoretical model of [68]	2001	Yablonskii et al. [200]
PEPI (called PAPI)	2D	Thin film	2D Photonic crystal		240		2001	Sumioka et al. [203]
PEPI	2D	Thin film	1D Photonic crystal			Non Linearities	2002	Shimizu et al. [201]
PEPI	2D	Thin film	2D photonic crystal		100		2003	Ishi Hayase et al.[202]
PEPB	2D	Thin film	Planar microcavity	200	162	+ ZnTPP in PMMA	2006	Wenus et al. [211]
PEPI	2D	Thin film	Planar microcavity	25	140		2006	Brehier et al.[206]
PEPI	2D	Thin film	Planar microcavity	25	136-150-190		2008	Lanty et al.[204]
PEPCl	2D	Thin film	Planar microcavity		230		2008	Lanty et al.[208]
CHPI	2D	Thin film	Planar microcavity	Low-Q	130 - 160	Metal-air Metal-Metal	2009	Pradeesh et al. [207]
PEPCl	2D	Thin film	Planar microcavity	15	230		2009	Lanty et al.[209]
MFMPB	2D	Thin film	Planar microcavity		52	+ZnO	2011	Lanty et al. [212]
pFPEPI doped PMMA	2D	Thin film	Planar microcavity		89.6		2012	Wei et al. [205]
PEPI	2D	Thin film	Planar microcavity	80	168		2012	Han et al. [213]
PEPI	2D	Thin film	Planar microcavity	85	unknown		2013	Han et al. [214]
PEPI	2D	Thin film	Planar microcavity	750	168	Same structure as [213]	2014	Nguyen et al. [215]
$CsPbBr_3$	3D	Nanowire	Nanowire			Photonic lasing	2016	Park et al. [219]
$MAPbBr_3$	3D	Micro-Nanowire	Micro-Nanowire		268 390	Photonic lasing	2017	Zhang et al. [220]
$CsPbCl_3$	3D	Nanoplatelets	Planar microcavity	300	265	Polariton lasing	2017	Su et al.[48]
$CsPbBr_3$	3D	Microwire	Planar microcavity	1150	120	Polariton lasing	2018	Su et al. [49]
PEPI BAI OCT	2D	Exfoliated crystal	Crystal ?		170 - 240 - 250 (?)		2018	Fieramosca et al. [216]
CsPbX3 (X= I, Br, Cl)	3D	Nanowire	Nanowire		103 - 146 - 210	Photonic lasing	2018	Wang et al. [222]
PEPI PEPB	2D	Exfoliated crystal	Planar microcavity	2200	242	Strong coupling with Cavity and Bragg modes	2018	Wang et al. [218]
$MAPbBr_3$	3D	Nanowire	Nanowire		267 up to 564	Enhanced with surface plasmons	2018	Shang et al. [223]
$CsPbBr_3$	3D	Micro-Nanowire	Micro-Nanowire		401 up to 656	Photonic lasing ($\hbar\Omega$ <400 meV) Polaritonic lasing ($\hbar\Omega$ >500 meV)	2018	Du et al. [224]
$CsPbBr_3$	3D	Nanowire	Nanowire		200	CW lasing	2018	Evans et al.[103]
$CsPbBr_3$	3D	Microplate	Planar microcavity		67?	Rydberg (n=2) exciton polariton Polariton lasing	2018	Bao et al. (ArXiv) [226]
$MAPbBr_3$	3D	Thin film	Planar microcavity	92	70		2018	Bouteyre et al. [15]
PEPI	2D	Exfoliated	Planar microcavity		170	Study of		
		AVCC Crystal	Crystal		170	polariton-polariton interaction	2019	Fieramosca et al. [56]
$CsPbBr_3$	3D	Micropillar array	Microcavity		120	Array of polariton condensate	2019	Su et al. (ArXiv) [225]
PbBr-based layered perovskite	2D	Thin film	Microcavity		116	Langmuir-Blodgett (LB) technique	2019	Era et al. [227]

Table 1.1: Summary of the halide perovskite-based polaritons

3 Conclusion of the chapter

In this chapter, the physical concepts concerning light-matter interaction in an optically active material were presented as well as the coupling between such a material with a microcavity confining light in photonic modes. The weak or strong coupling regime can occur in such a system, depending on whether the interactions compensate for cavity and material losses. From the strong coupling regime, the lower and upper polaritons were introduced, which are coherent superpositions of the photonic mode state and excitonic state. One of the main applications of the strong coupling regime was discussed: the polaritonic laser. In the following, two types of lasers have been considered: the laser in weak coupling regime, which is a conventional laser, and the laser in the strong coupling regime, i.e. the polaritonic lasing also known as polariton condensation.

The 3D halide perovskites and low dimensional halide perovskites were introduced as emerging materials in the context of the photovoltaic field and for the light-emitting devices such as LEDs and lasers. Halide perovskites present exceptional optical properties and advantages among the wavelength tunability via chemical substitution and the low cost of the solution-processed synthesis. Due to the tunability, the halide perovskites can address the "green gap" problem, which corresponds to the drop in efficiency of the commercial LEDs and laser diodes in the green region. The main obstacle today to the commercial development is the perovskite stability, which has been significantly improved in recent years and surely will be further improved.

The state of the art of halide perovskite-based lasers in weak coupling regime has been presented. Briefly, the lasing properties of the halide perovskite-based lasers are remarkable. However, the lasers suffer from the low thermal stability of the halide perovskites. For this reason, most of the lasing action could only be obtained under pulsed regime. Due to the improvement of the resonators quality factors, the heat management and the perovskite instabilities, lasing was recently demonstrated with continuous-wave pumping. These results are particularly significant as it is a crucial step before exploring electrical injection, which is required for commercialization. Progress on the engineering of the perovskite-based lasers, such as nanoimprint patterning, also gives hope towards commercial halide perovskites-based lasers.

Strong coupling and polaritonic lasing with halide perovskites have also been explored. The polaritonic lasers, due to the bosonic nature of polaritons, present very low thresholds and are consequently very interesting regarding commercial applications. Thanks to the excellent excitonic properties, the strong coupling could be obtained with low dimensional perovskites and with 3D halide perovskites. Polaritonic lasing could not be achieved so far with low dimensional perovskites even if the quality of these perovskites has dramatically improved after the emergence of the perovskite in the photovoltaic field

in 2012. The issues could come from the too-large Rabi splitting caused by the giant oscillator strength of these perovskites. Regarding the 3D perovskites, with modest excitonic properties, the polaritonic lasing could be obtained in high-quality nanowires, nanoplatelets and microwires embedded or not in microcavities. Exciting results concerning the Bose-Einstein condensation of the polaritons were obtained. However, the polaritonic lasing was only achieved in small surfaces, limited to a few micrometres. This reveals as a drawback for future commercialization as the small surfaces would prevent the engineering of the polariton-based devices.

In this PhD, we will present the strong coupling regime and the lasing action of microcavities containing large-surface (few cm^2) spin-coated MAPB ($CH_3NH_3PbBr_3$) thin-films. The choice of the MAPB perovskite is due to its energy gap in the green to address the "green gap" problem and the spin-coating deposition for its low cost and the achievement of large surfaces. In the following chapters, the experimental methods, the fabrication of the microcavities, the strong coupling demonstration and the lasing effects of the MAPB-based microcavities will be presented.

Chapter 2

Experimental methods

Contents

1 Deposition methods of the microcavity layers 70

1.1 Spin-coating method 70

1.2 Deposition of the MAPB perovskite 71

1.3 Deposition of the PMMA layer 73

1.4 Deposition of the silver layer 74

2 Methods for the layers characterizations 74

2.1 Optical microscope 74

2.2 Contact profilometry 74

2.3 Atomic Force Microscopy (AFM) 74

2.4 Spectrophotomer Perkim Elmer 75

3 Optical experimental set-ups 76

3.1 Optical instruments 76

3.2 PL spectroscopy 78

3.3 μPL 79

3.4 Fourier spectroscopy 79

4 Conclusion of the chapter 86

Introduction

This chapter introduces the experimental methods used during the PhD. The first part details the deposition techniques for the different layers of the MAPB-based microcavity: the spin coating methods for the deposition of the MAPB and PMMA layers and the evaporation method for the silver layer. The second part presents the measuring instruments used for the characterization of the layers and the microcavities and the third part describes the optical set-ups to characterize the microcavities.

The experiments have been carried out in Laboratoire Aimé Cotton (LAC) but also in collaboration with Groupe d'Etude de la Matière Condensée (GEMAC) in Versailles and Institut des Nanotechnologies de Lyon (INL) in Lyon.

1 Deposition methods of the microcavity layers

1.1 Spin-coating method

The spin-coating method, illustrated by figure 2.1, consists in depositing a solution containing precursors of a coating material in a volatile solvent onto a substrate. The substrate is rotated, and the centrifugal force spreads the solution along the surface of the substrate. The sample is later annealed for the remaining solvent to evaporate. In the case of hybrid perovskites, annealing also permits a better crystallization of the material. It results in a uniform thin film whose thickness depends on the rotation speed and acceleration, v_{rot} and a_{rot} respectively, the solution concentration, the duration of rotation, t_{rot}, and the solvent viscosity. The reader can find more information on the spin coating method on the spin-coating guide by Ossila corp. [228]. The spin-coating method was used to deposit thin films of $CH_3NH_3PbBr_3$, called MAPB, and polymer layer PMMA (Poly(methyl methacrylate)) and was carried out in Laboratoire Aimé Cotton (LAC).

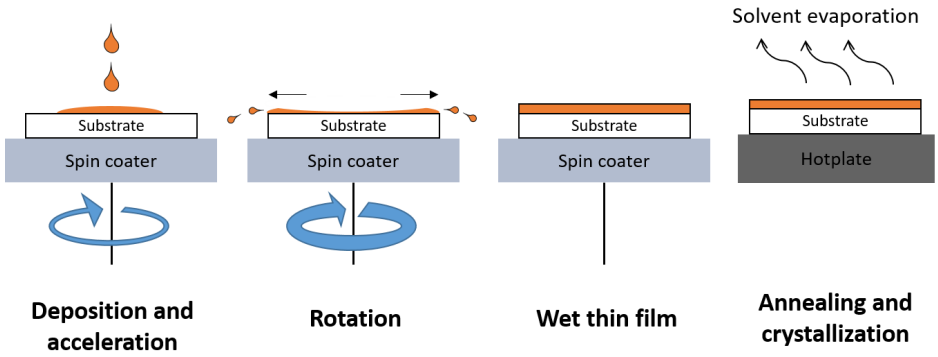

Figure 2.1: Sketch of the spin-coating method

1.2 Deposition of the MAPB perovskite

The following chemical reaction describes the crystallisation of MAPB:

$$PbBr_2 + CH_3NH_3Br \longrightarrow CH_3NH_3PbBr_3. \tag{2.1}$$

In our case, crystallisation occurs during the spin-coating deposition. Two methods of deposition of MAPB by spin-coating were used during the PhD: the one-step method and the two-step method.

1.2.1 One-step deposition

Figure 2.2 illustrates the one-step method for MAPB deposition. The first crucial step is the cleaning of the substrate to remove the dust and defects which would prevent the solution to spread evenly on the surface. The substrate is cleaned in ultrasound baths of acetone and ethanol for ten minutes each. The substrate is dried with air and is later treated with UV-ozone for five minutes. The second step is the spin coating of a 0.7 mol/L^{-1} solution of $PbBr_2$ + CH_3NH_3Br in DMF (Dimethylformamide) on the cleaned substrate. The spin-coating parameters are : v_{rot}=2000 rpm, a_{rot}=2000 rpm/s, t_{sp}=15s and the solution parameters: $V_{DMF} = 5mL$, $m_{CH_3NH_3Br} = 392mg$, $m_{PbBr_2} = 1.285g$. Finally, the perovskite thin film is annealed on a hot plate at 90°C for 15 minutes.

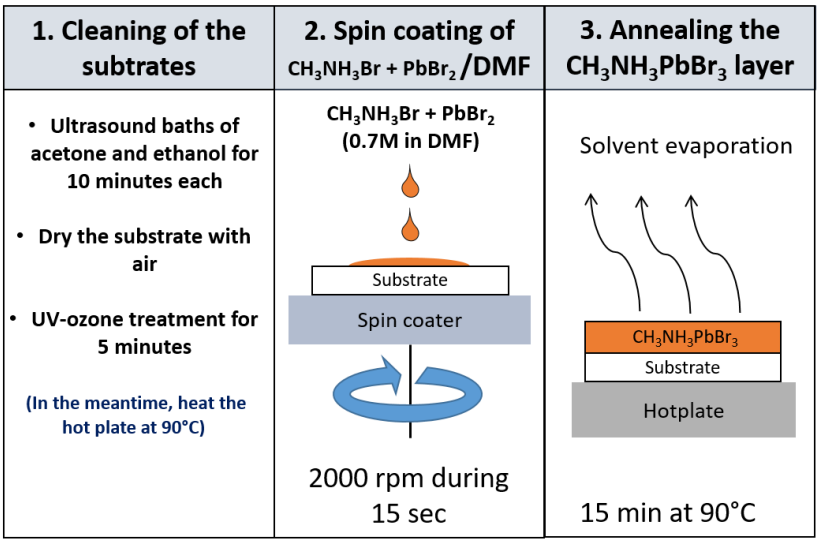

Figure 2.2: Method of the one-step deposition

The $PbBr_2$ powders were purchased (Sigma Aldrich, 211141, 98%) and the CH_3NH_3Br powders were synthesised by Gaëlle Trippé-Allard of Laboratoire Aimé Cotton (LAC) (See the supplementary information of [15] for the synthesis). The substrates were quartz substrates (1.1x1.1 cm^2), and the volume of solution used for the spin-coating was 100 µL.

1.2.2 Two-step deposition

The two-step method was inspired by the technique used in [229]. Figure 2.3 presents the two-step deposition method. The substrate is cleaned the same way as for the one-step method. A 0.5 mol/L^{-1} solution of $PbBr_2$ in DMF (2mL, $m_{PbBr_2} = 367mg$) heated at 70°C is spin-coated on the clean substrate (6500 rpm, 2000 rpm/s, 30s). The $PbBr_2$ thin film is then immersed vertically in a 7mg/mL of CH_3NH_3Br solution in isopropanol ($V_{isopropanol} = 30mL$, $m_{CH_3NH_3Br} = 210mg$). A 50 mL beaker was used to immerse the entire sample. The reacted thin film is placed in the spin-coater for rinsing (6500 rpm, 2000 rpm/s, 30s). Finally, the sample is annealed for 45 minutes at 100 °C.

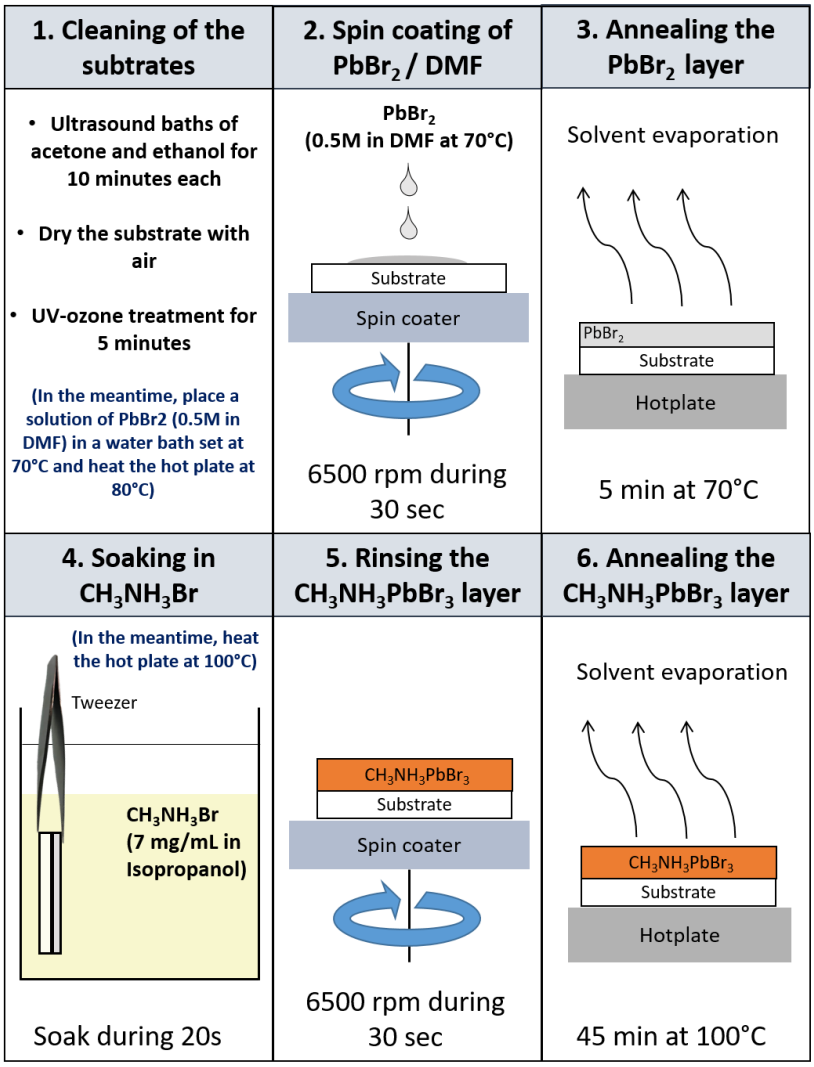

Figure 2.3: Method of the two-step deposition

The CH_3NH_3Br solution could be reused in general four or five times before using a new solution. For the depositions on the quartz substrates, the volume of $PbBr_2$ solution used for the spin-coating was 100 µL, and for the depositions on the half-inch diameter commercial Bragg mirrors (detailed in Chapter 3) 20 µL.

1.3 Deposition of the PMMA layer

Figures 2.4 and 2.5 show the deposition method of PMMA on a substrate or on a MAPB thin film already deposited, respectively. In the second case, there is no substrate cleaning step. The deposition consists of spin-coating at x rpm (2000 rpm/s, 30s) a y wt.% solution of PMMA (Sigma Aldrich, 182230, MW 120,000 by GPC) in toluene (10 mL), with x the spin-coater rotation speed and y the concentration in wt.%. The values of x ad y are changed to vary the PMMA thickness (More details in Chapter 3). The volume of solution for the spin-coating is 100 µL in the case of a quartz substrate and 20 µL in the case of a commercial Bragg mirror. The sample is later annealed at 100°C for 30 minutes.

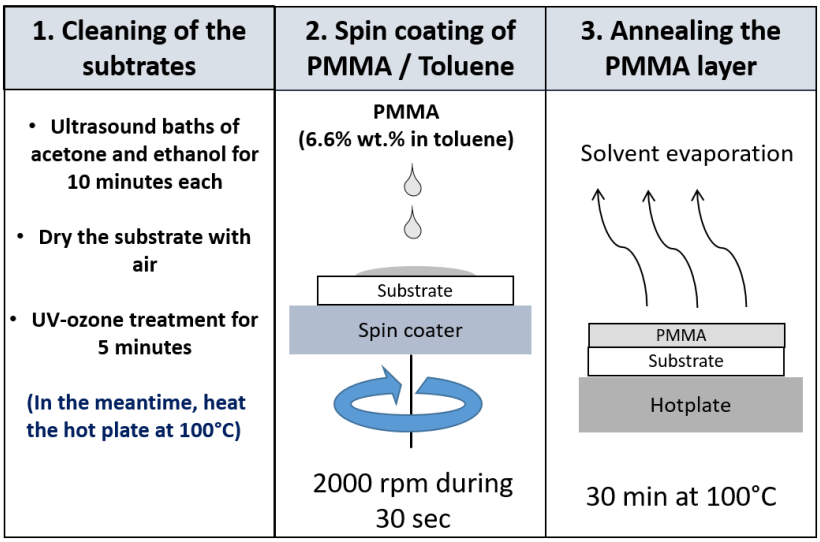

Figure 2.4: Method of PMMA deposition on a substrate

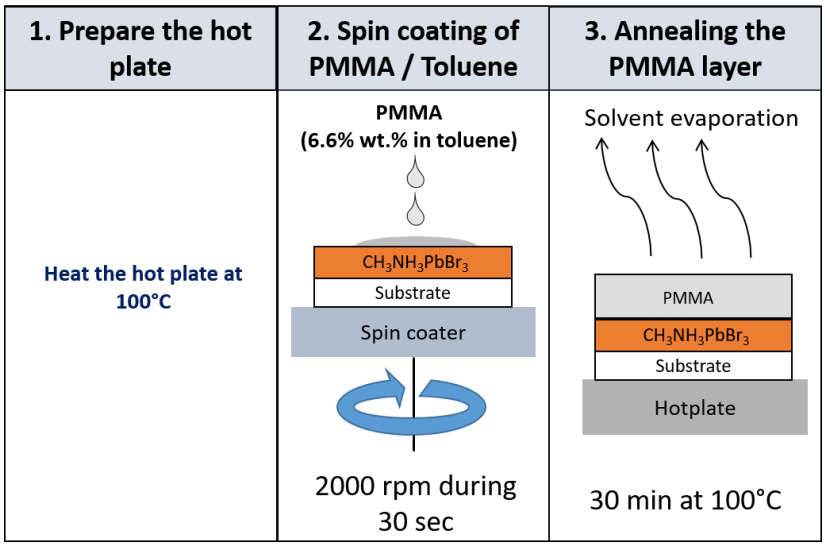

Figure 2.5: Method of PMMA deposition on a MAPB thin film already deposited.

1.4 Deposition of the silver layer

The silver (Ag) layers were deposited on half cavities (MAPB+PMMA on a Bragg mirror) by evaporation in a cleanroom using the Edwards Auto 306 thermal evaporator. Rasta Ghasemi, head of the cleanroom of Institut d'Alembert de l'École Normale Supérieure Paris-Saclay operated the deposition. The silver layer thickness is measured by a quartz crystal micro-balance positioned close to the sample during the evaporation.

2 Methods for the layers characterizations

2.1 Optical microscope

During the PhD, the interference contrast optical microscope (Nikon) was used in Groupe d'Etude de la Matière Condensée (GEMAC).

Optical microscopy was used as a first quick measurement to characterise the morphologies of the layers of MAPB and PMMA. The phase-contrast enables to discern the difference of heights and the grains better. However, optical microscopy does not give quantitative information on the vertical height of the observed objects.

2.2 Contact profilometry

The profilometer (Stylet dektak 8, Bruker) was used in Groupe d'Etude de la Matière Condensée (GEMAC) to measure the thicknesses of the different layers obtained in this PhD.

Contact profilometers measure thickness and surface roughness of layers by scanning a diamond stylus in contact on a sample. By measuring the variation in the stylus height, the profilometer can obtain the height profile of the sample along a horizontal direction. The vertical resolution is nanometric, and the horizontal resolution ranges from 100 nm to 100 µm. The profilometry technique is then useful for accurately measuring the thickness of layers and measuring large dimensional roughnesses on large scales. Atomic Force Microscopy (AFM) is needed to study the roughness at smaller scales.

2.3 Atomic Force Microscopy (AFM)

The commercial Atomic Force Microscopy (AFM) (MFP3D standalone, Asylum) was used in Laboratoire Aimé Cotton" (LAC) to measure the roughness of the different layers obtained in the PhD.

An Atomic Force Microscope (AFM) is composed of a very sharp tip (1-10 nm), mounted on a cantilever, which probes the surface of a sample. The Van der Waals forces between the surface and the tip deflect the cantilever. A laser beam is shined on the can-

tilever, and the deflection is measured by detecting the variation in the laser reflection with a photodiode array detector. A control feedback system keeps the value of the force constant during the scan by varying accordingly, with piezoelectric motors, the height of the tip to the surface. The variation of the cantilever height along the horizontal distance gives the sample height profile. With this technique, the horizontal resolution of AFM can reach a fraction of nanometers. For this reason, Atomic Force Microscopy (AFM) is useful to study the structure at the nanoscale of layers, but only on a small scan scale.

2.4 Spectrophotomer Perkim Elmer

The spectrophotometer Perkin-Elmer (Corp.) UV/visible Lambda950 was used in Laboratoire Aimé Cotton (LAC) for three types of characterizations : absorption measurements, diffuse reflectance measurements (with the integrating sphere accessory (150mm)) and Specular reflectivity measurements (with the Universal Reflectance Accessory(URA)).

2.4.1 Absorption measurements

Absorption measurements consist in measuring the Optical Density (OD) spectrum (or absorbance spectrum) of a material. During the measurement, a light beam at a specific wavelength λ is equally separated into two optical paths, the sample path and the reference path in which are placed the sample deposited on a substrate and a similar substrate, respectively. The intensities of the transmitted light by the sample, I_t, and by the substrate, I_0, are then measured. The optical density is then given by:

$$\mathrm{OD}(\lambda) = -log_{10}(\frac{\mathrm{I}_t(\lambda)}{\mathrm{I}_0(\lambda)}). \tag{2.2}$$

The optical density describes the amount of light absorbed by the material and thus, how much light is transmitted. An OD of 1(2) corresponds to a transmission coefficient of $10^{-1}(10^{-2})$.

2.4.2 Diffuse reflectance

Diffuse reflection is the reflection in all directions originating from multiple light scattering in a thin film. Diffuse reflectance measures the loss of light intensity due to scattering related to surface roughness. The optical density measured in the absorption measurements needs to be corrected to take into account only the absorption of the perovskite without the losses due to light scattering [16]:

$$\mathrm{OD}_{cor} = \mathrm{OD}_{nc} + log_{10}(1 - \mathrm{R_D}), \tag{2.3}$$

where OD_{cor} is the corrected OD, OD_{nc} is the non-corrected OD and $\mathrm{R_D}$ is the diffuse reflectance.

Diffuse reflection is measured with an integrating sphere which is a sphere covered in the inside by a diffuse white coating and is composed of small entrance and exit slots. Thanks to the multiple scattering inside the sphere, the detector detects the light refracted by the sample in all directions.

2.4.3 Specular reflectivity measurements

Specular reflectivity corresponds to the reflection of light at the opposite angle of the incident light angle. The reflectance $R(\lambda) = I_r(\lambda)/I_0(\lambda)$ is given by the ratio between the reflected light intensity, $I_r(\lambda)$, and the initial light intensity, $I_0(\lambda)$.

With the Perkin Elmer spectrophotomer, the reflectance can be measured at different angles, from 8° to 60°of incidence. The surface probed by the reflectivity measurements (as well as in the absorption measurements) was 1x1 mm^2. This large surface area will be an essential aspect to consider in the following chapters.

3 Optical experimental set-ups

3.1 Optical instruments

Different optical set-ups were used during the PhD in two different laboratories: in Laboratoire Aimé Cotton (LAC) and in Institut des Nanotechnologies de Lyon (INL). Before presenting the different optical set-ups, the various instruments of the two laboratories are described.

3.1.1 Laser and white light sources

The pump laser source used in Laboratoire Aimé Cotton (LAC) is a femtosecond pulsed laser ($t_{pulse} \approx$ 100 fs, f_{rep}=1 kHz, λ=800 nm) of the Hurricane integrated Ti:Sapphire Amplifier System (Spectra Physics corp). The femtosecond laser pulses were obtained using the Chirped Pulse Amplification (CPA) method with the Mai Tai Ti:Sapphire femtosecond pulse laser (Spectra Physics, 800 nm, 80MhZ, 100 fs) and the Evolution-15 pump laser (Spectra Physics). The output laser was doubled in frequency with a Barium borate (BBO) doubling crystal. The resulting pump laser is then a high intensity femtosecond pulsed laser ($t_{pulse} \approx$ 100 fs, f_{rep}=1 kHz) emitting at 400 nm.

This laser source was used for PL and Fourier spectroscopy measurements as a function of the pump power to study the microcavities lasing characteristics. Indeed, this pulsed laser can achieve high intensities enabling to reach the lasing thresholds. However, the Hurricane system was a limiting factor during the PhD because of its recurring failures. The system worked for eight months combined during the PhD, which was enough to obtain good results but prevented from carrying complementary experiments.

In Institut des Nanotechnologies de Lyon (INL), a halogen lamp (DH-2000, Ocean Optics) and a picosecond pulsed laser diode ($t_{pulse} \approx 50$ ps) emitting at 405 nm (PDL 800-D, PicoQuant) were used in a Fourier spectroscopy set-up for angle-resolved reflectivity and angle-resolved photoluminescence measurements, respectively. The laser diode could be in pulsed (31.5 kHz to 80 MHz) or continuous wave (CW) mode. The repetition rate of 80 MHz was chosen for the experiments. Lasing action could not be obtained with this picosecond pulsed laser diode during the PhD. For this reason, the lasing characterization measurements were carried on in Laboratoire Aimé Cotton (LAC).

3.1.2 Spectrometers and CCD

Two spectrometers were used in Laboratoire Aimé Cotton (LAC):

- The Princeton Instruments SP2500i spectrometer equipped with a monochromator (with three diffraction gratings: 150 g/mm, 1200 g/mm, 2400 g/mm), a CCD camera (Pixis: 100B Ropers Scientific) and a photodiode (demander à Damien). The 1200 g/mm grating, used in this PhD, leads to a spectral resolution $\Delta\lambda = 0.09$ nm.

- The Princeton Instruments SP2150 spectrometer equipped with a monochromator (with two gratings: 150 g/mm, 1200 g/mm) and a CCD camera (Pixis: 100B Ropers Scientific). The 1200 g/mm grating, used in this PhD, leads to a spectral resolution $\Delta\lambda = 0.4$ nm.

In both cases, the CCD camera is composed of 1340 pixels in the horizontal axis corresponding to the wavelength axis and 100 pixels in the vertical axis for imaging.

In Institut des Nanotechnologies de Lyon (INL), the spectrometer used was the MicroHR spectrometer (Horiba) equipped with a monochromator (grating of 1200 g/mm) and a Sincerity (Horiba) CCD camera. The spectral resolution is $\Delta\lambda = 0.3$ nm. The CCD camera is composed of 1024 pixels in the horizontal axis and 256 pixels in the vertical axis. This CCD camera with more vertical pixels is more suitable than the CCD camera used in Laboratoire Aimé Cotton (LAC) for imaging measurements, especially for Fourier spectroscopy measurements.

3.1.3 Objectives and Lenses

A 0.9 NA microscope objective (MPLFLN50x, Olympus), a 0.6 NA objective (CFI Plan Fluor ELWD 40x C, Nikon) and a 5 cm lens were used during the PhD to focus the pump laser on the sample.

3.2 PL spectroscopy

3.2.1 Principle

Photoluminescence (PL) spectroscopy consists of exciting a sample with a pumped laser and collecting the emitted photoluminescence with a spectrometer. Figure 2.6 shows a sketch of a PL spectroscopy set-up. The pump laser is focused by an objective or a lens to excite the sample. The PL signal is collected by the same objective/lens and is then focused with a large diameter lens onto the spectrometer slit. The focal length of this lens should be adapted to the spectrometer f-number. In the spectrometer, a diffraction grating disperses the light horizontally, and the output signal can be either be collected by a CCD camera or by an avalanche photodiode when a flip mirror is introduced. By changing the grating angle, it is possible to change the central wavelength of the measured spectrum. The wavelength window of the spectrum depends on the characteristics of the gratings. With the computer connected to the CCD camera and the spectrometer, one can read the resulting spectrum and can also change the spectrometer parameters.

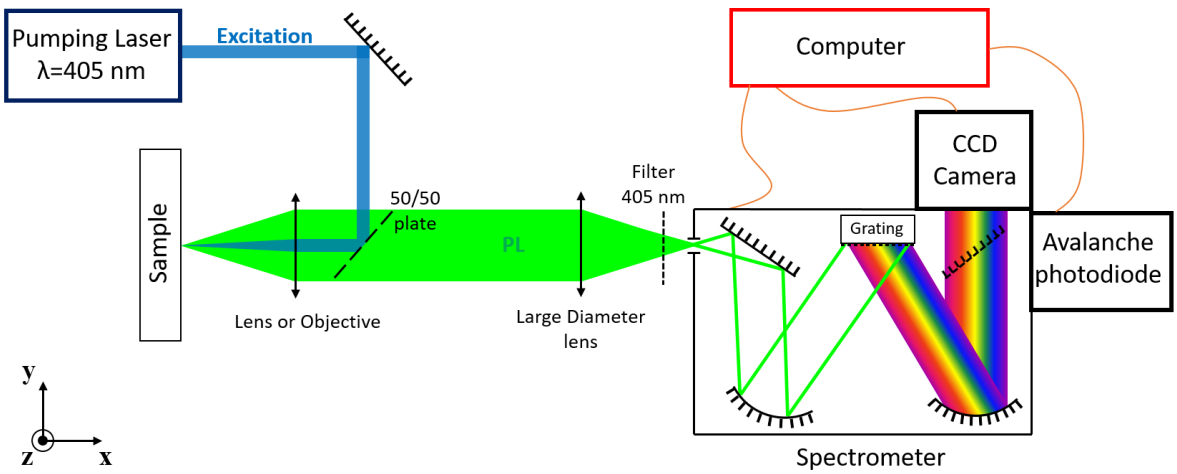

Figure 2.6: Sketch in top view of the PL spectroscopy set-up.

The sketch in figure 2.6 shows the reflection configuration in which the excitation and collection are performed with the same objective/lens from the same side. It is also possible to use the transmission configuration in which the pump laser is focused from behind the sample by another objective/lens, and the PL signal is collected from the other side.

3.2.2 Set-up number 1 in "LAC" laboratory

In the first PL spectroscopy set-up in Laboratoire Aimé Cotton (LAC), the sample is excited by the 100 femtoseconds pulsed laser at 1 kHz of repetition rate emitting at 400 nm. The 0.6 NA objective focuses the pump laser in the reflection configuration, and the Princeton Instruments SP2500 spectrometer collects the PL signal with a spectral resolution of 0.09 nm. The spectrometer lens is a 2-inch wide lens of focal 7.5 cm.

This optical set-up is the main PL spectroscopy set-up of our group in Laboratoire Aimé Cotton (LAC), which is also coupled to a cryostat for low-temperature measurements and with motorized actuators to perform μ-PL mappings (see next section). As this optical set-up was already packed with all the possible configurations, it was not possible to incorporate another lens for the Fourier spectroscopy. For this reason, a second PL spectroscopy set-up was mounted.

3.2.3 Set-up number 2 in "LAC" laboratory

In the second PL spectroscopy set-up, the sample is also excited by the 100 femtoseconds pulsed laser at 1 kHz of repetition rate emitting at 400 nm. The spectrometer is replaced by the Princeton Instruments SP2150 spectrometer with a spectral resolution of 0.4 nm. The pump laser is focused by the 0.9 NA objective in the reflection configuration or by a lens of focal 5 cm in the transmission configuration. The spectrometer lens is a 2-inch wide lens of focal 7.5 cm.

3.3 μPL

In the first PL spectroscopy set-up, the objective focusing the pump laser can be translated in the two directions perpendicular to the optical axis (y and z directions in figure 2.6) with the motorized actuators (demander a Damien) controlled by a Labview program. By scanning the sample with the objective, it is possible to map the PL signal of a specific area of the sample. The PL signal is collected with the avalanche photodiode at one given wavelength which can be chosen with the spectrometer. The spatial resolution, which depends on the focus of the pump laser and the step of the micro-controllers, was of 0.5 μm. The measurement of the PL maps is referred in this PhD as the μ-PL measurements.

3.4 Fourier spectroscopy

3.4.1 Principle

Fourier spectroscopy consists of placing a lens, the Fourier lens, in the PL spectroscopy set-up to image the sample's momentum k-space, also known as Fourier space. From another point of view, the Fourier lens is used to disperse the emission angles in one direction. These two perspectives are equivalent since the wavenumbers in the Fourier plane are dependent on the emission angle. As a consequence, the Fourier spectroscopy set-up permits to perform angle-resolved photoluminescence measurements, and angle-resolved reflectivity measurements when replacing the pump laser with a white light beam.

Figure 2.7 and figure 2.8 show the Fourier spectroscopy set-up in lateral view and three-quarter view, respectively. This set-up is similar to the PL spectroscopy set-up in figure 2.6. However, in this case a Fourier lens is placed at focal distance behind the sample's Fourier plane between the objective and the spectrometer lens. With this set-up,

light originating from a height +h in the vertical axis of the Fourier plane (z-axis in figure 2.7) is projected to the spectrometer slit at a height -d. The light is then spectrally dispersed horizontally in the spectrometer, and the emission from the h point occurs as a horizontal line at a height -d' in the CCD camera (see figure 2.8). In general, the height d at the spectrometer slit and d' at the CCD camera are the same, and in the following, it will be considered that $d = d'$. We have then shown that with the Fourier spectroscopy set-up, a vertical position in the Fourier plane can be imaged vertically in the CCD camera. Finally, an angle of emission, θ, can be imaged vertically in the CCD camera as the height h depends on the sample emission angle. Using geometric optics, one can find that :

$$|d| = \frac{f_S}{f_F} h, \quad h = f_\mu \tan(\theta), \quad |d| = \frac{f_\mu f_S}{f_F} \tan(\theta), \tag{2.4}$$

where f_μ, f_F and f_S are respectively the focal lengths of the objective, the fourier lens and the spectrometer lens.

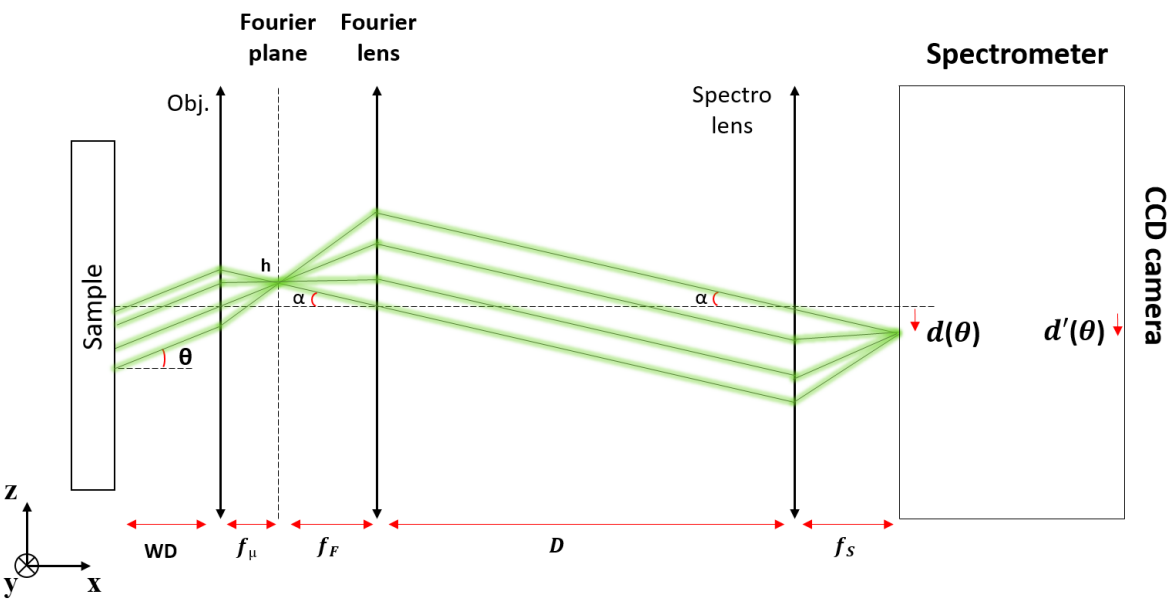

Figure 2.7: Sketch in lateral view of the Fourier spectroscopy set-up. The light originating from the sample at an angle θ is projected to the spectrometer slit at a height $d(\theta)$ and to a height $d'(\theta)$ to the CCD camera. The optical path in the spectrometer is perpendicular to the sketch plane and is therefore not represented. The term WD corresponds to the working distance of the objective.

3.4.2 Focal length of the Fourier Lens

The maximum emission angle which can be imaged, θ_{max}, is determined by the numerical aperture (NA) of the objective, i.e. $\theta_{max} = \text{asin}(\text{NA})$. Consequently, the focal length of the Fourier lens must be chosen so that all the emission angles, from 0° to θ_{max}, are dispersed in all the CCD vertical pixels. If the focal length is too small, the large angles are projected outside of the CCD camera. For this reason, the maximum height d_{max} of the projections in the CCD camera should be equal or lower than half of the size of the CCD camera, t_{CCD}, i.e. $d_{max} \leq t_{\text{CCD}}/2$. Using the equation 2.4 one finds that :

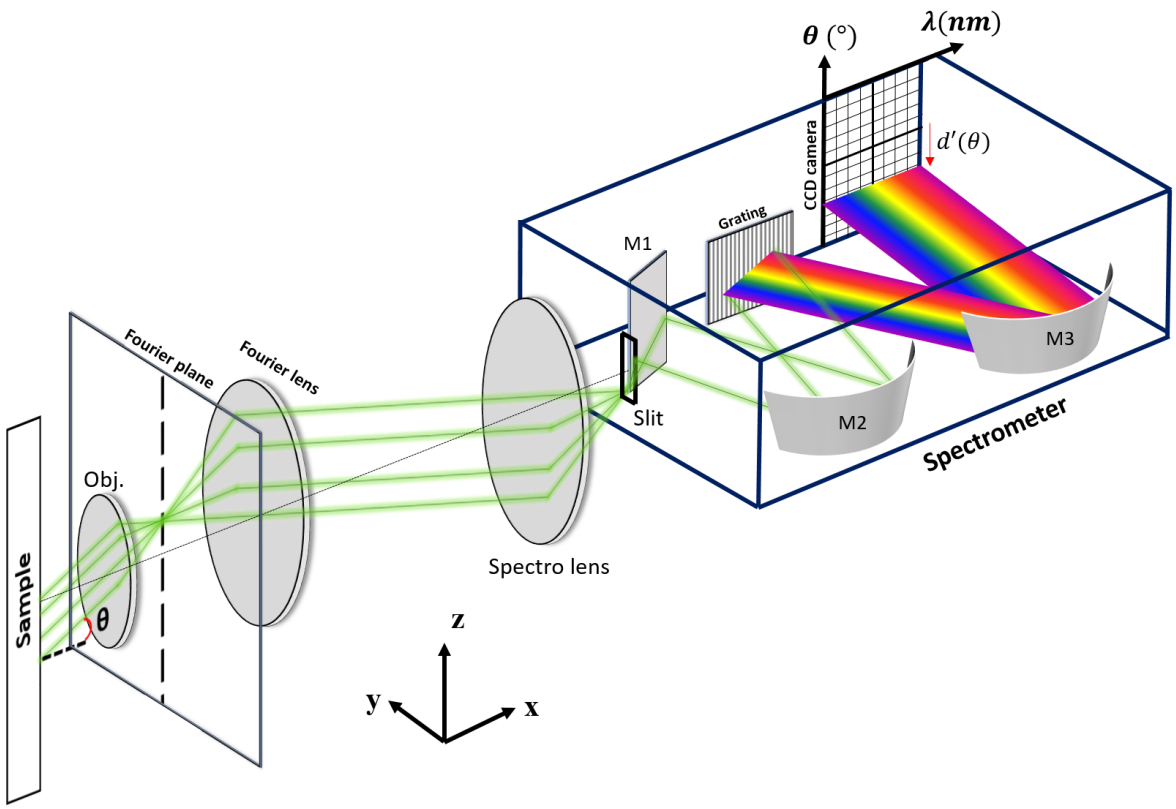

Figure 2.8: Sketch in three-quarter view of the Fourier spectroscopy set-up. The light originating from the sample at an angle θ is projected to the CCD camera a height $d'(\theta)$. The emission angles are dispersed vertically (z-axis), and the light is spectrally dispersed in the horizontal direction (x,y plane).

$$d_{max} = \frac{f_\mu f_s}{f_F} \tan(\mathrm{asin}(\mathrm{NA})), \tag{2.5}$$

which leads to :

$$f_F \geq \frac{2 f_\mu f_s}{t_{CDD}} \tan(\mathrm{asin}(\mathrm{NA})). \tag{2.6}$$

3.4.3 Maximum distance between the fourier lens and the spectrometer lens

Another parameter to consider is the distance, D, between the Fourier lens and the spectrometer lens (see figure 2.7 and figure 2.9). If this distance is too long, the spectrometer lens, of diameter d_{fs}, diaphragms the incoming light. The case of the critical distance is shown in the sketch of figure 2.9. From this sketch, the critical distance is:

$$\mathrm{D}_{max} = \frac{d_{fs}}{2} \frac{f_F}{f_\mu} \frac{1}{\tan(\mathrm{asin}(\mathrm{NA}))}, \tag{2.7}$$

However, this theoretical maximum distance as well as the Fourier focal length are obtained using geometric optics. In the case of Fourier spectroscopy set-ups with objectives of large numerical aperture (NA), geometric optics cannot describe well the system and

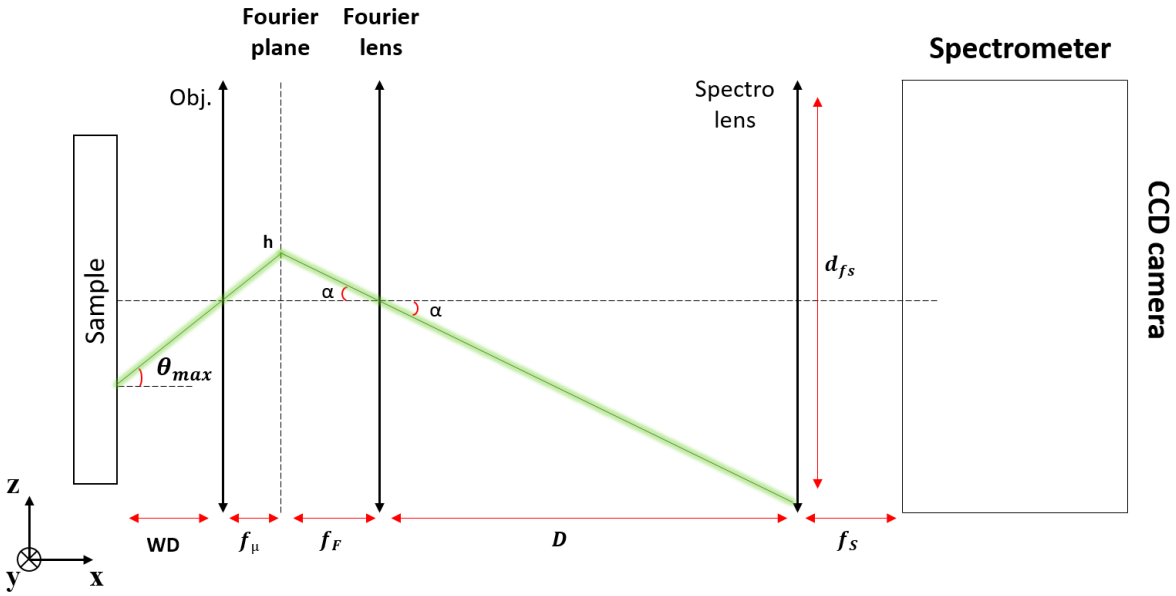

Figure 2.9: Sketch in lateral view of the Fourier spectroscopy set-up in the case of the critical distance between the Fourier lens and the spectrometer lens in which the spectrometer lens diaphragms the incoming light.

is used only as a first approach and for didactic purposes. In general, because of aberrations, the distance between the Fourier lens and the lens in front of the spectrometer can be larger than the critical distance given in equation 2.7.

3.4.4 Correction of the measured PL and reflectivity maps

For the angle-resolved photoluminescence measurements, one should collect the background signal, B_{PL}, of the experimental room. The corrected photoluminescence map is the difference between the measured photoluminescence, PL_m and the background signal B_{PL}, i.e. $PL = PL_m - B_{PL}$.

In the case of angle-resolved reflectivity measurements, one needs to know the value of the reflectivity. However, the CCD camera only measures the signal reflected by the sample, R_m, which depends on the white light source intensity. For this reason, one should measure the background signal but also measure the reflectivity of a reference mirror, R^m_{ref} whose real reflectivity R^r_{ref} is known. The reference mirror needs to be placed in the same position as the sample, and the reference mirror reflectivity should be measured in the same condition as for the sample. The corrected reflectivity is then given by:

$$R = (R_m - B_R)(\frac{R^r_{ref}}{R^m_{ref} - B_R}), \tag{2.8}$$

3.4.5 Raw data processing of the CCD camera results

Once corrected, the photoluminescence and reflectivity maps need to be numerically processed to obtain wavelength/angle(wavenumber) maps. Figure 2.10 a) shows a sketch of a typical map obtained with the CCD camera in a Fourier spectroscopy set-up. The map is characterised by two areas: an area with signal (white area) and another without signal (shaded area). The area without signal corresponds to the emission angles greater than the maximum angle, θ_{max}, which could not be imaged by Fourier spectroscopy. One can notice that the area with signal is not symmetrical. Indeed, the CCD camera is, in general, tilted with respect to the horizontal axis. The vertical dispersion of the angle is consequently not vertical on the CCD camera. One can then numerically rotate the signal maps since in practical a CCD camera is never perfectly aligned. Numerical rotation corresponds to the first step of the numerical process. Note that the tilting angle is exaggerated in the sketch.

Figure 2.10 b) shows a sketch of the photoluminescence or reflectivity maps after numerical rotation. The signal area is in the form of a trapeze as the upper and lower limits correspond to the maximum positive and negative angles(wavenumber), $\theta_{max}(k_{max})$ and $-\theta_{max}(-k_{max})$, which depends on the optical set-up overall chromatic aberration. The central line corresponds to the zero-angle(wavenumber).

The next step in the numerical process is to convert the x and y axes from pixels to wavelength and angle(wavenumber), respectively. In general, the wavelength axis is already converted by the spectrometer. For the angle(wavenumber), one can use the relation given by equation 2.4. However, this relation is obtained with geometric optics and therefore does not work in the case of Fourier spectroscopy set-up with high NA objectives. As a consequence, two alternative methods to convert the y-axis in angles were used in this PhD :

- The first method was used for the maps shown in Chapter 4. The dispersion curve of a Bragg mode of the microcavity is measured with both the Fourier configuration and the Perkin Elmer spectrophotometer. The Bragg mode comes from the Bragg mirror of the microcavity. As the angles of the Perkin Elmer spectrophotometer are well defined, the angle-dependent Bragg mode dispersion curve could be known with precision. The y-axis was then converted in angles such that the two measured angle-dependent Bragg modes matched.

- In the case of the maps in Chapter 5, only the photoluminescence was measured. Hence, the Bragg modes reflectivity could not be obtained, and the previous method could not be used. The method is then to consider that for each wavelength, the vertical axis is linear with the wavenumber varying from 0 μm^{-1} to $k_{max} = E/c\hbar \sin(\theta_{max})$. Indeed, the signal in the CCD is the direct image of the Fourier plane. Each y-axis at each wavelength

was then converted in angles using $\theta = c\hbar/\mathrm{E}\,\sin(k)$. This method requires that the upper and lower limits are visible in the maps and so the CCD is filled at around 80%. The focal length of the Fourier lens should then be:

$$f_{\mathrm{F}} = \frac{2}{0.8}\frac{f_{\mu} f_{s}}{t_{\mathrm{CDD}}}\tan(\mathrm{asin}(\mathrm{NA})). \tag{2.9}$$

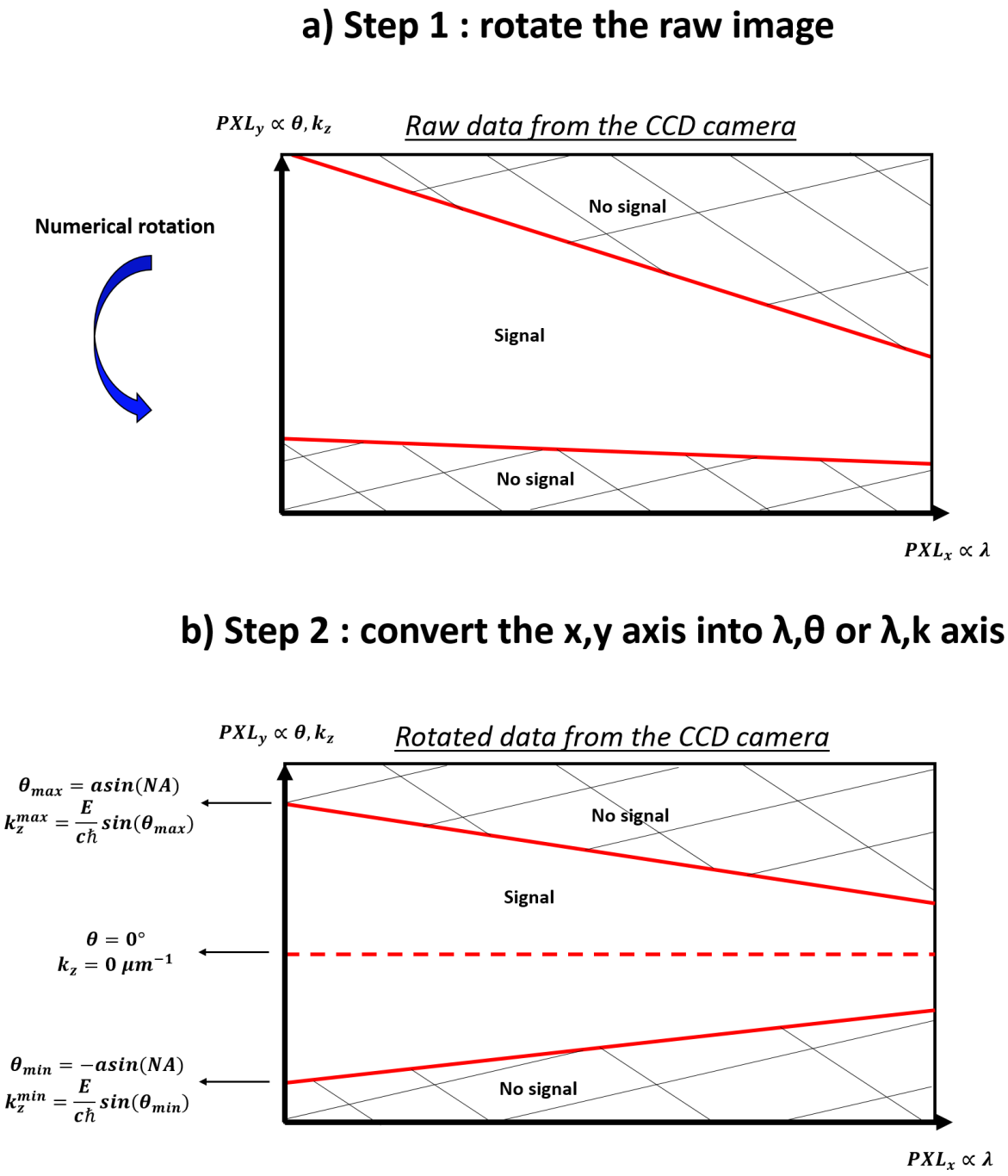

Figure 2.10: Sketches of a typical photoluminescence or reflectivity map obtained from the CCD camera in a Fourier spectroscopy set-up a) before and b) after numerical rotation.

3.4.6 Set-up in "INL" laboratory

In Institut des Nanotechnologies de Lyon (INL), the Fourier spectroscopy set-up was composed of the 0.9 NA microscope objective (MPLFLN50x, Olympus) of focal length 1.8 mm and working distance (WD) 3 mm, a Fourier lens of focal length 20cm, a spectrometer lens of focal length 15cm, the MicroHR spectrometer (Horiba) and a Sincerity (Horiba) CCD camera. The sample was either pumped by the picosecond laser diode emitting at 405nm (PDL 800-D, PicoQuant) for the angle-resolved photoluminescence measurements or shined by the halogen lamp (DH-2000, Ocean Optics) for angle-resolved reflectivity measurements.

The CCD camera is composed of 250 vertical pixels with a total vertical length of 7.7 mm. As a result, the angular resolution of the angle-resolved photoluminescence and reflectivity maps was better than in the Fourier spectroscopy set-up in Laboratoire Aimé Cotton (see the next section). However, the picosecond pulsed laser could not reach intensities high enough to reach the microcavity lasing thresholds. This set-up was then used for the angle-resolved measurements at low pump density described in chapter 4, demonstrating the strong coupling regime of the MAPB-based microcavity.

3.4.7 Set-up in "LAC" laboratory

The Fourier spectroscopy set-up in Laboratoire Aimé Cotton (LAC) is the same as the PL spectroscopy set-up number 2 presented previously in which a Fourier lens is added. The set-up could be switched from the PL spectroscopy configuration to the Fourier spectroscopy configuration by introducing the Fourier lens and inversely by removing the Fourier lens. The set-up was composed of the 0.9 NA microscope objective (MPLFLN50x, Olympus) of focal length 1.8 mm and working distance (WD) 3 mm, a Fourier lens of focal length 25cm, a spectrometer lens of focal length 6.3cm, the Princeton Instruments SP2150 spectrometer and a CCD camera (Pixis: 100B Ropers Scientific). The sample is excited by the 100 femtosecond pulsed laser at 1 kHz of repetition rate emitting at 400 nm either through the objective in the reflection configuration or by a 5cm lens in the transmission configuration.

The CCD camera is composed of 100 vertical pixels with a total vertical length of 2 mm. The angular resolution was therefore reduced compared to the one in the set-up in Institut des Nanotechnologies de Lyon (INL). However, the lasing thresholds could be reached with the femtosecond pumped lasers. This Fourier spectroscopy set-up was therefore used for the angle-resolved photoluminescence measurements as a function of the pumping power presented in Chapter 5.

4 Conclusion of the chapter

This chapter presented the experimental methods of this PhD. The deposition methods will be applied to fabricate the $3\lambda/2$ MAPB-based microcavity described and studied in the following chapters. The characterizations methods and the optical set-ups reported here will be used to characterize each layer of the microcavity and to study the microcavity optical and lasing properties.

Chapter 3

Design, fabrication and characteristics of the MAPB based microcavity

Contents

1 Simulation of the passive cavity 88

1.1 The commercial Bragg mirror 88

1.2 The refractive indices used for the simulation 90

1.3 Simulation of the passive microcavity 91

1.4 Calculation of the effective refractive index 92

2 Deposition and characterization of the optically active layer : the MAPB layer 93

2.1 Microscope images of the MAPB layers 93

2.2 Photoluminescence and absorption of the MAPB Layer 94

2.3 Profilometry of the MAPB layers 96

2.4 AFM image of the MAPB layer 97

3 Deposition and characterization of the spacing layer : the PMMA layer . 98

3.1 Empirical law for the PMMA thickness 98

3.2 Microscopy images of the PMMA layers 99

3.3 Profilometry of the deposited PMMA layer 99

3.4 AFM image of the MAPB+PMMA layer 100

4 Deposition of the closing silver mirror 101

5 Summary of the different roughnesses 101

6 Characterization of the complete microcavity 102

6.1 Variation of the detuning 102

6.2 Reflectivity spectrum 104

7 Conclusion of the chapter 106

Introduction

In this chapter, the design obtained with the transfer matrix method, the fabrication via spin coating and evaporation and the measurements of the microcavity characteristics will be presented. This work resulted in a 3λ/2 MAPB-based microcavity, which is further detailed for its strong coupling regime in Chapter 4 and its lasing effect in Chapter 5. This microcavity is composed of a commercial Bragg mirror (Layertec, corp), a 100 nm spin-coated layer of MAPB, a 350 nm spin-coated layer of PMMA and a layer of 30 nm of silver (Ag) deposited by evaporation as the closing mirror. An overall roughness of around 30 nm with grains of about 25-50µm size allows us to tune the detuning of the microcavity by changing the position probed in the microcavity.

1 Simulation of the passive cavity

Before fabricating the microcavity, it is necessary to know the layers to be used and the thicknesses to be applied. For the design, one can simulate the reflectivity spectra, and the electric field intensities of a microcavity with the transfer matrix method which was introduced in Chapter 1 in part 1.3.5. For the simulation, the dispersive complex refractive indices of the materials were collected from the literature. The desired result is a microcavity containing the gain material with a cavity mode energy close to the excitonic energy and an antinode of the absolute field covering the gain material.

The materials considered for the realization of the microcavity were a commercial Bragg mirror (Layertec (corp)), the perovskite MAPB, a spacer layer of PMMA (Poly(methyl) methacrylate) to control the thickness of the microcavity and a silver (Ag) layer as the closing mirror. The only constraint for the microcavity simulation concerns the MAPB layer. Indeed, the thickness of the best-quality MAPB layers obtained experimentally was of 100 nm, and for this reason, the MAPB thickness was set at 100 nm for the simulation.

1.1 The commercial Bragg mirror

The bottom mirror considered for the realization of the MAPB-based microcavity is the same commercial Bragg mirror (Layertec (corp)) described in the PhD manuscript (in french) of Gaëtan Lanty [210]. The mirror, whose schematic is presented in figure 3.1 a), is composed of 6.5 pairs of two alternative layers, named hereafter H and L, deposited on top of a fused silica substrate. The H and L layers are characterized by their refractive indices of $n_{\mathrm{H}} = 2.36$ and $n_{\mathrm{L}} = 1.46$ and thicknesses of $t_{\mathrm{H}} = 54.6nm$ and $t_{\mathrm{L}} = 88.2nm$. The exact nature of the two materials H and L is kept secret by the company LayerTec. Variations in layer thickness occur for the two bottom pairs (see figure 3.1). Finally, a 10 nm layer of Silica is deposited on top of the mirror to facilitate the perovskite deposition.

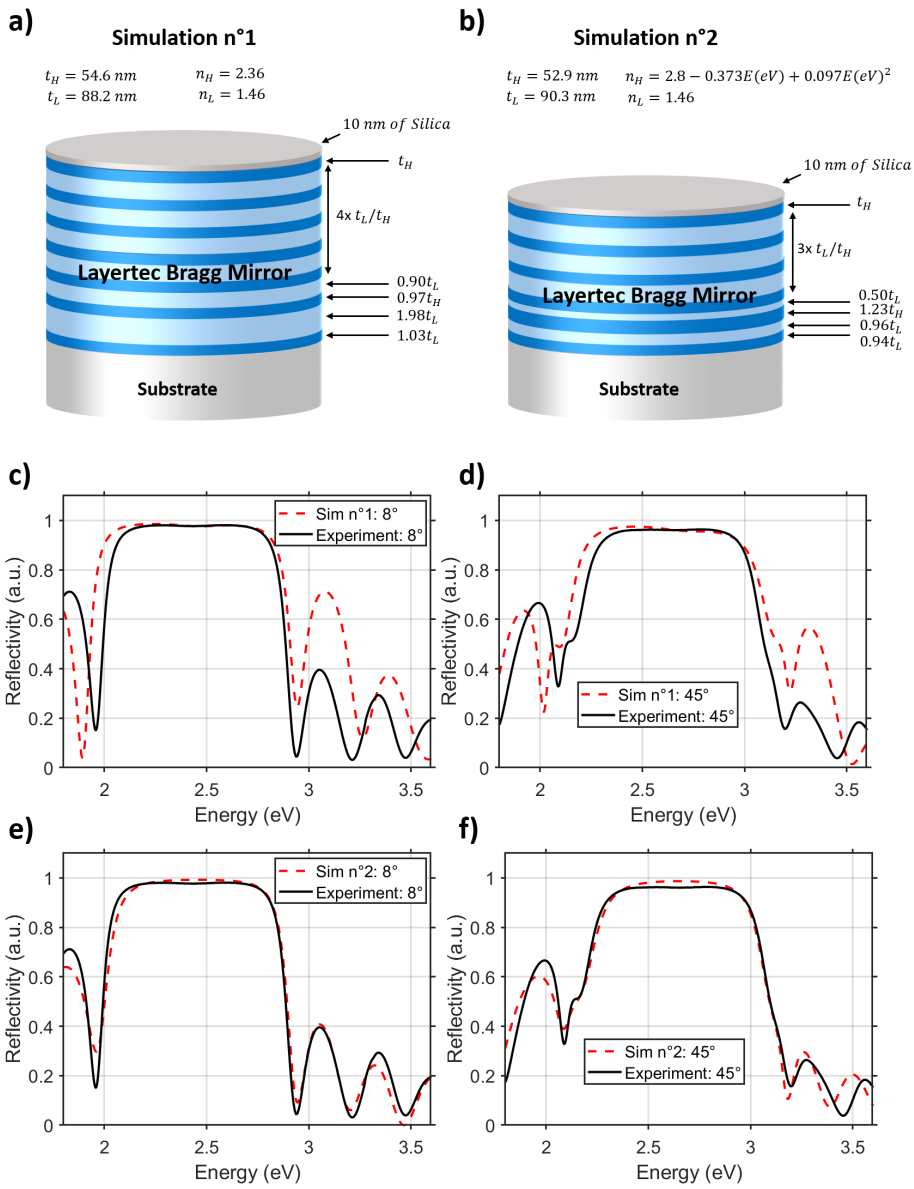

Figure 3.1: a) Structure of the commercial Bragg mirror (Layertec (corp)) as described in the PhD manuscript (in french) of Gaëtan Lanty [210]. This structure is noted as simulation 1 b) Structure of the commercial Bragg proposed in this PhD to better fit the commercial Bragg mirror experimental reflectivity spectra. This structure is purely used for the simulations and may not describe the actual structure of the mirror. This structure is noted as simulation 2. c) and d) Experimental (solid black line) and simulated with the simulation 1 (red dashed line) reflectivity spectra for an incidence angle of 8° (c)) and 45° (d)). e) and f) Experimental (solid black line) and simulated with the simulation 2 (red dashed line) reflectivity spectra for an incidence angle of 8° (e)) and 45° (f)).

The figures 3.1 c) and d) show the reflectivity spectra of the commercial mirror performed at 8° and 45° of incidence (solid black line) and the simulated reflectivity spectra using the parameters stated above (in red). The experimental reflectivity spectra were taken with the Perkin Elmer spectrophotometer described in Chapter 2. The experimental reflectivity at 8° shows a stopband (range of photon energy where the mirror reflectivity is near unity) centred at 2.4 eV with a reflectivity of 97.74% and extended from 2.1 to 2.78

eV. From figures 3.1 c) and d), one can observe a mismatch between the experimental reflectivity and the simulation. First of all, the stopband of the simulation is larger than the experimental stopband. Second, the experimental and simulated Bragg modes occur at different energies. The Bragg modes are the reflectivity dips outside of the stopband region. This mismatch suggests that the parameters used for the simulation are inaccurate. The difference of the stopband bandwidths indicates that the refractive index contrast ($n_H - n_L$) is larger in the case of the simulation.

Several reasons could explain the mismatch such as the limitations of the transfer matrix method to precisely simulate such a complex Bragg mirror or the use of constant instead of dispersive refractive indices. Nevertheless, another structure, shown in figure 3.1 b), has been proposed in this PhD to better simulate the Bragg mirror. This structure may not describe the real structure of the mirror and is purely used for the simulations as it allows us to better fit the experimental spectra at 8° and 45° of incidence (see figures 3.1 e) and f)).

1.2 The refractive indices used for the simulation

The refractive indices used for the bottom Bragg mirror layers are those given by the second simulated structure in figure 3.1 b). The extinction coefficient, k, of these layers is set to zero as we can neglect the absorption of the Bragg mirror. The refractive index of PMMA was considered constant at 1.5 with an extinction coefficient set to zero [230]. The dispersive complex refractive indices of the MAPB and the silver layers were extracted from the literature [231, 232] and are presented in figure 3.2. For the design of the microcavity, one needs to simulate the passive microcavity to measure the photonic mode energy without the effect of the optically active material which is here MAPB. For this reason, the absorption (extinction coefficient k) of the MAPB layer was set to zero, and its refractive index was set constant at 2.236, its mean value between 1.8 and 3.6 eV. The dispersive refractive index of MAPB will be used later on in Chapter 4 to simulate the reflectivity spectra of the fabricated microcavity.

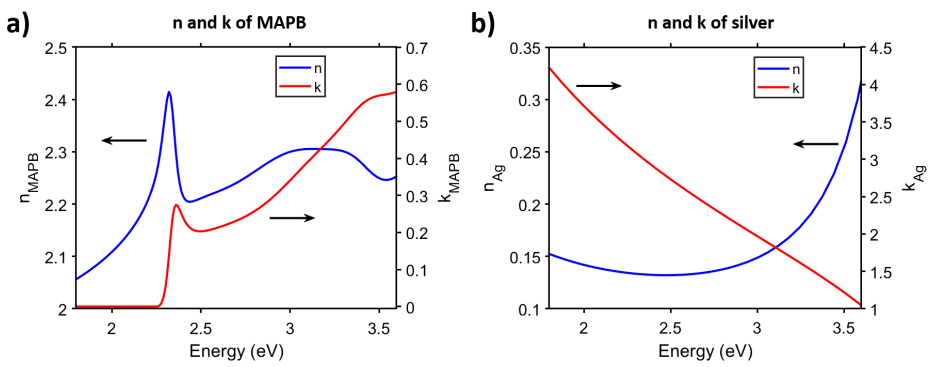

Figure 3.2: a) MAPB dispersive complex refractive index extracted from [231]. b) Silver dispersive complex refractive index extracted from [232].

1.3 Simulation of the passive microcavity

The final architecture obtained is the 3λ/2 microcavity presented in figure 3.3 composed of the commercial Bragg mirror, 100 nm of MAPB, 350 nm of PMMA, and 30 nm of silver.

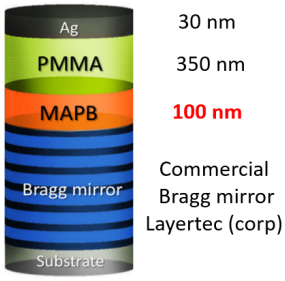

Figure 3.3: Final architecture obtained for the 3λ/2 MAPB-based microcavity composed of the commercial Bragg mirror, a 100 nm of MAPB, 350 nm of PMMA and 30 nm of silver (Ag).

Figure 3.4 shows the simulated microcavity reflectivity spectrum under normal incidence and the simulated absolute field distribution inside the microcavity. From the reflectivity spectrum, one can observe a cavity mode at 2.305 eV, which is close to the MAPB excitonic energy of 2.355 eV indicated by the vertical blue dashed line. The simulated quality factor of 113 was obtained by fitting the cavity mode with a Lorentzian function (red dashed line). The quality factor is mostly limited by the silver absorption. In figure 3.4 b), three antinodes can be observed inside the cavity (MAPB and PMMA), two in the PMMA and one in MAPB. Most importantly, the optically active material which is here MAPB is in one of the antinodes of the absolute field intensity.

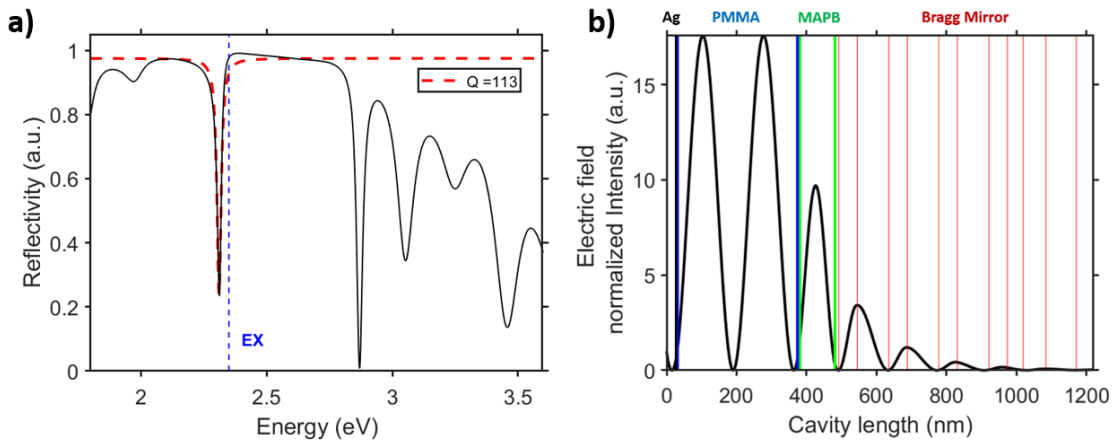

Figure 3.4: Simulated reflectivity spectrum (solid black line) of the passive microcavity under normal incidence with the matrix transfer method and Lorentzian fit (red dashed line) of the cavity mode to measure the cavity quality factor of 113. The vertical blue dashed line shows the MAPB excitonic energy of 2.355 eV b) Simulated absolute field distribution in the passive microcavity obtained with the matrix transfer method. Three antinodes can be seen inside the cavity (MAPB and PMMA), two in the PMMA layer and one in the MAPB layer making the architecture a 3λ/2 microcavity.

1.4 Calculation of the effective refractive index

Another physical quantity can be calculated from the design of the microcavity, which is the effective refractive index of the cavity n_{eff}. This effective refractive index is the average value of the refractive index inside the microcavity composed by the MAPB and PMMA layers and the penetration lengths of the mirrors. The penetration length inside the silver mirror can be neglected, and the penetration length in the Bragg mirror, L_{Bragg}, is calculated with the following equation 3.1 [233]:

$$L_{Bragg} = \frac{\lambda_0}{2} \frac{n_1 n_2}{n_c(n_2 - n_1)}, \tag{3.1}$$

where $n_{1,2}$ are the refractive indices of the two alternative layers of the Bragg mirror, λ_0 is the central wavelength of the Bragg mirror, and n_c=1.66 is the effective refractive index inside the cavity (MAPB and PMMA layers) without taking into account the penetration length :

$$n_c = \frac{(n_{\text{MAPB}} t_{\text{MAPB}} + n_{\text{PMMA}} t_{\text{PMMA}})}{(t_{\text{MAPB}} + t_{\text{PMMA}})}, \tag{3.2}$$

where n_{MAPB} and n_{PMMA} are respectively the MAPB and PMMA refractive indices, t_{MAPB}, t_{PMMA}, respectively the MAPB and PMMA thicknesses.

The effective refractive index of 1.75 can then be obtained from the equation 3.3 :

$$n_{eff} = \frac{n_{\text{MAPB}} t_{\text{MAPB}} + n_{\text{PMMA}} t_{\text{PMMA}} + n_{Bragg} L_{Bragg}}{t_{\text{MAPB}} + t_{\text{PMMA}} + L_{Bragg}} = 1.75, \tag{3.3}$$

where n_{Bragg} is the effective refractive index of the Bragg mirror given by equation 3.4, with $t_{1,2}$ the thicknesses of the two alternative layers of the Bragg mirror:

$$n_{Bragg} = \frac{n_1 t_1 + n_2 t_2}{t_1 + t_2}. \tag{3.4}$$

From this simulation, we could obtain a passive microcavity with a cavity mode close to the excitonic energy and with an antinode of the absolute field intensity covering the perovskite layer. The quality factor is of 113 and the effective refractive index of 1.75. As a remark, the microcavity is, in reality, a 2λ microcavity when the penetration length in the Bragg mirror is taken into account, however, the microcavity is called a $3\lambda/2$ microcavity as the optical length in the MAPB and PMMA layers is three times the half of the MAPB emission wavelength.

2 Deposition and characterization of the optically active layer : the MAPB layer

Now that the design of the microcavity is given, the microcavity can be fabricated. The first step consists in depositing the MAPB thin film. Two spin-coating methods detailed in Chapter 2 were studied in this PhD for the deposition of the MAPB perovskite: the one-step and the two-step methods. The best results in terms of film thickness and quality were obtained with the two-step spin-coating method. The difference in film quality could be seen by the naked eye. With the one-step process, the perovskite could not be homogeneously deposited on a quartz substrate, and the thin film presented many defects. This subsection will give the characterization results of the perovskite thin films deposited with the one-step and two-step techniques.

2.1 Microscope images of the MAPB layers

Figure 3.5 shows the microscope images of a MAPB thin film deposited with the one-step method at 20x magnification (figure 3.5 a)) and of a MAPB thin film deposited with the two-step method at 20x magnification (figure 3.5 b)) and at 100x magnification (figure 3.5 c)). From the first two images, the difference of quality between the thin films deposited with the one-step and two-step processes is undeniable. The colour difference between the two images comes from the different parameter settings used during the measurements with the interference contrast microscope. In the case of the thin film deposited with the two-step method, the perovskite covers the surface homogeneously while for the one-step process, the thin film is composed of grains of around 10*10 μm^2.

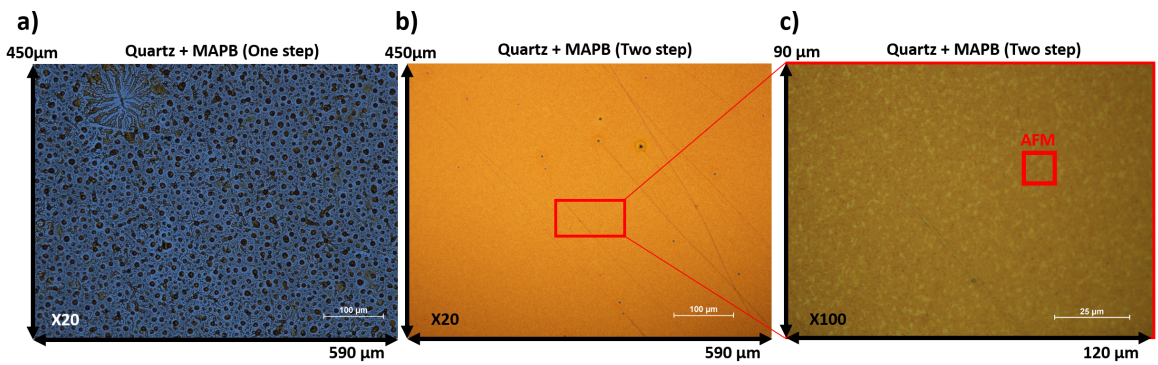

Figure 3.5: Microscope image of a MAPB thin film deposited with the one-step methods at 20x magnification a) and of a MAPB thin film deposited with the two-step method at 20x magnification b) and at 100x magnification c). The red square in b) indicates the region of the thin films visualized in c). The red square in c) gives the size of the AFM image presented later for comparison.

2.2 Photoluminescence and absorption of the MAPB Layer

Figure 3.6 shows the absorption spectra of two perovskite thin films deposited by spin coating on a quartz substrate with the one-step method and the two-step method, respectively. Four main differences can be noted between the two absorption spectra. First of all, the absorption at the excitonic energy, at 2.355 eV, is higher with the one-step MAPB thin film than with the two-step one. This suggests that the one-step thin film is thicker than the two-step thin film. Second, at low energy below 2.28 eV, i.e. below the bandgap and the excitonic resonance, the absorption of the one-step thin film is much higher than for the two-step thin film. As the residual absorption below the bandgap of a semiconductor generally comes from the defects of the crystal, we can speculate that the one-step thin film presents many more defects than in the two-step thin film. This is in accordance with the results obtained with optical microscopy. The third difference is the absorption above the bandgap, at energy higher than 2.37 eV. The absorption spectrum of the two-step thin film increases with energy as expected for a 3D semiconductor while the absorption is rather flat for the one-step thin film, which is unusual. Finally, the excitonic resonance at 2.355 eV is much more pronounced in the two-step thin film than in the one-step thin film (see figure 3.6 b)). In conclusion, based on the absorption spectra, the two-step spin-coating method gives better results for the MAPB thin films.

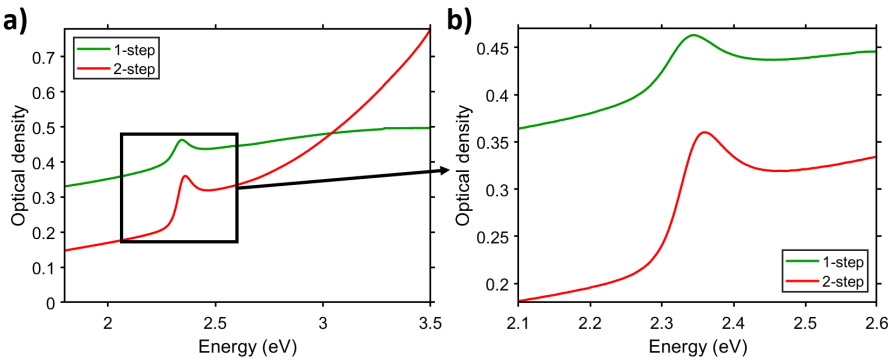

Figure 3.6: Absorption spectra of two MAPB thin films deposited by spin coating, one using the one-step method and the other using the two-step method in the range from 1 to 4.2 eV a) and in the range from 2.1 to 2.8 eV b).

Figure 3.7 a) shows the diffuse reflection of two MAPB thin film deposited with the one-step and two-step methods. The diffusion of the one-step MAPB thin film is twice as high as the two-step MAPB thin-film diffusion, indicating once again that the film quality is better with the two-step deposition method. The optical densities of the two thin films can then be corrected from the measured diffuse reflection [16]:

$$\mathrm{OD}_{cor} = \mathrm{OD}_{nc} + log_{10}(1 - \mathrm{R_D}), \tag{3.5}$$

where OD_{cor} is the corrected optical density, OD_{nc} is the non-corrected optical density, and $\mathrm{R_D}$ is the diffuse reflectivity of the thin film. The figures 3.7 b) and c) show the corrected optical densities (OD) along with the non-corrected optical densities (OD_{nc}) of the

MAPB thin films deposited with the one-step and two-step method, respectively. The difference between the corrected and non-corrected optical densities is more pronounced for the one-step MAPB thin film than the two-step MAPB thin film which is coherent with the larger diffuse reflection of the one-step MAPB thin film. However, in both cases, the absorption below the excitonic transition is non-zero, unlike usual semiconductors. The residual absorption could be due to either defect levels in the MAPB gap or unmeasured remaining diffuse reflection.

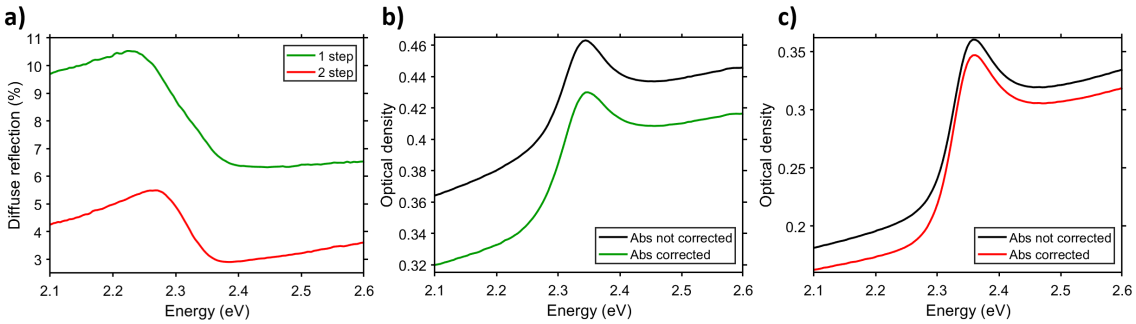

Figure 3.7: a) Diffuse reflection of two MAPB thin films deposited with the one-step and two-step method. b) Corrected and non-corrected optical density of a one-step MAPB thin film. c) Corrected and non-corrected optical density of a two-step MAPB thin film.

We have then shown with optical microscopy and with absorption and diffusion measurements that the MAPB layers are of better quality when deposited with the two-step method. For this reason, we only consider in the following the perovskite thin films deposited with the two-step spin-coating method.

Figure 3.8 shows the photoluminescence spectrum of a MAPB thin film deposited with the two-step method as well as the absorption spectrum presented in figure 3.7 c). The absorption spectrum is characterized by an excitonic resonance at 2.355 eV ($E_X = 2.355eV$) with a Half Width at Half Maximum (HWHM) of 39 meV and a band absorption continuum at higher energies. The photoluminescence is Stokes-shifted at an energy of 2.32 eV with a Full Width at Half Maximum (FWHM) of 96 meV. The excitonic linewidth, γ_X, can be estimated to be of 78 meV and 96 meV respectively from the absorption and photoluminescence spectra.

Finally, the absorption coefficient can be recovered from the optical density with the equation 3.6, where α is the absorption coefficient and t the thin film thickness:

$$\alpha = ln(10)\frac{\mathrm{OD}}{t}. \tag{3.6}$$

Figure 3.9 shows the MAPB absorption coefficient obtained from the two-step MAPB thin film optical density shown in figure 3.8. The result is very similar to the absorption coefficient measured in the literature [229] with an absorption coefficient of around 0.7 $10^5 cm^{-1}$ at the excitonic resonance.

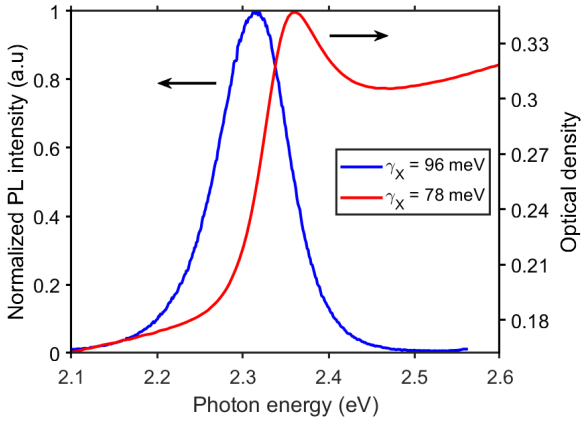

Figure 3.8: Absorption (in red) and Photoluminescence (in blue) spectra of a MAPB thin film deposited with the two-step method. The excitonic linewidth, γ_X, can be estimated to be of 78 meV and of 96 meV respectively from the absorption and photoluminescence spectra.

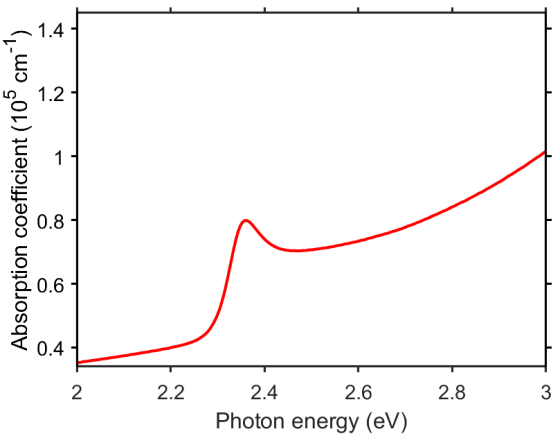

Figure 3.9: MAPB absorption coefficient obtained from the two-step MAPB thin film optical density shown in figure 3.8

2.3 Profilometry of the MAPB layers

Profilometry measurements were performed on MAPB thin films deposited with the two-step method on quartz substrates or on the Bragg mirrors to measure the thicknesses of the MAPB layers. In one part of the sample, the perovskite layer was removed with the help of a plastic tweezer to create a step between the substrate and the perovskite layer as it can be seen in figure 3.10 a) from a picture taken with the Profilometer. Profilometry scans were performed to measure the height of the step created, giving the thickness of the perovskite layer. Figure 3.10 b) shows one scan obtained with a MAPB thin film deposited on a Bragg mirror and gives a thickness of about 100 nm. The thicknesses measured with profilometry were around 100 nm for the perovskite layers, either deposited on quartz substrates or Bragg mirrors. Regions such as the sample extremities could exhibit higher thicknesses.

As a remark, a profilometry scan of a $PbBr_2$ layer deposited on the Bragg mirror is shown in figure 3.10 c) with the profilometry scan of the MAPB thin layer for comparison. The thickness of the $PbBr_2$ layer before its reaction with the solution containing MABr is about 60 nm. This indicates that after the reaction, which corresponds to the second step of the two-step deposition, the thin film gains 40 nm of thickness.

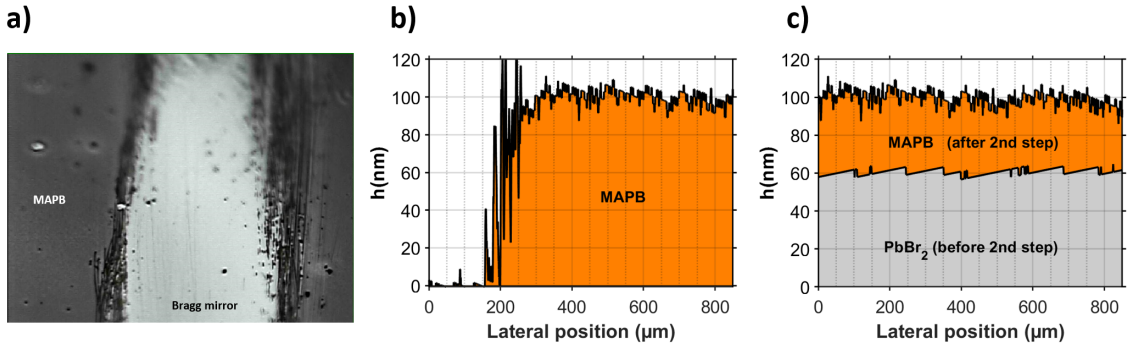

Figure 3.10: Profilometry measurements performed on a MAPB thin film deposited on a Bragg mirror a) Picture of the scanning surface taken with the profilometer. This picture shows the part where the perovskite has been removed to create a step between the Bragg mirror and the perovskite b) Profilometry scan of the MAPB layers deposited on the Bragg mirror. c) Profilo scan of a $PbBr_2$ layer before the second step of the two-step spin-coating method along with the profilometry scan of the MAPB layer.

2.4 AFM image of the MAPB layer

From the microscope image of figure 3.5 c), one can observe that the two-step thin film is not so homogeneous. Atomic force microscopy (AFM) has then been performed on the perovskite layer with the AFM set-up described in Chapter 2. The red square in figure 3.5 c) gives the size comparison of the surface area of the microscope image and the AFM image. Figure 3.11 presents the AFM image of a MAPB thin film deposited with the two-step spin-coating method. The AFM image reveals that the MAPB thin film is polycrystalline with a roughness of about 15 nm composed by grains of 500nm to 1µm size.

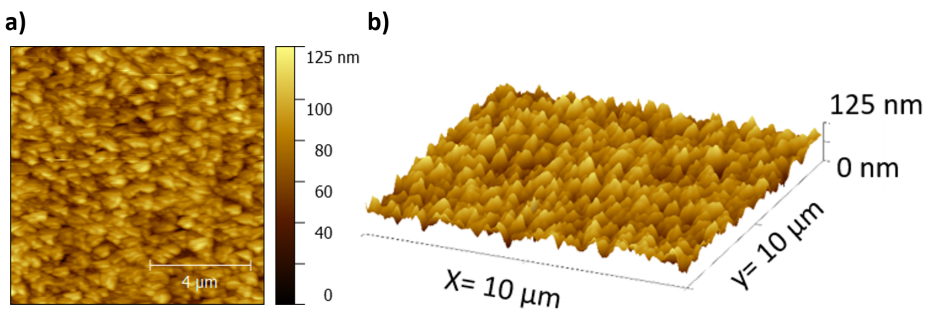

Figure 3.11: AFM image of a MAPB thin film deposited with the two-step spin-coating method. a) top view and b) side view of the AFM image.

3 Deposition and characterization of the spacing layer : the PMMA layer

The second step of the fabrication of the microcavity concerns the deposition of a 350 nm layer of PMMA. The following will present the characterization results of the PMMA deposition on a substrate (quartz substrate or Bragg mirror) and an already deposited MAPB layer.

3.1 Empirical law for the PMMA thickness

To obtain a thickness of 350nm, we used the results reported by Walsh et al. [234]. The authors proposed an empirical relation between the thickness of spin-coated PMMA layer on silicon wafers, the concentration of PMMA in Toluene solutions and the spin coating rotation speed (in rpm) 3.7 :

$$t_{\mathrm{PMMA}} = 0.92c^{-1.56}w^{-0.51}, \tag{3.7}$$

where t_{PMMA} is in μm, c is the concentration in wt.%, and ω is the rotation speed of the spin-coater in rpm. In the article, the spin-coating duration is of 60 seconds and the acceleration is not given.

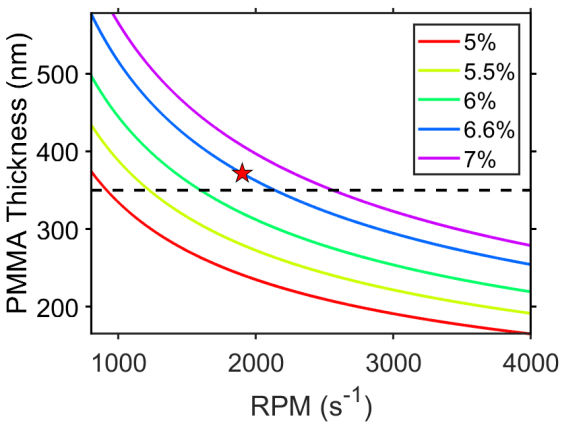

Figure 3.12: PMMA thickness against spin-coating rotation speed (in rpm) for five different concentrations (5%, 5.5%, 6%, 6.6% and 7%) for PMMA layers deposited on Silicon wafers with solutions of PMMA in Toluene using the equation 3.7. The black horizontal line corresponds to the desired thickness of PMMA of 350 nm, the red star to the concentration of 6.6% and the rotation speed of 1900rpm chosen in this PhD.

Figure 3.12 shows the relation between the PMMA thickness and the spin-coating rotation speed (in rpm) for 5 different concentrations (5%, 5.5%, 6%, 6.6% and 7%) using the equation 3.7. The thickness of the PMMA increases with increasing concentration and decreasing rotation speed. The black horizontal line indicates the desired thickness of PMMA of 350 nm. The red star corresponds to the concentration of 6.6% and the rotation speed of 1900 rpm chosen in this PhD. The acceleration was 200 rpm/s^2 and the

spin-coating duration time 30s. We chose a concentration and a speed which would theoretically give a PMMA thickness of 371.6 nm, however experimentally we would generally obtain thicknesses of around 350 nm. The difference between our experimental results and the empirical relation could come from the difference of substrate used in this PhD or other experimental considerations such as the spin-coating duration.

3.2 Microscopy images of the PMMA layers

Microscopic images of the PMMA layers deposited on the Bragg mirrors, see figure 3.13 a), and on the MAPB layers already deposited, see figure 3.13 b) and c), were taken. The microscope images of figures 3.13 a) and b) were taken at 5x magnification and the microscope image of figure 3.13 c) at 50x magnification. On the microscope image of the PMMA deposited directly on the Bragg mirror, one can observe that the PMMA layer is slightly rough in the form of grains of around 25*25 μm^2 at the centre of the microcavity (top right of the image) and the shape of "wavelets" of about 25 μm in width at the extremities of the Bragg mirror (bottom left of the image). The roughness shape depends on the distance of the microcavity area to the centre of rotation during the spin coating. When the PMMA is deposited on top of a MAPB layer, one can retrieve these grains. In figures 3.13 b) and c), the grains can be observed with an alternation of blue and yellow zones. The difference between the reflected colours comes from the local variation in the thickness of the two layers.

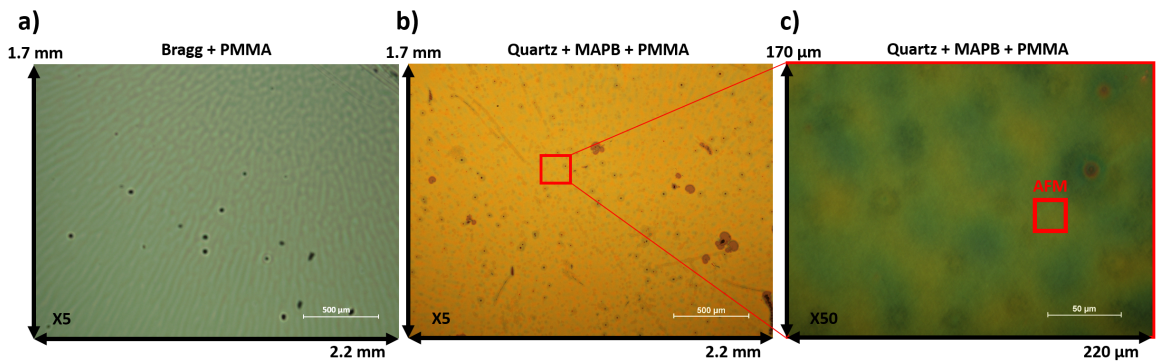

Figure 3.13: Microscope image of a PMMA thin film deposited on a Bragg mirror at 5x magnification a) and on a MAPB thin film at 5x magnification b) and at 50x magnification c). The red square in b) indicates the region of the region visualized in c). The red square in c) gives the size of the AFM image presented later for comparison.

3.3 Profilometry of the deposited PMMA layer

Profilometry measurements have been performed on a PMMA layer deposited on top of a MAPB layer deposited on a Bragg mirror. Figure 3.14 shows a picture of the part where the MAPB/PMMA layer has been removed to create a step. The profilometry scan of the MAPB/PMMA layer shown in figure 3.14 gives a total average thickness of 450 nm with a roughness of around 30 nm and grains of 25 to 50 µm in width. As the MAPB thickness

is 100 nm, we obtain the desired thickness of 350 nm for the PMMA layer. The size of the grains measured confirms the grains seen in the microscope images.

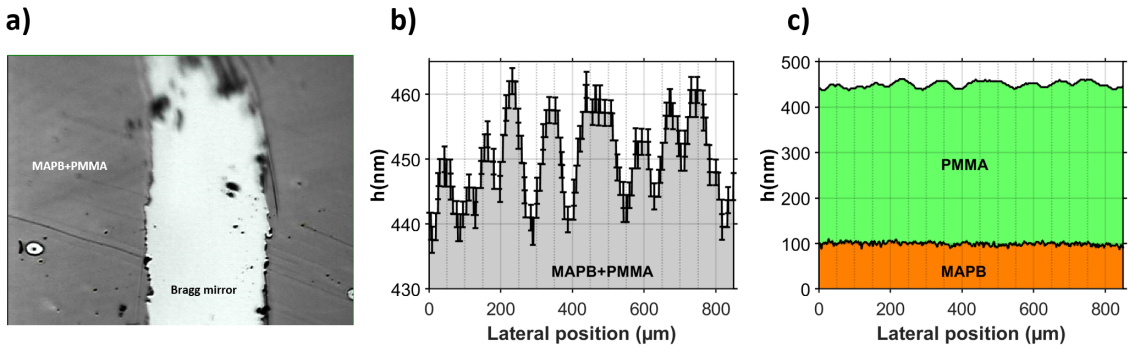

Figure 3.14: Profilometry measurements on a PMMA layer deposited on top of a MAPB layer deposited on a Bragg mirror a) Picture of the scanning surface taken with the profilometer. This picture shows the part where the MAPB/PMMA layer has been removed to create a step b) Profilometry scan of the PMMA layer deposited on MAPB. c) Comparison of the MAPB/PMMA profilometry scan and the MAPB profilometry scan to reveal the PMMA layer thickness of 350 nm.

3.4 AFM image of the MAPB+PMMA layer

Figure 3.15 presents the AFM image of a PMMA thin film deposited on a MAPB thin film deposited on a Bragg mirror in a surface area characteristic of the MAPB/PMMA grains size described before. The red square in figure 3.13 c) gives for comparison the size of the AFM image and the microscope image. The AFM reveals a roughness of about 3.6 nm, which is lower than the MAPB layer roughness of 15 nm and shows dips (black circles) of around 20 nm depth and 1-2 µm width in the MAPB/PMMA layer. This probably comes from the deposition of the PMMA on top of the previously presented MAPB grains of 500nm to 1µm size. The MAPB/PMMA layers are then composed of two types of roughness with different lateral characteristic dimensions, one with lateral size of about 1 μm and the other of lateral size of about 25 μm. Due to the limited resolution of the profilometer, only the roughness of large lateral dimensions could be observed in the profilometry measurements.

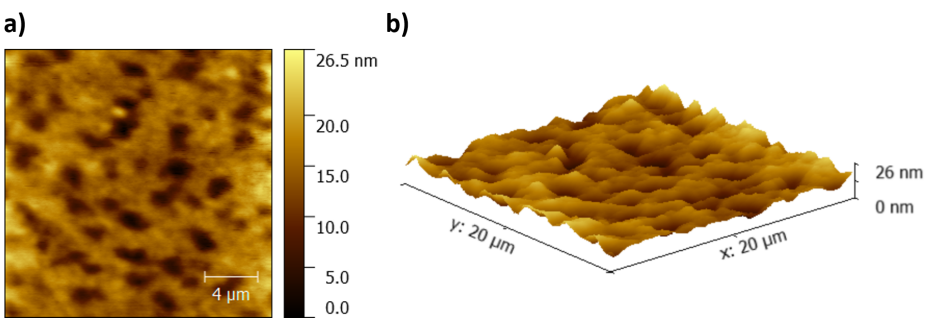

Figure 3.15: AFM image of a PMMA thin film deposited on a MAPB thin film deposited on a Bragg mirror. a) top view and b) side view of the AFM image.

4 Deposition of the closing silver mirror

The final step of the microcavity fabrication is the deposition of a 30 nm layer of silver (Ag) on top of a half cavity (MAPB+PMMA on a Bragg mirror) by evaporation in a cleanroom. The silver layer thickness is measured by a quartz crystal micro-balance positioned close to the sample during the evaporation. Figure 3.16 shows an AFM image of a silver layer deposited on top of a MAPB/PMMA layer deposited on a Bragg mirror. The AFM reveals a roughness of about 4.4 nm in the entire image and of 1 nm in the red box shown in figure 3.16 a). Figure 3.16 b) shows the thickness variation in the slice of the AFM image along the black line in figure 3.16 a).

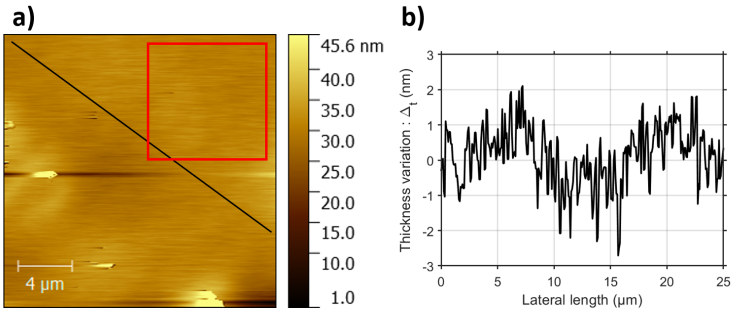

Figure 3.16: a) AFM image of a silver layer deposited on top of a MAPB/PMMA layer deposited on a Bragg mirror. The roughness in the total area is of 4.4 nm and in the red box of 1 nm. b) Thickness variation in the slice of the AFM image along the black line in a).

5 Summary of the different roughnesses

From the profilometry and AFM measurements, the vertical and lateral characteristic dimensions of each layer of the microcavity are known and are schematically presented in Figure 3.17. Figure 3.17 a) shows a schematic of the thickness against the lateral position of a complete microcavity on a large scale considering only the roughness with a large lateral dimension. The MAPB layer is flat with a thickness of 100 nm from the profilometry measurement. The PMMA layer has an average thickness of 350 nm and is composed of grains 25 μm wide and 20 nm deep from the profilometry measurement. Profilometry measurements have not been carried on a complete microcavity during the PhD, the thickness of the silver layer is then considered to be of 30 nm on every position from the evaporator micro-balance measurement and so the silver layer "follows" the PMMA roughness. Figure 3.17 b) shows a schematic of the thickness against the lateral position of a complete microcavity on a small scale by considering all the roughness. The MAPB and PMMA layers are composed of small grains of around 1 μm wide while the silver layer remains flat as no grains were observed in the AFM image of the silver layer (see figure 3.16).

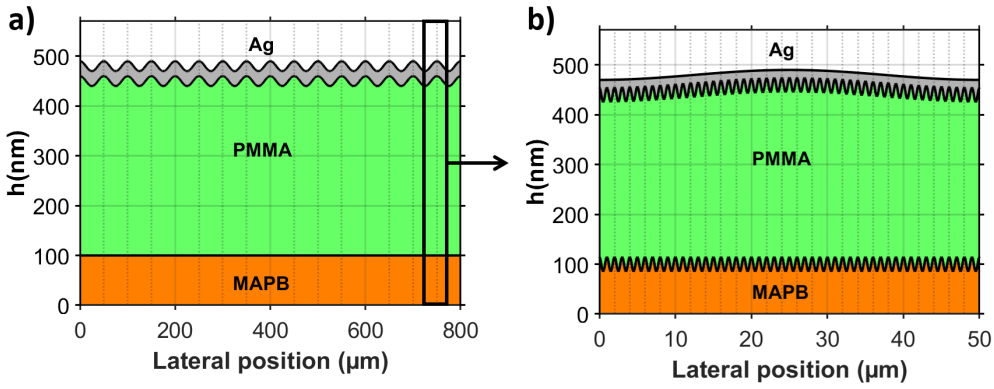

Figure 3.17: Schematic of the characteristic vertical and lateral dimensions of each layer of the microcavity obtained with profilometry and AFM measurements. a) Large scale vertical and lateral dimensions considering only the large lateral dimensional roughness b) Small scale vertical and lateral dimensions considering all roughness.

6 Characterization of the complete microcavity

During this PhD, batches of five microcavities were fabricated at once and in general, one or two microcavities among them were exploitable. Figure 3.18 shows the pictures of a microcavity after each step of fabrication. Experiments have been performed on several microcavities, but as the results did not differ much from one microcavity to another, only one microcavity will be considered in the following of this manuscript. In this section, two characterization measurements of the aforementioned complete microcavity will be presented: a spatially-resolved micro-photoluminescence measurement to obtain the spatial variation of the microcavity detuning and the microcavity reflectivity spectrum at normal incidence.

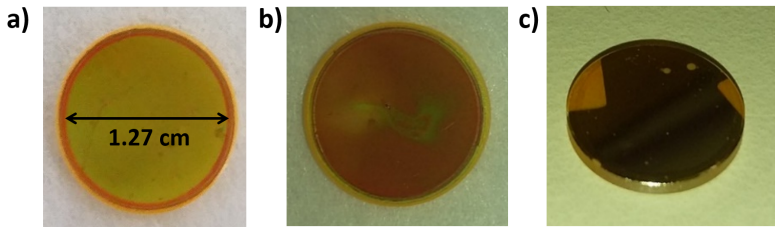

Figure 3.18: Pictures of the microcavity after each step of fabrication: a) after the MAPB deposition b) after the PMMA deposition and c) after the silver (Ag) deposition.

6.1 Variation of the detuning

As a reminder, the detuning, $\delta = E_{ph}(0°) - E_X$, is the difference between the photonic mode energy at normal incidence, $E_{ph}(0°)$, and the exciton energy, E_X. As the photonic mode energy at normal incidence is dependent on the microcavity thickness, the detuning is expected to vary spatially due to the microcavity overall roughness which was measured previously.

The spatially-resolved µPL set-up discussed in Chapter 2 has been used to measure the spatial variation of the microcavity detuning. In this set-up, the PL intensities of a sample area are collected by an NA 0.6 objective and an avalanche photodiode (APD) for a given wavelength. Several 100×100 μm^2 size maps with 2µm size pixels were measured for different wavelengths (from 534 to 556 nm every 2 nm) in the same area of the microcavity. Figure 3.19 a) shows six of the twelve collected maps. The PL intensity of each pixel was collected for every map resulting in the PL spectrum of the given pixel. Every spectrum was fitted by a Gaussian function, and the resulting fitting parameters gave the Full Width at Half Maximum (FWHM), integrated intensity and the cavity mode energy of each pixel. Figure 3.19 shows the example of the Gaussian fitting of the spectra collected from the pixels ((10µm,60µm), (50µm,50µm) and (8µm,4µm)). Finally, the difference between the excitonic energy of 2.355 eV and the spatially-resolved photonic mode energy at normal incidence was mapped, as shown in figure 3.20.

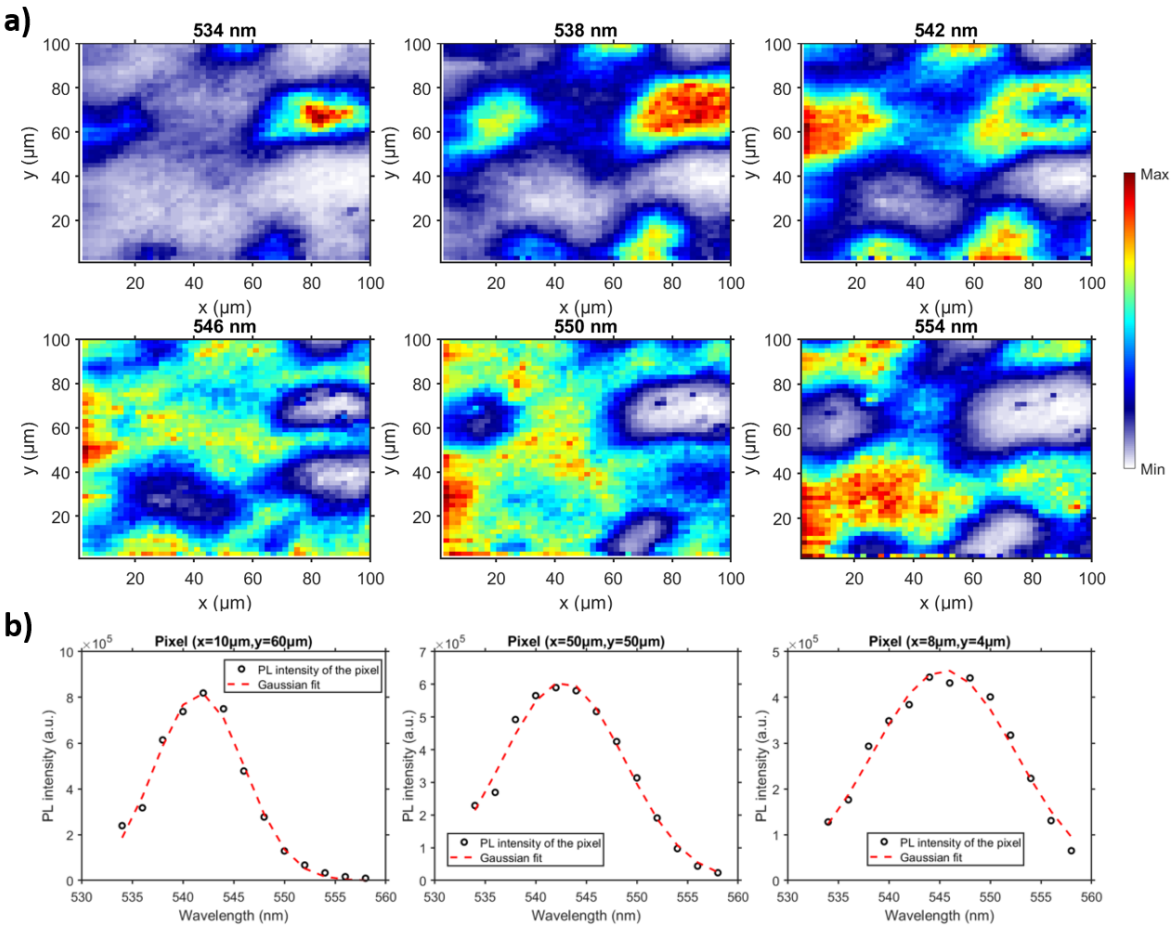

Figure 3.19: Spatially-resolved intensity pseudo-colour maps (in linear scale) of the microcavity. a) Six spatially-resolved µ-PL pseudo-colour maps of 100×100 μm^2 in size with pixels of 2µm size measured for different wavelengths (from 534 to 556 nm every 2 nm) in the same microcavity area. b) Example of Gaussian fittings of spectra collected from the pixels ((10µm,60µm), (50µm,50µm) and (8µm,4µm)). The spectrum at each pixel was obtained by collecting the PL intensities in every map taken at different wavelengths of the same pixel.

The detuning map of figure 3.20 a) reveals a spatial variation of the cavity detuning with areas of constant detuning of around 20 µm to 50 µm which is similar to the size of the grains measured of the MAPB/PMMA layer by profilometry in section 3.3.4. Moreover, the detunings range from -43 meV to -91 meV which represents a variation in PMMA layer thickness from 348 nm to 362 nm using the simulation and considering the MAPB and silver layer thicknesses as being constant. This variation in thickness of about 14 nm is of the same order as the roughness of the MAPB/PMMA layer of 30 nm from the profilometry in section 3.3.4. As an illustration, figure 3.20 b) shows the detuning pseudo-colour map placed to scale on top of the microscope image in section 3.3.2 of a MAPB/PMMA layer. As a conclusion, the map of the microcavity detuning confirms the roughness of the MAPB/PMMA layer measured in the previous sections. This variation will allow us in the next two chapters to tune the cavity detuning by changing the position probed on the microcavity in order to analyse the angle-resolved reflectivity and PL measurements as a function of the detuning.

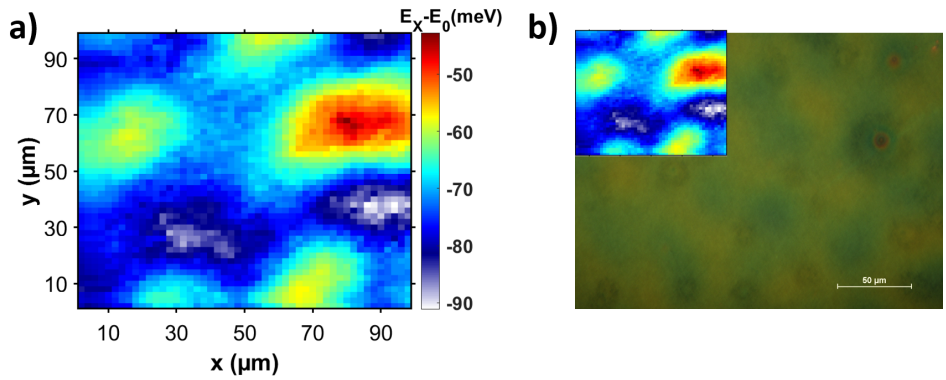

Figure 3.20: a) Spatial variation of the microcavity detuning obtained with a spatially-resolved micro-photoluminescence measurement. The detuning variation comes from the MAPB/PMMA roughness, which was measured in the previous sections. The pseudo-colour map is in linear scale. b) Same spatial pseudo-colour map of the detuning variation put to scale on top of the microscope image of the MAPB/PMMA layer presented in section 3.3.2. This illustrates that the characteristic size of areas with constant detuning is similar to the size of the area of the MAPB/PMMA layer with constant thickness.

6.2 Reflectivity spectrum

Figure 3.21 shows the reflectivity spectra at 8 ° of incidence as black solid lines at each step of the fabrication : after the MAPB deposition on the Bragg mirror (figure 3.21 a)), after the PMMA deposition (figure 3.21 b)), and after the silver deposition (figure 3.21 c)). The Bragg mirror reflectivity is shown as a black dashed line in each figure to indicate the original position of the stopband. In the three cases, the dips of the reflectivity spectra at energies higher or lower than the Bragg mirror stopband correspond to the Bragg mirror modes. In the following, only the dips which lie inside the stopband will be considered.

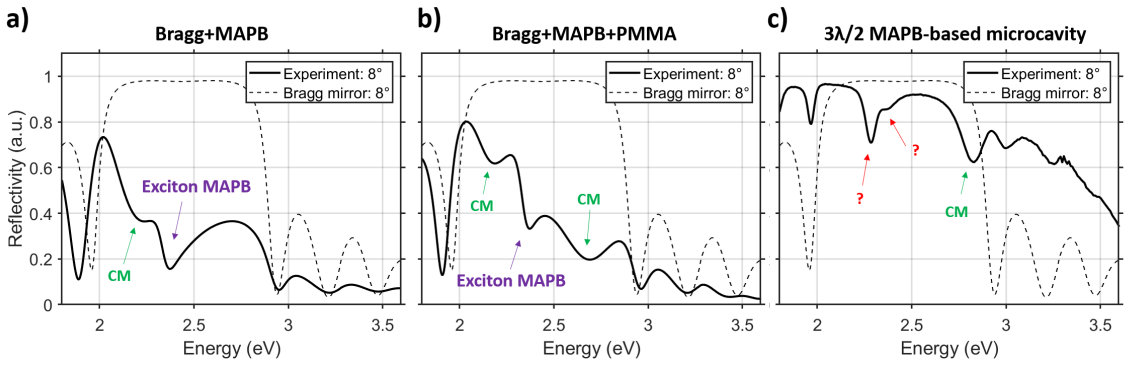

Figure 3.21: Reflectivity spectra at 8 ° of incidence at each step of the microcavity fabrication: after the MAPB deposition on the Bragg mirror a), after the PMMA deposition b), and after the silver deposition c). The Bragg mirror reflectivity is shown as a black dashed line in each figure to indicate the original position of the stopband. The dips corresponding to the MAPB exciton absorption are indicated by purple arrows and the dips corresponding to cavity modes by green arrows. The nature of the two dips indicated by red arrows is the subject of the next chapter.

In the reflectivity spectra after the MAPB deposition and after the PMMA deposition, a reflectivity dip in the middle of the stopband indicated by the purple arrow can be observed: this dip corresponds to the excitonic absorption of the MAPB layer. In these two cases, other broader dips indicated by the green arrows can be seen within the stopband, which correspond to cavity modes. These cavity modes are very broad as the quality factors of the cavity composed only by the MAPB layer or the MAPB and PMMA layers is very low. In the case of the reflectivity of the complete microcavity in figure 3.21 c) three dips can be observed, one indicated by a green arrow, considered to be a cavity mode, and two by red arrows. Whether the two other dips can be attributed to a cavity mode and the excitonic resonance or the lower and upper polaritons is the subject of the next chapter.

7 Conclusion of the chapter

In this Chapter, the design, the fabrication and the characteristics of the 3λ/2 MAPB-based microcavity were presented. The microcavity is composed of a commercial Bragg mirror, a 100 nm spin-coated layer of MAPB, a 350 nm spin-coated layer of PMMA and a layer of 30 nm of silver (Ag) deposited by evaporation as the closing mirror. Based on absorption and microscopy measurements, the two-step spin-coated method has revealed to be the best approach to obtain large-surface and homogeneous thin layers of MAPB. Homogeneous in the sense that the MAPB layer covers the whole Bragg mirror surface without any pinhole. AFM measurements have shown however that the MAPB layers with the two-step method present a roughness of about 14 nm and grains of 500 nm to 1µm size. An overall roughness of the MAPB/PMMA layer of around 30 nm with grains of about 25-50µm size was measured by profilometry. AFM measurements have shown that the silver layer is smooth compared to the MAPB and PMMA layers. A map of the detuning spatial variation of the complete microcavity confirmed the roughness measured previously by profilometry. Finally, the experimental reflectivity at 8° of incidence of the complete microcavity has shown two reflectivity dips. The origin of these two dips, bare exciton and cavity modes or upper and lower polaritons is the topic of the next Chapter.

Chapter 4

Strong coupling regime in the 3λ/2 MAPB-based microcavity

Contents

1 Motivations 108

2 Reflectivity spectra obtained with the spectrophotometer 108

3 Angle-resolved photoluminescence and angle-resolved reflectivity by Fourier spectroscopy 110

4 Fitting of the polaritonic dispersions 111

4.1 Collection of the experimental dispersions 111

4.2 Fitting of the experimental dispersions 111

4.3 Discussion on the obtained parameters 113

4.4 Final results on the ARR and ARPL maps 115

5 Bottleneck effect of the lower polariton photoluminescence 117

6 Discussion on the MAPB exciton stability at room temperature 118

7 Simulations of the results 120

7.1 Influence of the roughness on the simulated reflectivity and photoluminescence 120

7.2 Influence of the MAPB refractive index 126

7.3 Predictions of the strong coupling for other microcavity designs . . 133

8 Conclusion of the chapter 135

Introduction

This chapter will present the angle-resolved reflectivity, angle-resolved photoluminescence measurements and analysis carried on the 3λ/2 MAPB-based microcavity presented in the previous chapter to demonstrate the strong coupling regime. As a reminder, the microcavity is composed of a commercial Bragg mirror, a 100nm layer of MAPB, a 350 nm of PMMA and a 30nm layer of silver. The MAPB/PMMA layer is characterized by a roughness of around 30 nm and is composed of grains of 25 to 50 µm in width, which leads to a variation of the detuning along the microcavity surface. An effective refractive index, n_{eff} of 1.75 and a quality factor of 113 have been calculated from the microcavity design. Finally, the simulation of the angle-resolved reflectivity and photoluminescence maps will be discussed.

1 Motivations

The exciton-polaritons give hope toward the implementation of a novel optoelectronic technology. All-optical logical devices on a single chip are the perspective of the exciton-polaritons. In such a device, the polaritons must propagate over macroscopic distances to transport and process the information in logical blocks. For this reason, the desired material needs to sustain the strong coupling regime at room temperature, have good charge transport properties, have a low synthesis cost and be deposited over a large surface. Many materials have been explored such as GaAs, GaN, ZnO, organic materials, 2D perovskites and TMD (Transition metal dichalcogenides). Each of them presents its advantages, such as the low cost of synthesis of the organics, 2D perovskites and TMDs or the precision of deposition of the inorganic semiconductors allowing precise engineering of the polariton systems. However, the production cost of the inorganic materials is high, and for GaAs, the strong coupling regime can only be obtained at cryogenic temperatures. Organic materials suffer from their poor charge transport properties and the 2D perovskite from anisotropic charge transport properties. The TMDs are in the form of ultra-thin layers with small surface areas. In this context, we demonstrate in the following the strong coupling regime at room temperature in a 3λ/2 microcavity containing a large-surface MAPB thin-film. This result gives hope to MAPB-based polariton devices, possibly electrically injected, thanks to the good transport properties of the 3D perovskites.

2 Reflectivity spectra obtained with the spectrophotometer

Before discussing the angle-resolved reflectivity and photoluminescence results from the Fourier spectroscopy set-up, let us consider the reflectivity spectra taken at different incidence angles with the spectrophotometer presented in figure 4.1 a). Large areas of 1x1

mm^2 were detected by the spectrophotometer and therefore, a large number of different detunings. The measured reflectivity spectrum is then the average of reflectivity spectra with different detunings. One could expect to observe many reflectivity dips in the resulting reflectivity spectrum coming from the different cavity modes. However, only two reflectivity dips can be seen within the Bragg mirror stopband (see the dips in the red rectangle in figure 4.1 a)). This can be explained by the relatively homogeneous distribution of the detunings around an average value within the probed area. The averaging of the cavity modes results in broadened and shallower reflectivity dips than in a case without roughness. The reflectivity simulations at the end of the chapter further confirm this assumption.

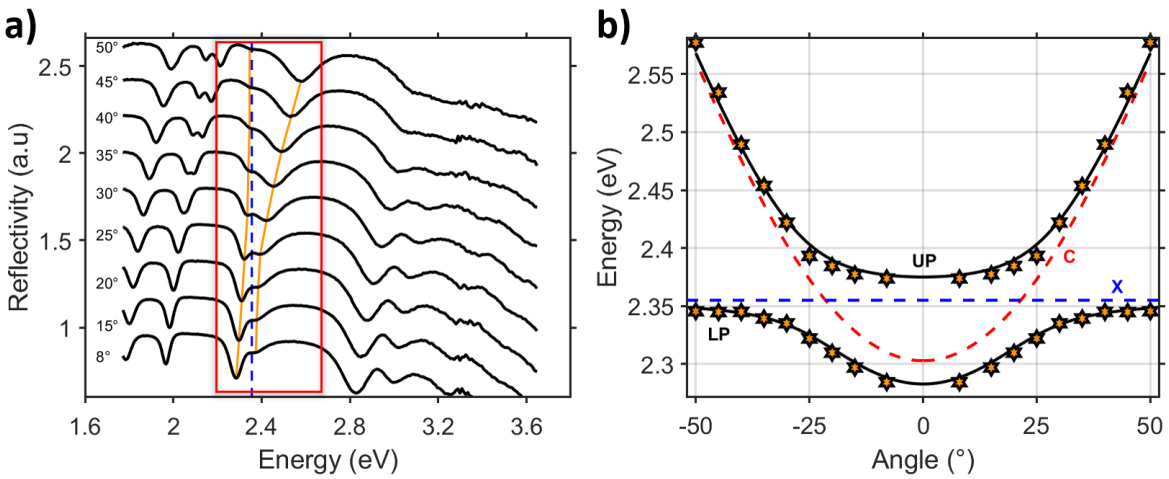

Figure 4.1: a) Reflectivity spectra at different incidence angles taken with the spectrophotometer (see Chapter 2). The area probed on the microcavity is 1mm x 1mm. The red rectangle represents the range of energy of interest. The yellow lines are guides for the eyes to follow the dispersion of the dips, and the blue dashed line represents the excitonic energy taken from the MAPB absorption spectrum in Chapter 3. b) Reflectivity dips energies collected at each spectrum with different incidences angles. The yellow stars are the collected experimental data. The two solid black lines are the lower and upper polaritonic dispersions of the two-level model fitted to the experimental data with the values of n_{eff}=1.75, E_X=2.355 eV, δ=-35 meV and g=38 meV. The blue and red dashed lines are the dispersions of the uncoupled exciton and photonic mode, respectively.

For each reflectivity spectrum at different angles of figure 4.1 a), the energies of the reflectivity dips were collected and reported as yellow stars in the energy/angle diagram of figure 4.1 b). These data points were fitted with the strong coupling two-level model presented in Chapter 1. The effective refractive index, n_{eff} was set at 1.75, and the excitonic energy, E_X, was set at 2.355 eV from the microcavity design and the MAPB absorption spectrum in Chapter 3. For simplicity, the excitonic and photonic linewidths were set at zero while the coupling strength, g, and the detuning, δ, were let as free parameters. A good agreement has been reached with g=38 meV, giving a Rabi splitting, $\hbar\Omega$, of 76 meV, and δ=-35 meV, corresponding to the average detuning probed in the large area by the spectrophotometer.

However, despite the good agreement between the two-level model and the collected experimental data, this result is not sufficient to demonstrate the strong coupling regime. The polaritonic dispersion from reflectivity and photoluminescence measurements must be obtained from the same microcavity position. Moreover, the probed area must be reduced to limit the inhomogeneous broadening induced by the roughness. Angle-resolved reflectivity and photoluminescence performed on the microcavity with a Fourier spectroscopy set-up will then be discussed.

3 Angle-resolved photoluminescence and angle-resolved reflectivity by Fourier spectroscopy

Angle-resolved reflectivity and photoluminescence have been performed on the microcavity with the Fourier spectroscopy set-up in collaboration with INL Lyon (see section 2.3.4.6 in Chapter 2). In the Fourier spectroscopy set-up, the microcavity is excited by a picosecond pulsed laser (50ps, 80 MHz) emitting at 405 nm with a spot size of 1 μm^2 for the photoluminescence and by a white light beam with a spot size of 10x10 μm^2 for the reflectivity. The two spot sizes are smaller than the MAPB/PMMA layers grains and the areas of constant detuning measured by profilometry and with the μ-PL set-up in Chapter 3. It is worth noting that inhomogeneities could come from another roughness with smaller characteristic sizes such as from the 1 μm MAPB grains. Nevertheless, we can consider that only one detuning is probed for a given position with the Fourier spectroscopy set-up.

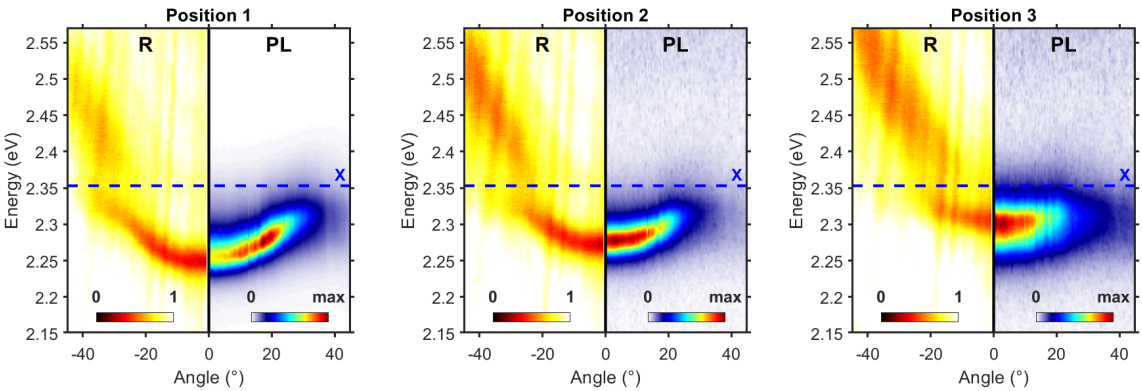

Figure 4.2: Angle-resolved reflectivity and photoluminescence results on three different positions of the microcavity and hence on three different detunings: a) Position 1, b) Position 2 and c) Position 3. The left panels, with negative angles, are the reflectivity maps and the right panels, with positive angles, are the photoluminescence maps. The pseudo-colour maps are in linear scale. The blue dashed line is the uncoupled exciton energy.

Figure 4.2 shows the angle-resolved reflectivity and photoluminescence results on three different microcavity positions and hence for three different detunings. The left panels, with negative angles, are the reflectivity maps and the right panels, with positive angles, are the photoluminescence maps. In the reflectivity maps, two different disper-

sion curves can be observed under and above the excitonic energy represented as the blue dashed line. At large angles, the lower dispersion is not really apparent as is the upper dispersion profile at small angles. An anti-crossing of the dispersion curves, signature of the strong coupling regime, can be distinguished. For the photoluminescence maps, only the dispersion curve below the excitonic energy is visible. One can notice a small vertical shift between the reflectivity and the photoluminescence lower dispersion profiles. This is due to a little variation in position of the white light beam spot and the pulsed laser spot. The dispersions will be later collected by taking vertical slices of the reflectivity and photoluminescence maps. This process, as well as the fitting of the dispersions, will be described in the next section.

4 Fitting of the polaritonic dispersions

4.1 Collection of the experimental dispersions

Slices of the reflectivity maps were taken at each angle as shown in figures 4.3 a), b), and c) to collect the dispersions of the three positions discussed previously. Each slice was fitted with a double-Lorentzian function. The energies of the Lorentzian functions centres were reported in energy/angle diagrams shown in figures 4.3 d), e) and f). With this technique, the lower and upper dispersions of the reflectivity are discernible, and a clear anticrossing can be observed, indicating the strong coupling regime. Similarly, the linewidths of the lower dispersions were collected by fitting with a single Lorentzian the photoluminescence spectra at each angle of the photoluminescence maps (see figure 4.4 a) b) and c)). The linewidths of the Lorentzian were then reported in Linewidth/angle diagrams (see figure 4.4 d) e) and f)).

4.2 Fitting of the experimental dispersions

In the following, the fitting process of the experimental data with the two-level model will be explained. The excitonic energy, E_X, is fixed at 2.355 eV and the effective refractive index, n_{eff}, is fixed at 1.75 from respectively the MAPB absorption spectra and the design of the microcavity in Chapter 3. The coupling strength g, the detuning δ, the excitonic and photonic linewidth, γ_X and γ_{ph}, are let as free parameters. One could directly fit the energy dispersions collected from the reflectivity maps (see figure 4.3) and find a good agreement between the experiment and the theoretical polaritonic dispersions. However, a good agreement can be found for an infinite number of sets of values of g, γ_X and γ_{ph}, as long as the fitted Rabi splitting $\hbar\Omega = \sqrt{4g^2 - (\gamma_{ph} - \gamma_X)^2}$ satisfies the experimental Rabi splitting. Indeed, a change of the set g, γ_X and γ_{ph} for which the Rabi splitting is constant only induces an insignificant change of the polaritonic dispersions around the anticrossing point. For this reason, the experimental reflectivity dips obtained with the spectrophotometer in part 4.1 could be fitted with γ_X and γ_{ph} set at zero. On the other

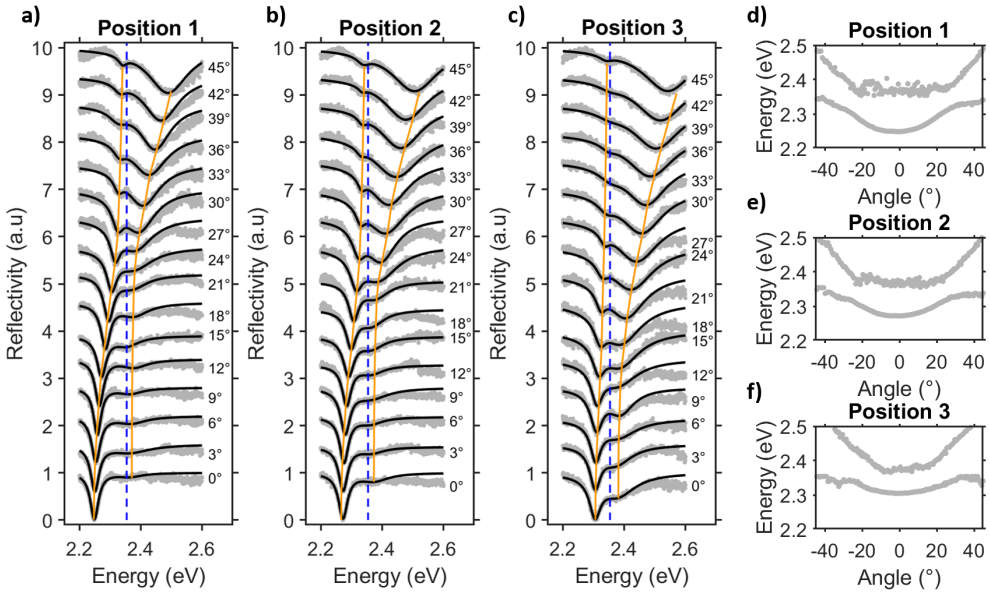

Figure 4.3: Slices of the reflectivity maps at different angles a) for the position 1, b) position 2 and c) position 3. Each reflectivity spectrum is fitted with a double Lorentzian function. The grey dotted lines correspond to the experimental slices and the solid black lines to the double Lorentzian fit. The yellow lines are guides for the eyes to follow the dispersion of the dips and the blue dashed line represents the excitonic energy. The energies of the Lorentzian functions centres are collected in energy/angle diagrams d) for the position 1, e) position 2 and f) position 3.

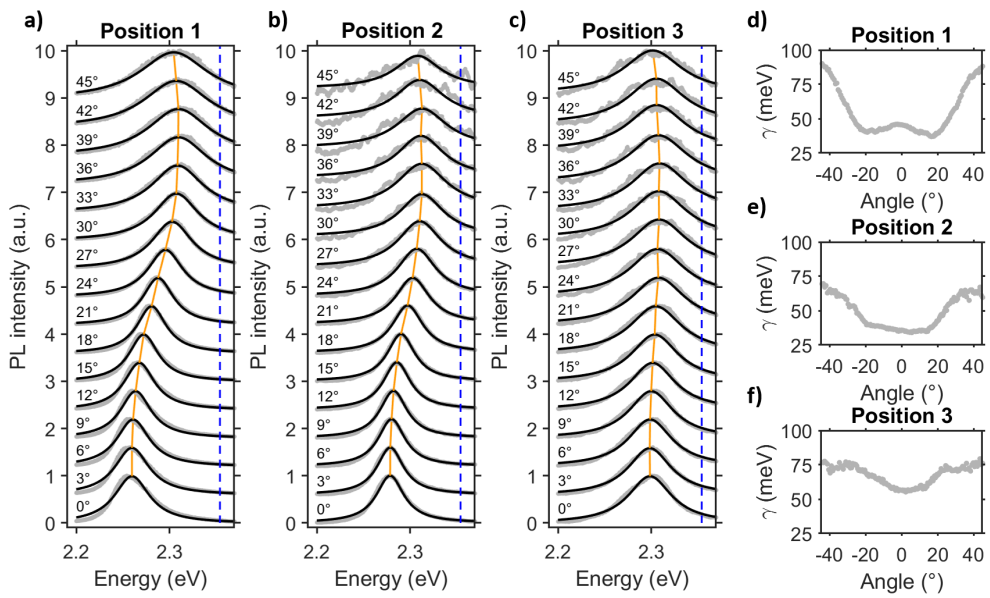

Figure 4.4: Slices of the photoluminescence maps at different angles a) for the position 1, b) position 2 and c) position 3. Each photoluminescence spectrum is normalized and fitted with a single Lorentzian function. The grey dotted lines correspond to the experimental slices and the solid black lines to the single Lorentzian fit. The yellow lines are guides for the eyes to follow the dispersion of the PL spectra and the blue dashed line represents the excitonic energy. The linewidths of the Lorentzian are collected in linewidth/angle diagrams d) for the position 1, e) position 2 and f) position 3.

hand, the linewidths γ_X and γ_{ph} are significant regarding the polariton linewidths since $\gamma_{LPB,UPB} = |\alpha_{LPB,UPB}|^2\gamma_{ph} + |\beta_{UPB,LPB}|^2\gamma_X$ (see eq 1.32 in Chapter 1), with $|\alpha_{LPB,UPB}|^2$ and $\beta_{UPB,LPB}|^2$ the photonic and excitonic weights of the polaritons.

For these reasons, the fitting of the angle-resolved reflectivity and photoluminescence dispersions will be done in three steps. The first step consists in fitting the dispersions collected from the reflectivity spectra (see figure 4.3) with the coupling strength g and the detuning δ as free parameters and the linewidths γ_X and γ_{ph} set as zero. The second step is the fitting of the linewidth obtained from the photoluminescence maps (see figure 4.4) with the theoretical lower polariton linewidth. The theoretical linewidth corresponds to the imaginary part of the eigenvalue of the two-level systems (see eq 1.30 in Chapter 1). The relation can be written as such: $\gamma_{LPB} = |X|^2\gamma_X + |C|^2\gamma_{ph}$ with $|X|^2$ and $|C|^2$ the lower polariton excitonic and photonic weights which depend on g, δ, E_X, n_{eff}, γ_X and γ_{ph}. In this fit, the linewidths γ_X and γ_{ph} are let as free parameters and the parameters g, and δ are set to the values found in the first step. The final step is to fit the dispersion from the reflectivity maps with g and δ as free parameters but this time with the linewidths set to the values found in the second fit. As a result, good agreements were met between the two-level model and simultaneously the experimental dispersion obtained from the reflectivity maps and the experimental linewidths from the photoluminescence maps.

Figure 4.5 shows the fitting results for the three positions presented previously. The figures in the left column correspond to the experimental dispersions collected from the reflectivity maps fitted with the polaritonic dispersions. The central figures are the experimental linewidths along with the theoretical lower polariton linewidth $\gamma_{LPB} = |X|^2\gamma_X + |C|^2\gamma_{ph}$ using the parameters obtained with the final fit. In this case, the linewidths are plotted against the difference between the excitonic energy and the lower polariton energy. The figures on the right correspond to the photonic and excitonic weights, $|X|^2$ and $|C|^2$, as a function of the angle.

4.3 Discussion on the obtained parameters

From the fit of the three studied positions, and of other positions not shown in this chapter, detunings were found ranging from -107.3 meV to 20.4 meV. The parameters, g, γ_{ph} and γ_X are reported as a function of the detunings in figures 4.6 a) and b). From these values, one can deduce the Rabi splitting $\hbar\Omega = \sqrt{4g^2 - (\gamma_{ph} - \gamma_X)^2}$ and the cavity quality factor $Q = E_{ph}/\gamma_{ph}$ with E_{ph} the photonic mode energy at normal incidence. The Rabi splittings and the quality factors as a function of the detunings are reported in figure 4.6 c) and d).

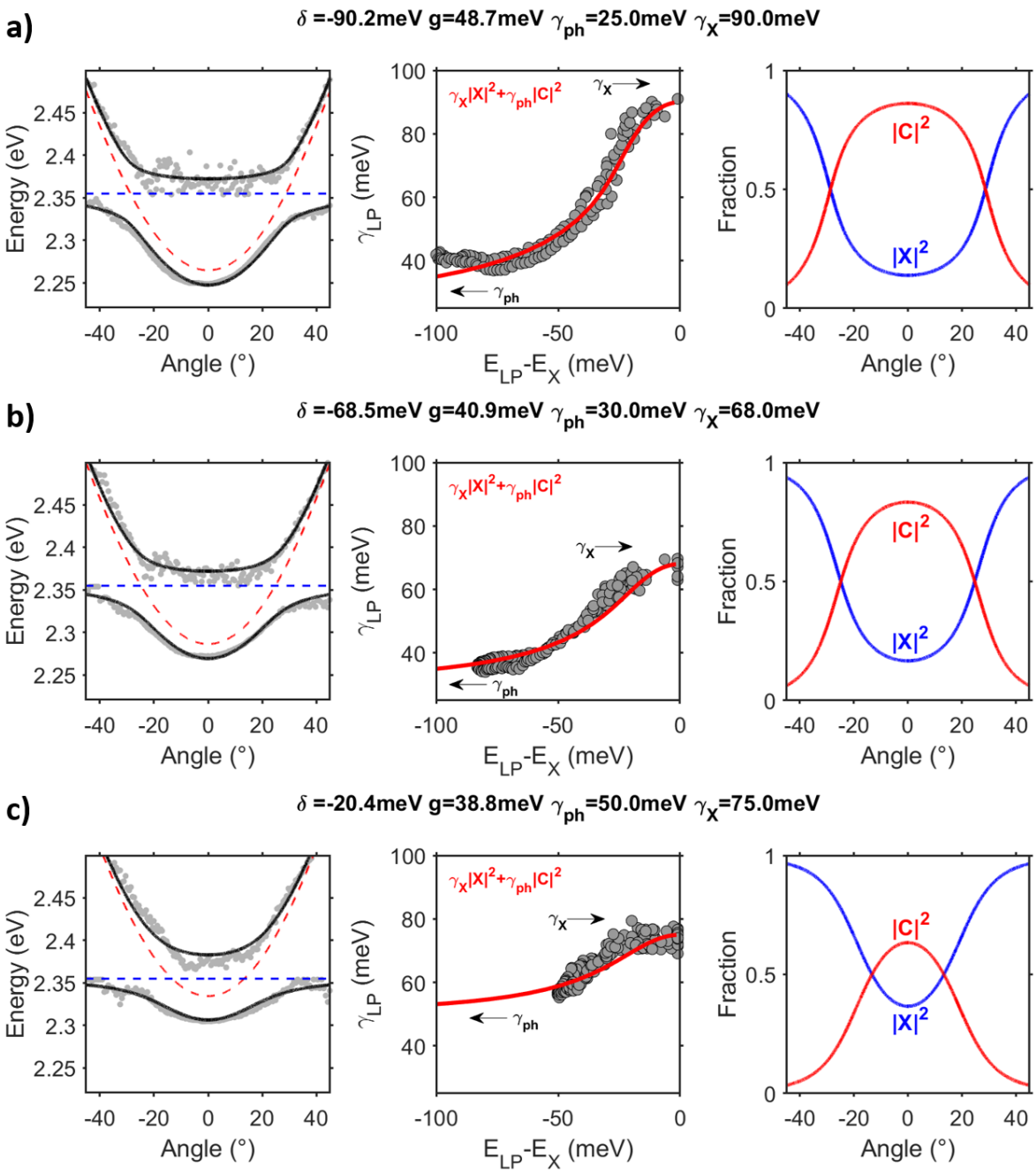

Figure 4.5: Fitting of the angle-resolved reflectivity and photoluminescence maps with the polaritonic dispersion a) for the position 1, b) position 2 and c) position 3. The parameters found from the fit are indicated on top of each subfigure. The figures in the left column correspond to the fitting of the experimental dispersions collected from the reflectivity maps with the polaritonic dispersions. The grey dotted lines are the experimental data, and the solid black lines are the lower and upper polariton dispersions from the two-level model. The blue and red dashed lines are the dispersions of the uncoupled exciton and photonic mode, respectively. The central figures correspond to the lower polariton linewidth collected from the photoluminescence maps along with the theoretical lower polariton linewidth using the final parameters. The linewidths are plotted against the difference between the excitonic energy and the lower polariton energy. The figures on the right are the photonic (in red) and excitonic (in blue) weights of the lower polariton as a function of the angle.

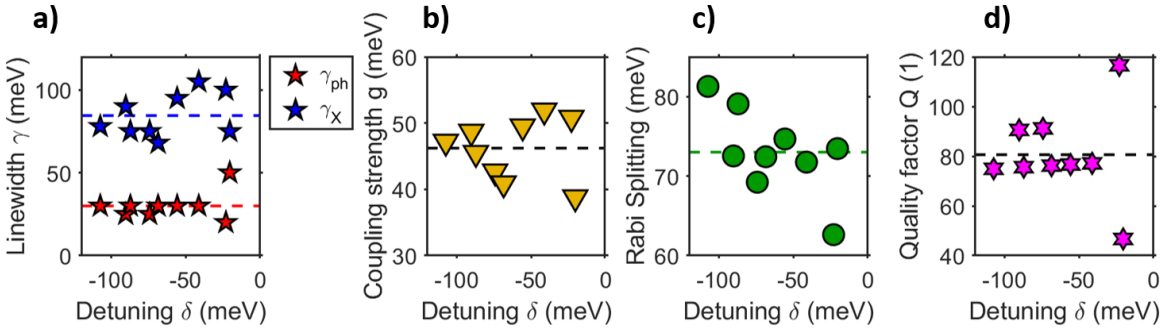

Figure 4.6: Fitting parameters found from the fit of the angle-resolved reflectivity and photoluminescence maps. a) Excitonic and photonic linewidth, γ_X and γ_{ph}. b) Coupling strength, g. c) Rabi splitting, $\hbar\Omega$. d) Quality factors, Q.

The values of the excitonic linewidths, γ_X range from 68 meV to 105 meV which is in agreement with the order of magnitude of the excitonic linewidths measured from the MAPB absorption and photoluminescence spectra of respectively 78 meV and 96 meV in Chapter 3. The average value of the excitonic linewidth is 84.6 meV. The values of the excitonic linewidths, γ_X, are comparable to those found in the literature from photoluminescence spectra with values from 88 meV to 120 meV [125, 143, 235–237]. The discrepancy of excitonic linewidths with respect to the probed position could be explained by the inhomogeneous distribution of the defects in the MAPB thin film.

The photonic linewidths range from 20 meV to 50 meV. The different values can be explained by a non-homogeneous distribution of defects along the microcavity. The linewidths are as sharp as the roughness is low. The photonic linewidths give a quality factor ranging from 46 to 116. The average value of the quality factor is 81, which is not far from the simulated passive microcavity quality factor of 113 given in Chapter 3. This result indicates that the quality factor is principally limited by the losses induced by the silver mirror rather than the defects and the roughness.

The coupling strength g ranges from 38.8 meV to 51.9 meV, which leads to a Rabi splitting ranging from 63 to 81 meV with an average value of 73 meV. These large Rabi Splittings are in the same order of magnitude as those of systems containing large band-gap materials such as GaN and ZnO [50, 238–240].

4.4 Final results on the ARR and ARPL maps

From the results of the dispersion fits, we have demonstrated the strong coupling regime in the 3λ/2 MAPB-based microcavity. Figure 4.7 shows the same angle-resolved reflectivity and photoluminescence maps previously presented along with the theoretical polaritonic dispersions. The two dispersions observed in each reflectivity map are the lower and upper polariton dispersions, and the dispersion observed in each photoluminescence map is the emission from the lower polariton.

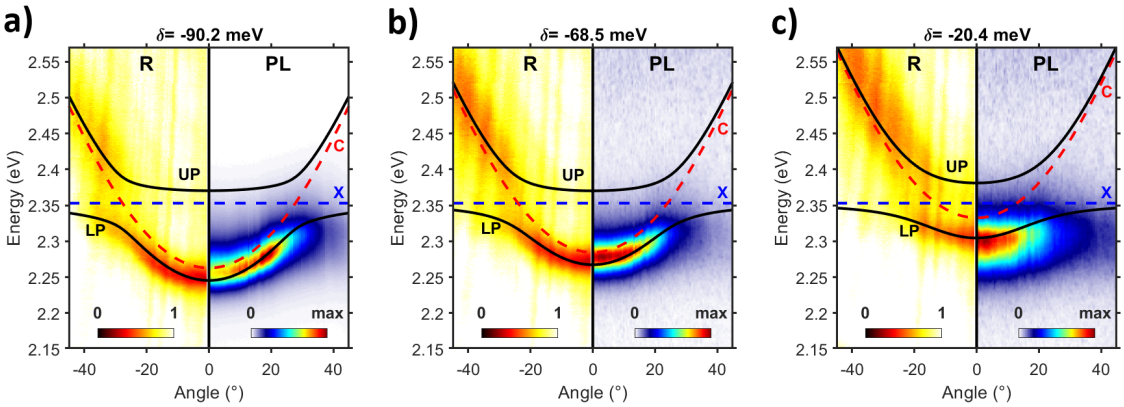

Figure 4.7: Angle-resolved reflectivity and photoluminescence results from three different positions of the microcavity and therefore from three different detunings: a) -90.2 meV, b) -68.5 meV and c) -20.4 meV. The left panels, with negative angles, are the reflectivity maps and the right panels, with positive angles, are the photoluminescence maps. The pseudo-colour maps are in linear scale. The two solid black lines are the lower and upper polaritonic dispersions from the two-level model fitted to the experimental data. The blue and red dashed lines are the dispersions of the uncoupled exciton and photonic mode, respectively.

As pointed out before, the lower and upper polariton dispersions in the reflectivity maps are not well defined respectively at large and small angles. The reason for the lack of discernibility of the polaritonic dispersions in these regions can be explained as follows: since the intensities of the polaritons dips are proportional to the photonic weights [241], the polaritons exhibit weak dips in their most excitonic parts at large and low angle regions for respectively the lower and upper polaritons (see for example the lower polariton excitonic weights in figure 4.5). Oppositely, the lower and upper polaritons show strong dips in their most photonic areas, respectively at small and large angles. At resonance, the lower and upper polaritons exhibit dips of the same intensity. Due to the lack of contrast, the polariton dispersion curves can not be well distinguished in the pseudo-colour maps (see figure 4.7) but can however be observed in vertical slices (see figure 4.3).

The photoluminescence of the upper polariton is not observed from the 3λ/2 MAPB-based microcavity as for microcavities containing large bandgap material in the strong coupling regime at room temperature [50, 238–240]. Besides, the inflexion point of the lower polariton emission, one of the signatures of the strong coupling, cannot be observed in the photoluminescence maps. The reasons for this situation were discussed in Chapter 1. First, the thermal occupation of the upper polariton branch is low due to the large Rabi splitting compared to the thermal energy at room temperature. Second, the relaxation pathways go directly from the highly occupied excitonic reservoir to the bottom of the lower polariton branch. In the PL maps, another characteristic of the polariton emission could also be observed, namely the bottleneck effect, which will be discussed in the next section.

5 Bottleneck effect of the lower polariton photoluminescence

In the two positions with the lowest detunings (in absolute value) presented so far in this chapter (see figure 4.7 b) and c)), there is no bottleneck effect since the maximum of the PL intensity lies at the normal incidence. However, for the largest detuning (see figures 4.7 a)) there is an accumulation of the PL signal at angles between 10° and 25°. Figures 4.8 a) to e) show the angle-resolved photoluminescence pseudo-colour maps for five different detunings, two of which were presented previously (those in figure 4.7 a) and b)). For detunings lower than -74 meV (d) and e), the PL signal accumulates at normal incidence, for the detunings higher (a),b) and c)) the PL signal accumulates again at angles between 10° and 25°. The accumulation of the photoluminescence signal at non-zero angles suggests the bottleneck effect.

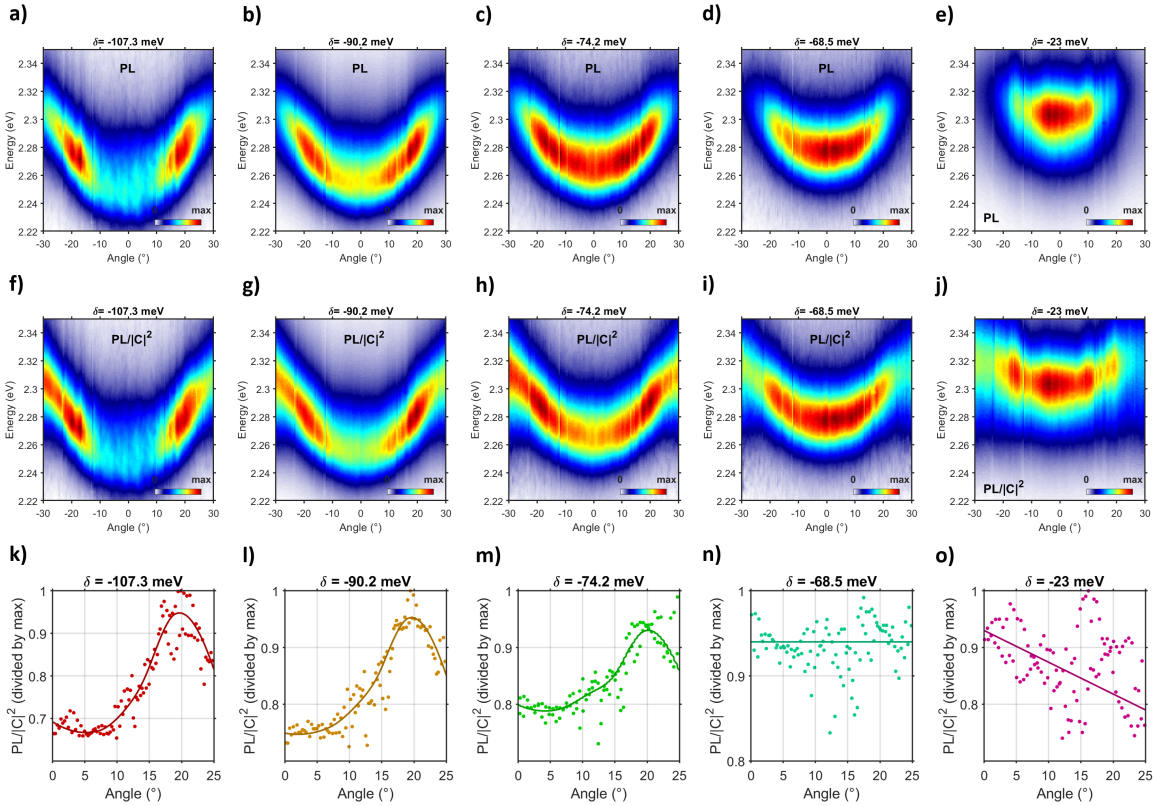

Figure 4.8: Bottleneck effect on the 3λ/2 MAPB-based microcavity. a) to e) Angle-resolved photoluminescence pseudo-colour maps for five different detunings: a) -107.3 meV b) -90.2 meV c) -74.2 meV d) -68.5 meV e) -23 meV. f) to j) Angle-resolved photoluminescence divided at each angle by the lower polariton photonic weight of the same five detunings. The polariton population is proportional to the photoluminescence divided by the photonic weight. The pseudo-colour maps are in linear scale. k) to o) Integrated intensity at each angles (normalized by max) of the photoluminescence divided by the photonic weight for the same five detunings. The points are the experimental data and the solid lines are guides for the eyes.

It is necessary to study the polariton population along the lower polariton branch to determine whether this accumulation is indeed due to the bottleneck effect. The polariton population can be recovered by dividing the photoluminescence signal at each angle by the corresponding lower polariton photonic weight $|C|^2$. The figures 4.8 f) to j) show the pseudo-colour maps of the photoluminescence divided by the photonic weight at each angle for the same detunings presented above. One can observe that for detunings lower than -74 meV, the population maxima are at normal incidence, and for larger detunings, the population maxima lie at around 20°. The figures 4.8 k) to o) show the integrated intensity at each angle (normalized by max) of the photoluminescence divided by the photonic weight of the same five detunings and confirm the accumulation of the PL signal at 20° for the detunings higher than 74 meV. To summarize, the Bottleneck effect occurred in the 3λ/2 MAPB-based microcavity when the detuning is larger than 74 meV.

6 Discussion on the MAPB exciton stability at room temperature

In the literature, the stability of the MAPB excitons at room temperature is still under discussion as values ranging from 15 to 110 meV can be found for their binding energies [75, 76, 78–88]. As a reminder, an exciton is stable at room temperature if its binding energy is higher than 25 meV, the thermal energy. In the case of the chloride-based perovskites, the values of the exciton binding energies were found higher than 25 meV, between 41 and 75 meV [69, 74–77]. Consequently, the exciton-polaritons could be obtained from micro/nanowires, nano/microplates-based $CsPbCl_3$ [48, 222] and even polaritonic lasing [48]. On the other hand, the iodine-based perovskites exhibit weak excitons with binding energies around 16 meV at low temperarure (10K) and close to zero at room temperature [73]. The strong coupling could be obtained with iodine-based 3D perovskites but only with nanowires in which the lateral confinements strengthen the exciton [222]. In a MAPI-based microcavity similar to the 3λ/2 MAPB-based microcavity of this PhD, only the weak coupling could be observed [242]. Therefore, the strong coupling regime in the 3λ/2 MAPB-based microcavity suggests that the excitons in the 3D bromide perovskites are stable at room temperature.

Regarding the issue of the exciton stability, the photoluminescence was further studied. Indeed a weak signal at energies higher than the exciton energy occurs in the photoluminescence maps. This signal is around ten times weaker than the lower polariton photoluminescence. Figure 4.9 shows angle-resolved photoluminescence maps for the detuning studied in this chapter with an enhancement by a factor of around 10 at negative angles and energies higher than 2.37 eV. One can then observe that a weak signal appears above the excitonic energies at angles corresponding to the angles of the cavity mode. The angle of the signal follows the cavity modes for the different detunings. As

this signal is not constant with angles, one can rule out the possibility of an emission of the uncoupled excitons. This signal could come from free carriers weakly coupled to the microcavity with a less efficient radiative relaxation. This assumption would be coherent with recent studies [87, 243] suggesting that the free carriers and excitons coexist at room temperature in bromide perovskites.

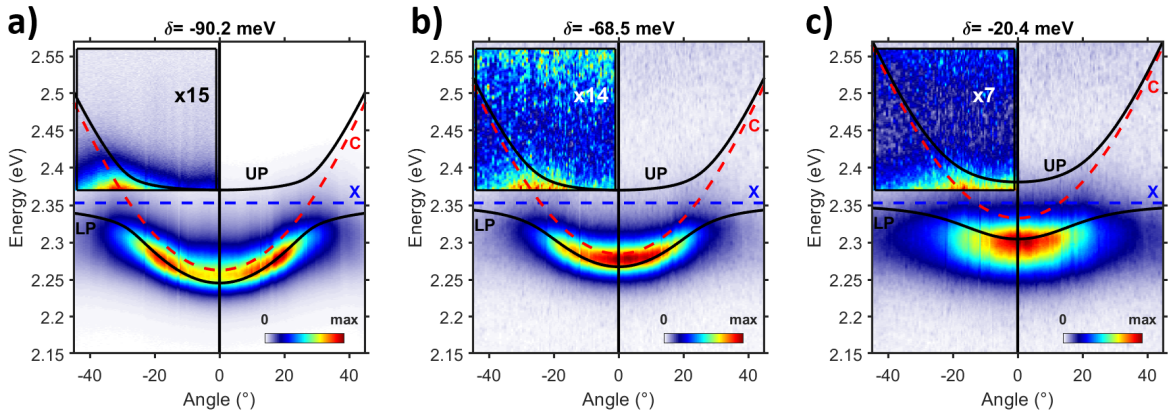

Figure 4.9: Enhancement at negative angles of the angle-resolved photoluminescence for energies higher than 2.37 eV for the detunings: a) -90.2 meV, b) -68.5 meV and c) -20.4 meV. The pseudo-colour maps are in linear scale. The enhancement factors are a) 15, b) 14 and c) 7. The two solid black lines are the lower and upper polaritonic dispersions from the two-level model fitted to the experimental data. The blue and red dashed lines are the dispersions of the uncoupled exciton and photonic mode, respectively.

7 Simulations of the results

This section presents the simulation by the matrix transfer method of the reflectivity spectra obtained with the spectrophotometer and the angle-resolved reflectivity and photoluminescence maps obtained with the Fourier set-up. The Bragg mirror parameters, the dispersive refractive index of the MAPB and silver layers used for the simulation are the ones presented in Chapter 3. The influence of the roughness of the MAPB and PMMA layers will be first studied which will give a better idea of the impact of the roughness on the two different kinds of measurements. Finally, the influence of the MAPB refractive index will be studied.

7.1 Influence of the roughness on the simulated reflectivity and photoluminescence

7.1.1 Simulation of reflectivity spectra obtained with the spectrophotometer

The reflectivity spectra of the 3λ/2 MAPB-based microcavity obtained with the Perkin Elmer spectrophotometer have been simulated using the matrix transfer method and with four sets of parameters reported in table 4.1. FSigure 4.10 presents the simulation results.

	MAPB thickness (nm)	PMMA thickness (nm)	Ag thickness (nm)	MAPB roughness (nm)	PMMA roughness (nm)
Simulation 1	110	344	30	0	0
Simulation 2	110	344	30	15	0
Simulation 3	110	344	30	15	25
Simulation 4	110	348	34	15	25

Table 4.1: Parameters used for the simulations of the reflectivity spectra obtained with the spectrophotometer using the extracted refractive index [231]

The first simulation presented in figure 4.10 a) has been performed with a MAPB thickness of 110 nm, a PMMA thickness of 344 nm and a silver thickness of 30 nm. The thicknesses used are close to the thicknesses measured with the profilometry in Chapter 3. The roughness has not been taken into account in this simulation. As a result, the two reflectivity dips (represented by green arrows in figure 4.10), corresponding to the lower and upper polariton dips are much sharper and deeper than the experimental dips. As already discussed at the beginning of this chapter, the experimental reflectivity spectra were collected over a large rough surface of 1mm x 1mm with a certain distribution of detunings.

The second simulation shown in figure 4.10 b) was obtained with the same parameters as the first simulation. However, the roughness of 15 nm of the MAPB layer, similar to the one measured in Chapter 3 (see part 2.4), was taken into account by averaging simulated reflectivity spectra with thicknesses of MAPB ranging from 103 to 197 nm. In this case,

the simulated dips are shallower and less sharp than those of the first simulation, but the dips remain deeper and sharper than the experimental ones. By adding the roughness of 25 nm of the PMMA layers, similar to the one measured in Chapter 3 (see part 3.3), in the third simulation shown in figure 4.10 c), the simulated reflectivity dips get as broad as the experimental reflectivity dips but remain deeper. Finally, the final simulation is shown in figure 4.10 d). The thickness of the silver layer was raised to 34 nm. The PMMA thickness had to be changed to 348 nm to compensate for the change of detuning. The last simulation reproduces well the experimental lower and upper polariton reflectivity dips of the experimental reflectivity spectrum obtained with the spectrophotometer at 8° of incidence.

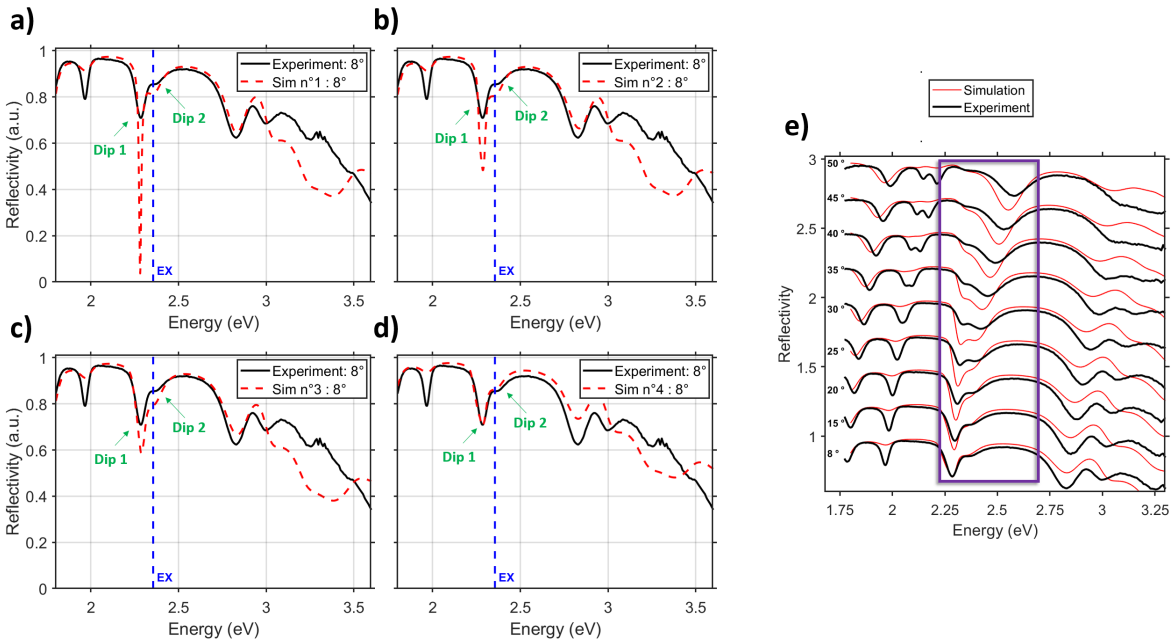

Figure 4.10: Simulations by the transfer matrix method of the reflectivity spectrum at 8° of incidence obtained with the spectrophotometer. The values of the parameters used for the simulations by the matrix transfer method are reported in table 4.1. a) Simulation with no roughness , b) Simulation with a MAPB roughness of 15 nm. c) Simulation with a MAPB roughness of 15 nm and a PMMA roughness of 25 nm. d) Same simulation as in c) with a silver thickness of 34 nm. e) Simulation of the reflectivity spectra at the different incidence angles using the simulation parameters of d).

These simulations have shown that the roughness of the MAPB and PMMA layers have to be taken into account. It further confirms that the reflectivity spectrum obtain from a large 1mm x 1mm area with the spectrophotometer is the average of reflectivity spectra of a large number of detunings as it was stated at the beginning of this chapter.

Finally, figure 4.10 e) shows the simulation for the other angles of incidence using the same parameters of figure 4.10 d). The range of energies of interest is indicated by the purple rectangle. From this figure, one can see that the simulation only works at low angles as the simulated reflectivity dips gets deeper than the experimental dips with the angle

increasing. Moreover, a shift in energy between the experimental and simulated upper polariton reflectivity dips appears at large angles. It will be shown in the following that this deviation comes from the dispersive MAPB refractive index extracted from the literature [231] which may not describe perfectly the MAPB thin-film refractive index.

7.1.2 Simulation of the angle-resolved reflectivity and photoluminescence maps

The angle-resolved reflectivity and photoluminescence maps of the three detunings studied in this chapter are simulated with the transfer matrix method. The photoluminescence is compared to the simulated absorption, $A_{sim} = 1 - R_{sim} - T_{sim}$, as the matrix transfer method can only simulate the reflectance and the transmittance. The simulations were performed with the MAPB refractive index extracted from [231] without or with taking into account the MAPB roughness.

Simulation without taking into account the layers roughness

Figure 4.11 shows the simulations using the MAPB refractive index extracted from [231] of the angle-resolved reflectivity maps for the three detunings studied in this Chapter. The left panels correspond to the experimental reflectivity maps and the right panels to the simulated reflectivity maps. The parameters used for the three detunings are reported in table 4.2. In all three cases, the roughness has not been taken into account. From these results, one can see that the simulated lower polariton branches are sharper than the experimental ones. Moreover, the colour of the simulated dispersion curves is darker than the experimental dispersions, which means that the reflectivity of the polariton branches is lower in the simulation than in the experiment. This scenario is similar to the cases in figures 4.10 a), b), and c).

Detuning (meV)	MAPB thickness (nm)	Ref: PMMA thickness (nm)	Abs: PMMA thickness (nm)	Ag thickness (nm)	MAPB roughness (nm)	PMMA roughness (nm)
-90.2	100	364	361	28	0	0
-68.5	100	355.5	354.5	28	0	0
-20.4	100	342	347	34.5	0	0

Table 4.2: Parameters used for the simulations of the angle-resolved reflectivity and photoluminescence maps using the extracted refractive index [231] and without taking into account the layers roughnesses

Figure 4.12 shows the angle-resolved photoluminescence maps compared with the simulated absorption maps of the same three detunings. The left panels correspond to the experimental photoluminescence maps and the right panels to the simulated absorption maps. The experimental photoluminescence and the simulated absorption are normalized for comparison purposes. The same parameters as for the reflectivity maps were used except for the PMMA thicknesses, which were slightly changed to compensate

for the small shift between the experimental reflectivity and photoluminescence detunings (see table 4.2). From the result, it is clear that the simulated absorption linewidth is much sharper than the experimental photoluminescence linewidth. Note that, the upper polariton branch is visible in the simulated absorption maps and not in the photoluminescence maps. Indeed, these two phenomena are different as the photoluminescence involves the absorption, the relaxation and the emission of the polaritons.

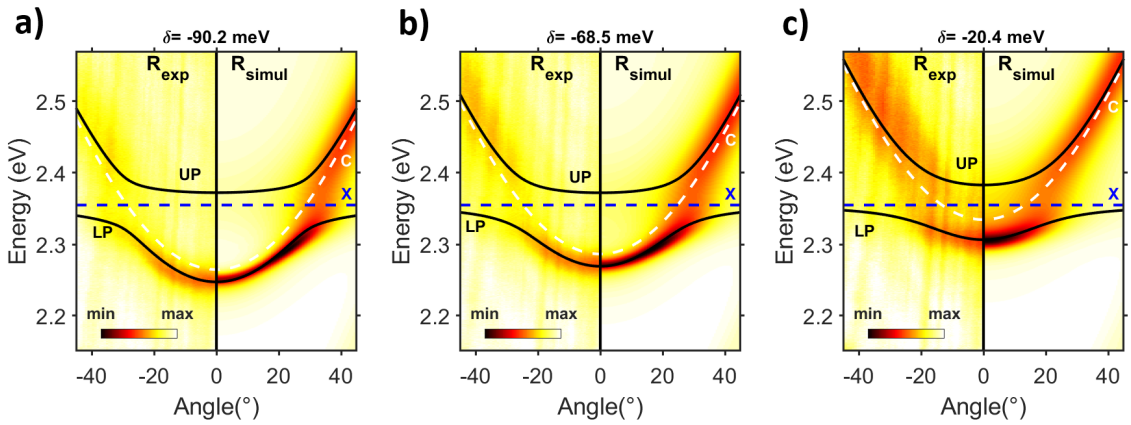

Figure 4.11: Simulation of the reflectivity maps with the MAPB refractive index extracted from [231] and without taking into account the layers roughness of the detunings: -90.2 meV a), -68.5 meV b) and -20.4 meV c). The left panels correspond to the experimental reflectivity maps and the right panels to the simulated reflectivity maps. The pseudo-colour maps are in linear scale. The two solid black lines are the lower and upper polaritonic dispersions from the two-level model fitted to the experimental data. The blue and white dashed lines are the dispersions of the uncoupled exciton and photonic mode, respectively. The values of the parameters used for the simulations by the matrix transfer method are reported in table 4.2.

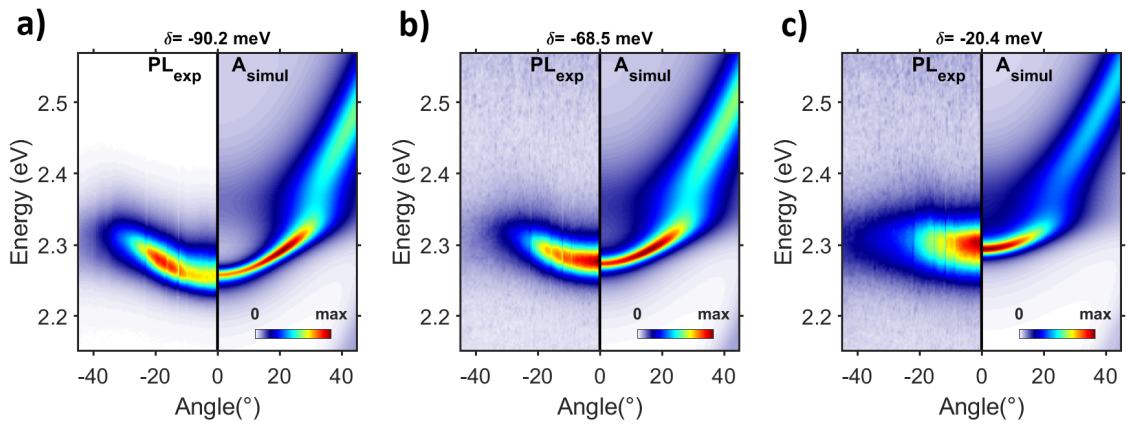

Figure 4.12: Comparison of the photoluminescence maps with the simulated absorption maps obtained with the MAPB refractive index extracted from [231] and without taking into account the layers roughness for the detunings: -90.2 meV a), -68.5 meV b) and -20.4 meV c). The left panels correspond to the experimental photoluminescence maps and the right panels to the simulated absorption maps. The pseudo-colour maps are in linear scale. The values of the parameters used for the simulations by the matrix transfer method are reported in table 4.2.

In summary, the experimental polariton linewidths are broader than the simulated polariton linewidths, and the simulated reflectivity dips are deeper than the experimental reflectivity dips. The broadening and the dip reduction of the experimental polaritons probably come from the roughness of the layers. As a consequence, the roughness of the layers will then be taken into account in the following section.

Simulation considering the roughness

The angle-resolved reflectivity and photoluminescence maps were then simulated by using the same parameters as in the previous section 4.7.2.1 but taking into account the roughness of the layers. Good results were obtained by considering the roughness of MAPB as 12 nm for the detunings -90.2 meV (see figure 4.13 a)) and -68.5 meV (see figure 4.13 b)), and 20 nm for the detuning -20.4 meV (see figure 4.13 c)) and the roughness of the PMMA layer at zero. The values of the parameters used for the simulation are reported in table 4.3. Unlike the case of the reflectivity spectra with the spectrophotometer, only the MAPB roughness was taken into account. This result is consistent with the spot size of the pump laser and the white beam of the Fourier spectroscopy set-up. Indeed, the area probed with the spectrophotometer was of 1mm x1mm which is much larger than the characteristic size of the MAPB roughness and the MAPB/PMMA roughness. For the Fourier spectroscopy set-up, the spot sizes are smaller than the characteristic size of the MAPB/PMMA roughness and in the order of magnitude of the MAPB layer roughness. As a consequence, it is coherent to consider only the MAPB roughness in the case of the angle-resolved reflectivity and photoluminescence maps obtained with the Fourier spectroscopy set-up.

Detuning (meV)	MAPB thickness (nm)	Ref: PMMA thickness (nm)	Abs: PMMA thickness (nm)	Ag thickness (nm)	MAPB roughness (nm)	PMMA roughness (nm)
-90.2	100	364	361	28	12	0
-68.5	100	355.5	354.5	28	12	0
-20.4	100	342	347	34.5	20	0

Table 4.3: Parameters used for the simulations of the angle-resolved reflectivity and photoluminescence maps using the extracted refractive index [231] and by taking into account the layers roughnesses

Figure 4.13 shows the simulation results for the reflectivity maps. For the case of the smallest detuning: -20.4 meV (see figure 4.13 c)), the simulation reproduces well the experiment. For the two other detunings, a good match between the simulation and the experiment maps occurs at low angles between 0° and 15°. At small angles, the simulated lower polariton reflectivity dispersions are as broad and as deep as the experimental lower polariton experimental dispersion. However, at larger angles, both the simulated lower and upper dispersions are deeper than the experimental polariton dispersions. Besides, an unusual decrease in reflectivity below the lower polariton inflexion point can be

noticed in the simulations of the same two detunings. This decrease can be observed as an increase of the simulated absorption below the lower polariton inflexion point in figure 4.14 a) and b). The photoluminescence is also not well reproduced by the absorption simulations (see figure 4.14) a) and b).

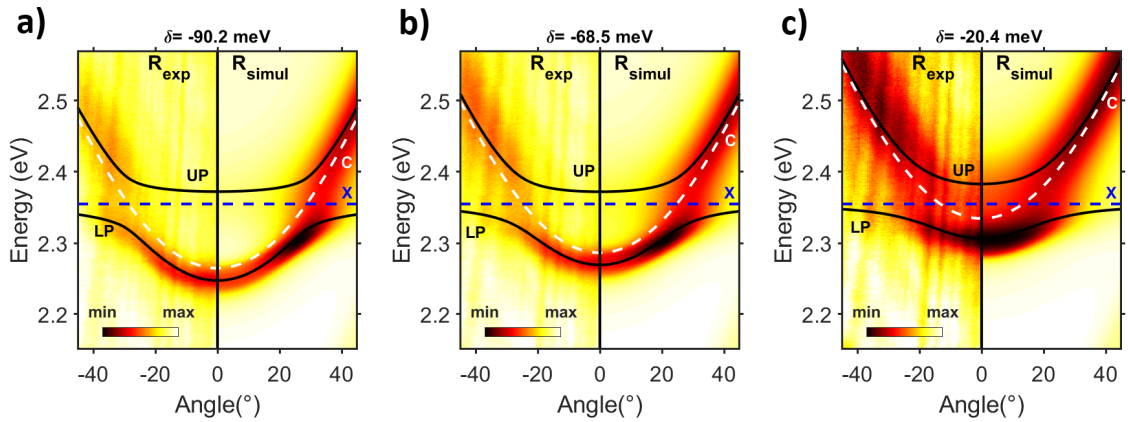

Figure 4.13: Simulation of the reflectivity maps with the MAPB refractive index extracted from [231] and by taking into account the MAPB roughness for the detunings: -90.2 meV a), -68.5 meV b) and -20.4 meV c). The left panels correspond to the experimental reflectivity maps and the right panels to the simulated reflectivity map. The pseudo-colour maps are in linear scale. The two solid black lines are the lower and upper polaritonic dispersions from the two-level model fitted to the experimental data. The blue and white dashed lines are the dispersions of the uncoupled exciton and photonic mode, respectively. The values of the parameters used for the simulations by the matrix transfer method are reported in table 4.3.

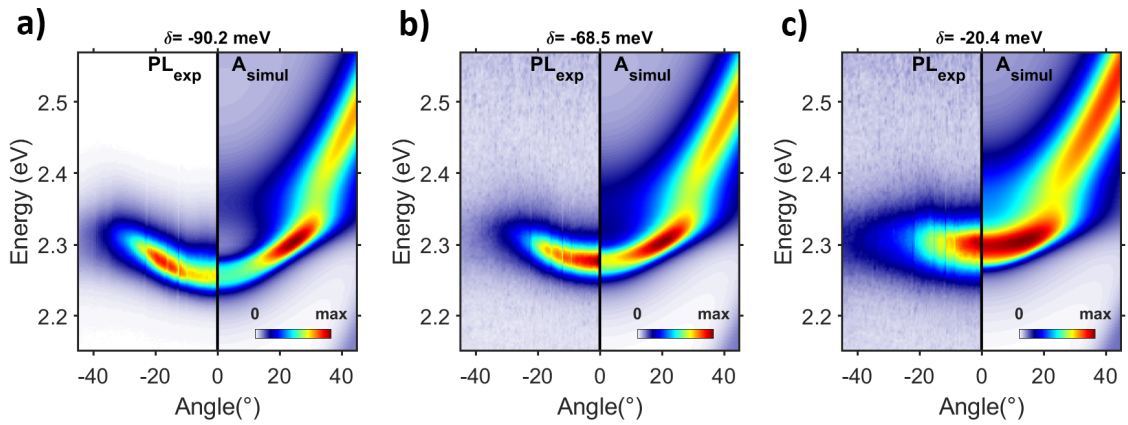

Figure 4.14: Comparison of the photoluminescence maps with the simulated absorption maps obtained with the MAPB refractive index extracted from [231] and by taking into account the MAPB roughness for the detunings: -90.2 meV a), -68.5 meV b) and -20.4 meV c). The left panels correspond to the experimental photoluminescence maps and the right panels to the simulated absorption maps. The pseudo-colour maps are in linear scale. The values of the parameters used for the simulations by the matrix transfer method are reported in table 4.3.

As with the simulations of the reflectivity spectra obtained with the spectrophotometer, when the reflectivity spectra are well simulated at low angles, the simulation does not work with large angles. Conversely, when the reflectivity is well simulated at large angles, the simulation does not work well at low angles. Therefore, with the set of parameters used so far, the experimental reflectivity and photoluminescence can not be well reproduced at the same time at low and high angles with the transfer matrix method. In fact, the problem is not angle related but related to the energy (wavelength). The mismatch between the simulated reflectivity in the case of the two large detunings (see 4.13 a) and b)) occurs when the polariton dispersions are at energies higher than 2.28 eV. In the case of the lowest detuning, the experimental reflectivity is well reproduced as the polariton dispersions are always above 2.28 eV. Therefore, the experimental reflectivity and photoluminescence can not be well simulated at the same time for energies lower and higher than 2.28 eV. The issue then comes from the energy-dependent parameters used in the simulation, which are the dispersive refractive indices of the MAPB layer and the silver layer.

In the following, we will consider that the problem only comes from the MAPB refractive index and not from the silver refractive index. Indeed, the extracted MAPB refractive index [231] was measured on a single crystal. It is known in the perovskite community that the optical properties of the same perovskite in the crystal form or the thin film form slightly differ. Therefore, the extracted MAPB refractive index may not describe well the refractive index of a MAPB thin film. One of the main problems with the extracted refractive index is that the extinction coefficient k is zero below the perovskite excitonic transition. However, because of the diffusion and defects, a constant absorption occurs below the excitonic transition in the MAPB thin-film absorption (see Chapter 3). The simulations performed so far could then not take into account this constant absorption at low energy. For these reasons, the influence of the MAPB refractive index on the simulations will be discussed in the following.

7.2 Influence of the MAPB refractive index

In this section, the influence of the MAPB refractive index on the simulation of the angle-resolved reflectivity and photoluminescence maps will be studied. First, the MAPB extinction coefficient will be replaced by the experimental extinction coefficient obtained from the absorption coefficient presented in Chapter 3. Then, a customized MAPB refractive index obtained with a modified Tauc-Lorentz model will be proposed. Finally, the customized refractive index will be used to fit the reflectivity spectra obtained with the spectrophotometer.

7.2.1 Simulation with an experimental extinction coefficient

The experimental extinction coefficient k can be obtained from the absorption coefficient α of the material with the following equation 4.1, where λ is the light wavelength :

$$k = \frac{\lambda\alpha}{4\pi}. \tag{4.1}$$

Figure 4.15 a) shows the experimental extinction coefficient obtained from the absorption coefficient presented in Chapter 3 and is compared in figure 4.15 b) with the extinction coefficient collected from the literature [231] noted as k_{lit}. Unlike the extinction coefficient extracted from the literature, the experimental extinction coefficient is different from zero at energies below the excitonic transition. Additionally, the experimental extinction coefficient is higher at each energy, but the excitonic transition is less pronounced.

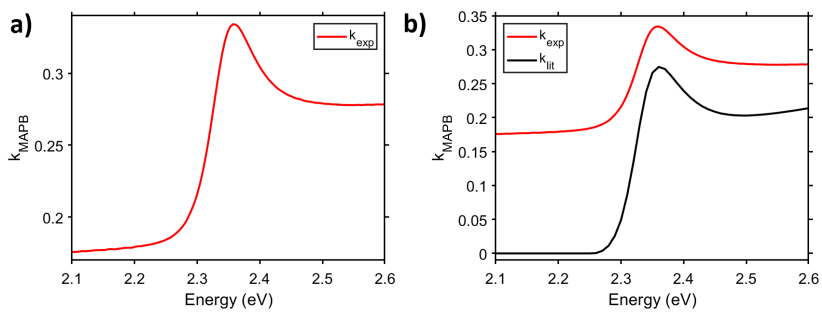

Figure 4.15: a) Experimental extinction coefficient obtained from the absorption coefficient discussed in Chapter 3. b) Comparison between the experimental extinction coefficient and the extinction coefficient collected from the literature [231]

Figures 4.16 and 4.17 show the simulation with the transfer matrix method of the experimental angle-resolved reflectivity and photoluminescence maps using the experimental MAPB extinction coefficient. The real part of the MAPB refractive index remains the one extracted from the literature [231]. The values of the parameters used for the simulation are reported in table 4.4. No roughness of the MAPB layer was needed which would mean that the experimental extinction coefficient already takes into account the MAPB roughness. This could be explained by the fact that the absorption measurements of the MAPB thin film were taken by the spectrophotometer on a large surface.

Detuning (meV)	MAPB thickness (nm)	Ref: PMMA thickness (nm)	Abs: PMMA thickness (nm)	Ag thickness (nm)	MAPB roughness (nm)	PMMA roughness (nm)
-90.2	100	365.5	361.5	30.5	0	0
-68.5	100	355	353	30.5	0	0
-20.4	100	340	344	33	0	0

Table 4.4: Parameters used for the simulations of the angle-resolved reflectivity and photoluminescence maps using the experimental extinction coefficient

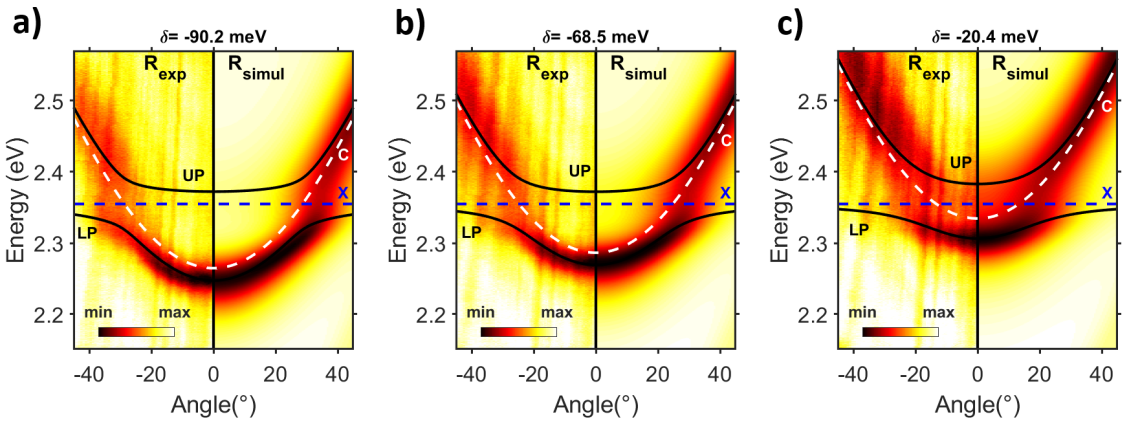

Figure 4.16: Simulation of the reflectivity maps by using the experimental extinction coefficient for the three detunings and without taking into account the layers roughness for the detunings: -90.2 meV a), -68.5 meV b) and -20.4 meV c). The left panels correspond to the experimental reflectivity maps and the right panels to the simulated reflectivity maps. The pseudo-colour maps are in linear scale. The two solid black lines are the lower and upper polaritonic dispersions from the two-level model fitted to the experimental data. The blue and white dashed lines are the dispersions of the uncoupled exciton and photonic mode, respectively. The values of the parameters used for the simulations by the matrix transfer method are reported in table 4.4.

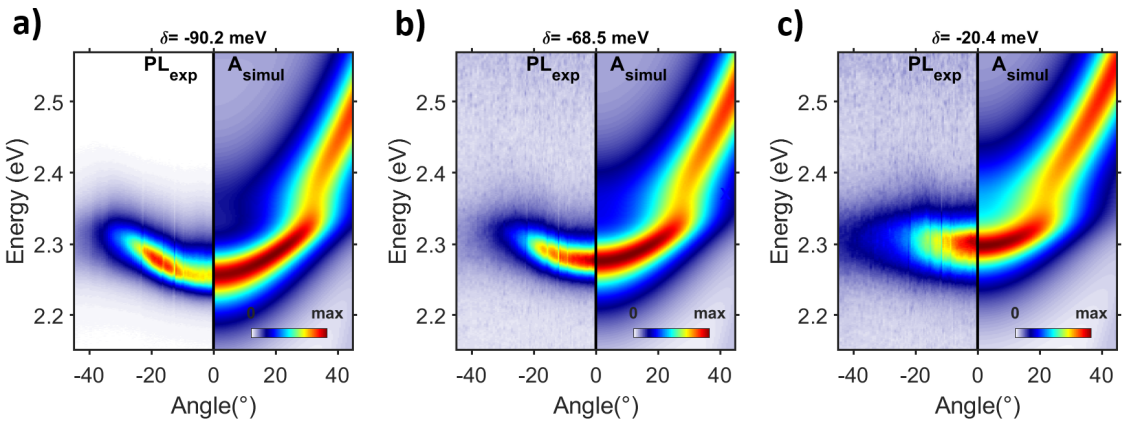

Figure 4.17: Comparison of the photoluminescence maps with the simulated absorption maps obtained by using the experimental extinction coefficient and without taking into account the layers roughness for the detunings: -90.2 meV a), -68.5 meV b) and -20.4 meV c). The left panels correspond to the experimental photoluminescence maps and the right panels to the simulated absorption maps. The pseudo-colour maps are in linear scale. The values of the parameters used for the simulations by the matrix transfer method are reported in table 4.4.

A good agreement is met between the experimental and simulated reflectivity maps regarding the intensity of the reflectivity dispersions. However, for the two large detunings of -90.2 meV (see figure 4.16 a)) and -68.5 meV (see figure 4.16 b)) the simulated lower polariton reflectivity is broader than the experimental lower polariton reflectivity. The difference in width can also be seen in the photoluminescence simulations (see figures 4.17 a) and b)). Moreover, the contrast between the lower and upper polariton branches at

the anticrossing point is decreased in the simulations due to the less prominent excitonic transition in the experimental extinction coefficient. For the lowest detuning of -20.4 meV (see figure 4.16 c)), a good agreement is met between the simulation and the experiment. Again, the problem of the simulations comes from the MAPB refractive index below the excitonic transition energy. Unlike the previous case where the absorption was zero under the excitonic transition, here the absorption is too strong at low energy. Indeed, the experimental extinction was obtained from an absorption measured on a large area and may not describe the extinction coefficient for smaller areas. In the following, a customized MAPB refractive index obtained with a slightly modified Tauc-Lorentz model will be proposed to simulate the angle-resolved absorption and photoluminescence maps better.

7.2.2 Simulation with a customized MAPB refractive index

The customized MAPB refractive index

For better simulations, the MAPB extinction coefficient needs to be a trade-off between the experimental extinction coefficient and the extinction coefficient extracted in the literature [231]. The extinction coefficient needs to be non-zero below the excitonic energy, the excitonic transition should be more pronounced than in the experiment and the extinction coefficient must be lower than the experimental extinction coefficient below and above the excitonic transition. For this reason, we propose in this PhD a simulated MAPB refractive index with a modified Tauc-Lorentz model. The Tauc-Lorentz model was discussed in Chapter 1 and is reminded in the following equation 4.2:

$$\begin{cases} \epsilon_2 = \sum \frac{A_j \gamma_j (E-E_G)^2}{(E^2-E_{0j}^2)^2+\gamma_j^2 E^2} \frac{1}{E} & (E > E_G), \\ \epsilon_2 = 0 \quad (E \leq E_G), \end{cases} \tag{4.2}$$

where $E_G(eV)$ is the semiconductor energy gap, $E_{0j}(eV)$, $\gamma_j(eV)$ and $A_j(eV)$ are respectively the position in energy, the linewidth and the Tauc-Lorentz coefficient of the j-th oscillator. The real part of the dielectric function, ϵ_1, can be retrieved by performing the Kramers-Krönig transformation of ϵ_2. Finally, the real and imaginary parts of the refractive index are obtained by using the equation 1.8 in Chapter 1. In our modified Tauc-Lorentz model, a constant permittivity $\epsilon_{defect} = \epsilon_{defect,1} + i\epsilon_{defect,2}$ is added to the Tauc-Lorentz permittivity $\epsilon = \epsilon_1 + i\epsilon_2$ to take into account the parasitic permittivity induced by the defects.

Figure 4.18 a) presents the proposed MAPB refractive index obtained with the modified Tauc-Lorentz model with two oscillators. The parameters used for the excitonic oscillator were: E_{01}=2.33 eV, Γ_1=65 meV, A_1=45 eV^2 and for the second oscillator: E_{02}=8 eV, Γ_2=87 meV, A_2=51 eV^2 . The other parameters were E_G =2.25 eV, $\epsilon_{defect,1}$ = 1.01 $F.m^{-1}$ and $\epsilon_{defect,2}$=0.55 $F.m^{-1}$. Figure 4.18 b) compares the real part of the proposed MAPB refrac-

tive index noted as n_{sim} and the real part of the refractive index extracted from [231]. The real part of the proposed refractive index is lower than the refractive index extracted from [231]. Figure 4.18 c) compares the extinction coefficients from the experiment, k_{exp}, the literature, k_{lit} and the modified Tauc-Lorentz model k_{sim}. The proposed extinction coefficient is non-zero below the excitonic transition, lower than the experimental extinction coefficient below and above the excitonic energy and with a more pronounced excitonic transition than obtained in the experiment. The desired requirements enunciated previously are met.

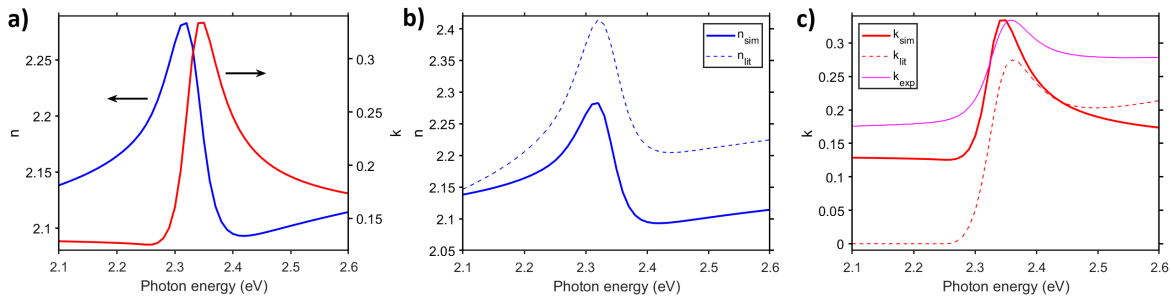

Figure 4.18: MAPB refractive index proposed with the modified Tauc-Lorentz model. a) Real part, n, and imaginary part, k, of the proposed MAPB refractive index. b) Comparison between the real part of the proposed MAPB refractive index, n_{sim}, and the real part of the refractive index extracted from [231], n_{lit}. c) Comparison of the extinction coefficients from the experiment, k_{exp}, the literature, k_{lit} and the modified Tauc-Lorentz model k_{sim}.

Simulation of the angle-resolved reflectivity and photoluminescence

The figures 4.19 and 4.20 show the simulations of the reflectivity and photoluminescence maps using the proposed MAPB refractive index. The values of the parameters used are reported in table 4.5. No roughness of the MAPB layer was needed. A really good match occurs between the experimental and simulated reflectivity maps in figure 4.19 and this for the three detunings. The match is not as good between the experimental photoluminescence maps and the simulated absorption maps in figure 4.20. As already mentioned, the comparison between the photoluminescence and the absorption is only used as an illustration.

Detuning (meV)	MAPB thickness (nm)	Ref: PMMA thickness (nm)	Abs: PMMA thickness (nm)	Ag thickness (nm)	MAPB roughness (nm)	PMMA roughness (nm)
-90.2	100	370	366	35	0	0
-68.5	100	361	358	35	0	0
-20.4	100	346	350	35	0	0

Table 4.5: Parameters used for the simulations of the angle-resolved reflectivity and photoluminescence maps using the customized refractive index

The good results from the reflectivity maps simulation could suggest that the proposed refractive index describes well the MAPB refractive index. However, there are many considerations to take into account. There is no certainty that the thicknesses used for

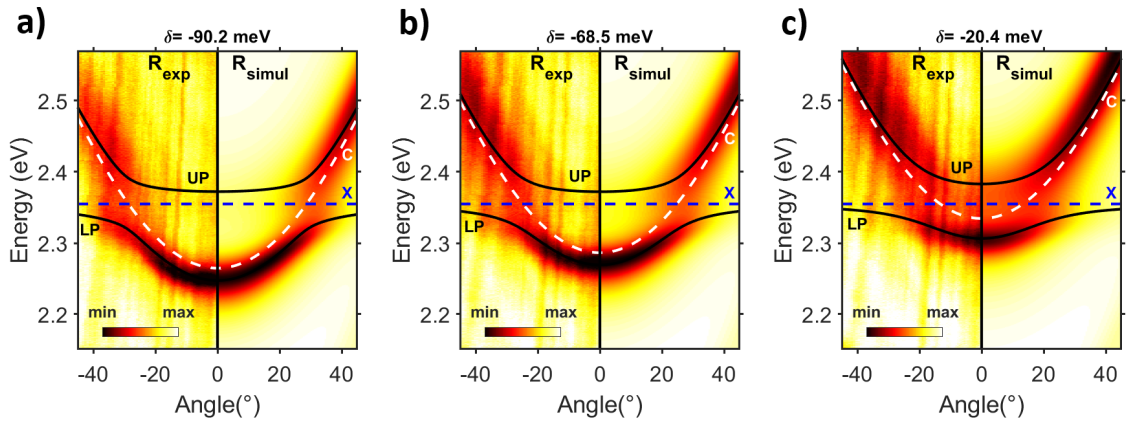

Figure 4.19: Simulation of the reflectivity maps with the proposed MAPB refractive index obtained with the Tauc-Lorentz model without taking into account the layers roughness for the detunings: -90.2 meV a), -68.5 meV b) and -20.4 meV c). The left panels correspond to the experimental reflectivity maps and the right panels to the simulated reflectivity maps. The pseudo-colour maps are in linear scale. The two solid black lines are the lower and upper polaritonic dispersions from the two-level model fitted to the experimental data. The blue and white dashed lines are the dispersions of the uncoupled exciton and photonic mode, respectively. The values of the parameters used for the simulations by the matrix transfer method are reported in table 4.5.

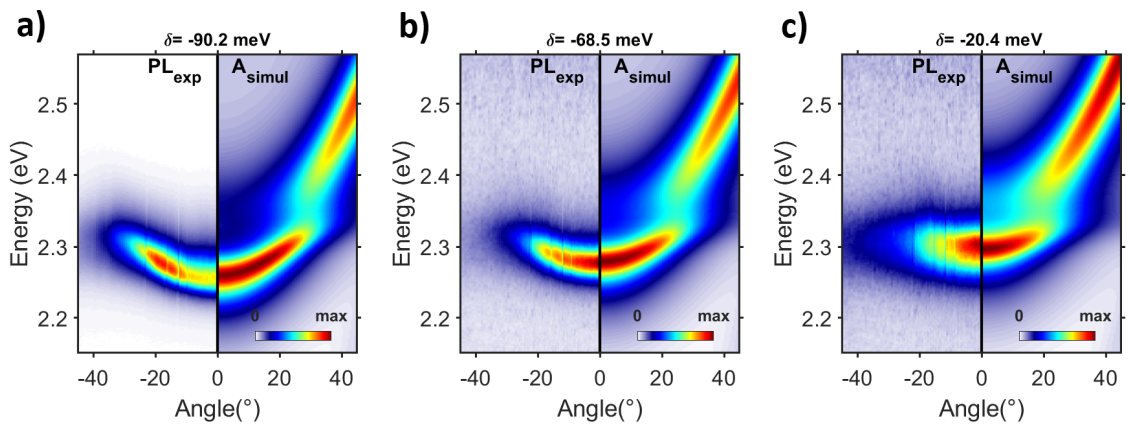

Figure 4.20: Comparison of the photoluminescence maps with the simulated absorption maps obtained with the proposed MAPB refractive index obtained with the Tauc-Lorentz model without taking into account the layers roughness for the detunings: -90.2 meV a), -68.5 meV b) and -20.4 meV c). The left panels correspond to the experimental photoluminescence maps and the right panels to the simulated absorption maps. The pseudo-colour maps are in linear scale. The values of the parameters used for the simulations by the matrix transfer method are reported in table 4.5.

the simulation are correct, neither the silver refractive index nor the Bragg mirror parameters. With a different set of parameters, the matching refractive index for the simulations would have changed. However, the proposed refractive index permits us to obtain good simulations for the different detunings and so could be used to predict the reflectivity and photoluminescence maps for other thicknesses of the MAPB, PMMA and silver layers.

Simulation of the reflectivity spectra obtained with the spectrophotometer

The customized refractive index was then used to fit the reflectivity spectra at different incidence angles obtained with the spectrophotometer. In this case, the roughness of the MAPB layer was set at zero, as the MAPB refractive supposedly already takes into account the MAPB roughness, and the roughness of the PMMA layer was of 25 nm, as in the case of the simulation using the extracted MAPB refractive index [231] in section 4.7.1.1. The values of the parameters used for the simulations are reported in table 4.6.

MAPB thickness (nm)	PMMA thickness (nm)	Ag thickness (nm)	MAPB roughness (nm)	PMMA roughness (nm)
110	347	37.5	0	25

Table 4.6: Parameters used for the simulations of the reflectivity spectra obtained with the spectrophotometer using the customized refractive index

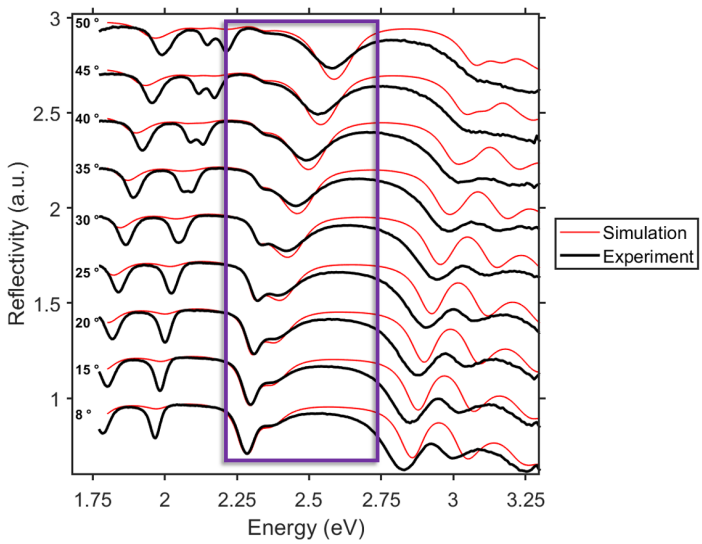

Figure 4.21: Simulations by the transfer matrix method using the customized refractive index of reflectivity spectra at different incidence angles obtained with the spectrophotometer. The parameters used for the simulation are reported in table 4.6.

Figure 4.21 shows the simulated results of the reflectivity spectra obtained with the spectrophotometer. We will only consider the reflectivity between 2.1 eV and 2.6 eV, the region of the polariton dips indicated by the purple rectangle. The reflectivity of the lower polariton is well reproduced at each angle which was not the case for the simulation using the extracted refractive index [231] in section 4.7.1.1. The reflectivity of the upper polariton is only well reproduced at low angles as the simulated upper reflectivity dips are deeper and slightly blueshifted compared to the experimental reflectivity dips at high angles. However, the differences between the upper reflectivity dips intensity and position of the experiment and simulation are much less pronounced than in the case using the extracted refractive index [231].

As in the previous section, this result shows that although better results are obtained, the customized refractive index may not describe well the real MAPB thin film refractive index as there are many considerations to take into account in the simulation (thicknesses, roughness, silver refractive index, etc...).

7.3 Predictions of the strong coupling for other microcavity designs

Even though the customized refractive may not describe the real MAPB thin film refractive index, good simulation results were obtained. For this reason, the customized refractive index can be used to predict the reflectivity and absorption of microcavities with different architectures. Figure 4.22 show two examples of angle-resolved reflectivity and absorption maps obtained with the transfer matrix method and the proposed refractive index along with the simulated absolute field distribution inside the microcavity. The first example corresponds to the same design of the microcavity studied in this PhD but without the layer of PMMA. The second example corresponds to a microcavity with a very thin layer of MAPB of 20 nm. The parameters used for the simulation are reported in table 4.7. In the first case (see figures 4.22 a) and b)), the strong coupling is obtained with a Rabi-splitting of 114 meV with an upper polariton branch slightly more visible at low angles than in the case of the experimental results presented in this chapter. This simulated architecture gives a higher Rabi splitting, but can not be performed practically as the MAPB layer needs to be protected by a spacer layer during the evaporation the silver layer. For the second example (see figures 4.22 c) and d)), only the weak coupling regime is obtained since the reflectivity and absorption dispersions cross the excitonic energy. This can be explained by the antinode of the electric field inside the microcavity not covering the MAPB unlike in the first example (see figures 4.22 b) and d)).

	MAPB thickness (nm)	PMMA thickness (nm)	Ag thickness (nm)	MAPB roughness (nm)	PMMA roughness (nm)
Simulation 1	100	0	40	0	0
Simulation 2	20	135	40	0	0

Table 4.7: Parameters used for the two examples of angle-resolved reflectivity and absorption maps using the customized refractive index

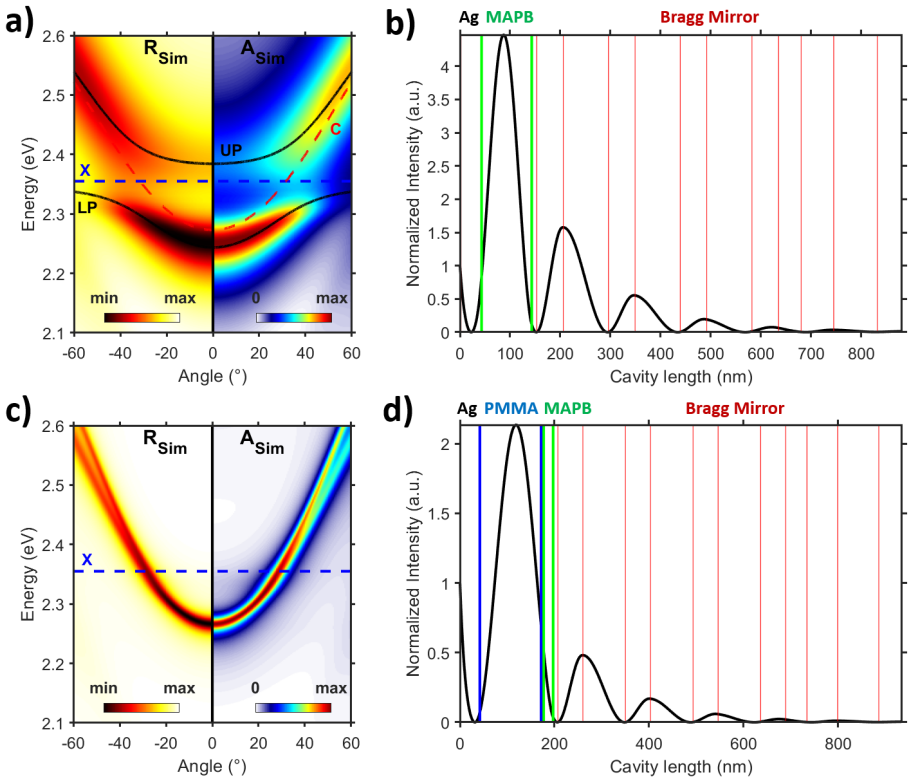

Figure 4.22: Two examples of simulated angle-resolved reflectivity and absorption maps using the proposed refractive index along with the simulated absolute field distribution inside the microcavity. In the simulated reflectivity and absorption figures (a) and c)), the left panels correspond to the simulated reflectivity maps and the right panels to the simulated absorption maps. The pseudo-colour maps are in linear scale. a) and b) First example where the strong coupling regime is achieved with a Rabi splitting of 114 meV. The two solid black lines are the lower and upper polaritonic dispersions. The blue and red dashed lines are the dispersions of the uncoupled exciton and photonic mode, respectively. c) and d) second example where only the weak coupling regime is achieved. The parameters used for the simulations are reported in table 4.7

8 Conclusion of the chapter

In this Chapter, the strong coupling regime at room temperature has been demonstrated in a $3\lambda/2$ microcavity containing a large-surface MAPB thin-film. The average Rabi splitting energy was of 73 meV and the average cavity quality factor of 81. For the applications, obtaining strong coupling at room temperature with a material deposited in a large-surface with a low cost of synthesis and good charge transport properties gives hope towards integrated, possibly electrically injected, MAPB-based polaritonic devices. Additionally, this result suggests that the MAPB exciton is stable at room temperature and is coherent with recent studies [87, 243] suggesting that the free carriers and excitons coexist at room temperature in bromide perovskites. The angle-resolved reflectivity and photoluminescence maps could be well simulated using a customized refractive index similar to the complex refractive index extracted in the literature [231]. All these results were obtained via reflectivity and photoluminescence measurements at low pumping densities. In the following Chapter, the behaviour of the microcavity at a high density of pumping, i.e. the microcavity lasing action, will be presented.

Chapter 5

Lasing action of the 3λ/2 MAPB-based microcavity

Contents

1 Concept of the random lasing 138

1.1 Introduction to random lasing 138

1.2 Characteristics of the random lasing with coherent feedback 139

2 Random lasing of the MAPB/PMMA layer 141

2.1 PL spectroscopy of the MAPB/PMMA sample 141

2.2 Angle-resolved photoluminescence of the MAPB/PMMA sample . . 144

2.3 Discussion on the nature of the random lasing 144

3 Lasing action of the 3λ/2 MAPB-based microcavity 145

3.1 PL spectroscopy of the 3λ/2 MAPB-based microcavity 145

3.2 Angle-resolved photoluminescence of the 3λ/2 MAPB-based microcavity 148

3.3 Expected emission angles and emission divergences 151

3.4 Discussion on the nature of the microcavity lasing 154

4 Conclusion of the chapter 155

Introduction

The main goal of this PhD is to study the lasing of green-emitting perovskites to address the green-gap problem for the LEDs and lasers diodes. As mentioned in Chapter 1, the green-gap problem refers to the wavelength region in which the commercial LEDs and lasers diodes are not efficient. The chosen perovskite is the perovskite $Ch_3NH_3PbBr_3$, called MAPB, as it emits in the green and the selected configuration is a dielectric/metal 3λ/2 microcavity in which the strong coupling regime has been demonstrated in Chapter 4. The active material in the cavity is a spin-coated polycrystalline MAPB thin film which is a disordered medium, as seen in Chapter 3. For this reason, we observed random lasing action. This chapter aims at demonstrating that this random lasing is directionally filtered by the lower polariton dispersion of the microcavity. This result is interesting because it allows reaching lasing at large angles as large as 20° and permits to control the random lasing directionality.

The first part of this chapter introduces the concept and the state of the art of random lasing. In the second part, we demonstrate random lasing action in a MAPB thin-film covered by a PMMA thin-film, called MAPB/PMMA sample, having the same characteristics as the MAPB and PMMA layers in the microcavity. In the third part, the lasing of the cavity is explored. The influence of the microcavity, in particular the impact of the lower polariton dispersion, on the random lasing is studied. A numerical approach is then proposed to support our hypothesis that the random lasing is filtered by the polariton dispersion and permits the control of the lasing directionality.

1 Concept of the random lasing

1.1 Introduction to random lasing

The word "laser" comes from the acronym "Light Amplification by Stimulated Emission of Radiation" which is the light amplification using stimulated emission, a process in which an excited atom or electron decays by interacting with a photon and releasing another photon of the same frequency and momentum. However, the current definition of a laser is a device containing a gain medium amplifying the light and an optical resonator providing optical feedback. Therefore, light is not only amplified but also possesses increased temporal and spatial coherence from the selection of specific modes by the resonator [1].

Generally, the lasers are composed of optical resonators with a specific architecture, for example, Fabry-Pérot or Distributed FeedBack (DFB) cavities. In these cases, the optical modes are well defined. However, in highly disordered systems, optical feedback can

[1] By this definition, the Erbium amplifiers using stimulated emission or gain media exhibiting Amplified Spontaneous Emission (ASE) are not considered to be lasers.

occur via multiple random scattering of light. When light is amplified by stimulated emission in these random resonators, and the gain compensates for the losses, lasing occurs and is called random lasing. There are two categories of random lasing described in the literature depending on the coherence or incoherence of the optical feedback [244]. In this PhD, only the coherent random lasing will be discussed.

The pioneering work for random lasing was held by Ambartsumyan et al. who studied in 1966 the lasing action of a Fabry-Pérot cavity for which a mirror was replaced by a highly scattering plane [245]. Later in 1968, Letokhov et al. theoretically predicted that multiple scattering could serve as the optical feedback in a laser [246]. The random lasing with coherent feedback was first demonstrated in the late 1990s [247, 248]. Since then, the random lasing has been demonstrated in various materials and configurations (see the reviews [249–252]). Due to the high gain and high refractive index of the perovskites, the random lasing has been demonstrated in iodine-based perovskites [66, 67, 115–117], chloride-based perovskites [118] and bromide-based perovskites [118–127, 253, 254].

1.2 Characteristics of the random lasing with coherent feedback

In a scattering medium, when the scattering is strong enough to scatter some light back to the original position, optical closed loops are formed and provide the necessary coherent feedback for the random lasing action [247, 255]. These loops act as random cavities leading to random cavity modes. Part of the random lasing emission is scattered out of the sample. The lasing emission can then be either collected from the side or from the surface of the sample (see figure 5.1 a)). Above the random lasing threshold, the PL spectrum is characterized by narrow peaks which are the modes of the random cavities (see figures 5.1 b) and c)). The different loops possess different losses and therefore, different lasing thresholds. When the pumping is increased, more loops start to lase, which adds lasing peaks in the PL spectrum.

Optical random loops have been directly observed in different studies [255, 257]. However, Polson et al. proposed to use the Power Fourier Transform (PFT) to determine the size of the pseudo-cavities without directly imaging the loops. The Power Fourier Transform of a random lasing spectrum (as a function of the wavenumber $1/\lambda$) gives rise to Fourier peaks, as shown in the example in figure 5.2. The cavity length, L_{cav}, is proportional to the position of the m_{th} Fourier peak in the spatial frequency, p_m, as $L_{cav} = p_m \pi / mn$, with n the gain medium refractive index. In the case of the example from [258] in figure 5.2, the average retrieved cavity length is of 37 µm. In general, in thin films, the size of the loops is much larger than the film thickness, meaning that the gain occurs in the sample plane and the loops are two-dimensional (see for example [255]).

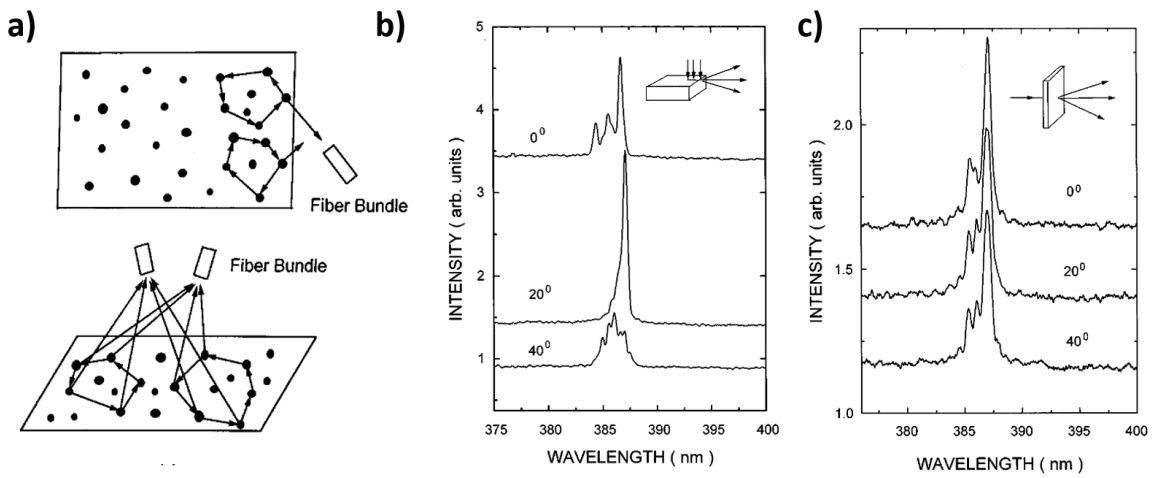

Figure 5.1: Measurement of random lasing spectra. a) Schematic of the random loops and measurement of their random lasing emission from the surface or the side of the sample. In this example, measurements are done with fibre bundles. b) and c) Random lasing spectra obtained at different angles of observation b) from the side and c) from the surface of a ZnO polycrystalline thin film from [256]. The figures are extracted from [256].

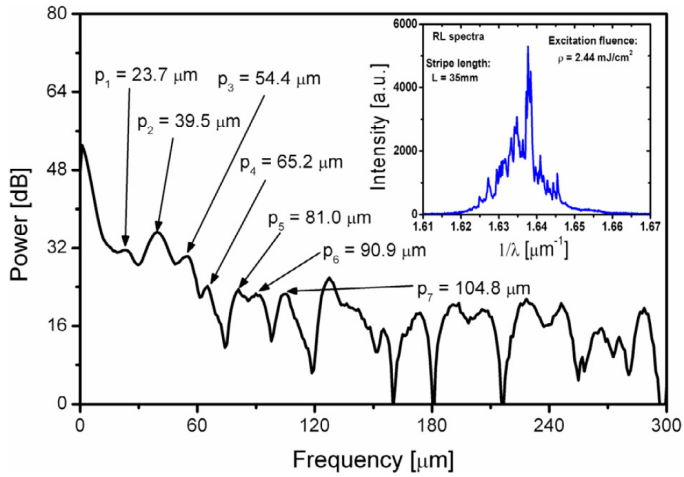

Figure 5.2: Example of the power Fourier transform of a random lasing spectrum from [258]. The inset is the corresponding random lasing spectrum as a function of the inverse wavelength $1/\lambda$. Extracted from [258]

Due to multiple scattering, the random lasing output emission is multi-directional. When the random lasing emission is observed from the side, the random lasing spectra differ with the observing angle, and when observed from the surface the PL spectra are angle-independent (see two examples in figure 5.1 b) and c)). The random lasing multi-directionality can be used for some applications such as display technologies [259]. However, for conventional lasers applications, the control of the random lasing directionality is required. For this reason, random lasing media have been coupled to optical fibers [260], to a Bragg grating [261], photonic crystals [262], and planar microcavities [263–267]. The directionality can also be controlled by pump shaping [268].

Finally, the random lasing threshold depends on several factors: the gain medium (gain, quantum efficiency, refractive index), the scattering strength, the scatterers density and the pumping spot size [249]. Indeed, for the latter, the pumping spot size should be large enough to cover the optical loops for efficient pumping. For this reason, the threshold is minimized when the pumping spot size is close to the loop size and increases with decreasing spot size.

2 Random lasing of the MAPB/PMMA layer

In this section, the attention is focused on the random lasing of a MAPB thin-film covered by a PMMA thin-film, called MAPB/PMMA sample. The PL spectroscopy and angle-resolved photoluminescence measurements as a function of the pumping power of the MAPB/PMMA sample are presented. The polaritonic or photonic nature of the random lasing is discussed later at the end of this section.

As a reminder, the sample is excited with the femtosecond pulsed laser ($t_{pulse} \approx 100$ fs, f_{rep}=1 kHz) emitting at 400nm. Because of the low thermal stability of the perovskites, the sample can be damaged for very high densities. Control measurements (see Appendix A) were then performed on the MAPB/PMMA sample to determine the pumping powers for which the perovskite was not damaged. Only these pumping powers are presented in this section.

2.1 PL spectroscopy of the MAPB/PMMA sample

Photoluminescence spectroscopy as a function of the excitation power has been performed on the MAPB/PMMA sample using the experimental set-up number 2 presented in Chapter 2 (section 2.4.2.3). The 0.9 NA objective was used to focus the pump laser on the sample on the PMMA side and collect the signal as shown in figure 5.3. In this section, the energy resolution is of 1.7 meV.

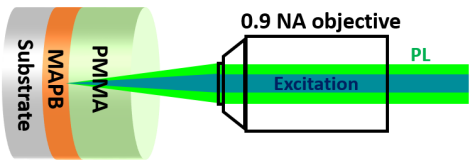

Figure 5.3: Sketch of the excitation configuration of the MAPB/PMMA sample measurements.

Figure 5.4 presents results of the PL spectroscopy as a function of the excitation power on a position (named position RL 1) of the MAPB/PMMA sample. The PL spectra for excitation power ranging from 0.8 to 2 times the lasing threshold (P_{th}) are shown in figure 5.4 a). The photoluminescence below threshold is similar to the MAPB thin-film photoluminescence spectrum presented in Chapter 3. In this case, the Full Width at Half Maximum (FWHM) is 100 meV. Three small peaks with a line width of about 3 meV appear when

the excitation power reaches 0.65 µW. At higher pumping, the peaks gain more intensity, and new peaks appear. The overall signal is broadened at high excitation powers, which is probably due to the appearance of many lasing peaks in close spectral proximity. The lasing modes occur in the same range of energy, between 2.26 and 2.29 eV, in which the Amplification of Spontaneous Emission (ASE) takes place in MAPB thin films [229] corresponding to the region of MAPB highest net gain. Figure 5.4 b) showing the pseudo-colour map of the normalized PL spectra as a function of the ratio of the pump power to the threshold power, P/P_{th}, helps to discern the lasing peaks and their behaviour with the pump increase. The lasing peaks slightly blueshift when the pumping power is increased (around 2 meV between 1 P_{th} and $2P_{th}$). The integrated photoluminescence intensity (between 2.26 and 2.29 eV) as a function of the ratio of P/P_{th} (in log-scale) showing a slope discontinuity is presented in figure 5.4 c). All these lasing characteristics occurring in the MAPB/PMMA sample without an external resonator are in favour of the random lasing. We note that the power threshold of 0.65 µW, which gives a threshold in fluence of 221.9 mJ/cm^2 (see the conversion method in Appendix B), is two orders of magnitude higher than the thresholds found for other MAPB random lasing actions of 2.5 mJ/cm^2 [129] and of around 0.5 mJ/cm^2 [253]. We explain this discrepancy by the fact that our spot is much smaller than the spots used in [129] and [253] (for example in [129], a two-fold decrease is obtained when the spot size varies from 500 µm^2 to 4000 µm^2).

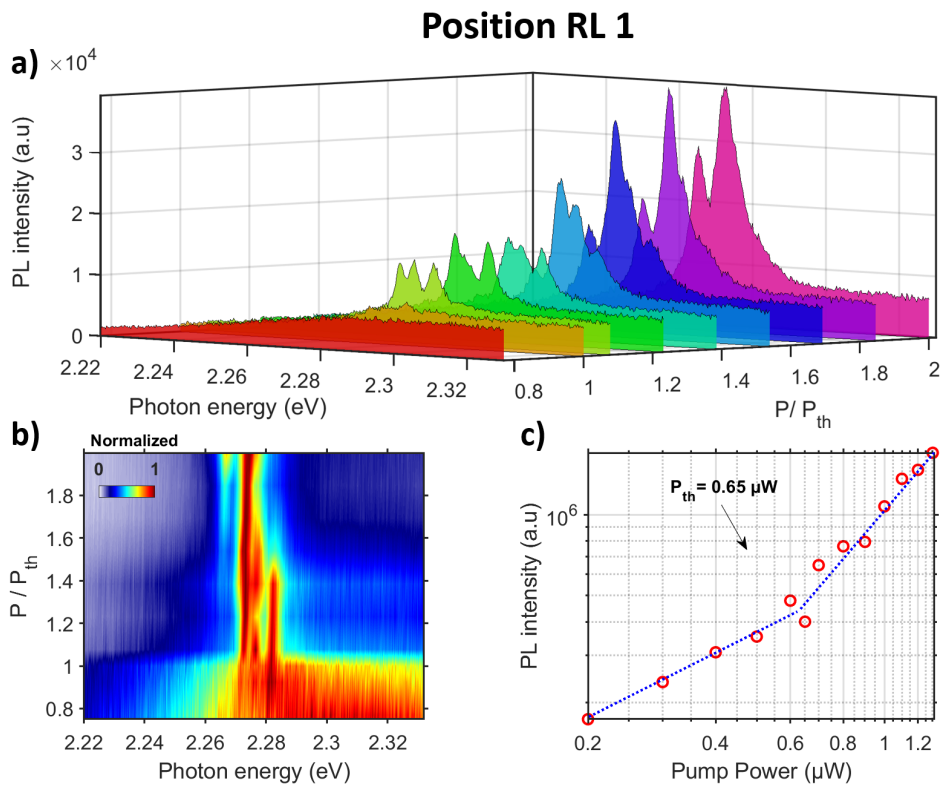

Figure 5.4: a) PL spectroscopy as a function of the ratio of the pump power to the threshold power, P/P_{th}, on a position on the MAPB/PMMA sample. The energy resolution is of 1.7 meV. b) Pseudo-colour map (in linear scale) of the normalized PL spectra as a function of P/P_{th}. c) Integrated photoluminescence intensity as a function of the excitation power, in log-scale

This random lasing is made possible by the roughness of the MAPB layer. Indeed, it was shown with AFM scans in Chapter 3 (see figure 3.11) that the MAPB layer is polycrystalline and composed of grains of 500 nm to 1 µm size. Also, a waveguide confining the light is formed between the quartz substrate and the PMMA layer (refractive indices around 1.5) sandwiching the MAPB layer (refractive index of around 2.3). The grains in the MAPB layer scatter the light within the plane of the layer and create the necessary optical closed-loops for random lasing.

Power Fourier Transform was performed on the PL spectra above the lasing threshold to evaluate the characteristic lengths of the optical loops. However, due to the small number of visible lasing peaks, the results were not satisfactory. Instead, the free spectral range, FSR = $\nu_{m+1} - \nu_m$ with m an integer, of the PL spectra was studied. Figure 5.5 a) shows five lasing spectra of the MAPB/PMMA sample for which the free spectral range is studied. Blue triangles indicate the lasing modes and blue dotted lines link the same lasing modes occurring at different pump powers. A vertical offset is applied between successive spectra for better readability. Figure 5.5 b) shows the difference in energy between the mth modes and the 1st mode against the modes numbers. The curve is fitted with a linear function (red dashed line). The characteristic length of 100 µm of the optical loops is retrieved from L = $hc/(ns)$ [2], where $n = 2.3$ is the MAPB refractive index, c is the light velocity and s is the slope of the linear function. This size is much larger than the thickness of the sample (of around 500 nm) and confirms that the random lasing occurs in the sample plane.

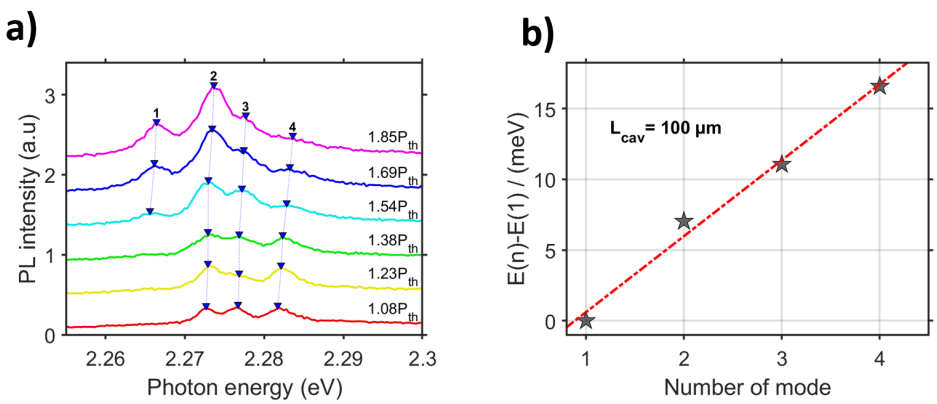

Figure 5.5: a) Lasing spectra of the MAPB/PMMA sample for which the free spectral range, FSR = $\nu_{m+1} - \nu_m$, is studied. Blue triangles indicate the lasing modes and blue dotted lines link the same lasing modes occurring at different pump powers. A vertical offset is applied between each spectrum for better readability. b) Energy difference between the mth and 1st modes with respect to the mode numbers. The curve is fitted with a linear function (red dashed line). The characteristic length of 100 µm of the optical loops is retrieved from L = $hc/(ns)$, where $n = 2.3$ is the MAPB refractive index, c is the light velocity and s is the slope of the linear function.

[2]For planar cavities, a factor of 2 appears in the denominator as the round trip must be taken into account. Here the cavity length represents the perimeter of the optical loop.

2.2 Angle-resolved photoluminescence of the MAPB/PMMA sample

Angle-resolved photoluminescence as a function of the pumping power was performed on the MAPB/PMMA sample using the Fourier spectroscopy set-up in Aimé Cotton Laboratory (LAC) presented in Chapter 2 (section 2.4.4.7). The excitation configuration is the same as the one presented in figure 5.3: a 0.9 NA objective focus the pump laser on the PMMA side and collect the signal. In this section, the energy resolution is of 1.7 meV.

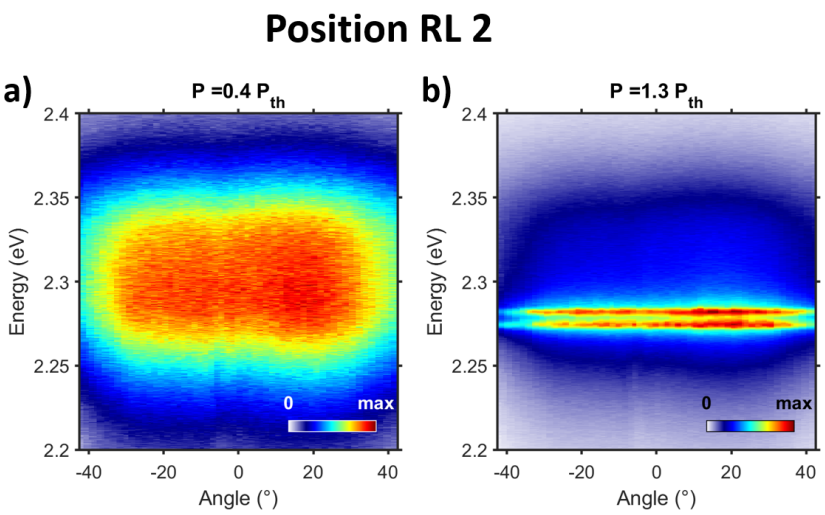

Figure 5.6: Angle-resolved photoluminescence maps a) below (0.4 P_{th}) and b) above (1.3 P_{th}) the random lasing threshold of the MAPB/PMMA sample. The pseudo-colour maps are in linear scale.

The ARPL pseudo-colour maps below (0.4 P_{th}) and above (1.3 P_{th}) the random lasing threshold of another position (named position RL 2) on the MAPB/PMMA sample are shown respectively in figures 5.6 a) and b). The ARPL maps at other powers of excitation as well as the angle-integrated PL spectra and the integrated PL intensity as a function of the pumping power curve are given in Appendix C. Below the lasing threshold, at 0.4 P_{th}, the emission of the MAPB/PMMA sample is angle-independent, centered at 2.3 eV with an FWHM of 100 meV. Above the lasing threshold, at 1.3 P_{th}, the same broadband signal appears in dark blue, and two random laser peaks appear as two horizontal red lines at 2.275 eV and 2.283 eV. As expected for a random lasing emission, the laser peaks emit in all directions when the signal is observed from the surface of the sample [256]. Indeed, the random lasing signal originating from the sample surface is scattered in all directions out of the surface.

2.3 Discussion on the nature of the random lasing

It is reasonable to question the photonic or polaritonic nature of the lasing occurring in the MAPB/PMMA sample as Niyuki et al. did with resonance-controlled ZnO random lasers [269]. Indeed, as discussed in previous chapters (Chapter 1 and Chapter 4), the strong coupling regime could be observed in MAPB nanowires [220, 223] and also in our 3λ/2 microcavity [15] (see Chapter 4). The blueshift of the lasing peaks observed in figure 5.4 (of around 2 meV between 1 P_{th} and 2P_{th}) could be an argument in favour of

the polaritonic lasing but could be explained by the blueshift of the MAPB emission with increasing temperature (of around 24 meV between 300K and 370K) [236]. However, to demonstrate the strong coupling regime unambiguously, the polariton mode dispersions should be measured, which is impossible in practise here because of the multiple scattering. Thus, the polaritonic or photonic nature of the lasing of the MAPB/PMMA sample remains unanswered.

3 Lasing action of the 3λ/2 MAPB-based microcavity

In this section, we study the lasing action of the 3λ/2 MAPB-based microcavity and expose arguments to support our hypothesis: the random lasing from the MAPB layer is filtered directionally by the lower polariton dispersion of the microcavity in strong coupling regime. First, the PL spectroscopy and angle-resolved photoluminescence measurements as a function of the pumping power of the microcavity are presented. Second, a numerical approach is proposed to support our hypothesis. And finally, we confront our hypothesis with other possible lasing mechanisms.

As for the MAPB/PMMA sample, the microcavity is excited with the femtosecond pulsed laser ($t_{pulse} \approx$ 100 fs, f_{rep}=1 kHz) emitting at 400nm and control measurements (see Appendix A) were performed on the microcavity to rule out the pumping powers for which the perovskite is damaged.

3.1 PL spectroscopy of the 3λ/2 MAPB-based microcavity

Photoluminescence spectroscopy as a function of the excitation power has been performed on the 3λ/2 MAPB-based microcavity using the experimental set-up number 1 presented in Chapter 2 (section 2.4.2.2). The 0.6 NA objective was used to focus the pump laser on the silver side and collect the signal as shown in figure 5.7. In this section, the energy resolution is of 0.38 meV.

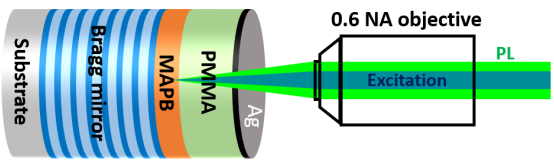

Figure 5.7: Sketch of the excitation configuration of the microcavity PL spectroscopy measurements.

The results measured at a position A on the MAPB-based microcavity are presented in figure 5.8. The PL spectra for excitation powers ranging from 0.9 P_{th} and 1.35 P_{th} are shown in figure 5.8 a). Due to the coupling of the perovskite to the microcavity, the PL spectrum below the threshold is shifted to 2.272 eV, compared to the PL spectrum of the uncoupled MAPB thin film (see figure 3. in Chapter 3) and the uncoupled MAPB/PMMA

sample (see figure 5.4), the FWHM is 53 meV. One lasing peak appears on top of the broadband PL at 2.273 eV with a FWHM of 3 meV when the lasing threshold is reached. Other peaks occur at other energies followed by a broadening of the overall signal at higher pumping due to the overlapping of several lasing modes. The other modes are not really perceptible in figure 5.8 a) as one mode dominates but are discernible in the pseudo-colour map of the normalized PL spectra as a function of P/P_{th} in figure 5.8 b). As in the case of the MAPB/PMMA sample, the laser peaks slightly blueshift (around 1 meV between 1 P_{th} and 1.2P_{th}), which is probably due to the MAPB emission blueshift with increasing temperature [236]. The integrated PL intensity as a function of the pumping power curve in figure 5.8 c) demonstrates the lasing of the microcavity with a threshold of 135 µW, which gives a threshold in fluence of 2.62 mJ/cm^2 (see the conversion method in Appendix B) which is two orders of magnitude lower than the MAPB/PMMA random lasing threshold (around 200 mJ/cm^2). Indeed, this decrease of lasing threshold is probably due to the presence of the cavity as it has been shown that the effect of external feedback (e.g. an external mirror or a cavity) can dramatically reduce the random lasing threshold [256, 263, 270]. For example, in [253], the MAPB random lasing threshold is reduced from 500 µJ/cm^2 to 20-30 µJ/cm^2 when the MAPB film is placed in a microcavity.

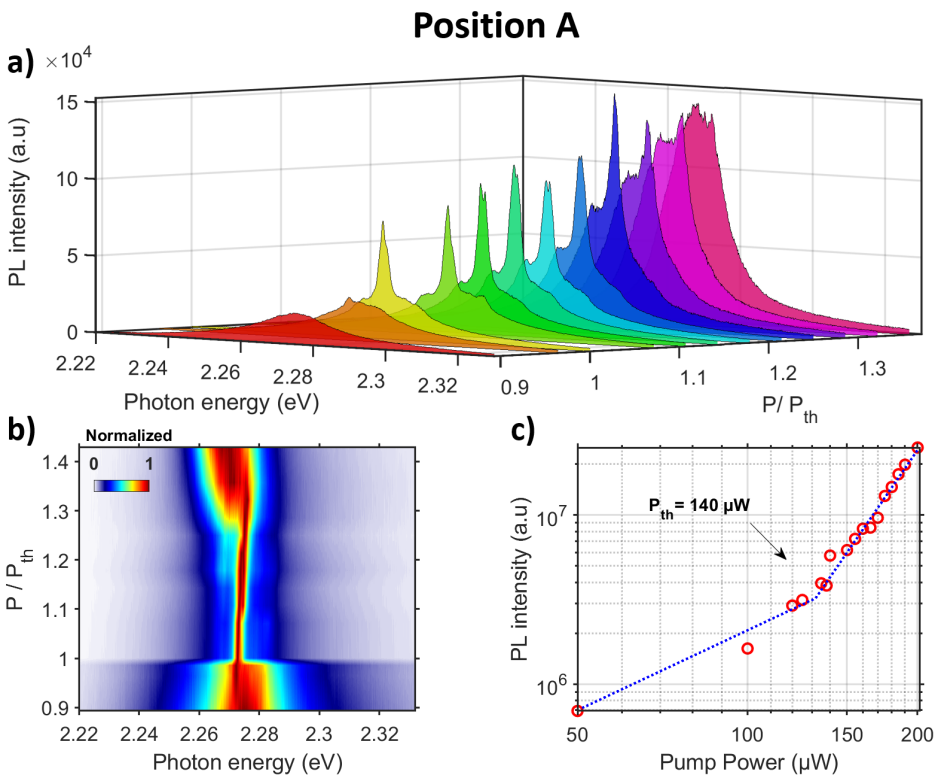

Figure 5.8: a) PL spectroscopy as a function of the ratio of the pump power to the threshold power, P/P_{th}, on a position of the 3λ/2 MAPB-based microcavity. The energy resolution is of 0.38 meV. b) Pseudo-colour map (in linear scale) of the normalized PL spectra as a function of P/P_{th}. c) Integrated photoluminescence intensity as a function of the excitation power, in log-scale

Figure 5.9 presents the PL spectroscopy results on another position (named position B) of the MAPB-based microcavity. The PL spectrum is also coupled to the cavity and is shifted to 2.3 eV with an FWHM of 66 meV. Slightly above the lasing threshold, three lasing peaks can be observed with a dominant mode at 2.285 eV presenting an FWHM of 2 meV. The threshold power is 90 µW leading to the threshold fluence of 1.68 mJ/cm^2, of the same order of magnitude as for position A. In both the position A and position B, the lasing peaks of the microcavity occur at the same range of energy as the random lasing peaks of the MAPB/PMMA sample, between 2.26 and 2.29 eV.

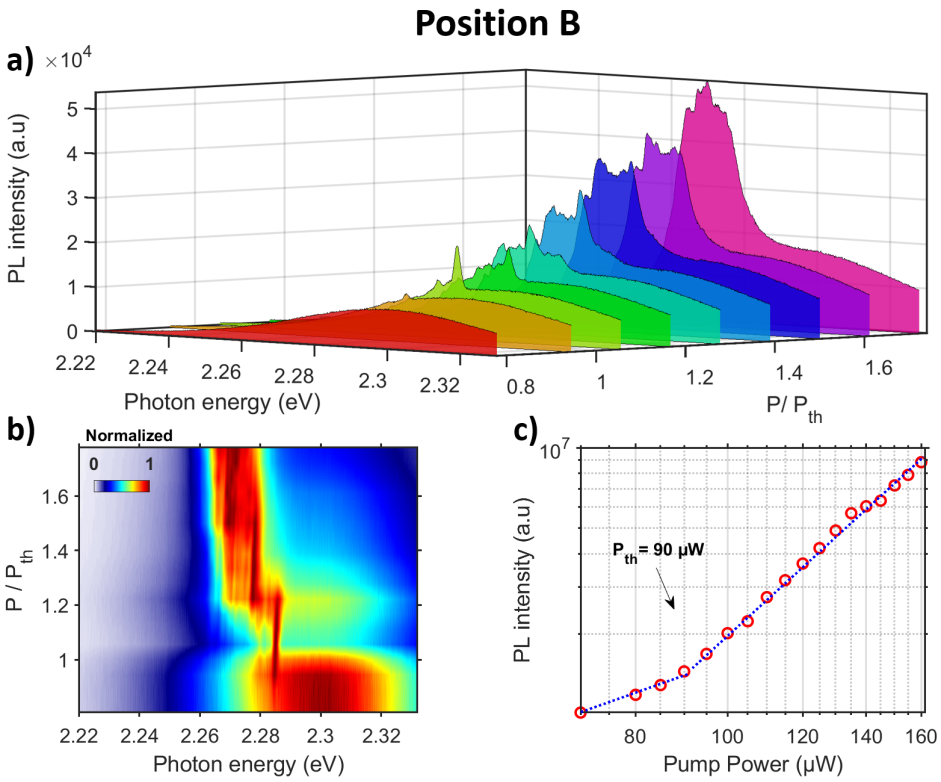

Figure 5.9: a) PL spectroscopy as a function of the ratio of the pump power to the threshold power, P/P_{th}, on another position of the 3λ/2 MAPB-based microcavity. The energy resolution is of 0.38 meV. b) Pseudo-colour map (in linear scale) of the normalized PL spectra as a function of P/P_{th}. c) Integrated photoluminescence intensity as a function of the excitation power, in log-scale

Figure 5.10 shows the study of the free spectral range of the position A (see figure 5.8) and the position B (see figure 5.9) to evaluate the characteristic lengths of the optical loops. For the position A in figure 5.10 a) and b), the characteristic length obtained is of 144 µm, and for the position B in figure 5.10 c) and d), of 215 µm. In both cases, the characteristic cavity lengths are similar to the characteristic length found for the random lasing of the MAPB/PMMA layer. Moreover, these characteristic lengths are much larger than the microcavity vertical length, suggesting that the gain occurs in optical loops within the MAPB plane.

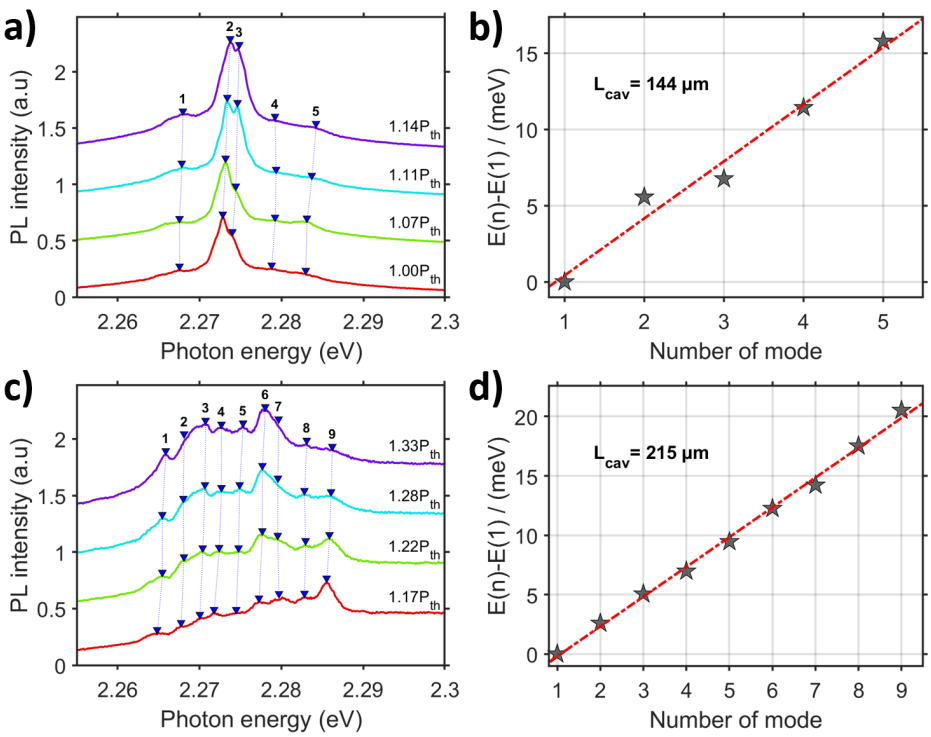

Figure 5.10: a) and c), Lasing spectra with vertical offsets for which the free spectral range is studied for the microcavity a) position A and c) position B. Blue triangles indicate the lasing modes. b) and d) Energy difference between the mth and 1st modes with respect to the mode numbers for the microcavity b) position A and d) position B. The curves are fitted with linear functions (red dashed lines). The characteristic cavity lengths are retrieved from L = $hc/(ns)$, where $n = 2.3$ is the MAPB refractive index, c is the light velocity and s is the linear function slope.

3.2 Angle-resolved photoluminescence of the 3λ/2 MAPB-based microcavity

Angle-resolved photoluminescence as a function of the pumping power was performed on the microcavity using the Fourier spectroscopy set-up in Aimé Cotton Laboratory (LAC) presented in Chapter 2 (section 2.4.4.7). For the first position studied (see figure 5.12 a)), the focus and the collection were done on the silver side with a 0.9 NA objective as shown in figure 5.11 a). For the three other positions (see figure 5.12 b) c) and d)), a 5-cm lens focuses the pump laser on the Bragg mirror and a 0.9 NA objective collects the signal from the silver side as shown in figure 5.11 b). In this section, the energy resolution is of 1.7 meV.

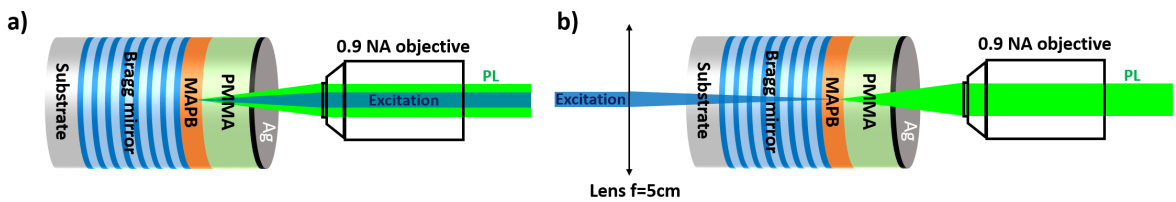

Figure 5.11: Sketch of the two excitation configurations of the microcavity angle-resolved photoluminescence measurements.

Figures 5.12 a) to d) show the angle-resolved photoluminescence results on four different positions (named position 1,2,3 and 4) of the microcavity corresponding to four different detunings. The row noted as i) corresponds to the photoluminescence maps below the lasing threshold (at 0.1, 0.2, 0.1, 0.2 P_{th}), and the row ii) to the photoluminescence maps above threshold (at 1.4, 1.6, 1.4, 1.1 P_{th}). The ARPL maps at other powers of excitation as well as the angle-integrated PL spectra and the integrated PL intensity as a function of the pumping power curves of these positions are given in Appendix C.

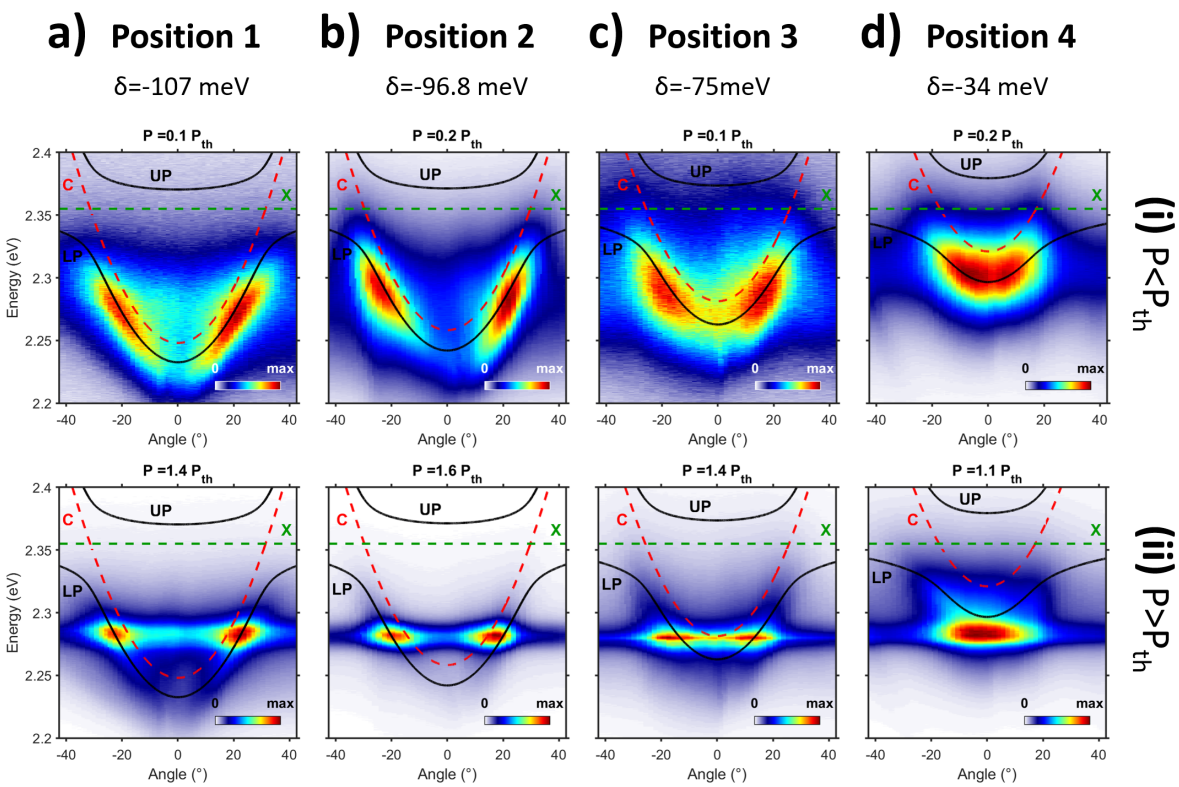

Figure 5.12: Angle-resolved photoluminescence pseudo-colour maps on four different positions of the microcavity with detunings, δ, of : a) -107 meV, b) -96.8 meV, c) -75 meV and d) -34 meV. The resolution for the energy axis is 0.38 meV and for the angle axis 0.7°. The row (i) corresponds to the maps below the lasing threshold (at 0.1, 0.2, 0.1, 0.2 P_{th}), the row (ii) above the threshold (at 1.4, 1.6, 1.4, 1.1 P_{th}). The pseudo-colour maps are in linear scale. On top of each ARPL map are plotted the fitted polariton dispersions (in black) along with the uncoupled excitonic energy (in green) and photonic modes (in red).

In the four photoluminescence maps below the threshold (see figure 5.12 a-i), b-i), c-i) and d-i)), a parabolic dispersion can be observed. As the strong coupling regime has already been demonstrated previously in this microcavity, these parabolic dispersions are attributed to the lower polariton photoluminescence. For each different position, the dispersion was collected by fitting slices of the photoluminescence maps (between -20 ° and 20 °) with a Lorentzian function and reporting the Lorentzian centres in an energy/angle diagram. The collected dispersions were then fitted to the two-level model using the parameters found in figure 4.5 a) of Chapter 4 (n_{eff}=1.75, E_X = 2.355 eV, g=48.7 meV, γ_X=90

meV and γ_{ph}=25 meV) and with the detuning, δ, as the only free parameter. The results of the dispersion collection and fitting are shown in Appendix D. The detuning, δ, are found respectively -107 meV, -96.8 meV, -75 meV and -34 meV for the figures 5.12 a), b), c) and d). A good agreement is met between the theoretical and experimental lower polariton dispersions using the parameters found previously confirming the strong coupling regime. The lower and upper polariton dispersions (in black) are plotted on top of the photoluminescence maps of figure 5.12 along with the excitonic energy (in green) and the uncoupled photonic mode dispersion (in red).

Above the lasing threshold for the four positions (see figures 5.12 a-ii), b-ii), c-ii) and d-ii))), laser peaks appear in dark red and the lower polariton emission in dark blue. Because another spectrometer was used for the angle-resolved measurements, the energy resolution of 1.7 meV is lower in the photoluminescence maps than the resolution of 0.38 meV in the PL spectra presented in the previous section. As a consequence, the lasing peaks are not well resolved and not clear in the pseudo-colour maps, but are more visible in slices taken at given angles as shown in Appendix E.

In the four cases, the energies of the laser peaks lie between 2.26 and 2.29 eV, in the same range of energies already seen for the random laser peaks of the MAPB/PMMA sample (see figure 5.4 and figure 5.6). For the three first positions with the largest detunings in figures 5.12 a), b) and c), the laser peaks only arise at the intersection between the lower polariton dispersion and the energy of the lasing peaks at the angles of ± ~ 22.4°, ± ~ 18.2° and ± ~ 15.8° with divergences in angle of ~ 12.5°, ~ 11.9° and ~ 12.3°, respectively. In the three cases, the energies of the lasing peaks are around 2.28 eV. However, in the last position corresponding to the lowest detuning in figure 5.12 d), two laser peaks emerge at 2.281 eV and 2.285 eV under the theoretical lower polariton dispersion at 0° with a divergence of ~ 29.7°. The values of the lasing peaks angles and divergences were obtained by taking a slice of the ARPL maps at the energy of the lasing peaks and by fitting the slices with Lorentzian and Gaussian functions. The slices and the fits are shown in Appendix E.

These observations support the hypothesis of the random lasing emission being filtered by the lower polariton dispersion curve. Indeed, as for the positions A and B of the cavity, the lasing peaks of these four positions occur at the same energy range as the random lasing peaks of the MAPB/PMMA sample. Moreover, in the three first positions, the angle of the lasing emission occurs at the intersection between the lasing peak energies and the lower polariton dispersions. However, the result obtained in the last position remains intriguing. In the following, a numerical approach is proposed to explain the random lasing filtering by the lower polariton dispersion curve. It will be shown that the result in position 4 (see figure 5.12 d)) is not contradictory with the hypothesis.

3.3 Expected emission angles and emission divergences

To further study the lasing mechanism proposed, the expected emission angle and emission divergence as a function of the detuning will be calculated. The emission angle and divergence are determined by the intersection between the energy of a random lasing peak and the lower polariton dispersion. As the lasing peaks observed in the photoluminescence maps of the MAPB/PMMA sample (figure 5.6) and of the cavity (figure 5.12) are around 2.28 eV, the random lasing peak energy will be considered to be 2.28 eV. The lower polariton dispersion is obtained using the theoretical polariton equation and using the parameters found in figure 4.5 a) of Chapter 4 (n_{eff}=1.75, E_X = 2.355 eV, g=48.7 meV, γ_X=90 meV and γ_{ph}=25 meV) except for the detuning, δ, let as the only free variable. As a reminder, the resolution of the two-level model gives rise to two eigenvalues, one of which is the lower polariton eigenvalue :

$$\mu_{LP}(\theta) = \frac{1}{2}[E_{ph}(\theta) + E_X - i(\gamma_{ph} + \gamma_X)] - \sqrt{g^2 + \frac{1}{4}[E_X - E_{ph}(\theta) + i(\gamma_{ph} - \gamma_X)]^2},$$
$$\text{with} \quad E_{ph}(\theta) = \frac{\delta + E_X}{\sqrt{1 - \frac{sin^2(\theta)}{n_{eff}^2}}}. \tag{5.1}$$

The lower polariton dispersion corresponds to the real part of the lower polariton eigenvalue μ_{LP} of equation 5.1. To obtain the expected emission angle of a random laser peak coupled to the lower polariton branch, one needs to find the angle for which the lower polariton branch equals the random lasing peak energy, i.e. $RE[\mu_{LP}(\theta_{emission})] = E_{peak}$. The analytic solution is not trivial, and, moreover, the calculation of the emission divergence is even more difficult as it requires to take into account the lower linewidth, which corresponds to the imaginary part of the lower polariton eigenvalue μ_{LP} of equation 5.1.

For this reason, a numerical approach is proposed and is illustrated in line (ii) of figure 5.13 for the four positions on the microcavity. The line (i) of figure 5.13 presents for the sake of comparison the same angle-resolved PL pseudo-colour maps above the threshold as in figure 5.12. For each detuning, the lower polariton dispersion, E_{LP}, is plotted as a solid black line and the lower polariton linewidth, γ_{LP}, is taken into account by plotting as a grey shaded area the region of the lower polariton dispersion delimited by the linewidth. The emission angle is given by the intersection between the random lasing peak energy, plotted as a green dashed line, and the lower polariton dispersion. The emission divergence is given by the angular width of the intersection in the shaded area.

For the three detunings shown in figures 5.13 a), b) and c), the lasing emission is composed of two symmetric lasing lobes at non-zero angles of opposite signs with two equal divergences. However, in the fourth position in figure 5.13 d), the lasing emission is in the form of one lasing lobe at normal incidence with a large divergence. The numerical approach reproduces well the results and predicts the transition between the two-lobe

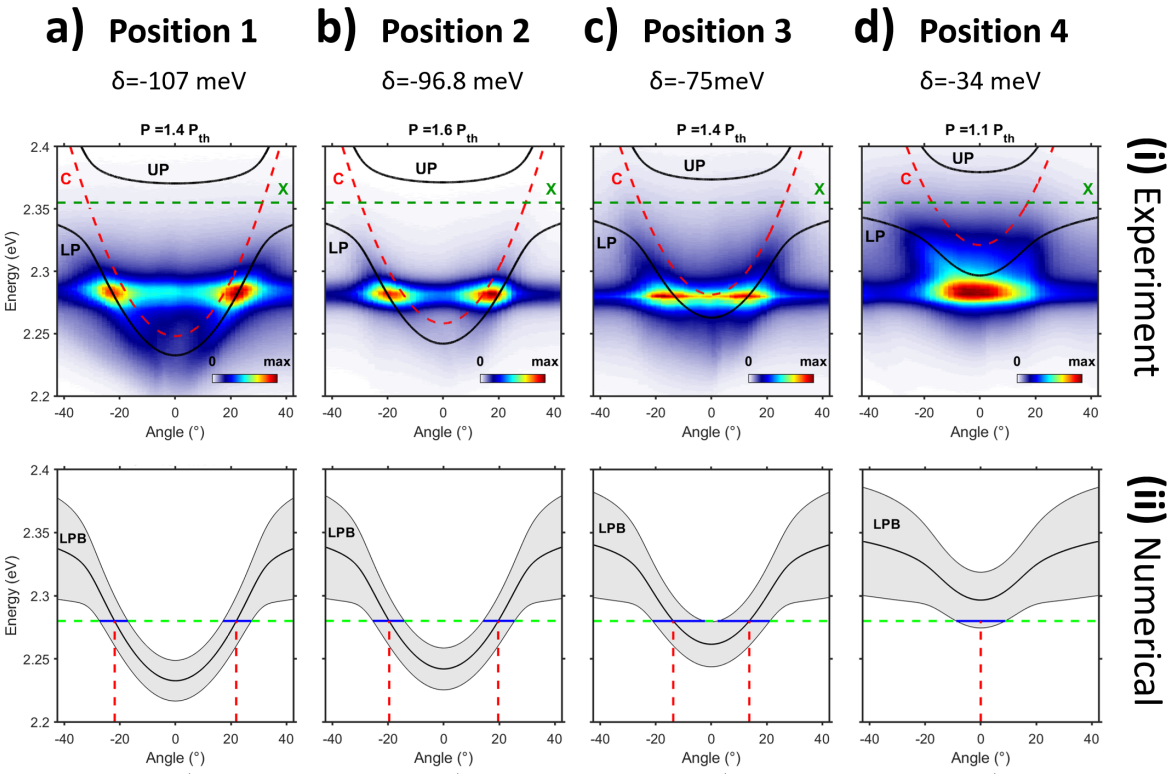

Figure 5.13: Illustration of the numerical approach to predict the angle and divergence of lasing for the different positions. The line (i) corresponds to the same angle-resolved PL pseudo-colour maps as in figure 5.12 of the four position on the microcavity above the threshold. The pseudo-colour maps are in linear scale. The line (ii) is the numerical results corresponding to the detuning of the same four positions. The solid black lines correspond to the lower polariton dispersions. The grey shaded areas correspond to the regions of the lower polariton dispersions delimited by their linewidths. The green dashed line corresponds to the random lasing peak energy. The red dashed lines indicate the lasing angles and the blue solid lines the lasing emission divergences.

and one-lobe configuration. The transition occurs because when the absolute value of the negative detuning decreases, the emission angle decreases while the divergence increases. When the detuning of -74 meV is reached, the two lasing lobes are wide enough and close enough to each other to merge into one lasing lobe centered at normal incidence. The two-lobe configuration occurs for negative detunings larger than -74 meV and the one-lobe configuration for detunings lower than -74 meV. Figure 5.14 illustrates the transition from the detuning -75 meV to -73 meV.

The numerical results for the expected emission angles and divergences are shown in figure 5.15 a) and b), respectively. Only the absolute value of the emission angle is considered. The green and pink stars correspond to the detunings shown in figure 5.14 before and after the transition mentioned above, and the experimental emission angles and divergences are plotted as black crosses. The good agreement met between the results from the experiment and the numerical results is another argument in favour of the lasing mechanism proposed in this PhD.

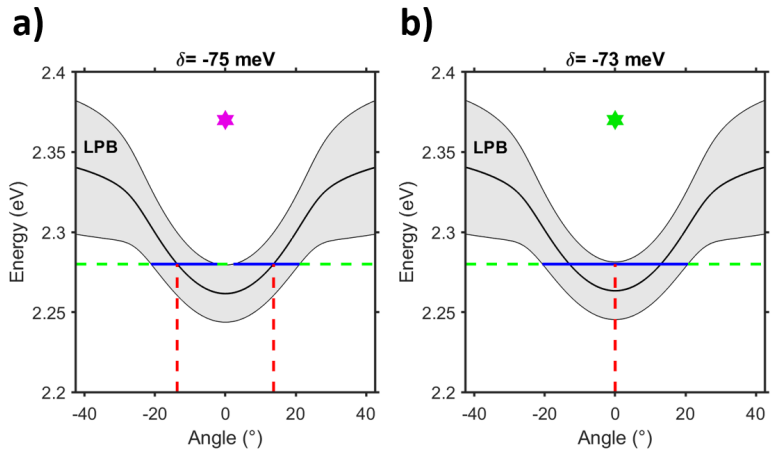

Figure 5.14: Illustration of the transition between the two-lobe and one-lobe configuration from the detuning a) -75 meV to b) -73 meV. The solid black lines correspond to the lower polariton dispersions. The grey shaded areas correspond to the regions of the lower polariton dispersions delimited by their linewidths. The green dashed line corresponds to the random lasing peak energy. The red dashed lines indicate the lasing angles and the blue solid lines the lasing emission divergences.

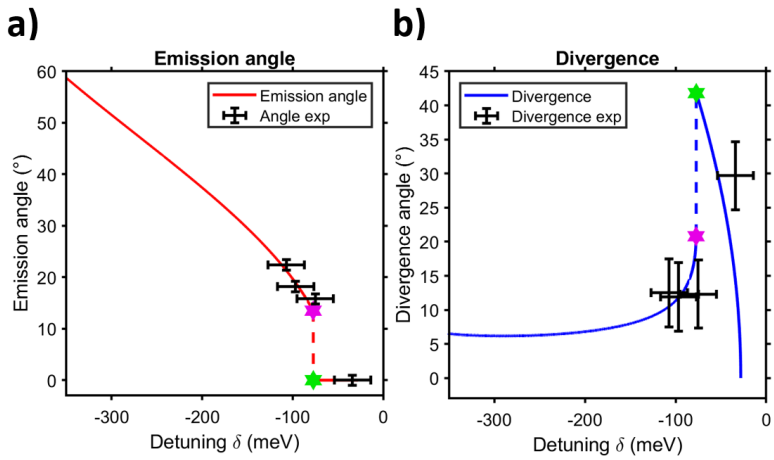

Figure 5.15: Expected emission a) angle and b) divergence obtained with the numerical approach. The black crosses are the experimental data. The purple and pink stars correspond to the detunings before and after the transition mentioned above and shown in figure 5.14.

With the numerical approach, we can see that by varying the detuning it is possible to control the emission angle of the microcavity lasing either at normal incidence or between 13.5 ° and 60 °. However, the divergence of the lasing emission is higher than 10°, and the angles between 0 ° and 13.5 °, called hereafter critical angle, are not accessible. The divergence and critical angle are limited by the lower polariton linewidth, thus by the exciton and the photonic mode linewidths. As the exciton linewidth is intrinsic to the gain material, the only way to decrease the lasing emission divergence and the critical angle is to lower the photonic mode linewidth and thus to improve the microcavity quality factor. Figure 5.16 presents the influence of the microcavity quality factor on the critical angle and the divergence of a lasing emission at 20° (in semilog). The black stars indicate the

quality factor of around 90 of our case. Both the divergence and the critical angles are reduced with the quality factor increasing. However, the reduction is saturated for quality factors higher than 1000, which means that for a MAPB-based microcavity, a quality factor of 1000 is enough to obtain the best performance of the lasing emission directional filtering. The critical angle cannot be lower than 8° and the divergence of a lasing emission at 20° cannot be lower than 3.7°. This is due to the excitonic linewidth, which limits the reduction of the lower polariton linewidth with the quality factor increasing. As a consequence, another way to achieve better filtering would be to use a gain medium exhibiting an exciton with a smaller linewidth.

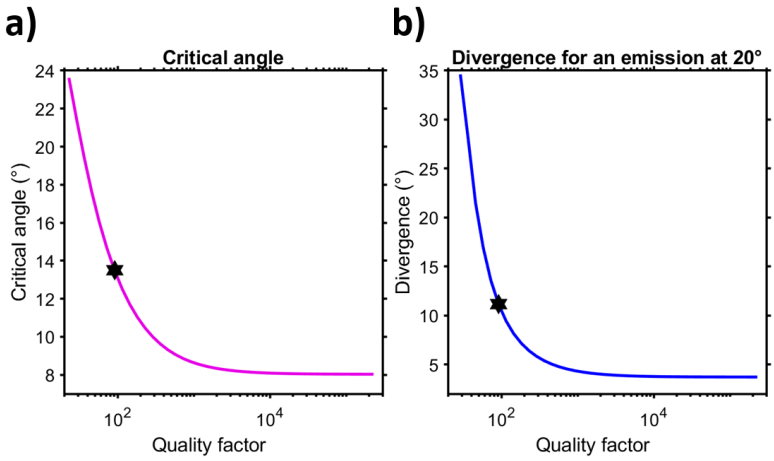

Figure 5.16: Influence of the cavity quality factor on the a) critical angle under which the emission angle cannot be controlled (in semilog) and b) the divergence of a lasing emission at 20° (in semilog). The black stars indicate the quality factor of around 90 of our case.

3.4 Discussion on the nature of the microcavity lasing

Throughout the chapter, we have exposed arguments to support our hypothesis of a random lasing occurring in the MAPB layer and directionally filtered by the microcavity lower polariton dispersion. However, this interpretation needs to be confronted with other types of lasing: the polaritonic lasing of a microcavity in strong coupling regime or the photonic lasing of a Vertical Cavity Surface-Emitting Laser (VCSEL).

First of all, the result obtained on the last position in figure 5.12 d) shows a lasing emission at energies lower than the theoretical lower polariton dispersion, which is in contradiction with polaritonic lasing. In the case of the three positions corresponding to large detunings in figures 5.12 a), b) and c), the lasing emission at large angles could suggest a propagation of a polariton condensate (see section 1.4.3 in Chapter 1), in which the polariton condensate can be observed at non-zero in-plane wavevectors. As a reminder, this phenomenon is due to the polariton interactions with the excitonic reservoir, which ejects the polariton condensate radially from the center of the pump spot and provide the

condensate with kinetic energy [55]. This only takes place when the pump spot size is smaller than the polariton condensate propagation length. For larger spots, the polariton condensate lies at $k_{//}$=0. In our system, the estimated polariton condensate propagation length is around 500nm (see Appendix F). However, lasing emission occurs at large angles whether the microcavity is pumped with a small or a large spot, which discredits the hypothesis of a propagation of polariton condensate. Indeed, the pump laser beam was focused by a 0.9 NA objective for the first position in figure 5.12 a) and by a 5 cm lens for the positions in figures 5.12 b) and c). Consequently, these two arguments lead us to rule out the polaritonic lasing.

It is also questionable whether the lasing is simply the case of a photonic lasing of a VCSEL. However, only one mode would have been expected in the range of energy of the MAPB emission, between 2.2 and 2.4 eV, as the microcavity length is three times the half MAPB emission wavelength ($3\lambda/2$). In our case, several modes were observed at the same time in the PL spectroscopy (see figure 5.8 and figure 5.8) and angle-resolved photoluminescence measurements (see Appendix C for the angle-integrated PL spectra). The multi-modal aspect of the microcavity lasing is then the main argument for excluding the VCSEL photonic lasing as a possible explanation for the lasing.

4 Conclusion of the chapter

In this chapter, the lasing action of the $3\lambda/2$ MAPB-based microcavity, as well as the random lasing action of a sample of MAPB thin-film covered by PMMA, have been studied via PL spectroscopy and angle-resolved photoluminescence measurements. The lasing of the microcavity results in a multi-modal lasing emission at large angles or zero-angle. The emission angle and emission divergence depends on the detunings, and we can obtain the angles of 0°, 22.4°, 18.2° and 15.8° experimentally. This result can not be explained in term of a classical lasing occurring in a VCSEL or by the polaritonic lasing. A hypothesis has been proposed to explain the phenomenon: the lasing takes place as random lasing in the MAPB layer and is filtered directionally by the lower polariton dispersion. Several arguments support this hypothesis. The microcavity is composed of the same MAPB and PMMA layers in which random lasing was observed. The microcavity lasing peaks are at the same range of energy as the random lasing peaks. The characteristic pseudo-cavity lengths obtained for the microcavity lasing and the MAPB/PMMA random lasing are similar. Finally, a numerical approach can reproduce and predict the lasing emission angle and emission divergence of such a lasing. In summary, we have shown that in such a structure, the angle and divergence of the lasing emission can be controlled by changing the detuning and the cavity quality factor. If one can achieve a laser in which the detuning can be controlled dynamically after fabrication, one could change the lasing direction at will, which could be interesting for lasing mapping applications, similar to the LIDAR (light imaging, detection, and ranging) technology.

Conclusion

The halide perovskites have recently emerged in the framework of photovoltaics and light-emitting devices such as LEDs and lasers, and the state of the art is already rich and various. The good optical properties of halide perovskites make them candidates for future polaritonic devices. Indeed, the strong coupling was demonstrated with different types of perovskites, and polaritonic lasing could be obtained with some of the best systems. The perovskites lasers, conventional and polaritonic, are today optically pumped in the pulsed regime. However, the good charge transport properties of the perovskites and the recent results on continuous wave laser pumped perovskites lasers give hope to a future electrical injection of the perovskite lasers. Due to the cost-effectiveness of the perovskite deposition and their good performance, commercialized perovskite light-emitting devices could appear in the near future. The remaining barriers for this perspective are the low stability and low heat tolerance of the perovskites. However, much progress has been obtained on these points over the past few years.

The search for cost-effective and performing lasers devices can be done by optimizing either the gain medium or the lasing mechanism. The aforementioned polaritonic laser is an example of a lasing mechanism permitting reaching efficient lasers due to their very low thresholds. Coupled with perovskite, the polaritonic devices would also be cost-effective. On the other hand, random lasing is an example of a lasing mechanism which would reduce the production costs. Indeed, random lasing occurs in highly disordered gain media in which a fine design of the laser structure is not necessary. The multi-directionality and low coherence, compared to usual lasers, can satisfy various applications such as speckle-free imaging. However, for typical laser applications, the directionality of the lasing devices is desired.

The result of this thesis is a part of this broad context combining the quest of cost-effective and performing laser and the halide perovskites.

Strong coupling regime at room temperature was first demonstrated in chapter 4 in a large surface spin-coated bromide perovskite-based $3\lambda/2$ microcavity. Because of the overall roughness studied in chapter 3, the detuning of the microcavity (the difference between the excitonic energy and the photonic mode energy at normal incidence) could be tuned by changing the position probed. A large average Rabi splitting of 70 meV and an average microcavity quality factor of 90 were measured. Besides the polaritonic lasers,

the perspectives of the exciton-polaritons are all-optical logical devices in which the polaritons carrying the information would propagate over macroscopic distance to be processed in logical blocks such as polaritonic transistors. Therefore, the strong coupling regime demonstrated in this thesis shows that the cavity exciton-polaritons can be obtained at room temperature over a large surface thin film whose deposition is at low cost. Moreover, recent demonstrations on perovskite thin-film patterning into microstructures via nanoimprint and lithography technologies could go in the way of a perovskite polaritonic single-chip logical device. For these reasons, this work was published on ACS photonics [15].

In Chapter 5, the lasing of the bromide perovskite-based microcavity was studied. A random lasing emitting in the green and directionally filtered by the lower polariton dispersion curve was demonstrated in the bromide perovskite-based microcavity. The random lasing directionality can be controlled by changing the detuning of the microcavity, which here could be tuned by changing the position probed. The angles of 0°, 15.8°, 18.2°, and 22.4° were experimentally obtained. We confirmed numerically that the emission angle can be controlled with the microcavity detuning and emission angles from 10° to 60° or higher can be reached. The lasing divergences were rather large, but it was shown numerically that the emission divergence can be reduced by increasing the cavity quality factor. The quality factor could be increased in our case by replacing the silver mirror by a Bragg mirror, however it would represent as a challenge due to the fragility of the perovskites at high temperatures.

This result is interesting in terms of fundamental physics by the original mechanism proposed which combines two intriguing physical concepts: the cavity exciton-polaritons and the random lasing. Regarding the applications, the control of random lasing emission could reveal interesting in the area of optoelectronics, for example, for the LIDAR technology. Additionally, the lasing emission of the bromide perovskite-based perovskite was in the green region. As a consequence, this result is currently under preparation for publication.

Other perspectives can be envisioned, such as the study of electrical injection of polycrystalline $CH_3NH_3PbBr_3$ thin films in the prospect of obtaining random lasing. This work would be carried out in collaboration with the XLIM laboratory in Limoges, which is specialized in light-emitting devices and collaborate with our team. Working on $CH_3NH_3PbBr_3$ thin single crystals using the AVCC methods elaborated by Ferdinand Lédée in our team could be another future project [217]. The quality factor of the cavity would be increased due to the better crystal quality, which would increase the polariton lifetime. Thanks to the internal reflection in the $CH_3NH_3PbBr_3$ crystal, one could consider a cavity composed of only one Bragg mirror, with one of the crystal facet serving as the closing mirror. Finally, with a much smaller roughness, the random lasing would be suppressed or strongly decreased, which would give hope on obtaining polaritonic lasing.

Appendices

A Control measurements for the pump power-dependent measurements in Chapter 5

For the PL spectroscopy and angle-resolved photoluminescence measurements as a function of the pumping power of the MAPB/PMMA sample and the 3λ/2 MAPB-based microcavity (in Chapter 5, section 2 and 3), control measurements were carried on to determine the pumping powers for which the perovskite was not damaged. The PL intensities, I_{P0}, from the samples excited at a low fixed pumping power, P_0, are measured at the beginning of the experiment. During the experiment, the pumping power is increased, and after the measurements at certain pumping powers (control points), the PL intensity at low pumping power, I'_{P0}, is measured again. If the PL intensity, I'_{P0}, is decreased by more than 20% compared to I_{P0}, the results obtained with this power or with higher powers are excluded.

B Conversion of the lasing thresholds

This appendix details the conversion of the pumping threshold of Chapter 5 in average power (in μW) to pumping threshold in Fluences (in $\mu J/cm^2$) which can be retrieved with the following equation:

$$F_{th} = \frac{P_{th}}{f_{rep}S} = \frac{P_{th}}{f_{rep}\pi(\frac{\omega}{2})^2}, \tag{B1}$$

where P_{th} is the threshold in average power, F_{th} is the threshold in fluence, f_{rep} is the repetition rate of the pumping laser (1 kHz), $S = \pi * (\omega/2)^2$ and ω are respectively the area and the waist of the pump laser beam, which depend on the objective or lens used to focus the pump beam on the sample.

During the experiments, the laser pump power was measured with a power-meter before the laser was focused. Hence, the pump laser could be absorbed by, the objective or the lens and by the layers before attaining the MAPB layer where the gain occurs. Moreover, Fresnel reflections occur at the interfaces between two consecutive layers. These losses are then taken into account for the conversion of the threshold from power to fluence. The absorptions and Fresnel reflections were calculated using the layers refractive indices at 400 nm and the Fresnel equations. The values of the losses are reported in table B1.

Layer	Losses by absorption (%)	Interfaces	Reflectivity at interfaces (%)
Ag	86.2	Air/Ag	96.38
PMMA	7.7	Ag/PMMA	95.61
Bragg mirror	0	PMMA/MAPB	5.43
Lens	0	Bragg mirror	34.1
		SiO2/MAPB	6.24
		Lens (2 interfaces)	4

Table B1: Losses of the pumping laser by the layers absorptions and the reflections at the interfaces

The waist of the pump laser was measured to be 50 μm when focused with a 5 cm lens. However, the size of the pump spot has not been measured when focused with the 0.6 and 0.9 NA objectives. This prevents to precisely calculate the thresholds in fluence. The laser spot size for the 0.9 NA objective will be considered to be 0.5 μm, around the diffraction limit, and for the 0.6 NA objective 1 μm in order to have orders of magnitude of the fluences.

C Additionnal data for the ARPL maps in Chapter 5

This appendix gives additional data of the positions studied on the MAPB/PMMA sample and the 3λ/2 MAPB-based microcavity with the Fourier spectroscopy set-up in figure 5.6 and figure 5.12 a), b), c), and d).

C.1 Position RL2 in figure 5.6

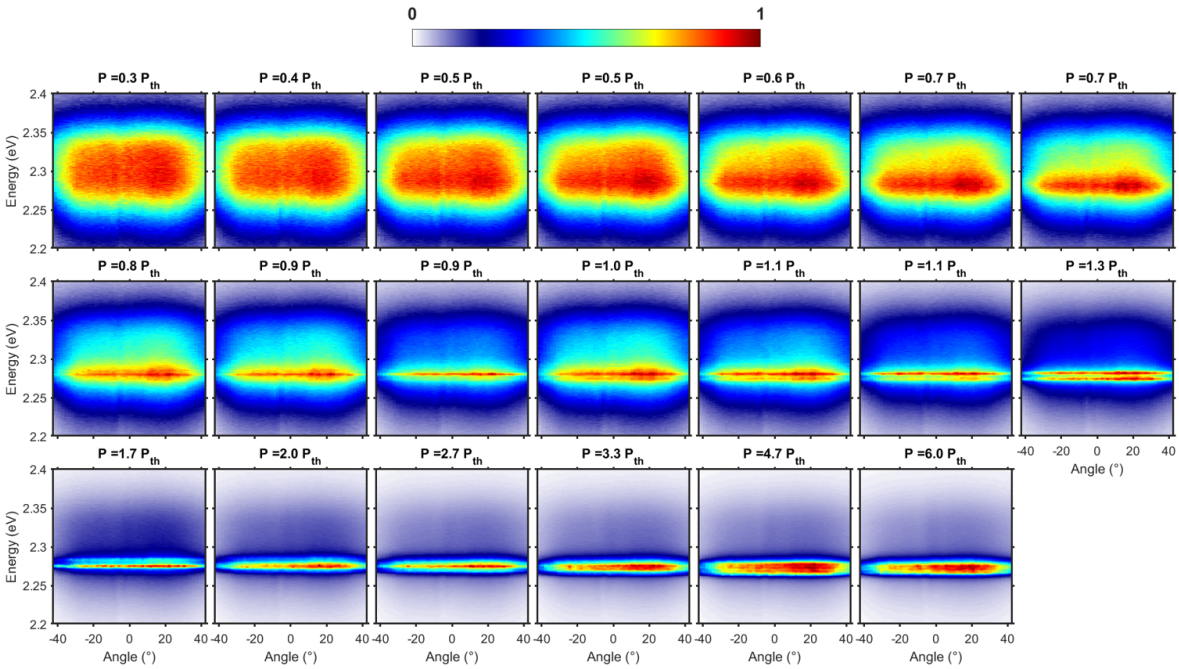

Figure C1: Angle-resolved photoluminescence maps of the position RL2 on the MAPB/PMMA sample at different pumping powers (from 0.3 to 6.0 P_{th}). The pseudo-colour maps are in linear scale.

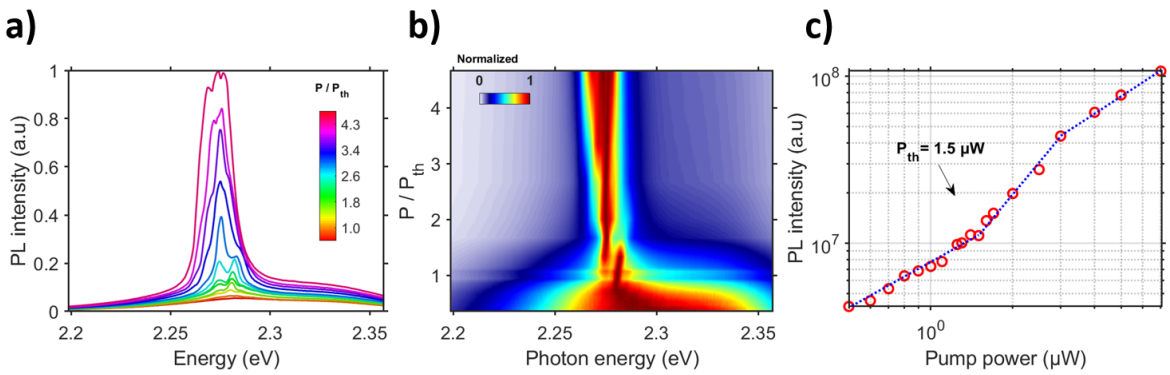

Figure C2: Angle-integrated PL of the position RL2 on the MAPB/PMMA. a) Angle-integrated PL spectra at different pumping powers. b) Pseudo-colour map (in linear scale) of the normalized Angle-integrated PL spectra as a function of P/P_{th}. c) Curve of the integrated PL intensity as a function of the pumping power.

C.2 Position 1 in figure 5.12 a)

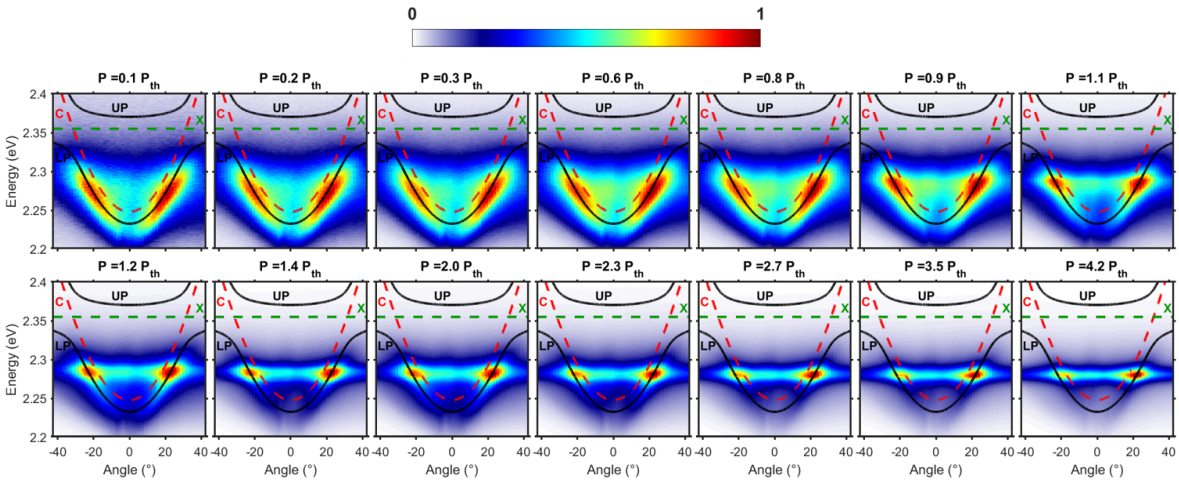

Figure C3: Angle-resolved photoluminescence maps of the position 1 on the 3λ/2 MAPB-based microcavity at different pumping powers (from 0.1 to 15.4 P_{th}). The pseudo-colour maps are in linear scale. On top of each ARPL map are plotted the fitted polariton dispersions (in black) along with the uncoupled excitonic energy (in green) and photonic modes (in red).

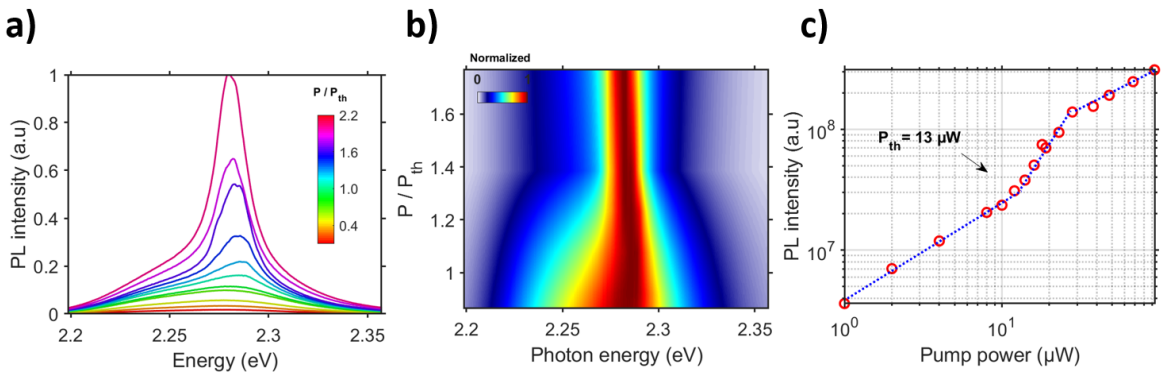

Figure C4: Angle-integrated PL of the position 1 on the 3λ/2 MAPB-based microcavity. a) Angle-integrated PL spectra at different pumping powers. b) Pseudo-colour map (in linear scale) of the normalized Angle-integrated PL spectra as a function of P/P_{th}. c) Curve of the integrated PL intensity as a function of the pumping power.

C.3 Position 2 in figure 5.12 b)

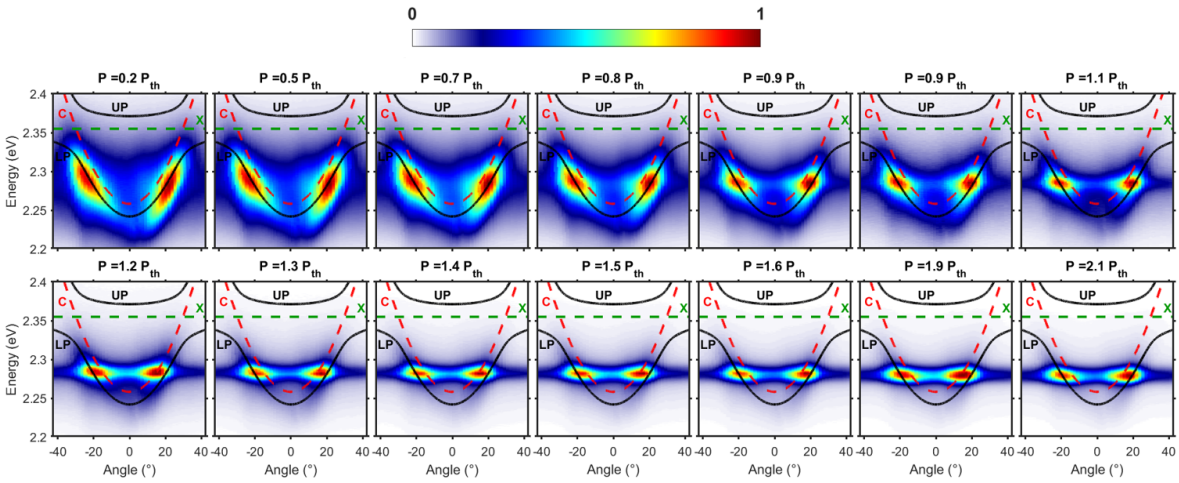

Figure C5: Angle-resolved photoluminescence maps of the position 2 on the 3λ/2 MAPB-based microcavity at different pumping powers (from 0.1 to 15.4 P_{th}). The pseudo-colour maps are in linear scale. On top of each ARPL map are plotted the fitted polariton dispersions (in black) along with the uncoupled excitonic energy (in green) and photonic modes (in red).

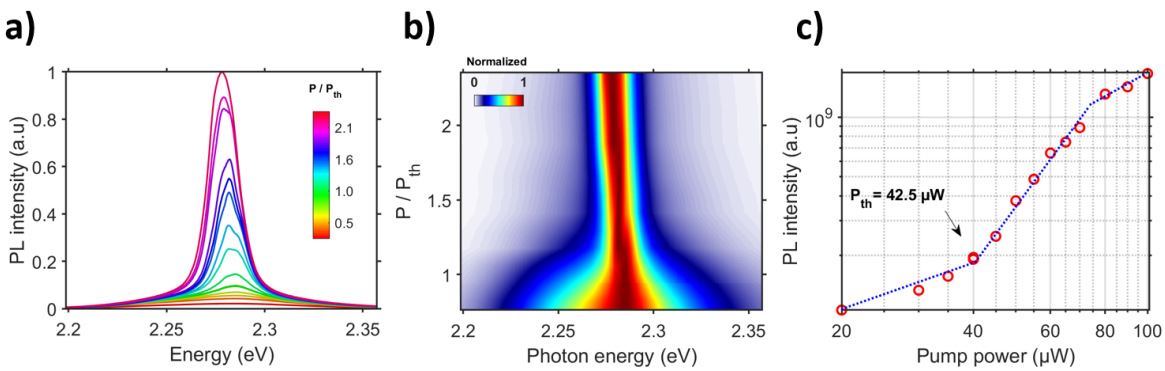

Figure C6: Angle-integrated PL of the position 2 on the 3λ/2 MAPB-based microcavity. a) Angle-integrated PL spectra at different pumping powers. b) Pseudo-colour map (in linear scale) of the normalized Angle-integrated PL spectra as a function of P/P_{th}. c) Curve of the integrated PL intensity as a function of the pumping power.

C.4 Position 3 in figure 5.12 c)

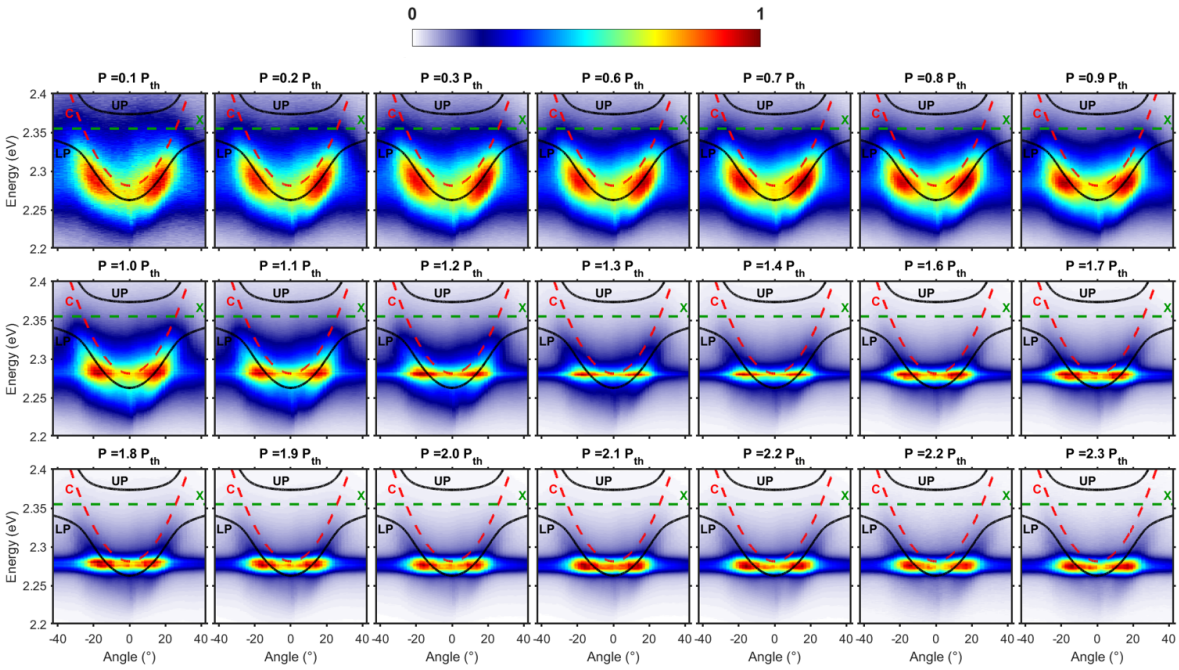

Figure C7: Angle-resolved photoluminescence maps of the position 2 on the 3λ/2 MAPB-based microcavity at different pumping powers (from 0.1 to 15.4 P_{th}). The pseudo-colour maps are in linear scale. On top of each ARPL map are plotted the fitted polariton dispersions (in black) along with the uncoupled excitonic energy (in green) and photonic modes (in red).

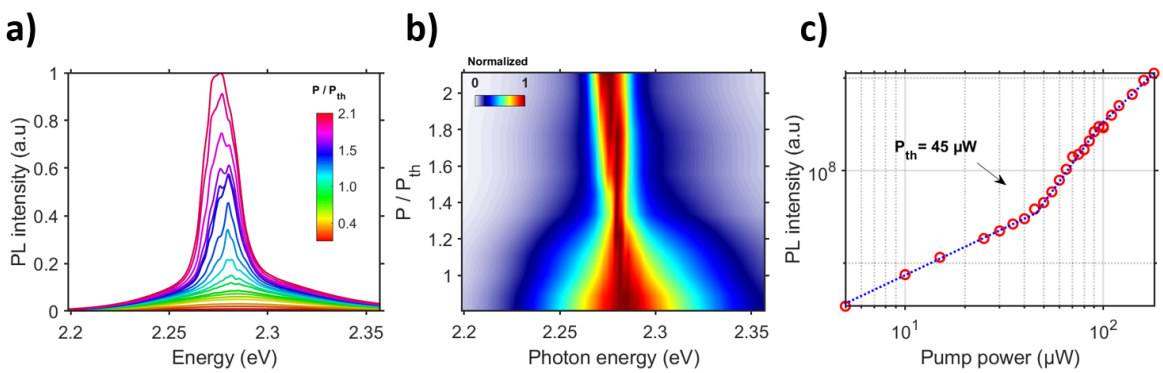

Figure C8: Angle-integrated PL of the position 3 on the 3λ/2 MAPB-based microcavity. a) Angle-integrated PL spectra at different pumping powers. b) Pseudo-colour map (in linear scale) of the normalized Angle-integrated PL spectra as a function of P/P_{th}. c) Curve of the integrated PL intensity as a function of the pumping power.

C.5 Position 4 in figure 5.12 d)

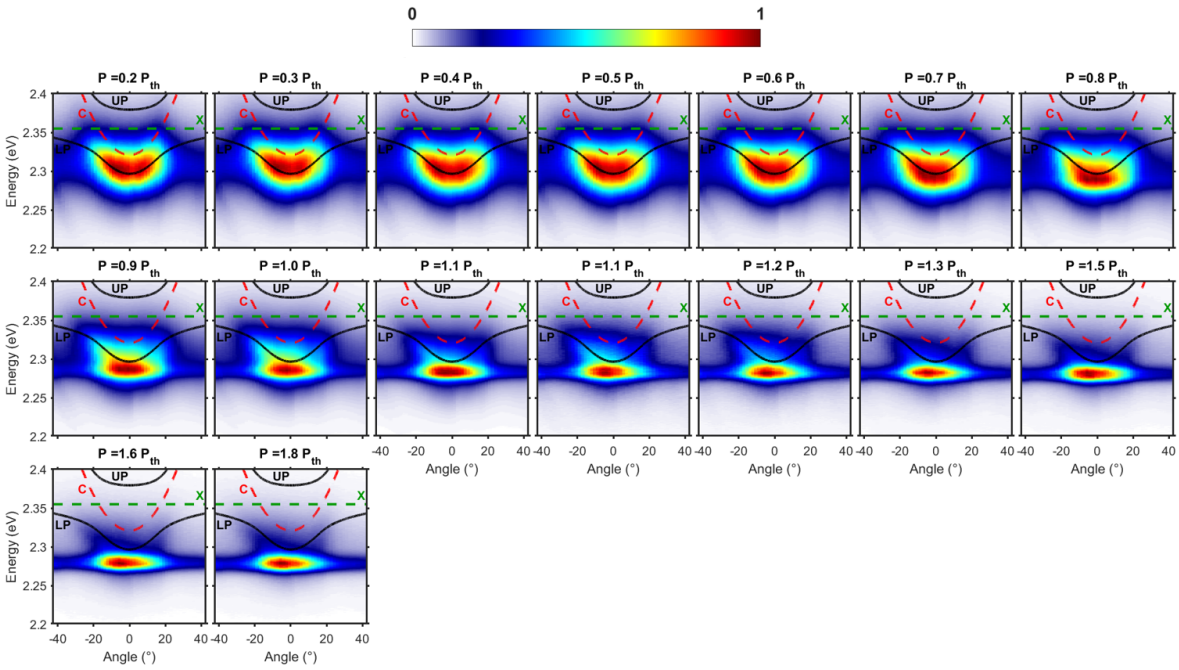

Figure C9: Angle-resolved photoluminescence maps of the position 2 on the 3λ/2 MAPB-based microcavity at different pumping powers (from 0.1 to 15.4 P_{th}). The pseudo-colour maps are in linear scale. On top of each ARPL map are plotted the fitted polariton dispersions (in black) along with the uncoupled excitonic energy (in green) and photonic modes (in red).

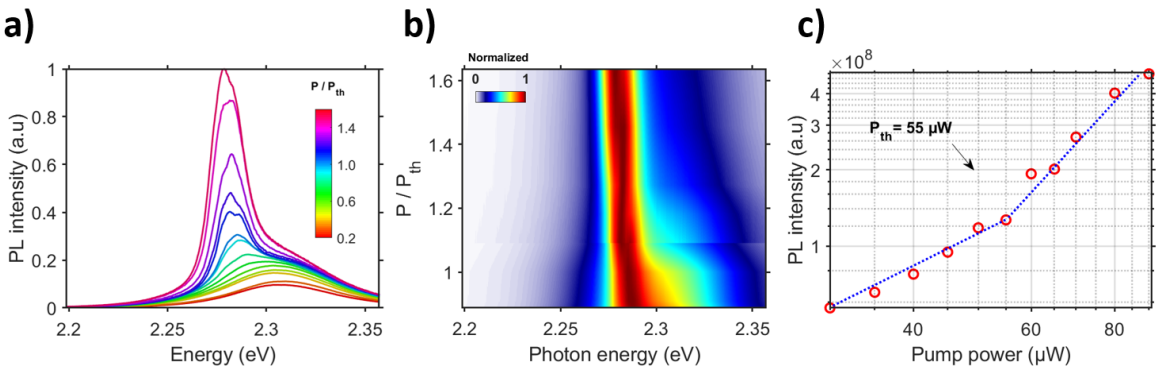

Figure C10: Angle-integrated PL of the position 4 on the 3λ/2 MAPB-based microcavity. a) Angle-integrated PL spectra at different pumping powers. b) Pseudo-colour map (in linear scale) of the normalized Angle-integrated PL spectra as a function of P/P_{th}. c) Curve of the integrated PL intensity as a function of the pumping power.

D Fit with the two-level system of the ARPL maps in Chapter 5

This appendix shows the fitting method of the lower polariton dispersion curves of the four position in figures 5.12 a-i), b-i), c-i) and d-i). The experimental dispersion curves are obtained by fitting slices of the photoluminescence maps (between -20 ° and 20 °) with a Lorentzian function. The Lorentzian centres are reported in energy/angle diagrams shown in figure D1. The collected dispersions curves are then fitted to the two-level model using the parameters found in figure 4.5 a) of Chapter 4 (n_{eff}=1.75, E_X = 2.355 eV, g=48.7 meV, γ_X=90 meV and γ_{ph}=25 meV) and with the detuning, δ, as the only free parameter.

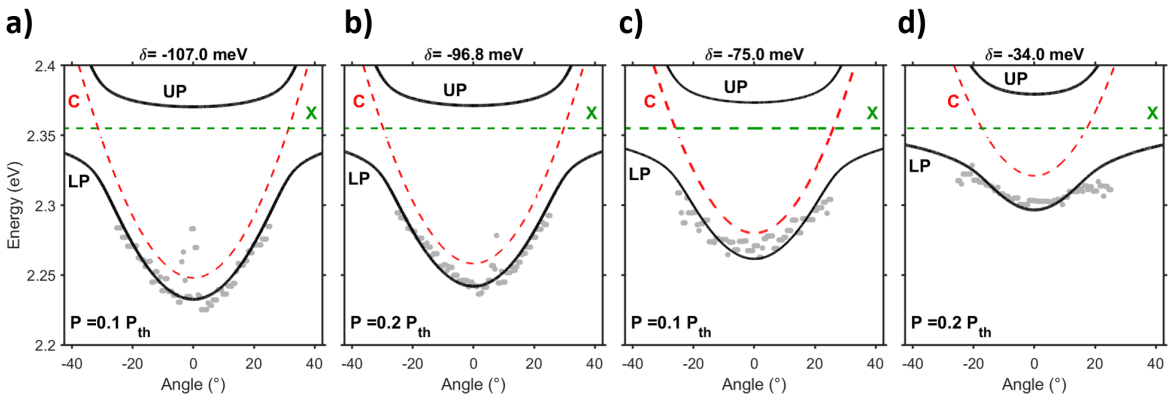

Figure D1: a) to d) Fitting of the lower polariton dispersion curves of the four positions in figures 5.12 a-i), b-i), c-i) and d-i), respectively. The grey dots represent the experimental data from the Lorentzian fits of the slices at different angles. The fitted polariton dispersions are plotted in black, the uncoupled excitonic energy in green and the uncoupled photonic mode in red.

E Slices at given angles and energies of the ARPL maps in Chapter 5

This appendix shows the slices taken at given angles and at given energies of the ARPL maps in figures 5.12 a-ii), b-ii), c-ii), and d-ii). In figure E1, the ARPL maps are reproduced in the row (i), the slices taken at given angles (vertical slices) are shown in the row (ii), and the slices taken at given energies (horizontal slices) are shown in the row (iii). The vertical slices of the row (ii) helps to better discern the lasing peaks. The fitting of the horizontal slices in row (III) with Lorentzian and Gaussian functions permits to obtain the values of the lasing peaks angles and divergences.

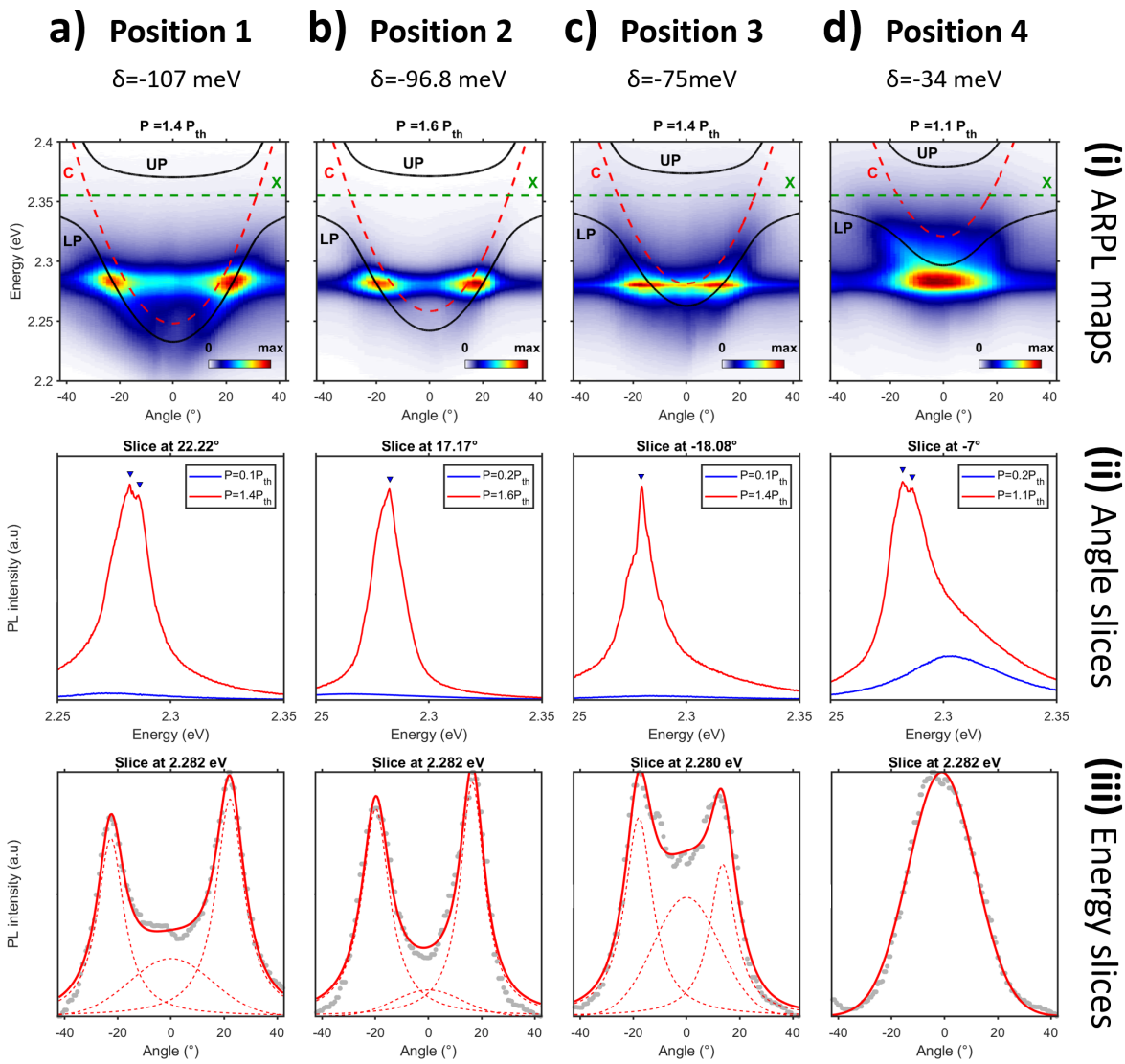

Figure E1: a) to d) Slices at given angles and given energies of the ARPL maps in figures 5.12 a-ii), b-ii), c-ii), and d-ii), respectively. The row (i) shows the ARPL maps with the fitted polariton dispersions plotted in black the uncoupled excitonic energy and photonic modes in green and red respectively. The pseudo-colour maps are in linear scale. The row (ii) shows the slices of the ARPL maps for given angles. The row (iii) shows the slices of the ARPL maps for given energies fitted with Lorentzian and Gaussian functions.

F Estimation of the polariton propagation length

The polariton propagation length is given by :

$$L = v_{LP} \times t_{LP}, \tag{F1}$$

where t_{LP} is the polariton lifetime and v_{LP} is the polariton velocity.

The polariton lifetime can be considered to be close to the photonic mode lifetime $t_{ph} = \hbar Q/2E_0$, where $\hbar$ is the reduced Planck constant, E_0 the photonic mode energy at normal incidence, and Q the quality factor. In our case, Q = 92 and E_0 = 2.248, 2.258, and 2.28 eV for the figures 5.12 a), b) and c), respectively. The polariton lifetime is estimated to be $t_{LP} \approx 13$ fs.

The polariton velocity is given by:

$$v_{LP} = (\hbar \times k_{prop})/m_{LP}, \tag{F2}$$

where k_{prop} is the wavenumber of the propagated polariton condensate [55], and m_{LP} is the lower polariton effective mass.

The propagated polariton condensate wavenumber, k_{prop}, is related to the polariton condensate energy, E_{BEC}, and emission angle, θ_{BEC} as $k_{prop} = (E_{BEC}/c\hbar)\sin(\theta_{BEC})$. In our case, E_{BEC} and θ_{BEC} are the lasing emission energy and angle: $E_{lasing} \approx 2.28$ eV and θ_{lasing}= 22.4°, 18.2° and 15.8° for the figures 5.12 a), b) and c), respectively.

The polariton effective mass, m_{LP}, is related to the curvature of the lower polariton branch at $k_{//} = 0$. It can be obtained by fitting the lower polariton dispersion at low $k_{//}$ with a parabola ($E_p = E_0^p + Ck_{//}^2$). The polariton effective mass, m_{LP}, is retrieved with $m_{LP} = \hbar^2/(2 \times C)$, where C is the coefficient of the parabola. The lower polariton effective mass is found respectively to be 8.3, 8.4 and 8.9 $eV.ps^2.\mu m^{-2}$ in the case of the figures 5.12 a), b) and c) .

The polariton propagation lengths of 470 nm, 377 nm, and 309 nm are found respectively for the figures 5.12 a), b) and c).

Bibliography

[1] "The nobel prize in physics 2014. nobelprize.org. nobel media ab 2019. fri. 2 aug 2019.," *https://www.nobelprize.org/prizes/physics/2014/summary/*.

[2] M. Auf der Maur, A. Pecchia, G. Penazzi, W. Rodrigues, and A. Di Carlo, "Efficiency drop in green InGaN/GaN light emitting diodes: The role of random alloy fluctuations," *Phys. Rev. Lett.*, vol. 116, p. 027401, Jan 2016.

[3] S. Karpov, "Strategies for creating efficient, beautiful whites," *Compound Semiconductor*, pp. 44–47, 2015.

[4] D. Schiavon, M. Binder, M. Peter, B. Galler, P. Drechsel, and F. Scholz, "Wavelength-dependent determination of the recombination rate coefficients in single-quantum-well gainn/gan light emitting diodes," *physica status solidi (b)*, vol. 250, no. 2, pp. 283–290, 2013.

[5] C. Weisbuch, M. Nishioka, A. Ishikawa, and Y. Arakawa, "Observation of the coupled exciton-photon mode splitting in a semiconductor quantum microcavity," *Phys. Rev. Lett.*, vol. 69, pp. 3314–3317, Dec 1992.

[6] A. Imamog¯lu, R. J. Ram, S. Pau, and Y. Yamamoto, "Nonequilibrium condensates and lasers without inversion: Exciton-polariton lasers," *Phys. Rev. A*, vol. 53, pp. 4250–4253, Jun 1996.

[7] J. Kasprzak, M. Richard, S. Kundermann, A. Baas, P. Jeambrun, J. M. J. Keeling, F. M. Marchetti, M. H. Szymańska, R. André, J. L. Staehli, V. Savona, P. B. Littlewood, B. Deveaud, and L. S. Dang, "Bose-einstein condensation of exciton polaritons," *Nature*, vol. 443, p. 409, Sept. 2006.

[8] "Nrel efficiency chart (accessed jul04, 2019)," *https://www.nrel.gov/pv/assets/pdfs/best-research-cell-efficiencies.20190923.pdf*.

[9] G. Xing, N. Mathews, S. S. Lim, N. Yantara, X. Liu, D. Sabba, M. Grätzel, S. Mhaisalkar, and T. C. Sum, "Low-temperature solution-processed wavelength-tunable perovskites for lasing," *Nature Materials*, vol. 13, p. 476, Mar. 2014.

[10] F. Deschler, M. Price, S. Pathak, L. E. Klintberg, D.-D. Jarausch, R. Higler, S. Hüttner, T. Leijtens, S. D. Stranks, H. J. Snaith, M. Atatüre, R. T. Phillips, and R. H. Friend, "High photoluminescence efficiency and optically pumped lasing in solution-processed mixed halide perovskite semiconductors," *The Journal of Physical Chemistry Letters*, vol. 5, no. 8, pp. 1421–1426, 2014.

[11] B. R. Sutherland, S. Hoogland, M. M. Adachi, C. T. O. Wong, and E. H. Sargent, "Conformal organohalide perovskites enable lasing on spherical resonators," *ACS Nano*, vol. 8, no. 10, pp. 10947–10952, 2014. PMID: 25313937.

[12] Z.-K. Tan, R. S. Moghaddam, M. L. Lai, P. Docampo, R. Higler, F. Deschler, M. Price, A. Sadhanala, L. M. Pazos, D. Credgington, F. Hanusch, T. Bein, H. J. Snaith, and R. H. Friend, "Bright light-emitting diodes based on organometal halide perovskite," *Nature Nanotechnology*, vol. 9, p. 687, Aug. 2014.

[13] C. S. Ponseca, T. J. Savenije, M. Abdellah, K. Zheng, A. Yartsev, T. Pascher, T. Harlang, P. Chabera, T. Pullerits, A. Stepanov, J.-P. Wolf, and V. Sundström, "Organometal halide perovskite solar cell materials rationalized: Ultrafast charge generation, high and microsecond-long balanced mobilities, and slow recombination," *Journal of the American Chemical Society*, vol. 136, no. 14, pp. 5189–5192, 2014.

[14] G. Xing, N. Mathews, S. Sun, S. S. Lim, Y. M. Lam, M. Grätzel, S. Mhaisalkar, and T. C. Sum, "Long-range balanced electron- and hole-transport lengths in organic-inorganic ch3nh3pbi3," *Science*, vol. 342, no. 6156, pp. 344–347, 2013.

[15] P. Bouteyre, H. S. Nguyen, J.-S. Lauret, G. Trippé-Allard, G. Delport, F. Lédée, H. Diab, A. Belarouci, C. Seassal, D. Garrot, F. Bretenaker, and E. Deleporte, "Room-temperature cavity polaritons with 3d hybrid perovskite: Toward large-surface polaritonic devices," *ACS Photonics*, vol. 6, no. 7, pp. 1804–1811, 2019.

[16] M. Fox, "Optical properties of solids," 2002.

[17] L. Zheng, N. F. Polizzi, A. R. Dave, A. Migliore, and D. N. Beratan, "Where is the electronic oscillator strength? mapping oscillator strength across molecular absorption spectra," *The Journal of Physical Chemistry A*, vol. 120, no. 11, pp. 1933–1943, 2016. PMID: 26950828.

[18] E. N. Forsman and K. C. Clark, "Measurement of the oscillator strength of the o I($^1s-^1p^o$) transition at 1217.6 å," *Phys. Rev. A*, vol. 7, pp. 1203–1208, Apr 1973.

[19] G. E. Jellison and F. A. Modine, "Parameterization of the optical functions of amorphous materials in the interband region," *Applied Physics Letters*, vol. 69, no. 3, pp. 371–373, 1996.

[20] J. Tauc, R. Grigorovici, and A. Vancu, "Optical properties and electronic structure of amorphous germanium," *physica status solidi (b)*, vol. 15, no. 2, pp. 627–637, 1966.

[21] D. M. Whittaker, P. Kinsler, T. A. Fisher, M. S. Skolnick, A. Armitage, A. M. Afshar, M. D. Sturge, and J. S. Roberts, "Motional narrowing in semiconductor microcavities," *Phys. Rev. Lett.*, vol. 77, pp. 4792–4795, Dec 1996.

[22] L. C. Andreani, G. Panzarini, and J.-M. Gérard, "Strong-coupling regime for quantum boxes in pillar microcavities: Theory," *Phys. Rev. B*, vol. 60, pp. 13276–13279, Nov 1999.

[23] E. M. Purcell, "Spontaneous transition probabilities in radio-frequency spectroscopy," *Phys. Rev*, vol. 69, p. 681, 1946.

[24] T. Freixanet, B. Sermage, A. Tiberj, and R. Planel, "In-plane propagation of excitonic cavity polaritons," *Phys. Rev. B*, vol. 61, pp. 7233–7236, Mar 2000.

[25] M. Galbiati, L. Ferrier, D. D. Solnyshkov, D. Tanese, E. Wertz, A. Amo, M. Abbarchi, P. Senellart, I. Sagnes, A. Lemaître, E. Galopin, G. Malpuech, and J. Bloch, "Polariton condensation in photonic molecules," *Phys. Rev. Lett.*, vol. 108, p. 126403, Mar 2012.

[26] D. Tanese, H. Flayac, D. Solnyshkov, A. Amo, A. Lemaître, E. Galopin, R. Braive, P. Senellart, I. Sagnes, G. Malpuech, and J. Bloch, "Polariton condensation in solitonic gap states in a one-dimensional periodic potential," *Nature Communications*, vol. 4, p. 1749, Apr. 2013.

[27] H. S. Nguyen, D. Vishnevsky, C. Sturm, D. Tanese, D. Solnyshkov, E. Galopin, A. Lemaître, I. Sagnes, A. Amo, G. Malpuech, and J. Bloch, "Realization of a double-barrier resonant tunneling diode for cavity polaritons," *Phys. Rev. Lett.*, vol. 110, p. 236601, Jun 2013.

[28] C. Ciuti, P. Schwendimann, and A. Quattropani, "Parametric luminescence of microcavity polaritons," *Phys. Rev. B*, vol. 63, p. 041303, Jan 2001.

[29] I. Carusotto and C. Ciuti, "Quantum fluids of light," *Rev. Mod. Phys.*, vol. 85, pp. 299–366, Feb 2013.

[30] A. Amo, J. Lefrère, S. Pigeon, C. Adrados, C. Ciuti, I. Carusotto, R. Houdré, E. Giacobino, and A. Bramati, "Superfluidity of polaritons in semiconductor microcavities," *Nature Physics*, vol. 5, pp. 805–810, Nov. 2009.

[31] K. G. Lagoudakis, M. Wouters, M. Richard, A. Baas, I. Carusotto, R. André, L. S. Dang, and B. Deveaud-Plédran, "Quantized vortices in an exciton-polariton condensate," *Nature Physics*, vol. 4, pp. 706–710, Sept. 2008.

[32] H. S. Nguyen, D. Gerace, I. Carusotto, D. Sanvitto, E. Galopin, A. Lemaître, I. Sagnes, J. Bloch, and A. Amo, "Acoustic black hole in a stationary hydrodynamic flow of microcavity polaritons," *Phys. Rev. Lett.*, vol. 114, p. 036402, Jan 2015.

[33] P. St-Jean, V. Goblot, E. Galopin, A. Lemaître, T. Ozawa, L. Le Gratiet, I. Sagnes, J. Bloch, and A. Amo, "Lasing in topological edge states of a one-dimensional lattice," *Nature Photonics*, vol. 11, pp. 651–656, Oct. 2017.

[34] S. Klembt, T. H. Harder, O. A. Egorov, K. Winkler, R. Ge, M. A. Bandres, M. Emmerling, L. Worschech, T. C. H. Liew, M. Segev, C. Schneider, and S. Höfling, "Exciton-polariton topological insulator," *Nature*, vol. 562, pp. 552–556, Oct. 2018.

[35] T. Gao, P. S. Eldridge, T. C. H. Liew, S. I. Tsintzos, G. Stavrinidis, G. Deligeorgis, Z. Hatzopoulos, and P. G. Savvidis, "Polariton condensate transistor switch," *Phys. Rev. B*, vol. 85, p. 235102, Jun 2012.

[36] C. Sturm, D. Tanese, H. S. Nguyen, H. Flayac, E. Galopin, A. Lemaître, I. Sagnes, D. Solnyshkov, A. Amo, G. Malpuech, and J. Bloch, "All-optical phase modulation in a cavity-polariton mach-zehnder interferometer," *Nature Communications*, vol. 5, p. 3278, Feb. 2014.

[37] F. Marsault, H. S. Nguyen, D. Tanese, A. Lemaître, E. Galopin, I. Sagnes, A. Amo, and J. Bloch, "Realization of an all optical exciton-polariton router," *Applied Physics Letters*, vol. 107, no. 20, p. 201115, 2015.

[38] M. Born and E. Wolf, "Principles of optics," 1964.

[39] R. P. Stanley, R. Houdré, C. Weisbuch, U. Oesterle, and M. Ilegems, "Cavity-polariton photoluminescence in semiconductor microcavities: Experimental evidence," *Phys. Rev. B*, vol. 53, pp. 10995–11007, Apr 1996.

[40] P. Cilibrizzi, A. Askitopoulos, M. Silva, F. Bastiman, E. Clarke, J. M. Zajac, W. Langbein, and P. G. Lagoudakis, "Polariton condensation in a strain-compensated planar microcavity with InGaAs quantum wells," *Applied Physics Letters*, vol. 105, no. 19, p. 191118, 2014.

[41] J. Zuniga-Perez, E. Mallet, R. Hahe, M. J. Rashid, S. Bouchoule, C. Brimont, P. Disseix, J. Y. Duboz, G. Gommé, T. Guillet, O. Jamadi, X. Lafosse, M. Leroux, J. Leymarie, F. Li, F. Réveret, and F. Semond, "Patterned silicon substrates: A common platform for room temperature GaN and ZnO polariton lasers," *Applied Physics Letters*, vol. 104, no. 24, p. 241113, 2014.

[42] A. Einstein, "Quantentheorie des idealen einatomigen gases, zweite abhandlung," *Sitzungsberichte der Preußischen Akademie der Wissenschaften, Physikalisch-Mathematische Klasse, Berlin*, pp. 3–14, 1925.

[43] M. H. Anderson, J. R. Ensher, M. R. Matthews, C. E. Wieman, and E. A. Cornell, "Observation of bose-einstein condensation in a dilute atomic vapor," *Science*, vol. 269, no. 5221, pp. 198–201, 1995.

[44] J. Kasprzak, D. D. Solnyshkov, R. André, L. S. Dang, and G. Malpuech, "Formation of an exciton polariton condensate: Thermodynamic versus kinetic regimes," *Phys. Rev. Lett.*, vol. 101, p. 146404, Oct 2008.

[45] G. Christmann, R. Butté, E. Feltin, J.-F. Carlin, and N. Grandjean, "Room temperature polariton lasing in a GaN/AlGaN multiple quantum well microcavity," *Applied Physics Letters*, vol. 93, no. 5, p. 051102, 2008.

[46] T.-C. Lu, Y.-Y. Lai, Y.-P. Lan, S.-W. Huang, J.-R. Chen, Y.-C. Wu, W.-F. Hsieh, and H. Deng, "Room temperature polariton lasing vs. photon lasing in a zno-based hybrid microcavity," *Opt. Express*, vol. 20, pp. 5530–5537, Feb 2012.

[47] S. Kéna-Cohen and S. R. Forrest, "Room-temperature polariton lasing in an organic single-crystal microcavity," *Nature Photonics*, vol. 4, p. 371, Apr. 2010.

[48] R. Su, C. Diederichs, J. Wang, T. C. H. Liew, J. Zhao, S. Liu, W. Xu, Z. Chen, and Q. Xiong, "Room-temperature polariton lasing in all-inorganic perovskite nanoplatelets," *Nano Letters*, vol. 17, no. 6, pp. 3982–3988, 2017.

[49] R. Su, J. Wang, J. Zhao, J. Xing, W. Zhao, C. Diederichs, T. C. H. Liew, and Q. Xiong, "Room temperature long-range coherent exciton polariton condensate flow in lead halide perovskites," *Science Advances*, vol. 4, no. 10, p. eaau0244, 2018.

[50] Y.-Y. Lai, Y.-P. Lan, and T.-C. Lu, "Strong light-matter interaction in zno microcavities," *Light: Science &Amp; Applications*, vol. 2, p. e76, June 2013.

[51] A. I. Tartakovskii, M. Emam-Ismail, R. M. Stevenson, M. S. Skolnick, V. N. Astratov, D. M. Whittaker, J. J. Baumberg, and J. S. Roberts, "Relaxation bottleneck and its suppression in semiconductor microcavities," *Phys. Rev. B*, vol. 62, pp. R2283–R2286, Jul 2000.

[52] R. Houdré, J. L. Gibernon, P. Pellandini, R. P. Stanley, U. Oesterle, C. Weisbuch, J. O'Gorman, B. Roycroft, and M. Ilegems, "Saturation of the strong-coupling regime in a semiconductor microcavity: Free-carrier bleaching of cavity polaritons," *Phys. Rev. B*, vol. 52, pp. 7810–7813, Sep 1995.

[53] D. Sanvitto and S. Kéna-Cohen, "The road towards polaritonic devices," *Nature Materials*, vol. 15, p. 1061, July 2016.

[54] R. Balili, B. Nelsen, D. W. Snoke, L. Pfeiffer, and K. West, "Role of the stress trap in the polariton quasiequilibrium condensation in gaas microcavities," *Phys. Rev. B*, vol. 79, p. 075319, Feb 2009.

[55] M. Wouters, I. Carusotto, and C. Ciuti, "Spatial and spectral shape of inhomogeneous nonequilibrium exciton-polariton condensates," *Phys. Rev. B*, vol. 77, p. 115340, Mar 2008.

[56] A. Fieramosca, L. Polimeno, V. Ardizzone, L. De Marco, M. Pugliese, V. Maiorano, M. De Giorgi, L. Dominici, G. Gigli, D. Gerace, D. Ballarini, and D. Sanvitto, "Two-dimensional hybrid perovskites sustaining strong polariton interactions at room temperature," *Science Advances*, vol. 5, no. 5, 2019.

[57] A. Kojima, K. Teshima, Y. Shirai, and T. Miyasaka, "Organometal halide perovskites as visible-light sensitizers for photovoltaic cells," *Journal of the American Chemical Society*, vol. 131, no. 17, pp. 6050–6051, 2009. PMID: 19366264.

[58] H.-S. Kim, C.-R. Lee, J.-H. Im, K.-B. Lee, T. Moehl, A. Marchioro, S.-J. Moon, R. Humphry-Baker, J.-H. Yum, J. E. Moser, M. Grätzel, and N.-G. Park, "Lead iodide perovskite sensitized all-solid-state submicron thin film mesoscopic solar cell with efficiency exceeding 9p. 591, Aug. 2012.

[59] H. J. Snaith, "Present status and future prospects of perovskite photovoltaics," *Nature Materials*, vol. 17, pp. 372–376, May 2018.

[60] A. Babayigit, A. Ethirajan, M. Muller, and B. Conings, "Toxicity of organometal halide perovskite solar cells," *Nature Materials*, vol. 15, p. 247, Feb. 2016.

[61] J. M. Kadro, N. Pellet, F. Giordano, A. Ulianov, O. Müntener, J. Maier, M. Grätzel, and A. Hagfeldt, "Proof-of-concept for facile perovskite solar cell recycling," *Energy Environ. Sci.*, vol. 9, pp. 3172–3179, 2016.

[62] M. Lyu, J.-H. Yun, P. Chen, M. Hao, and L. Wang, "Addressing toxicity of lead: Progress and applications of low-toxic metal halide perovskites and their derivatives," *Advanced Energy Materials*, vol. 7, no. 15, p. 1602512, 2017.

[63] Y.-H. Kim, H. Cho, J. H. Heo, T.-S. Kim, N. Myoung, C.-L. Lee, S. H. Im, and T.-W. Lee, "Multicolored organic/inorganic hybrid perovskite light-emitting diodes," *Advanced Materials*, vol. 27, no. 7, pp. 1248–1254, 2015.

[64] H. Zhu, Y. Fu, F. Meng, X. Wu, Z. Gong, Q. Ding, M. V. Gustafsson, M. T. Trinh, S. Jin, and X.-Y. Zhu, "Lead halide perovskite nanowire lasers with low lasing thresholds and high quality factors," *Nature Materials*, vol. 14, p. 636, Apr. 2015.

[65] Q. Zhang, S. T. Ha, X. Liu, T. C. Sum, and Q. Xiong, "Room-temperature near-infrared high-q perovskite whispering-gallery planar nanolasers," *Nano Letters*, vol. 14, no. 10, pp. 5995–6001, 2014.

[66] T. S. Kao, Y.-H. Chou, C.-H. Chou, F.-C. Chen, and T.-C. Lu, "Lasing behaviors upon phase transition in solution-processed perovskite thin films," *Applied Physics Letters*, vol. 105, no. 23, p. 231108, 2014.

[67] R. Dhanker, A. N. Brigeman, A. V. Larsen, R. J. Stewart, J. B. Asbury, and N. C. Giebink, "Random lasing in organo-lead halide perovskite microcrystal networks," *Applied Physics Letters*, vol. 105, no. 15, p. 151112, 2014.

[68] T. Fujita, Y. Sato, T. Kuitani, and T. Ishihara, "Tunable polariton absorption of distributed feedback microcavities at room temperature," *Phys. Rev. B*, vol. 57, pp. 12428–12434, 1998.

[69] L. Protesescu, S. Yakunin, M. I. Bodnarchuk, F. Krieg, R. Caputo, C. H. Hendon, R. X. Yang, A. Walsh, and M. V. Kovalenko, "Nanocrystals of cesium lead halide perovskites (cspbx3, x = cl, br, and i): Novel optoelectronic materials showing bright emission with wide color gamut," *Nano Letters*, vol. 15, no. 6, pp. 3692–3696, 2015.

[70] T. C. Sum and N. Mathews, "Advancements in perovskite solar cells: photophysics behind the photovoltaics," *Energy Environ. Sci.*, vol. 7, pp. 2518–2534, 2014.

[71] S. D. Stranks, G. E. Eperon, G. Grancini, C. Menelaou, M. J. P. Alcocer, T. Leijtens, L. M. Herz, A. Petrozza, and H. J. Snaith, "Electron-hole diffusion lengths exceeding 1 micrometer in an organometal trihalide perovskite absorber," *Science*, vol. 342, no. 6156, pp. 341–344, 2013.

[72] Y. Rong, Y. Hu, A. Mei, H. Tan, M. I. Saidaminov, S. I. Seok, M. D. McGehee, E. H. Sargent, and H. Han, "Challenges for commercializing perovskite solar cells," *Science*, vol. 361, no. 6408, 2018.

[73] A. Miyata, A. Mitioglu, P. Plochocka, O. Portugall, J. T.-W. Wang, S. D. Stranks, H. J. Snaith, and R. J. Nicholas, "Direct measurement of the exciton binding energy and effective masses for charge carriers in organic-inorganic tri-halide perovskites," *Nature Physics*, vol. 11, p. 582, June 2015.

[74] Q. Zhang, R. Su, X. Liu, J. Xing, T. C. Sum, and Q. Xiong, "High-quality whispering-gallery-mode lasing from cesium lead halide perovskite nanoplatelets," *Advanced Functional Materials*, vol. 26, no. 34, pp. 6238–6245, 2016.

[75] R. Comin, G. Walters, E. S. Thibau, O. Voznyy, Z.-H. Lu, and E. H. Sargent, "Structural, optical, and electronic studies of wide-bandgap lead halide perovskites," *J. Mater. Chem. C*, vol. 3, pp. 8839–8843, 2015.

[76] M. Saba, F. Quochi, A. Mura, and G. Bongiovanni, "Excited state properties of hybrid perovskites," *Accounts of Chemical Research*, vol. 49, no. 1, pp. 166–173, 2016.

[77] T. Yamada, T. Aharen, and Y. Kanemitsu, "Near-band-edge optical responses of $ch_3nh_3pbcl_3$ single crystals: Photon recycling of excitonic luminescence," *Phys. Rev. Lett.*, vol. 120, p. 057404, Feb 2018.

[78] S. Chen and A. Nurmikko, "Excitonic gain and laser emission from mixed-cation halide perovskite thin films," *Optica*, vol. 5, pp. 1141–1149, Sep 2018.

[79] K. Tanaka, T. Takahashi, T. Ban, T. Kondo, K. Uchida, and N. Miura, "Comparative study on the excitons in lead-halide-based perovskite-type crystals ch3nh3pbbr3 ch3nh3pbi3," *Solid State Communications*, vol. 127, no. 9, pp. 619 – 623, 2003.

[80] Y. Yang, M. Yang, Z. Li, R. Crisp, K. Zhu, and M. C. Beard, "Comparison of recombination dynamics in ch3nh3pbbr3 and ch3nh3pbi3 perovskite films: Influence of exciton binding energy," *The Journal of Physical Chemistry Letters*, vol. 6, no. 23, pp. 4688–4692, 2015.

[81] A. M. Soufiani, F. Huang, P. Reece, R. Sheng, A. Ho-Baillie, and M. A. Green, "Polaronic exciton binding energy in iodide and bromide organic-inorganic lead halide perovskites," *Applied Physics Letters*, vol. 107, no. 23, p. 231902, 2015.

[82] B. Wu, H. T. Nguyen, Z. Ku, G. Han, D. Giovanni, N. Mathews, H. J. Fan, and T. C. Sum, "Discerning the surface and bulk recombination kinetics of organic-inorganic halide perovskite single crystals," *Advanced Energy Materials*, vol. 6, no. 14, p. 1600551, 2016.

[83] K. Galkowski, A. Mitioglu, A. Miyata, P. Plochocka, O. Portugall, G. E. Eperon, J. T.-W. Wang, T. Stergiopoulos, S. D. Stranks, H. J. Snaith, and R. J. Nicholas, "Determination of the exciton binding energy and effective masses for methylammonium and formamidinium lead tri-halide perovskite semiconductors," *Energy Environ. Sci.*, vol. 9, pp. 962–970, 2016.

[84] J. Tilchin, D. N. Dirin, G. I. Maikov, A. Sashchiuk, M. V. Kovalenko, and E. Lifshitz, "Hydrogen-like wannier-mott excitons in single crystal of methylammonium lead bromide perovskite," *ACS Nano*, vol. 10, no. 6, pp. 6363–6371, 2016.

[85] C. Wolf, J.-S. Kim, and T.-W. Lee, "Structural and thermal disorder of solution-processed ch3nh3pbbr3 hybrid perovskite thin films," *ACS Applied Materials & Interfaces*, vol. 9, no. 12, pp. 10344–10348, 2017.

[86] D. Niesner, O. Schuster, M. Wilhelm, I. Levchuk, A. Osvet, S. Shrestha, M. Batentschuk, C. Brabec, and T. Fauster, "Temperature-dependent optical spectra of single-crystal $(ch_3nh_3)pbbr_3$ cleaved in ultrahigh vacuum," *Phys. Rev. B*, vol. 95, p. 075207, Feb 2017.

[87] N. Droseros, G. Longo, J. C. Brauer, M. Sessolo, H. J. Bolink, and N. Banerji, "Origin of the enhanced photoluminescence quantum yield in mapbbr3 perovskite with reduced crystal size," *ACS Energy Letters*, vol. 3, no. 6, pp. 1458–1466, 2018.

[88] H. Linnenbank, M. Saliba, L. Gui, B. Metzger, S. G. Tikhodeev, J. Kadro, G. Nasti, A. Abate, A. Hagfeldt, M. Graetzel, and H. Giessen, "Temperature dependent two-photon photoluminescence of ch3nh3pbbr3: structural phase and exciton to free carrier transition," *Opt. Mater. Express*, vol. 8, pp. 511–521, Mar 2018.

[89] K. Jemli, H. Diab, F. Lédée, G. Trippé-Allard, D. Garrot, B. Geffroy, J.-S. Lauret, P. Audebert, and E. Deleporte, "Using low temperature photoluminescence spectroscopy to investigate ch3nh3pbi3 hybrid perovskite degradation," *Molecules*, vol. 21, no. 7, 2016.

[90] Y. Rong, Y. Hu, A. Mei, H. Tan, M. I. Saidaminov, S. I. Seok, M. D. McGehee, E. H. Sargent, and H. Han, "Challenges for commercializing perovskite solar cells," *Science*, vol. 361, no. 6408, 2018.

[91] G. Grancini, C. Roldán-Carmona, I. Zimmermann, E. Mosconi, X. Lee, D. Martineau, S. Narbey, F. Oswald, F. De Angelis, M. Graetzel, and M. K. Nazeeruddin, "One-year stable perovskite solar cells by 2d/3d interface engineering," *Nature Communications*, vol. 8, p. 15684, June 2017.

[92] L. Cheng, T. Jiang, Y. Cao, C. Yi, N. Wang, W. Huang, and J. Wang, "Multiple-quantum-well perovskites for high-performance light-emitting diodes," *Advanced Materials*, vol. 0, no. 0, p. 1904163.

[93] S. Nakamura, M. Senoh, and T. Mukai, "P-GaN/n-InGaN/n-GaN double-heterostructure blue-light-emitting diodes," *Japanese Journal of Applied Physics*, vol. 32, pp. L8–L11, jan 1993.

[94] S. Nakamura, T. Mukai, and M. Senoh, "Candela-class high-brightness InGaN/AlGaN double-heterostructure blue-light-emitting diodes," *Applied Physics Letters*, vol. 64, no. 13, pp. 1687–1689, 1994.

[95] I. L. Braly, D. W. deQuilettes, L. M. Pazos-Outón, S. Burke, M. E. Ziffer, D. S. Ginger, and H. W. Hillhouse, "Hybrid perovskite films approaching the radiative limit with over 90% photoluminescence quantum efficiency," *Nature Photonics*, vol. 12, pp. 355–361, June 2018.

[96] B. R. Sutherland, S. Hoogland, M. M. Adachi, P. Kanjanaboos, C. T. O. Wong, J. J. McDowell, J. Xu, O. Voznyy, Z. Ning, A. J. Houtepen, and E. H. Sargent, "Perovskite thin films via atomic layer deposition," *Advanced Materials*, vol. 27, no. 1, pp. 53–58, 2015.

[97] Y. Fu, H. Zhu, A. W. Schrader, D. Liang, Q. Ding, P. Joshi, L. Hwang, X.-Y. Zhu, and S. Jin, "Nanowire lasers of formamidinium lead halide perovskites and their stabilized alloys with improved stability," *Nano Letters*, vol. 16, no. 2, pp. 1000–1008, 2016. PMID: 26727024.

[98] Y. Fu, H. Zhu, C. C. Stoumpos, Q. Ding, J. Wang, M. G. Kanatzidis, X. Zhu, and S. Jin, "Broad wavelength tunable robust lasing from single-crystal nanowires of cesium lead halide perovskites (cspbx3, x = cl, br, i)," *ACS Nano*, vol. 10, no. 8, pp. 7963–7972, 2016. PMID: 27437566.

[99] Q. Zhang, R. Su, W. Du, X. Liu, L. Zhao, S. T. Ha, and Q. Xiong, "Advances in small perovskite-based lasers," *Small Methods*, vol. 1, no. 9, p. 1700163, 2017.

[100] Y. Jia, R. A. Kerner, A. J. Grede, A. N. Brigeman, B. P. Rand, and N. C. Giebink, "Diode-pumped organo-lead halide perovskite lasing in a metal-clad distributed feedback resonator," *Nano Letters*, vol. 16, no. 7, pp. 4624–4629, 2016. PMID: 27331618.

[101] M. S. Alias, Z. Liu, A. Al-atawi, T. K. Ng, T. Wu, and B. S. Ooi, "Continuous-wave optically pumped green perovskite vertical-cavity surface-emitter," *Opt. Lett.*, vol. 42, pp. 3618–3621, Sep 2017.

[102] Y. Jia, R. A. Kerner, A. J. Grede, B. P. Rand, and N. C. Giebink, "Continuous-wave lasing in an organic-inorganic lead halide perovskite semiconductor," *Nature Photonics*, vol. 11, pp. 784–788, Dec. 2017.

[103] T. J. S. Evans, A. Schlaus, Y. Fu, X. Zhong, T. L. Atallah, M. S. Spencer, L. E. Brus, S. Jin, and X.-Y. Zhu, "Continuous-wave lasing in cesium lead bromide perovskite nanowires," *Advanced Optical Materials*, vol. 6, no. 2, p. 1700982, 2018.

[104] Z. Li, J. Moon, A. Gharajeh, R. Haroldson, R. Hawkins, W. Hu, A. Zakhidov, and Q. Gu, "Room-temperature continuous-wave operation of organometal halide perovskite lasers," *ACS Nano*, vol. 12, no. 11, pp. 10968–10976, 2018. PMID: 30383358.

[105] J. Moon, M. Alahbakhshi, A. Gharajeh, R. Haroldson, R. Hawkins, Z. Li, W. Hu, A. Zakhidov, and Q. Gu, "Continuous wave green lasing at room temperature in two-dimensional photonic crystal perovskite laser," in *Conference on Lasers and Electro-Optics*, p. SW4N.2, Optical Society of America, 2019.

[106] L. Wang, L. Meng, L. Chen, S. Huang, X. Wu, G. Dai, L. Deng, J. Han, B. Zou, C. Zhang, and H. Zhong, "Ultralow-threshold and color-tunable continuous-wave lasing at room-temperature from in situ fabricated perovskite quantum dots," *The Journal of Physical Chemistry Letters*, vol. 10, no. 12, pp. 3248–3253, 2019. PMID: 31084011.

[107] L. Jiang, R. Liu, R. Su, Y. Yu, H. Xu, Y. Wei, Z.-K. Zhou, and X. Wang, "Continuous wave pumped single-mode nanolasers in inorganic perovskites with robust stability and high quantum yield," *Nanoscale*, vol. 10, pp. 13565–13571, 2018.

[108] K. Wang, S. Wang, S. Xiao, and Q. Song, "Recent advances in perovskite micro- and nanolasers," *Advanced Optical Materials*, vol. 6, no. 18, p. 1800278, 2018.

[109] M. M. Stylianakis, T. Maksudov, A. Panagiotopoulos, G. Kakavelakis, and K. Petridis, "Inorganic and hybrid perovskite based laser devices: A review," *Materials*, vol. 12, no. 6, 2019.

[110] H. Yu, K. Ren, Q. Wu, J. Wang, J. Lin, Z. Wang, J. Xu, R. F. Oulton, S. Qu, and P. Jin, "Organic–inorganic perovskite plasmonic nanowire lasers with a low threshold and a good thermal stability," *Nanoscale*, vol. 8, pp. 19536–19540, 2016.

[111] A. P. Schlaus, M. S. Spencer, K. Miyata, F. Liu, X. Wang, I. Datta, M. Lipson, A. Pan, and X.-Y. Zhu, "How lasing happens in cspbbr3 perovskite nanowires," *Nature Communications*, vol. 10, p. 265, Jan. 2019.

[112] Q. Liao, K. Hu, H. Zhang, X. Wang, J. Yao, and H. Fu, "Perovskite microdisk microlasers self-assembled from solution," *Advanced Materials*, vol. 27, no. 22, pp. 3405–3410, 2015.

[113] K. Wang, Z. Gu, S. Liu, J. Li, S. Xiao, and Q. Song, "Formation of single-mode laser in transverse plane of perovskite microwire via micromanipulation," *Opt. Lett.*, vol. 41, pp. 555–558, Feb 2016.

[114] K. Wang, S. Sun, C. Zhang, W. Sun, Z. Gu, S. Xiao, and Q. Song, "Whispering-gallery-mode based ch3nh3pbbr3 perovskite microrod lasers with high quality factors," *Mater. Chem. Front.*, vol. 1, pp. 477–481, 2017.

[115] Z.-F. Shi, X.-G. Sun, D. Wu, T.-T. Xu, Y.-T. Tian, Y.-T. Zhang, X.-J. Li, and G.-T. Du, "Near-infrared random lasing realized in a perovskite CH3nh3pbi3 thin film," *Journal of Materials Chemistry C*, vol. 4, no. 36, pp. 8373–8379, 2016.

[116] T. S. Kao, Y.-H. Chou, K.-B. Hong, J.-F. Huang, C.-H. Chou, H.-C. Kuo, F.-C. Chen, and T.-C. Lu, "Controllable lasing performance in solution-processed organic–inorganic hybrid perovskites," *Nanoscale*, vol. 8, no. 43, pp. 18483–18488, 2016.

[117] A. Safdar, Y. Wang, and T. F. Krauss, "Random lasing in uniform perovskite thin films," *Optics Express*, vol. 26, no. 2, pp. A75–A84, 2018.

[118] S. Yakunin, L. Protesescu, F. Krieg, M. I. Bodnarchuk, G. Nedelcu, M. Humer, G. De Luca, M. Fiebig, W. Heiss, and M. V. Kovalenko, "Low-threshold amplified spontaneous emission and lasing from colloidal nanocrystals of caesium lead halide perovskites," *Nature communications*, vol. 6, p. 8056, 2015.

[119] X. Li, Y. Wang, H. Sun, and H. Zeng, "Amino-mediated anchoring perovskite quantum dots for stable and low-threshold random lasing," *Advanced Materials*, vol. 29, p. 1701185, jul 2017.

[120] C. Li, Z. Zang, C. Han, Z. Hu, X. Tang, J. Du, Y. Leng, and K. Sun, "Highly compact CsPbBr 3 perovskite thin films decorated by ZnO nanoparticles for enhanced random lasing," *Nano Energy*, vol. 40, pp. 195–202, oct 2017.

[121] S. Yuan, D. Chen, X. Li, J. Zhong, and X. Xu, "In situ crystallization synthesis of CsPbBr3 perovskite quantum dot-embedded glasses with improved stability for solid-state lighting and random upconverted lasing," *ACS Applied Materials & Interfaces*, vol. 10, pp. 18918–18926, may 2018.

[122] L. Xu, Y. Meng, C. Xu, and P. Chen, "Room temperature two-photon-pumped random lasers in FAPbBr3/polyethylene oxide (PEO) composite perovskite thin film," *RSC Advances*, vol. 8, no. 64, pp. 36910–36914, 2018.

[123] S. Liu, W. Sun, J. Li, Z. Gu, K. Wang, S. Xiao, and Q. Song, "Random lasing actions in self-assembled perovskite nanoparticles," *Optical Engineering*, vol. 55, p. 057102, may 2016.

[124] P. K. Roy, G. Haider, H.-I. Lin, Y.-M. Liao, C.-H. Lu, K.-H. Chen, L.-C. Chen, W.-H. Shih, C.-T. Liang, and Y.-F. Chen, "Multicolor ultralow-threshold random laser assisted by vertical-graphene network," *Advanced Optical Materials*, vol. 6, p. 1800382, may 2018.

[125] G. Weng, J. Xue, J. Tian, X. Hu, X. Bao, H. Lin, S. Chen, Z. Zhu, and J. Chu, "Picosecond random lasing based on three-photon absorption in organometallic halide CH3nh3pbbr3 perovskite thin films," *ACS Photonics*, vol. 5, pp. 2951–2959, may 2018.

[126] T. Fan, J. Lü, Y. Chen, W. Yuan, and Y. Huang, "Random lasing in cesium lead bromine perovskite quantum dots film," *Journal of Materials Science: Materials in Electronics*, vol. 30, pp. 1084–1088, Jan 2019.

[127] A. Mikosch, S. Ciftci, G. Tainter, R. Shivanna, B. Haehnle, F. Deschler, and A. J. C. Kuehne, "Laser emission from self-assembled colloidal crystals of conjugated polymer particles in a metal-halide perovskite matrix," *Chemistry of Materials*, vol. 31, no. 7, pp. 2590–2596, 2019.

[128] G. Weng, J. Tian, S. Chen, J. Xue, J. Yan, X. Hu, S. Chen, Z. Zhu, and J. Chu, "Giant reduction of the random lasing threshold in ch3nh3pbbr3 perovskite thin films by using a patterned sapphire substrate," *Nanoscale*, pp. –, 2019.

[129] Y.-C. Wang, H. Li, Y.-H. Hong, K.-B. Hong, F.-C. Chen, C.-H. Hsu, R.-K. Lee, C. Conti, T. S. Kao, and T.-C. Lu, "Flexible organometal–halide perovskite lasers for speckle reduction in imaging projection," *ACS Nano*, vol. 13, no. 5, pp. 5421–5429, 2019. PMID: 31009199.

[130] K. Cyprych, L. Sznitko, and J. Mysliwiec, "Starch: Application of biopolymer in random lasing," *Organic Electronics*, vol. 15, no. 10, pp. 2218 – 2222, 2014.

[131] S. Chen, C. Zhang, J. Lee, J. Han, and A. Nurmikko, "High-q, low-threshold monolithic perovskite thin-film vertical-cavity lasers," *Advanced Materials*, vol. 29, no. 16, p. 1604781, 2017.

[132] M. Saliba, S. M. Wood, J. B. Patel, P. K. Nayak, J. Huang, J. A. Alexander-Webber, B. Wenger, S. D. Stranks, M. T. Hörantner, J. T.-W. Wang, R. J. Nicholas, L. M. Herz, M. B. Johnston, S. M. Morris, H. J. Snaith, and M. K. Riede, "Structured organic–inorganic perovskite toward a distributed feedback laser," *Advanced Materials*, vol. 28, no. 5, pp. 923–929, 2016.

[133] S. Chen, K. Roh, J. Lee, W. K. Chong, Y. Lu, N. Mathews, T. C. Sum, and A. Nurmikko, "A photonic crystal laser from solution based organo-lead iodide perovskite thin films," *ACS Nano*, vol. 10, no. 4, pp. 3959–3967, 2016. PMID: 26997122.

[134] H. Cha, S. Bae, M. Lee, and H. Jeon, "Two-dimensional photonic crystal band-edge laser with hybrid perovskite thin film for optical gain," *Applied Physics Letters*, vol. 108, no. 18, p. 181104, 2016.

[135] S. Wang, K. Wang, Z. Gu, Y. Wang, C. Huang, N. Yi, S. Xiao, and Q. Song, "Solution-phase synthesis of cesium lead halide perovskite microrods for high-quality micro-lasers and photodetectors," *Advanced Optical Materials*, vol. 5, no. 11, p. 1700023, 2017.

[136] B. Tang, H. Dong, L. Sun, W. Zheng, Q. Wang, F. Sun, X. Jiang, A. Pan, and L. Zhang, "Single-mode lasers based on cesium lead halide perovskite submicron spheres," *ACS Nano*, vol. 11, no. 11, pp. 10681–10688, 2017. PMID: 28991452.

[137] S. Chen and A. Nurmikko, "Stable green perovskite vertical-cavity surface-emitting lasers on rigid and flexible substrates," *ACS Photonics*, vol. 4, no. 10, pp. 2486–2494, 2017.

[138] Z. Gu, K. Wang, W. Sun, J. Li, S. Liu, Q. Song, and S. Xiao, "Two-photon pumped ch3nh3pbbr3 perovskite microwire lasers," *Advanced Optical Materials*, vol. 4, no. 3, pp. 472–479, 2016.

[139] Y. Xu, Q. Chen, C. Zhang, R. Wang, H. Wu, X. Zhang, G. Xing, W. W. Yu, X. Wang, Y. Zhang, and M. Xiao, "Two-photon-pumped perovskite semiconductor nanocrystal lasers," *Journal of the American Chemical Society*, vol. 138, no. 11, pp. 3761–3768, 2016. PMID: 26938656.

[140] S. Wang, K. Wang, Z. Gu, Y. Wang, C. Huang, N. Yi, S. Xiao, and Q. Song, "Solution-phase synthesis of cesium lead halide perovskite microrods for high-quality micro-lasers and photodetectors," *Advanced Optical Materials*, vol. 5, no. 11, p. 1700023, 2017.

[141] Q. Wei, B. Du, B. Wu, J. Guo, M. Li, J. Fu, Z. Zhang, J. Yu, T. Hou, G. Xing, T. C. Sum, and W. Huang, "Two-photon optical properties in individual organic–inorganic perovskite microplates," *Advanced Optical Materials*, vol. 5, no. 24, p. 1700809, 2017.

[142] Y. Wang, X. Li, X. Zhao, L. Xiao, H. Zeng, and H. Sun, "Nonlinear absorption and low-threshold multiphoton pumped stimulated emission from all-inorganic perovskite nanocrystals," *Nano Letters*, vol. 16, no. 1, pp. 448–453, 2016. PMID: 26652773.

[143] Y. Gao, S. Wang, C. Huang, N. Yi, K. Wang, S. Xiao, and Q. Song, "Room temperature three-photon pumped ch3nh3pbbr3 perovskite microlasers," *Scientific Reports*, vol. 7, p. 45391, Mar. 2017.

[144] X. Wang, H. Zhou, S. Yuan, W. Zheng, Y. Jiang, X. Zhuang, H. Liu, Q. Zhang, X. Zhu, X. Wang, and A. Pan, "Cesium lead halide perovskite triangular nanorods as high-gain medium and effective cavities for multiphoton-pumped lasing," *Nano Research*, vol. 10, pp. 3385–3395, Oct 2017.

[145] D. Yang, C. Xie, X. Xu, P. You, F. Yan, and S. F. Yu, "Lasing characteristics of ch3nh3pbcl3 single-crystal microcavities under multiphoton excitation," *Advanced Optical Materials*, vol. 6, no. 3, p. 1700992, 2018.

[146] Y. Mi, Y. Zhong, Q. Zhang, and X. Liu, "Continuous-wave pumped perovskite lasers," *Advanced Optical Materials*, vol. 0, no. 0, p. 1900544, 2019.

[147] C. Guhrenz, A. Benad, C. Ziegler, D. Haubold, N. Gaponik, and A. Eychmüller, "Solid-state anion exchange reactions for color tuning of cspbx3 perovskite nanocrystals," *Chemistry of Materials*, vol. 28, no. 24, pp. 9033–9040, 2016.

[148] N. Pellet, J. Teuscher, J. Maier, and M. Grätzel, "Transforming hybrid organic inorganic perovskites by rapid halide exchange," *Chemistry of Materials*, vol. 27, no. 6, pp. 2181–2188, 2015.

[149] D. Solis-Ibarra, I. C. Smith, and H. I. Karunadasa, "Post-synthetic halide conversion and selective halogen capture in hybrid perovskites," *Chem. Sci.*, vol. 6, pp. 4054–4059, 2015.

[150] G. Li, J. Y.-L. Ho, M. Wong, and H. S. Kwok, "Reversible anion exchange reaction in solid halide perovskites and its implication in photovoltaics," *The Journal of Physical Chemistry C*, vol. 119, no. 48, pp. 26883–26888, 2015.

[151] N. Zhang, K. Wang, H. Wei, Z. Gu, W. Sun, J. Li, S. Xiao, and Q. Song, "Postsynthetic and selective control of lead halide perovskite microlasers," *The Journal of Physical Chemistry Letters*, vol. 7, no. 19, pp. 3886–3891, 2016. PMID: 27640525.

[152] C. Zhang, K. Wang, N. Yi, Y. Gao, M. Zhu, W. Sun, S. Liu, K. Xu, S. Xiao, and Q. Song, "Improving the performance of a ch3nh3pbbr3 perovskite microrod laser through hybridization with few-layered graphene," *Advanced Optical Materials*, vol. 4, no. 12, pp. 2057–2062, 2016.

[153] S. Wang, J. Fang, C. Zhang, S. Sun, K. Wang, S. Xiao, and Q. Song, "Maskless fabrication of aluminum nanoparticles for plasmonic enhancement of lead halide perovskite lasers," *Advanced Optical Materials*, vol. 5, no. 21, p. 1700529, 2017.

[154] J. Pan, S. P. Sarmah, B. Murali, I. Dursun, W. Peng, M. R. Parida, J. Liu, L. Sinatra, N. Alyami, C. Zhao, E. Alarousu, T. K. Ng, B. S. Ooi, O. M. Bakr, and O. F. Mohammed, "Air-stable surface-passivated perovskite quantum dots for ultra-robust, single- and two-photon-induced amplified spontaneous emission," *The Journal of Physical Chemistry Letters*, vol. 6, no. 24, pp. 5027–5033, 2015. PMID: 26624490.

[155] M. T. Hörantner, W. Zhang, M. Saliba, K. Wojciechowski, and H. J. Snaith, "Templated microstructural growth of perovskite thin films via colloidal monolayer lithography," *Energy Environ. Sci.*, vol. 8, pp. 2041–2047, 2015.

[156] K. Chen and H. Tüysüz, "Morphology-controlled synthesis of organometal halide perovskite inverse opals," *Angewandte Chemie International Edition*, vol. 54, no. 46, pp. 13806–13810, 2015.

[157] S. Schünemann, S. Brittman, K. Chen, E. C. Garnett, and H. Tüysüz, "Halide perovskite 3d photonic crystals for distributed feedback lasers," *ACS Photonics*, vol. 4, no. 10, pp. 2522–2528, 2017.

[158] H. Wang, R. Haroldson, B. Balachandran, A. Zakhidov, S. Sohal, J. Y. Chan, A. Zakhidov, and W. Hu, "Nanoimprinted perovskite nanograting photodetector with improved efficiency," *ACS Nano*, vol. 10, no. 12, pp. 10921–10928, 2016. PMID: 28024335.

[159] A. Gharajeh, R. Haroldson, Z. Li, J. Moon, B. Balachandran, W. Hu, A. Zakhidov, and Q. Gu, "Continuous-wave operation in directly patterned perovskite distributed feedback light source at room temperature," *Opt. Lett.*, vol. 43, pp. 611–614, Feb 2018.

[160] B. Gholipour, G. Adamo, D. Cortecchia, H. N. S. Krishnamoorthy, M. D. Birowosuto, N. I. Zheludev, and C. Soci, "Organometallic perovskite metasurfaces," *Advanced Materials*, vol. 29, no. 9, p. 1604268, 2017.

[161] N. Pourdavoud, S. Wang, A. Mayer, T. Hu, Y. Chen, A. Marianovich, W. Kowalsky, R. Heiderhoff, H.-C. Scheer, and T. Riedl, "Photonic nanostructures patterned by thermal nanoimprint directly into organo-metal halide perovskites," *Advanced Materials*, vol. 29, no. 12, p. 1605003, 2017.

[162] N. Zhang, W. Sun, S. P. Rodrigues, K. Wang, Z. Gu, S. Wang, W. Cai, S. Xiao, and Q. Song, "Highly reproducible organometallic halide perovskite microdevices based on top-down lithography," *Advanced Materials*, vol. 29, no. 15, p. 1606205, 2017.

[163] B. Jeong, I. Hwang, S. H. Cho, E. H. Kim, S. Cha, J. Lee, H. S. Kang, S. M. Cho, H. Choi, and C. Park, "Solvent-assisted gel printing for micropatterning thin organic–inorganic hybrid perovskite films," *ACS Nano*, vol. 10, no. 9, pp. 9026–9035, 2016. PMID: 27571339.

[164] F. Palazon, Q. A. Akkerman, M. Prato, and L. Manna, "X-ray lithography on perovskite nanocrystals films: From patterning with anion-exchange reactions to enhanced stability in air and water," *ACS Nano*, vol. 10, no. 1, pp. 1224–1230, 2016. PMID: 26617344.

[165] J. Chen, Y. Wu, X. Li, F. Cao, Y. Gu, K. Liu, X. Liu, Y. Dong, J. Ji, and H. Zeng, "Simple and fast patterning process by laser direct writing for perovskite quantum dots," *Advanced Materials Technologies*, vol. 2, no. 10, p. 1700132, 2017.

[166] S. S. Chou, B. S. Swartzentruber, M. T. Janish, K. C. Meyer, L. B. Biedermann, S. Okur, D. B. Burckel, C. B. Carter, and B. Kaehr, "Laser direct write synthesis of lead halide perovskites," *The Journal of Physical Chemistry Letters*, vol. 7, no. 19, pp. 3736–3741, 2016. PMID: 27593712.

[167] J. Wu, J. Chen, Y. Zhang, Z. Xu, L. Zhao, T. Liu, D. Luo, W. Yang, K. Chen, Q. Hu, F. Ye, P. Wu, R. Zhu, and Q. Gong, "Pinhole-free hybrid perovskite film with arbitrarily-shaped micro-patterns for functional optoelectronic devices," *Nano Letters*, vol. 17, no. 6, pp. 3563–3569, 2017. PMID: 28445643.

[168] M. S. Alias, I. Dursun, D. Shi, M. I. Saidaminov, E. M. Diallo, D. Priante, T. K. Ng, O. M. Bakr, and B. S. Ooi, "Focused-ion beam patterning of organolead trihalide perovskite for subwavelength grating nanophotonic applications," *Journal of Vacuum Science & Technology B*, vol. 33, no. 5, p. 051207, 2015.

[169] M. S. Alias, Y. Yang, T. K. Ng, I. Dursun, D. Shi, M. I. Saidaminov, D. Priante, O. M. Bakr, and B. S. Ooi, "Enhanced etching, surface damage recovery, and submicron patterning of hybrid perovskites using a chemically gas-assisted focused-ion beam for subwavelength grating photonic applications," *The Journal of Physical Chemistry Letters*, vol. 7, no. 1, pp. 137–142, 2016. PMID: 26688008.

[170] G. Wang, D. Li, H.-C. Cheng, Y. Li, C.-Y. Chen, A. Yin, Z. Zhao, Z. Lin, H. Wu, Q. He, M. Ding, Y. Liu, Y. Huang, and X. Duan, "Wafer-scale growth of large arrays of perovskite microplate crystals for functional electronics and optoelectronics," *Science Advances*, vol. 1, no. 9, 2015.

[171] Z. Gu, K. Wang, H. Li, M. Gao, L. Li, M. Kuang, Y. S. Zhao, M. Li, and Y. Song, "Direct-writing multifunctional perovskite single crystal arrays by inkjet printing," *Small*, vol. 13, no. 8, p. 1603217, 2017.

[172] X. He, P. Liu, H. Zhang, Q. Liao, J. Yao, and H. Fu, "Patterning multicolored microdisk laser arrays of cesium lead halide perovskite," *Advanced Materials*, vol. 29, no. 12, p. 1604510, 2017.

[173] S. Sun, C. Zhang, K. Wang, S. Wang, S. Xiao, and Q. Song, "Lead halide perovskite nanoribbon based uniform nanolaser array on plasmonic grating," *ACS Photonics*, vol. 4, no. 3, pp. 649–656, 2017.

[174] J. J. Hopfield, "Theory of the contribution of excitons to the complex dielectric constant of crystals," *Phys. Rev.*, vol. 112, pp. 1555–1567, Dec 1958.

[175] J. J. Hopfield and D. G. Thomas, "Polariton absorption lines," *Phys. Rev. Lett.*, vol. 15, pp. 22–25, Jul 1965.

[176] F. Semond, I. R. Sellers, F. Natali, D. Byrne, M. Leroux, J. Massies, N. Ollier, J. Leymarie, P. Disseix, and A. Vasson, "Strong light-matter coupling at room temperature

in simple geometry GaN microcavities grown on silicon," *Applied Physics Letters*, vol. 87, no. 2, p. 021102, 2005.

[177] S. Christopoulos, G. B. H. von Högersthal, A. J. D. Grundy, P. G. Lagoudakis, A. V. Kavokin, J. J. Baumberg, G. Christmann, R. Butté, E. Feltin, J.-F. Carlin, and N. Grandjean, "Room-temperature polariton lasing in semiconductor microcavities," *Phys. Rev. Lett.*, vol. 98, p. 126405, Mar 2007.

[178] D. G. Lidzey, D. D. C. Bradley, M. S. Skolnick, T. Virgili, S. Walker, and D. M. Whittaker, "Strong exciton-photon coupling in an organic semiconductor microcavity," *Nature*, vol. 395, p. 53, Sept. 1998.

[179] K. S. Daskalakis, S. A. Maier, R. Murray, and S. Kéna-Cohen, "Nonlinear interactions in an organic polariton condensate," *Nature Materials*, vol. 13, p. 271, Feb. 2014.

[180] J. D. Plumhof, T. Stöferle, L. Mai, U. Scherf, and R. F. Mahrt, "Room-temperature bose-einstein condensation of cavity exciton-polaritons in a polymer," *Nature Materials*, vol. 13, p. 247, Dec. 2013.

[181] S. Dufferwiel, S. Schwarz, F. Withers, A. A. P. Trichet, F. Li, M. Sich, O. Del Pozo-Zamudio, C. Clark, A. Nalitov, D. D. Solnyshkov, G. Malpuech, K. S. Novoselov, J. M. Smith, M. S. Skolnick, D. N. Krizhanovskii, and A. I. Tartakovskii, "Exciton-polaritons in van der waals heterostructures embedded in tunable microcavities," *Nature Communications*, vol. 6, p. 8579, Oct. 2015.

[182] X. Liu, T. Galfsky, Z. Sun, F. Xia, E.-c. Lin, Y.-H. Lee, S. Kéna-Cohen, and V. M. Menon, "Strong light-matter coupling in two-dimensional atomic crystals," *Nature Photonics*, vol. 9, p. 30, Dec. 2014.

[183] C. Schneider, A. Rahimi-Iman, N. Y. Kim, J. Fischer, I. G. Savenko, M. Amthor, M. Lermer, A. Wolf, L. Worschech, V. D. Kulakovskii, I. A. Shelykh, M. Kamp, S. Reitzenstein, A. Forchel, Y. Yamamoto, and S. Höfling, "An electrically pumped polariton laser," *Nature*, vol. 497, p. 348, May 2013.

[184] P. Bhattacharya, B. Xiao, A. Das, S. Bhowmick, and J. Heo, "Solid state electrically injected exciton-polariton laser," *Phys. Rev. Lett.*, vol. 110, p. 206403, May 2013.

[185] M. Z. Baten, P. Bhattacharya, T. Frost, S. Deshpande, A. Das, D. Lubyshev, J. M. Fastenau, and A. W. K. Liu, "GaAs-based high temperature electrically pumped polariton laser," *Applied Physics Letters*, vol. 104, no. 23, p. 231119, 2014.

[186] P. Bhattacharya, T. Frost, S. Deshpande, M. Z. Baten, A. Hazari, and A. Das, "Room temperature electrically injected polariton laser," *Phys. Rev. Lett.*, vol. 112, p. 236802, Jun 2014.

[187] E. Wertz, L. Ferrier, D. D. Solnyshkov, P. Senellart, D. Bajoni, A. Miard, A. Lemaître, G. Malpuech, and J. Bloch, "Spontaneous formation of a polariton condensate in a planar GaAs microcavity," *Applied Physics Letters*, vol. 95, no. 5, p. 051108, 2009.

[188] J. R. Tischler, M. S. Bradley, V. Bulović, J. H. Song, and A. Nurmikko, "Strong coupling in a microcavity led," *Phys. Rev. Lett.*, vol. 95, p. 036401, Jul 2005.

[189] C. R. Gubbin, S. A. Maier, and S. Kéna-Cohen, "Low-voltage polariton electroluminescence from an ultrastrongly coupled organic light-emitting diode," *Applied Physics Letters*, vol. 104, no. 23, p. 233302, 2014.

[190] N. Christogiannis, N. Somaschi, P. Michetti, D. M. Coles, P. G. Savvidis, P. G. Lagoudakis, and D. G. Lidzey, "Characterizing the electroluminescence emission from a strongly coupled organic semiconductor microcavity led," *Advanced Optical Materials*, vol. 1, no. 7, pp. 503–509, 2013.

[191] A. Graf, M. Held, Y. Zakharko, L. Tropf, M. C. Gather, and J. Zaumseil, "Electrical pumping and tuning of exciton-polaritons in carbon nanotube microcavities," *Nature Materials*, vol. 16, p. 911, July 2017.

[192] Z. Zhang, Y. Wang, S. Yin, T. Hu, Y. Wang, L. Liao, S. Luo, J. Wang, X. Zhang, P. Ni, X. Shen, C. Shan, and Z. Chen, "Exciton-polariton light-emitting diode based on a zno microwire," *Opt. Express*, vol. 25, pp. 17375–17381, Jul 2017.

[193] T.-C. Lu, J.-R. Chen, S.-C. Lin, S.-W. Huang, S.-C. Wang, and Y. Yamamoto, "Room temperature current injection polariton light emitting diode with a hybrid microcavity," *Nano Letters*, vol. 11, no. 7, pp. 2791–2795, 2011. PMID: 21675759.

[194] A. A. Khalifa, A. P. D. Love, D. N. Krizhanovskii, M. S. Skolnick, and J. S. Roberts, "Electroluminescence emission from polariton states in GaAs-based semiconductor microcavities," *Applied Physics Letters*, vol. 92, no. 6, p. 061107, 2008.

[195] D. Bajoni, E. Semenova, A. Lemaître, S. Bouchoule, E. Wertz, P. Senellart, and J. Bloch, "Polariton light-emitting diode in a GaAs-based microcavity," *Phys. Rev. B*, vol. 77, p. 113303, Mar 2008.

[196] S. I. Tsintzos, N. T. Pelekanos, G. Konstantinidis, Z. Hatzopoulos, and P. G. Savvidis, "A GaAs polariton light-emitting diode operating near room temperature," *Nature*, vol. 453, p. 372, May 2008.

[197] S. I. Tsintzos, P. G. Savvidis, G. Deligeorgis, Z. Hatzopoulos, and N. T. Pelekanos, "Room temperature GaAs exciton-polariton light emitting diode," *Applied Physics Letters*, vol. 94, no. 7, p. 071109, 2009.

[198] J. Gu, B. Chakraborty, M. Khatoniar, and V. M. Menon, "A Room Temperature Polariton Light-Emitting Diode Based on Monolayer WS2," *arXiv e-prints*, p. arXiv:1905.12227, May 2019.

[199] T. Fujita and T. Ishihara, "Directionally enhanced photoluminescence from distributed feedback cavity polaritons," *Journal of the Physical Society of Japan*, vol. 68, no. 9, pp. 2918–2921, 1999.

[200] A. L. Yablonskii, E. A. Muljarov, N. A. Gippius, S. G. Tikhodeev, T. Fujita, and T. Ishihara, "Polariton effect in distributed feedback microcavities," *Journal of the Physical Society of Japan*, vol. 70, no. 4, pp. 1137–1144, 2001.

[201] M. Shimizu and T. Ishihara, "Subpicosecond transmission change in semiconductor–embedded photonic crystal slab: Toward ultrafast optical switching," *Applied Physics Letters*, vol. 80, no. 16, pp. 2836–2838, 2002.

[202] J. Ishi-Hayase and T. Ishihara, "Fundamental optical properties of photonic crystal slabs in the strong coupling regime," *Semiconductor Science and Technology*, vol. 18, no. 10, pp. S411–S418, 2003.

[203] K. Sumioka, H. Nagahama, and T. Tsutsui, "Strong coupling of exciton and photon modes in photonic crystal infiltrated with organic–inorganic layered perovskite," *Applied Physics Letters*, vol. 78, no. 10, pp. 1328–1330, 2001.

[204] G. Lanty, A. Bréhier, R. Parashkov, J. S. Lauret, and E. Deleporte, "Strong exciton–photon coupling at room temperature in microcavities containing two-dimensional layered perovskite compounds," *New Journal of Physics*, vol. 10, no. 6, p. 065007, 2008.

[205] Y. Wei, J. S. Lauret, L. Galmiche, P. Audebert, and E. Deleporte, "Strong exciton-photon coupling in microcavities containing new fluorophenethylamine based perovskite compounds," *Opt. Express*, vol. 20, no. 9, pp. 10399–10405, 2012.

[206] A. Brehier, R. Parashkov, J. S. Lauret, and E. Deleporte, "Strong exciton-photon coupling in a microcavity containing layered perovskite semiconductors," *Applied Physics Letters*, vol. 89, no. 17, p. 171110, 2006.

[207] K. Pradeesh, J. J. Baumberg, and G. V. Prakash, "Strong exciton-photon coupling in inorganic-organic multiple quantum wells embedded low-q microcavity," *Opt. Express*, vol. 17, no. 24, pp. 22171–22178, 2009.

[208] G. Lanty, J. S. Lauret, E. Deleporte, S. Bouchoule, and X. Lafosse, "Uv polaritonic emission from a perovskite-based microcavity," *Applied Physics Letters*, vol. 93, no. 8, p. 081101, 2008.

[209] G. Lanty, J. Lauret, E. Deleporte, S. Bouchoule, and X. Lafosse, "Uv polaritons at room temperature in a microcavity containing perovskites," *Journal of Luminescence*, vol. 129, no. 12, pp. 1985 – 1988, 2009.

[210] G. Lanty, *Réalisation et caractérisation optique de microcavités en régime de couplage fort mettant à profit la structure en multi-puits quantiques auto-organisés des pérovskites en couches minces.* PhD thesis, École normale supérieure de Cachan-ENS Cachan, 2011.

[211] J. Wenus, R. Parashkov, S. Ceccarelli, A. Brehier, J.-S. Lauret, M. S. Skolnick, E. Deleporte, and D. G. Lidzey, "Hybrid organic-inorganic exciton-polaritons in a strongly coupled microcavity," *Phys. Rev. B*, vol. 74, p. 235212, 2006.

[212] G. Lanty, S. Zhang, J. S. Lauret, E. Deleporte, P. Audebert, S. Bouchoule, X. Lafosse, J. Zuñiga Pérez, F. Semond, D. Lagarde, F. Médard, and J. Leymarie, "Hybrid cavity polaritons in a zno-perovskite microcavity," *Phys. Rev. B*, vol. 84, p. 195449, 2011.

[213] Z. Han, H.-S. Nguyen, F. Boitier, Y. Wei, K. Abdel-Baki, J.-S. Lauret, J. Bloch, S. Bouchoule, and E. Deleporte, "High-q planar organic–inorganic perovskite-based microcavity," *Opt. Lett.*, vol. 37, no. 24, pp. 5061–5063, 2012.

[214] Z. Han, H.-S. Nguyen, F. Réveret, K. Abdel-Baki, J.-S. Lauret, J. Bloch, S. Bouchoule, and E. Deleporte, "Top-mirror migration for the fabrication of high-QPlanar microcavities containing fragile active materials," *Applied Physics Express*, vol. 6, no. 10, p. 106701, 2013.

[215] H. S. Nguyen, Z. Han, K. Abdel-Baki, X. Lafosse, A. Amo, J.-S. Lauret, E. Deleporte, S. Bouchoule, and J. Bloch, "Quantum confinement of zero-dimensional hybrid organic-inorganic polaritons at room temperature," *Applied Physics Letters*, vol. 104, no. 8, p. 081103, 2014.

[216] A. Fieramosca, L. De Marco, M. Passoni, L. Polimeno, A. Rizzo, B. L. T. Rosa, G. Cruciani, L. Dominici, M. De Giorgi, G. Gigli, L. C. Andreani, D. Gerace, D. Ballarini, and D. Sanvitto, "Tunable out-of-plane excitons in 2d single-crystal perovskites," *ACS Photonics*, vol. 5, no. 10, pp. 4179–4185, 2018.

[217] F. Lédée, G. Trippé-Allard, H. Diab, P. Audebert, D. Garrot, J.-S. Lauret, and E. Deleporte, "Fast growth of monocrystalline thin films of 2d layered hybrid perovskite," *CrystEngComm*, vol. 19, pp. 2598–2602, 2017.

[218] J. Wang, R. Su, J. Xing, D. Bao, C. Diederichs, S. Liu, T. C. Liew, Z. Chen, and Q. Xiong, "Room temperature coherently coupled exciton–polaritons in two-dimensional organic–inorganic perovskite," *ACS Nano*, vol. 12, no. 8, pp. 8382–8389, 2018.

[219] K. Park, J. W. Lee, J. D. Kim, N. S. Han, D. M. Jang, S. Jeong, J. Park, and J. K. Song, "Light–matter interactions in cesium lead halide perovskite nanowire lasers," *The Journal of Physical Chemistry Letters*, vol. 7, no. 18, pp. 3703–3710, 2016.

[220] S. Zhang, Q. Shang, W. Du, J. Shi, Z. Wu, Y. Mi, J. Chen, F. Liu, Y. Li, M. Liu, Q. Zhang, and X. Liu, "Strong exciton–photon coupling in hybrid inorganic–organic

perovskite micro/nanowires," *Advanced Optical Materials*, vol. 6, no. 2, p. 1701032, 2018.

[221] S. Makarov, A. Furasova, E. Tiguntseva, A. Hemmetter, A. Berestennikov, A. Pushkarev, A. Zakhidov, and Y. Kivshar, "Halide-perovskite resonant nanophotonics," *Advanced Optical Materials*, vol. 7, no. 1, p. 1800784, 2019.

[222] X. Wang, M. Shoaib, X. Wang, X. Zhang, M. He, Z. Luo, W. Zheng, H. Li, T. Yang, X. Zhu, L. Ma, and A. Pan, "High-quality in-plane aligned cspbx3 perovskite nanowire lasers with composition-dependent strong exciton–photon coupling," *ACS Nano*, vol. 12, no. 6, pp. 6170–6178, 2018.

[223] Q. Shang, S. Zhang, Z. Liu, J. Chen, P. Yang, C. Li, W. Li, Y. Zhang, Q. Xiong, X. Liu, and Q. Zhang, "Surface plasmon enhanced strong exciton–photon coupling in hybrid inorganic–organic perovskite nanowires," *Nano Letters*, vol. 18, no. 6, pp. 3335–3343, 2018.

[224] W. Du, S. Zhang, J. Shi, J. Chen, Z. Wu, Y. Mi, Z. Liu, Y. Li, X. Sui, R. Wang, X. Qiu, T. Wu, Y. Xiao, Q. Zhang, and X. Liu, "Strong exciton–photon coupling and lasing behavior in all-inorganic cspbbr3 micro/nanowire fabry-pérot cavity," *ACS Photonics*, vol. 5, no. 5, pp. 2051–2059, 2018.

[225] R. Su, S. Ghosh, S. Liu, C. Diederichs, T. C. H. Liew, and Q. Xiong, "Observation of Exciton Polariton Condensation in a Perovskite Lattice at Room Temperature," *arXiv e-prints*, p. arXiv:1906.11566, Jun 2019.

[226] W. Bao, X. Liu, F. Zheng, Y. Xia, M. Zhao, J. Kim, S. Yang, Y. Wang, Y. Wang, L.-W. Wang, and X. Zhang, "Observation of solid state Rydberg exciton polariton and its condensate in a perovskite cavity," *arXiv e-prints*, p. arXiv:1803.07282, 2018.

[227] M. Era and N. Takada, "Squeezed-out technique to prepare high-quality pbbr-based layered perovskite langmuir–blodgett films applicable to cavity polariton devices," *Langmuir*, vol. 35, no. 37, pp. 12224–12228, 2019. PMID: 31339325.

[228] "Ossila guide for the spin-coating method," *https://www.ossila.com/pages/spin-coating*.

[229] M. Cadelano, V. Sarritzu, N. Sestu, D. Marongiu, F. Chen, R. Piras, R. Corpino, C. M. Carbonaro, F. Quochi, M. Saba, A. Mura, and G. Bongiovanni, "Can trihalide lead perovskites support continuous wave lasing?," *Advanced Optical Materials*, vol. 3, no. 11, pp. 1557–1564, 2015.

[230] N. Sultanova, S. Kasarova, and I. Nikolov, "Dispersion properties of optical polymers," *ACTA PHYSICA POLONICA A*, vol. 116, pp. 585–587, 10 2009.

[231] J.-S. Park, S. Choi, Y. Yan, Y. Yang, J. M. Luther, S.-H. Wei, P. Parilla, and K. Zhu, "Electronic structure and optical properties of α–$CH_3NH_3PbBr_3$ perovskite single crystal," *The Journal of Physical Chemistry Letters*, vol. 6, no. 21, pp. 4304–4308, 2015.

[232] P. B. Johnson and R. W. Christy, "Optical constants of the noble metals," *Phys. Rev. B*, vol. 6, pp. 4370–4379, Dec 1972.

[233] V. Savona, L. Andreani, P. Schwendimann, and A. Quattropani, "Quantum well excitons in semiconductor microcavities: Unified treatment of weak and strong coupling regimes," *Solid State Communications*, vol. 93, no. 9, pp. 733 – 739, 1995.

[234] C. B. Walsh and E. I. Franses, "Ultrathin pmma films spin-coated from toluene solutions," *Thin Solid Films*, vol. 429, no. 1, pp. 71 – 76, 2003.

[235] H. C. Woo, J. W. Choi, J. Shin, S.-H. Chin, M. H. Ann, and C.-L. Lee, "Temperature-dependent photoluminescence of ch3nh3pbbr3 perovskite quantum dots and bulk counterparts," *The Journal of Physical Chemistry Letters*, vol. 9, no. 14, pp. 4066–4074, 2018. PMID: 29975057.

[236] A. D. Wright, C. Verdi, R. L. Milot, G. E. Eperon, M. A. Pérez-Osorio, H. J. Snaith, F. Giustino, M. B. Johnston, and L. M. Herz, "Electron-phonon coupling in hybrid lead halide perovskites," *Nature Communications*, vol. 7, p. 11755, May 2016.

[237] M. I. Dar, G. Jacopin, S. Meloni, A. Mattoni, N. Arora, A. Boziki, S. M. Zakeeruddin, U. Rothlisberger, and M. Grätzel, "Origin of unusual bandgap shift and dual emission in organic-inorganic lead halide perovskites," *Science Advances*, vol. 2, no. 10, 2016.

[238] L. C. Flatten, S. Christodoulou, R. K. Patel, A. Buccheri, D. M. Coles, B. P. L. Reid, R. A. Taylor, I. Moreels, and J. M. Smith, "Strong exciton-photon coupling with colloidal nanoplatelets in an open microcavity," *Nano Letters*, vol. 16, no. 11, pp. 7137–7141, 2016.

[239] T. Virgili, D. Coles, A. M. Adawi, C. Clark, P. Michetti, S. K. Rajendran, D. Brida, D. Polli, G. Cerullo, and D. G. Lidzey, "Ultrafast polariton relaxation dynamics in an organic semiconductor microcavity," *Phys. Rev. B*, vol. 83, p. 245309, Jun 2011.

[240] G. Christmann, R. Butté, E. Feltin, A. Mouti, P. A. Stadelmann, A. Castiglia, J.-F. m. c. Carlin, and N. Grandjean, "Large vacuum rabi splitting in a multiple quantum well gan-based microcavity in the strong-coupling regime," *Phys. Rev. B*, vol. 77, p. 085310, Feb 2008.

[241] D. Baxter, M. S. Skolnick, A. Armitage, V. N. Astratov, D. M. Whittaker, T. A. Fisher, J. S. Roberts, D. J. Mowbray, and M. A. Kaliteevski, "Polarization-dependent phenomena in the reflectivity spectra of semiconductor quantum microcavities," *Phys. Rev. B*, vol. 56, pp. R10032–R10035, oct 1997.

[242] J. Wang, R. Cao, P. Da, Y. Wang, T. Hu, L. Wu, J. Lu, X. Shen, F. Xu, G. Zheng, and Z. Chen, "Purcell effect in an organic-inorganic halide perovskite semiconductor microcavity system," *Applied Physics Letters*, vol. 108, no. 2, p. 022103, 2016.

[243] V. Sarritzu, N. Sestu, D. Marongiu, X. Chang, Q. Wang, M. A. Loi, F. Quochi, M. Saba, A. Mura, and G. Bongiovanni, "Perovskite excitonics: Primary exciton creation and crossover from free carriers to a secondary exciton phase," *Advanced Optical Materials*, vol. 6, no. 3, p. 1700839, 2018.

[244] Hui Cao, J. Y. Xu, Yong Ling, A. L. Burin, E. W. Seeling, Xiang Liu, and R. P. H. Chang, "Random lasers with coherent feedback," *IEEE Journal of Selected Topics in Quantum Electronics*, vol. 9, pp. 111–119, Jan 2003.

[245] R. Ambartsumyan, N. Basov, P. Kryukov, and V. Letokhov, "5a10(b) - a laser with a nonresonant feedback," *IEEE Journal of Quantum Electronics*, vol. 2, pp. 442–446, Sep. 1966.

[246] V. Letokhov, "Generation of light by a scattering medium with negative resonance absorption," *Soviet Journal of Experimental and Theoretical Physics*, vol. 26, p. 835, 1968.

[247] H. Cao, Y. G. Zhao, S. T. Ho, E. W. Seelig, Q. H. Wang, and R. P. H. Chang, "Random laser action in semiconductor powder," *Phys. Rev. Lett.*, vol. 82, pp. 2278–2281, Mar 1999.

[248] S. V. Frolov, Z. V. Vardeny, K. Yoshino, A. Zakhidov, and R. H. Baughman, "Stimulated emission in high-gain organic media," *Phys. Rev. B*, vol. 59, pp. R5284–R5287, Feb 1999.

[249] F. Luan, B. Gu, A. S. Gomes, K.-T. Yong, S. Wen, and P. N. Prasad, "Lasing in nanocomposite random media," *Nano Today*, vol. 10, no. 2, pp. 168 – 192, 2015.

[250] L. Sznitko, J. Mysliwiec, and A. Miniewicz, "The role of polymers in random lasing," *Journal of Polymer Science Part B: Polymer Physics*, vol. 53, no. 14, pp. 951–974, 2015.

[251] D. S. Wiersma, "The physics and applications of random lasers," *Nature Physics*, vol. 4, p. 359, May 2008.

[252] H. Cao, "Review on latest developments in random lasers with coherent feedback," *Journal of Physics A: Mathematical and General*, vol. 38, pp. 10497–10535, nov 2005.

[253] Y. Liu, W. Yang, S. Xiao, N. Zhang, Y. Fan, G. Qu, and Q. Song, "Surface-emitting perovskite random lasers for speckle-free imaging," *ACS Nano*, vol. 13, no. 9, pp. 10653–10661, 2019. PMID: 31430124.

[254] X. Tang, Y. Bian, Z. Liu, J. Du, M. Li, Z. Hu, J. Yang, W. Chen, and L. Sun, "Room-temperature up-conversion random lasing from cspbbr3 quantum dots with tio2 nanotubes," *Opt. Lett.*, vol. 44, pp. 4706–4709, Oct 2019.

[255] H. Cao, Y. G. Zhao, H. C. Ong, S. T. Ho, J. Y. Dai, J. Y. Wu, and R. P. H. Chang, "Ultraviolet lasing in resonators formed by scattering in semiconductor polycrystalline films," *Applied Physics Letters*, vol. 73, pp. 3656–3658, dec 1998.

[256] H. Cao, Y. G. Zhao, H. C. Ong, and R. P. H. Chang, "Far-field characteristics of random lasers," *Phys. Rev. B*, vol. 59, pp. 15107–15111, Jun 1999.

[257] R. C. Polson and Z. V. Vardeny, "Spatially mapping random lasing cavities," *Optics Letters*, vol. 35, p. 2801, aug 2010.

[258] L. Sznitko, A. Szukalski, K. Cyprych, P. Karpinski, A. Miniewicz, and J. Mysliwiec, "Surface roughness induced random lasing in bio-polymeric dye doped film," *Chemical Physics Letters*, vol. 576, pp. 31–34, jun 2013.

[259] B. Redding, M. A. Choma, and H. Cao, "Speckle-free laser imaging using random laser illumination," *Nature Photonics*, vol. 6, pp. 355–359, June 2012.

[260] S. K. Turitsyn, S. A. Babin, A. E. El-Taher, P. Harper, D. V. Churkin, S. I. Kablukov, J. D. Ania-Castañón, V. Karalekas, and E. V. Podivilov, "Random distributed feedback fibre laser," *Nature Photonics*, vol. 4, pp. 231–235, feb 2010.

[261] Q. Song, L. Liu, and L. Xu, "Directional random-laser emission from bragg gratings with irregular perturbation," *Optics Letters*, vol. 34, p. 344, jan 2009.

[262] X. T. Long, Q. F. Dai, H. H. Fan, Z. C. Wei, M. M. Wu, and H. Z. Wang, "Dominant mode in closed photonic crystal microcavity filled with high scattering irregular gain medium," *Applied Physics Letters*, vol. 89, p. 251105, dec 2006.

[263] Q. Song, L. Liu, S. Xiao, X. Zhou, W. Wang, and L. Xu, "Unidirectional high intensity narrow-linewidth lasing from a planar random microcavity laser," *Phys. Rev. Lett.*, vol. 96, p. 033902, Jan 2006.

[264] Q. Song, S. Xiao, X. Zhou, L. Liu, L. Xu, Y. Wu, and Z. Wang, "Liquid-crystal-based tunable high-q directional random laser from a planar random microcavity," *Opt. Lett.*, vol. 32, pp. 373–375, Feb 2007.

[265] Q. Song, L. Liu, L. Xu, Y. Wu, and Z. Wang, "Electrical tunable random laser emission from a liquid-crystal infiltrated disordered planar microcavity," *Optics Letters*, vol. 34, p. 298, jan 2009.

[266] P. N. Ni, C. X. Shan, S. P. Wang, Y. J. Lu, B. H. Li, and D. Z. Shen, "Fabry-perot resonance enhanced electrically pumped random lasing from ZnO films," *Applied Physics Letters*, vol. 107, p. 231108, dec 2015.

[267] S. Schönhuber, M. Brandstetter, T. Hisch, C. Deutsch, M. Krall, H. Detz, A. M. Andrews, G. Strasser, S. Rotter, and K. Unterrainer, "Random lasers for broadband directional emission," *Optica*, vol. 3, pp. 1035–1038, Oct 2016.

[268] T. Hisch, M. Liertzer, D. Pogany, F. Mintert, and S. Rotter, "Pump-controlled directional light emission from random lasers," *Phys. Rev. Lett.*, vol. 111, p. 023902, Jul 2013.

[269] R. Niyuki, H. Fujiwara, T. Nakamura, Y. Ishikawa, N. Koshizaki, T. Tsuji, and K. Sasaki, "Double threshold behavior in a resonance-controlled zno random laser," *APL Photonics*, vol. 2, no. 3, p. 036101, 2017.

[270] Y. Feng and K.-i. Ueda, "One-mirror random laser," *Phys. Rev. A*, vol. 68, p. 025803, Aug 2003.

Résumé de la thèse

Depuis 2012, les pérovskites hybrides halogénées de type $CH_3NH_3PbX_3$ (X = I, Br ou Cl) sont apparues comme très prometteuses non seulement dans le domaine du photovoltaïque mais aussi pour les dispositifs émetteurs de lumière comme les diodes électroluminescentes (LEDs) et les lasers. L'un des avantages cruciaux de ces matériaux semiconducteurs est leur méthode de déposition à basse température et en solution. L'ajustement de la longueur d'onde d'émission des pérovskites dans tout le spectre visible par de simples substitutions chimiques dand la partie halogénée est un autre atout. En particulier, les pérovskites halogénées montrent une grande efficacité de luminescence dans le vert et pourraient répondre au problème du « green gap » dans les sources laser (le « green gap » fait référence à la faible efficacité des diodes électroluminescente et diodes laser à semi-conducteurs dans le vert).

Par ailleurs, les polaritons excitoniques de cavité suscitent un vif intérêt dans la recherche car permettant l'élaboration de lasers polaritoniques à très bas seuil. Les polaritons excitoniques de cavité sont des quasiparticules, mi-lumière mi-matière, résultant du régime de couplage fort entre un mode photonique dans une microcavité et les excitons d'un semiconducteur, paires électron-trou liées par l'interaction de Coulomb. D'intrigantes propriétés physiques proviennent de la nature hybride des polaritons excitoniques et l'une d'entre elles est la condensation de Bose-Einstein des polaritons excitoniques. La condensation de polaritons dans une microcavité entraîne l'émission d'une lumière cohérente amplifiée et est par conséquent également appelée laser polaritonique. Ce mécanisme particulier permet d'atteindre des seuils lasers de deux ordres de grandeur inférieurs à ceux des lasers habituels.

Ce manuscript s'inscrit dans les contextes des pérovskites halogénées, du problème du « green gap » pour les LEDS et les diodes lasers, et des polaritons excitoniques de cavités. Il présente l'étude de microcavités contenant la pérovskite bromée $CH_3NH_3PbBr_3$ émettant dans le vert dans la perspective de réaliser des microlasers.

Le chapitre 1 présente dans un premier temps les concepts physiques des régimes de couplage faible et fort et les différences entre les lasers conventionnels et les lasers polaritoniques. La deuxième partie du chapitre concerne l'état de l'art des pérovskites halogénées dans les domaines des lasers conventionnels, des polaritons excitoniques et des lasers polaritoniques.

Le chapitre 2 présente les méthodes expérimentales utilisées au cours de la thèse : méthodes de dépôt de la pérovskite, caractérisations du matériau, montages optiques tels que spectroscopie de photoluminescence (PL) et spectroscopie de Fourier permettant de réaliser des mesures de réflectivité et de photoluminescence résolues en angle.

Le chapitre 3 détaille la conception, la réalisation et les mesures de caractérisation de la microcavité à base de $CH_3NH_3PbBr_3$. Une microcavité de grande surface à base de $CH_3NH_3PbBr_3$ est ensuite fabriquée et sa rugosité est étudiée.

Dans le chapitre 4, le régime de couplage fort de la microcavité à base de $CH_3NH_3PbBr_3$ est démontré par des mesures de réflectivité et de photoluminescence résolues en angle. Dans ce chapitre, la microcavité est pompée à de faibles densités. Ce résultat constitue la première observation du régime de couplage fort contenant une couche de pérovskite 3D déposée par spin-coating. De plus, le régime de couplage fort est obtenu avec un milieu à gain de grande surface, à faible coût de production et avec de bonnes propriétés de transport de charge, ce qui est intéressant pour réaliser des dispositifs polaritoniques.

Dans le chapitre 5, l'action laser de la microcavité à base de $CH_3NH_3PbBr_3$ est étudiée. Une émission de laser aléatoire (« Random lasing » en anglais) dans le vert, filtrée directionnellement par la courbe de dispersion des polaritons de basses énergies, est démontrée. L'angle d'émission peut être contrôlé en modifiant le désaccord de la microcavité, c'est-à-dire la différence entre l'énergie du mode photonique de la cavité et l'énergie de l'exciton de la pérovskite. En plus de son intérêt fondamental, le système étudié dans cette thèse, permettant le contrôle de l'angle de l'émission du laser aléatoire jusqu'à de grandes valeurs d'angle, présente un intérêt pour certaines applications optoélectroniques, de type LIDAR notamment.

université PARIS-SACLAY

ÉCOLE DOCTORALE
Ondes et Matière
(EDOM)

Titre : Lasers à pérovskites hybrides halogénées en microcavité

Mots clés : Laser, Pérovskite hybride, Couplage fort, Polariton, Laser Aléatoire

Résumé :
Depuis 2012, les pérovskites hybrides halogénées de type $CH_3NH_3PbX_3$ (X = I, Br ou Cl) sont apparues comme très prometteuses non seulement dans le domaine du photovoltaïque mais aussi pour les dispositifs émetteurs de lumière comme les diodes électroluminescentes et les lasers. L'un des avantages cruciaux de ces matériaux semiconducteurs est leur méthode de déposition à basse température et en solution. Le réglage de la longueur d'onde d'émission des pérovskites dans tout le spectre visible par de simples substitutions chimiques dans la partie halogénée est un autre atout. En particulier, les pérovskites halogénées montrent une grande efficacité de luminescence dans le vert et pourraient répondre au problème du "green gap" dans les sources laser (le "green gap" fait référence à la baisse d'efficacité des diodes électroluminescente et diodes laser à semi-conducteurs émettant dans le vert).
Le travail de doctorat mené ici a porté sur la réalisation d'un laser pompé optiquement à base de la pérovskite hybride $CH_3NH_3PbBr_3$ émettant dans le vert. La structure réalisée consiste en une microcavité verticale à base d'une couche mince de 100 nanomètres de $CH_3NH_3PbBr_3$ déposé par "spin-coating" (dépôt par enduction centrifuge), insérée entre un miroir diélectrique et un miroir métallique. Nous avons démontré, à température ambiante, le régime de couplage fort entre le mode photonique de la microcavité et l'exciton de la pérovskite. Ce régime de couplage fort conduit à la création de quasi-particules appelées les polaritons excitoniques, qui sont une superposition cohérente d'états photonique et excitonique. En augmentant la puissance injectée optiquement, nous avons obtenu un effet laser dans cette microcavité. L'étude des propriétés d'émission de ce laser met en évidence que nous avons réalisé un laser aléatoire, émettant dans le vert, filtré directionnellement par la courbe de dispersion du polariton de basse énergie. Ce filtrage par la courbe de dispersion du polariton permet le contrôle de la directionnalité de l'émission laser sur une grande gamme d'angles : des angles aussi grands que 22° ont été obtenus expérimentalement.

Title : Hybrid halide perovskite-based microcavity lasers

Keywords : Laser, Hybrid perovskite, Strong coupling, Polariton, Random lasing

Abstract :
Since 2012, the hybrid halide perovskites of $CH_3NH_3PbX_3$ (X = I, Br or Cl) type have emerged as very promising not only in the field of photovoltaics but also for light-emitting devices such as light-emitting diodes and lasers. One of the crucial advantages of these semiconductor materials is their low temperature and solution deposition method. The tuning of the perovskites emission wavelength throughout the visible spectrum by simple chemistry substitutions in the halogenated part is another asset. In particular, the halide perovskites show a high luminescence efficiency in the green and could address the "green gap" problem in laser sources (the "green gap" refers to the drop in efficiency of light-emitting diodes and laser diodes emitting in the green).
The thesis work carried out here is focused on the development of an optically pumped laser based on the hybrid halide perovskite $CH_3NH_3PbBr_3$ emitting in the green. The structure consists of a vertical microcavity based on a 100-nanometre thin film of $CH_3NH_3PbBr_3$ deposited by spin-coating, inserted between a dielectric mirror and a metal mirror. We have demonstrated, at room temperature, the strong coupling regime between the microcavity photonic mode and the exciton of the perovskite. This strong coupling regime leads to the creation of quasi-particles called exciton-polaritons, which are a coherent superposition of photonic and excitonic states. By increasing the optically injected power, we obtained a laser effect in this microcavity. The study of the emission properties of this laser shows that we have produced a random laser, emitting in the green, filtered directionally by the dispersion curve of the lower polariton. This filtering by the polariton dispersion curve allows the directionality of the laser emission to be controlled over a wide range of angles: angles as large as 22° were obtained experimentally.

Université Paris-Saclay
Espace Technologique / Immeuble Discovery
Route de l'Orme aux Merisiers RD 128 / 91190 Saint-Aubin, France